



UNIVERSITÀ DEGLI STUDI DI PADOVA

Dipartimento di Geoscienze
Scuola di Dottorato di Ricerca in Scienze della Terra
Ciclo XXI

SNOW AVALANCHES: HAZARD MAPS AND PASSIVE DEFENCE STRUCTURES

Direttore della Scuola: Ch.mo Prof. Gilberto ARTIOLI

Supervisore: Ch.mo Prof. Rinaldo GENEVOIS

Cotutore: Ch.mo Prof. Paolo SCOTTON

Dottorando: Francesca MORO



UNIVERSITÀ DEGLI STUDI DI PADOVA

Dipartimento di Geoscienze
Scuola di Dottorato di Ricerca in Scienze della Terra
Ciclo XXI

SNOW AVALANCHES: HAZARD MAPS AND PASSIVE DEFENCE STRUCTURES

Direttore della Scuola: Ch.mo Prof. Gilberto ARTIOLI

Supervisore: Ch.mo Prof. Rinaldo GENEVOIS

Cotutore: Ch.mo Prof. Paolo SCOTTON

Dottorando: Francesca MORO

2 febbraio 2009

To my husband

Abstract

In Alpine regions snow avalanches are a severe threat for human settlements, activities, and infrastructures. Such natural phenomena may be of two types: powder avalanches and dense snow avalanches. The countermeasures against powder avalanches consist in preventing the initiation of the motion by means of active structures built in the detachment area, or artificially triggering avalanche events. Passive defence structures along the path and in the run-out zone can instead be very effective in deflecting, retarding, or stopping dense snow avalanches.

In this thesis some aspects of dense snow avalanches have been experimentally investigated using a granular mass. Small-scale laboratory tests have been performed to study the different types of deposit that dense snow avalanches can form and to measure the impact force on retarding structures positioned along the run-out zone.

A procedure for the estimation of dense snow avalanches hazard maps has been defined and the effects of the selected parameters have been analysed.

Introduction

Much field evidence proves that dense snow avalanches, after a first phase of granulation, move downstream and stop in almost the same way as granular materials.

Recent detailed measurements [Rognon, 2006], made in a large scale channel using real snow, evidenced a thin layer -just above the base- made of granular snow, as a result of granulation. Most of the velocity occurs in this layer whilst the upper mass moves almost undisturbed.

Due to the above observations dense snow avalanches are often modelled adopting small-scale laboratory experiments, using dry granular materials that flow down an inclined plane.

Many small-scale [Sheikh et al., 2008; Faug et al., 2004] and large-scale laboratory tests [Hákonardóttir et al., 2003; Jaedicke et al., 2008] on snow avalanches have evidenced an important dissipation of the flow energy in the presence of retarding structures, and have investigated the impact force to define project parameters [for instance Isaenko; Favier & Daudon; Kulibaba & Eglit, 2008; Jóhannesson et al., 2008].

1.1 Experimental analysis on the characterization of avalanche deposits

In order to analyse the influence of grain size distribution of the granular material mixture that simulates dense snow avalanches, experimental investigation was carried out at the *Laboratoire Avalanche ETNA – Cemagref – Groupement de Grenoble* in France.

The tests consisted in releasing from a feeding-box a mass of glass beads that first flowed down an inclined channel and finally spread out on an inclined unconfined deposition zone. The mass ratio between fine grains (150 μm – 250 μm) and large grains (1 mm), in the released mass, was systematically changed to determine its influence on:

- 1) the incoming flow depth and front velocity in the channel, measured by a laser line technique;
- 2) the shape of the deposited mass, measured by an accurate fringe analysis technique [Surrel, 1993].

1.2 Passive defence structures: experimental analysis on retarding mounds

So far the design of passive defence structures has been empirical and based mostly on the experience of technicians. The problem can be faced studying the effect of the use of retarding elements in terms of energy dissipation of the moving mass and analysing the impact against these same retarding elements. This second point of view has been adopted in this research.

In order to analyse the behaviour of some defence structures used in the practice of environmental engineering to slow down dense snow avalanches, an experimental investigation

was performed at the *Laboratorio di Idraulica – Università di Trento*. Retarding cone-shaped and tooth-shaped structures organized in a system of three elements arranged in two lines were used.

The tests were performed in a flume using granular zeolite (average diameter of about 1 mm). The experimental set-up of the physical model can simulate real phenomena following the Froude similarity with a geometrical scale of about 1/100.

1.3 The *Val dei Spini* avalanche site

Avalanche zoning plans are usually the result of government decisions [Barbolini et al., 2005]. Normally, in Italy, the hazard zone is divided into three areas with respect to a return period T_r : a red area ($T_r = 30$ years), a blue area ($T_r = 100$ years), and a yellow area ($T_r = 300$ years). The different areas are defined by the conjunction of the points representing the stopping distances, along different trajectories, that the mass can travel for the same return period.

A procedure for the determination of the snow avalanches hazard maps was sketched and the physical parameters of the numerical-mathematical model were calibrated on the basis of the knowledge of two events related.

Conclusions

The experimental analyses show that the main characteristics of the deposits are strongly influenced by the ratio between fine and large particles. It was observed that the maximum stopping distance was obtained with a poorly sorted material composition.

Similar results, attributed to segregation processes, were also shown in recent literature concerning laboratory tests made by Phillips et al. (2006) and numerical simulations made by Linares-Guerrero et al. (2007).

Moreover, the experimental analyses offer some criteria for the estimation of the total impact force against retarding elements designed to reduce stopping distance and to favour the spread of the flowing mass. The most efficient layout of the elements is presented and it has been observed that the maximum efficiency occurs with the maximum dimensionless force.

Riassunto

Nelle regioni Alpine le valanghe di neve rappresentano una grave minaccia per gli insediamenti, le attività e le infrastrutture realizzate dall'uomo. Tali fenomeni sono suddivisi in valanghe polverose e valanghe di neve densa. La difesa contro le valanghe di neve polverosa è quella di prevenire l'innesco della valanga per mezzo di opere di difesa attiva, realizzate nell'area di distacco, o di provocare artificialmente gli eventi valanghivi. Le opere di difesa passiva, invece, possono essere molto efficaci nel deviare, rallentare o arrestare valanghe di neve densa lungo il percorso e nella zona di arresto.

In questa tesi sono stati presi in considerazione alcuni aspetti delle valanghe di neve densa utilizzando una massa granulare. Test sperimentali in scala ridotta sono stati realizzati per studiare i differenti tipi di deposito che le valanghe di neve densa possono formare e per misurare la forza d'impatto sulle opere di rallentamento, posizionate lungo la zona di deposito.

È stata definita una procedura per la definizione delle carte di pericolosità per le valanghe di neve densa e sono stati analizzati gli effetti dei parametri scelti.

Introduzione

Molte osservazioni di campo dimostrano che le valanghe di neve densa, dopo una prima fase di granulazione, si muovono verso valle e si arrestano quasi allo stesso modo dei materiali granulari.

Recenti e dettagliate misure [Rognon, 2006], ottenute in un canale a grande scala utilizzando neve reale, hanno messo in evidenza un sottile strato -appena al di sopra del fondo- costituito da neve granulare prodotta dalla granulazione. Il maggior gradiente di velocità si verifica in questo strato mentre la massa superiore si muove quasi indisturbata.

A causa delle osservazioni precedenti le valanghe di neve densa sono spesso modellate con modelli sperimentali in scala ridotta, utilizzando materiale granulare secco che scende giù da un piano inclinato.

Molte analisi sperimentali in scala ridotta [Sheikh et al., 2008; Faug et al., 2004] e in grande scala [Hákonardóttir et al., 2003; Jaedicke et al., 2008] sulle valanghe di neve hanno evidenziato un'importante dissipazione dell'energia di flusso in presenza delle opere di rallentamento, e hanno indagato la forza di impatto per definire i parametri di progetto [per esempio Isaenko; Favier & Daudon; Kulibaba & Eglit, 2008; Jóhannesson et al., 2008].

1.1 Analisi sperimentale sulla caratterizzazione dei depositi valanghivi

Per studiare l'influenza della distribuzione della dimensione dei grani della miscela granulare che simula le valanghe di neve densa, è stata realizzata un'analisi sperimentale al *Laboratoire Avalanches ETNA – Cemagref – Groupement de Grenoble* in Francia.

I test sono stati realizzati rilasciando da un serbatoio una massa di biglie di vetro che, dopo essere scivolata giù per un piano inclinato, si sparge su una zona inclinata e non confinata. Il rapporto di massa tra grani fini (150 μm – 250 μm) e grani grossi (1 mm), nella massa rilasciata, è stato sistematicamente cambiato per quantificare la sua influenza su:

- 1) l'altezza di flusso e la velocità del fronte nel canale, misurato con la tecnica del segmento laser;
- 2) la forma del deposito, misurata con un'accurata tecnica di frange interferometriche [Surrel, 1993].

1.2 Opere di difesa passiva: analisi sperimentale su cumuli frenanti

Fino ad oggi la progettazione di opere di difesa passive è stata sperimentale e basata principalmente sull'esperienza dei tecnici. Il problema può essere affrontato studiando l'effetto

della presenza delle opere di rallentamento in termini di energia di dissipazione della massa in movimento e analizzando l'impatto contro gli stessi elementi di rallentamento. Questo secondo punto di vista è stato scelto in questa ricerca.

Per analizzare il comportamento di alcune strutture di difesa utilizzate nella pratica dell'ingegneria ambientale per rallentare valanghe di neve densa, è stato realizzato uno studio sperimentale al *Laboratorio di Idraulica – Università di Trento*. Sono stati utilizzati coni e denti frenanti in un sistema di tre elementi disposti su due linee.

I test sono stati eseguiti su una canaletta utilizzando zeolite granulare (diametro medio di circa 1 mm). L'apparato sperimentale del modello fisico può simulare fenomeni reali seguendo la similitudine di Froude con una scala geometrica di circa 1/100.

1.3 Il sito valanghivo della *Val dei Spini*

I piani di zonazione valanghiva sono spesso il risultato di decisioni governative [Barbolini et al., 2005]. Normalmente, in Italia, la zona di pericolosità è divisa in tre aree relative ad un periodo di ritorno T_r : la zona rossa ($T_r = 30$ anni), la zona blu ($T_r = 100$ anni), e la zona gialla ($T_r = 300$ anni). Le differenti aree sono definite dall'unione dei punti che rappresentano le distanze di arresto, lungo differenti traiettorie, che la massa può raggiungere per lo stesso tempo di ritorno.

Una procedura per la determinazione della mappa della pericolosità valanghiva è stata presentata, e i parametri fisici del modello numerico-matematico sono stati calibrati sulla base della conoscenza di due relativi eventi.

Conclusioni

Le analisi sperimentali mostrano che le principali caratteristiche dei depositi sono fortemente influenzate dal rapporto tra grani fini e grani grossi. È stato osservato che la massima distanza d'arresto è stata ottenuta nel caso di una composizione del materiale distribuita granulometricamente.

Risultati simili, attribuiti a processi di segregazione, sono stati presentati recentemente anche in letteratura da test di laboratorio in Phillips et al. (2006) e da simulazioni numeriche in Linares-Guerrero et al. (2007).

Inoltre, le analisi sperimentali forniscono alcuni criteri per la stima della forza d'impatto totale contro le opere di rallentamento, progettate per ridurre la distanza d'arresto e favorire lo spargimento della massa in movimento. È presentata la disposizione delle opere più efficiente e si è osservato che la massima efficienza si è verificata con la massima forza adimensionalizzata.

Acknowledgements

This doctoral thesis was written at the *Dipartimento di Geoscienze – Università degli Studi di Padova* between 2006–2008.

I would like to thank the two reviewers of my thesis to obtain the label of *Doctor Europaeus* and my Ph.D. Commission:

- ~ Prof. Pascal Allemand, *Université Claude Bernard Lyon 1*;
- ~ Prof. Wilfried Haeblerli, *Universität Zürich*;

- ~ Prof. Johannes Hübl, *Universität für Bodenkultur Wien*;
- ~ Prof. Luigi Natale, *Università degli Studi di Pavia*;
- ~ Prof. Fabio Trivellato, *Università degli Studi di Trento*.

Parts of this thesis were written while visiting the *Cemagref de Grenoble* and the *Università di Trento*. The friendly welcome from each research groups made my stay both rewarding and pleasant.

I would like to thank:

ETNA – Unité de Recherche Erosion Torrentielle Neige et Avalanches – Cemagref – Groupement de Grenoble

Thierry Faug, “*mon maître de stage*”, to have followed my research and advancement during my training, for his availability and to have worked with me in the “*Soufflerie*” of *ETNA*; Hervé Bellot, to have allowed the realization of the fringe analysis technique in the experimental analysis and to have developed the protocol for the image processing; Frédéric Ousset, to have allowed a logistic support during all my experimental tests; Richard Didier and Mohamed Naaim, for the opportunity of visiting and conducting experiments at the *Laboratoire Avalanche*;

DICA – Dipartimento di Ingegneria Civile e Ambientale – Università di Trento

Patrizia Pederzoli, for her teachings on experimental analysis and to have worked with me in the laboratory of *DICA*; Fabio Sartori and Andrea BOMPI, to have allowed a logistic support during all my experimental tests and Prof. Aronne Armanini for the opportunity of visiting and conducting experiments at the *Laboratorio di Idraulica e Difesa del Suolo*.

I would like also to acknowledge:

CVA – Centro Valanghe di Arabba ARPAV

Alvise Tommaselli, for his advices and the trip to visiting avalanche sites with passive defence structures; Francesca Pasqualini, for her teachings on *Monte Pizazzac* test site; Piergiorgio Pallua, for his very precious teachings on avalanche modelling and the review of my thesis and Francesco Sommavilla, for the opportunity of visiting the Centre;

SLF – Swiss Federal Institute of Snow and Avalanche Research of Davos

Betty Sovilla, for her advices on my Ph.D. project and for her teachings on *Monte Pizazzac* and *Vallée de la Sionne* test sites and Perry Bartelt, for the opportunity of visiting the Institute;

Ufficio Previsioni e Organizzazione – Provincia Autonoma di Trento

Alberto Trenti, Marco Gadotti and Sergio Benigni, for the technical support in the study of the *Val dei Spini*.

I would like also to acknowledge my supervisors:

Prof. Rinaldo Genevois, for his scientific and also personal advices in these three Ph.D. years and Prof. Paolo Scotton, for his invaluable help, scientific advices and the several reviews of my thesis proof;

and all my office-mates:

Giordano Teza, for the personal and technical advices on my research and the publication, like co-author, of my first paper on a international revue; Cristina Squarzoni, for her constant encouragement and her reviews in French language; Luca Bertoldi, for helping me in the realisation of the GIS model to study the *Val dei Spini*; Silvia Mittempergher, for the references about the tectonical setting of the *Val dei Spini* and the “unforgettable” trip to Vienna for the EGU Congress; Maria Concetta Armento, to have divided with me her office at *Palazzo Cavalli* in my first Ph.D. year, her infinite patience with my personal problems and her advices about FLO-2D model; Prof. Silvana Martin, for her availability to contact the reviewers to obtain the label of *Doctor Europaeus*; Prof. Roberto Sedeà, for his joy in all my depression moments and to calling me “Signora Ingegnere”. Thanks also to: Lidia Pittarello, Lorenza Giacomini, Matteo Cultrera, Enrico Marcolongo, Alessia Rosignoli, Elisa Destro, Martina Stefani and Alessia Viero.

At last, thank you to all the people who have expenses a little of your precious time to help me on my research work.

CONTENTS

Abstract	I
Riassunto	III
Acknowledgements	V
List of Figures	XI
List of Tables	XXI
1. INTRODUCTION	1
1.1. Snow avalanche defence.....	1
1.2. Avalanche forecasting.....	1
1.3. Avalanche hazard mapping.....	2
1.4. Technical defence measures.....	2
2. SNOW AVALANCHES	5
2.1. Snow and avalanches rheology.....	5
2.2. Snow metamorphism.....	7
2.3. Avalanche formation.....	9
2.4. Avalanche path.....	10
2.5. Avalanche classification.....	11
3. AVALANCHE STUDY	15
3.1. Data collection.....	15
3.1.1. Historical analysis.....	15
3.1.2. Field measurements.....	16
3.1.3. Statistical analysis of snow-meteorological data.....	19
3.1.4. Monitoring systems.....	22
3.1.4.1. Monte Pizzac – Italy.....	23
3.1.4.2. Vallée de la Sionne – Switzerland.....	24
3.1.4.3. Col du Lautaret – France.....	25
3.2. Experimental analysis.....	26
3.2.1. Models theory.....	28
3.2.2. Froude Number.....	29
3.3. Numerical-mathematical analysis.....	29
3.3.1. Avalanche statistical models.....	30
3.3.2. Dense avalanche dynamic models.....	30
4. HAZARD MAPS AND PASSIVE DEFENCE STRUCTURES	35
4.1. Avalanche hazard zoning.....	35
4.1.1. European avalanche hazard scale.....	35
4.1.2. Snow-meteorological bulletins.....	36
4.1.3. Maps of avalanche probable localisation.....	38
4.1.4. Italian law references.....	38
4.1.5. Avalanches hazard zones and hazard maps.....	39

4.2.	Avalanche protection structures.....	42
4.2.1.	Preventive or temporary protection.....	42
4.2.2.	Permanent protection: active defence structures.....	46
4.2.3.	Permanent protection: passive defence structures.....	51
4.2.3.1.	Deflecting dams.....	52
4.2.3.2.	Retarding or braking mounds.....	61
4.2.3.3.	Catching dams.....	67
4.2.3.4.	Direct protection structures.....	73
4.2.4.	Criteria to choose protection structures.....	86
5.	EXPERIMENTAL ANALYSIS ON THE CHARACTERIZATION OF AVALANCHE DEPOSITS.....	89
5.1.	Experimental set-up.....	89
5.2.	Instrumentation.....	92
5.3.	The material.....	97
5.4.	The calibration.....	97
5.5.	Preliminary tests.....	98
5.5.1.	Measurements techniques of the preliminary tests.....	99
5.5.2.	Preliminary results.....	99
5.6.	Measurements techniques of the tests.....	100
5.6.1.	Laser line technique.....	101
5.6.2.	Fringe analysis technique.....	104
5.7.	Experimental tests.....	112
5.8.	Test results.....	113
5.9.	Conclusions.....	118
6.	EXPERIMENTAL ANALYSIS OF RETARDING STRUCTURES IN THE DEFENCE AGAINST DENSE SNOW AVALANCHES.....	119
6.1.	Experimental set-up.....	119
6.2.	Instrumentation.....	122
6.3.	The retarding structures.....	127
6.4.	The support of the slowing down elements.....	131
6.5.	The material.....	135
6.6.	The calibration.....	135
6.7.	Measurement techniques.....	137
6.8.	Experimental tests.....	140
6.9.	Test results.....	142
6.10.	Conclusions.....	157
7.	NUMERICAL-MATHEMATICAL ANALYSIS OF A STUDY SITE: THE <i>VAL DEI SPINI</i> AVALANCHE.....	159
7.1.	The study site: the <i>Val dei Spini</i> avalanche.....	160
7.1.1.	Geographical setting.....	160
7.1.2.	Geological setting.....	161
7.1.3.	Geomorphological setting.....	163
7.1.4.	Forestral setting.....	165
7.1.5.	Climatic setting.....	165
7.1.6.	Statistical analysis of snow-meteorological data.....	170

7.1.7.	Avalanche protection structures.....	171
7.1.8.	Historical analysis of avalanche events.....	173
7.1.9.	Surveys on the avalanche site and topographical measurements.....	176
7.2.	Numerical-mathematical analysis.....	177
7.2.1.	Models description.....	177
7.2.2.	Models calibrations.....	183
7.3.	Conclusions.....	187
8.	CONCLUSIONS.....	189
	REFERENCES.....	193
	APPENDIX	
	DATA SHEETS OF AVALANCHE SITES WITH PASSIVE DEFENCE STRUCTURES.....	199
	Deflecting dams.....	202
Mestriago	Val di Sole (TN) Italy	202
Trafoi	Valle di Trafoi (BZ) Italy	203
Foppolo	Valle Brembana (BG) Italy	204
Caminata	Val di Vizze (BZ) Italy	205
	Retarding cone-shaped structures.....	206
Tassè	Val di Rabbi (TN) Italy	206
Zanon	Val Nigolaia (TN) Italy	207
Passo Tonale	Val Vermiglio (TN) Italy	208
Trafoi	Valle di Trafoi (BZ) Italy	209
Lago Cavia	Val di S. Pellegrino (BL) Italy	210
Passo Brocon	Valle del Tesino (TN) Italy	211
Plan	Val di Plan (BZ) Italy	212
	Direct Protection Structures.....	213
Pequerel	Val Chisone (TO) Italy	213
S. Lucano	Valle di S. Lucano (BL) Italy	214
Davos Frauenkirche	Landwasser Switzerland	215
Presson	Val di Sole (TN) Italy	216
Tassè	Val di Rabbi (TN) Italy	217
Portavescovo (1)	Val di Livinallongo (BL) Italy	218
Portavescovo (2)	Val di Livinallongo (BL) Italy	219
	Catching dams.....	220
Ville Cloze	Val Chisone (TO) Italy	220
Certosa	Val Senales (BZ) Italy	221
	Combinations of avalanche protection structures.....	222
Vernago	Val Senales (BZ) Italy	222
Son Forca	Valle d'Ampezzo (BL) Italy	224
Foppolo (1)	Valle Brembana (BG) Italy	225
Foppolo (2)	Valle Brembana (BG) Italy	227
Trabuchello	Valle Mencucca (BG) Italy	229
Taconnaz	Vallée de Chamonix Mont Blanc France	231

List of Figures

2.1	Deformation components of the snowpacks: a) settlement (compressive deformation produces densification); b) shear deformation promotes failure [McClung & Schaerer, 1996].	6
2.2	Different types of snow crystals: a) simple prism; b)d) sectored plate; c) stellar plate; e) stellar dendrite; f) hollow column; g) needle; h) capped column; i) bullet rosette [http://www.snowcrystals.com].	7
2.3	Transformation of the crystals at the variation of the temperature [http://www.snowcrystals.com].	7
2.4	Illustration of the temperature variations in a snowpack. Diurnal variation occurs in the upper portion. A temperature gradient of 10°C/m is strong enough to produce facets in the snowpack [McClung & Schaerer, 1996].	8
2.5	a)b) The avalanche path [http://cagem.bayindirlik.gov.tr ; http://utahavalanchecentre.org].	9
2.6	a) Dry slab avalanche; b) loose snow avalanche; c) wet slab avalanche [http://cagem.bayindirlik.gov.tr].	12
2.7	a) Dry snow avalanche; b) powder avalanche; c) wet avalanche [http://cagem.bayindirlik.gov.tr].	13
3.1	a) Meteorological station; b) ram profile; c) snow profile; d) shovel shear test; e) shear frame test; f) compression test; g) rutschblock test; h) probing test; i) stuffblock test; l) ski shear test; m) hand shear test; n) test slopes; o) tilt board test; p) loaded column test; q) cornice test [Tremper, 1994; http://cagem.bayindirlik.gov.tr ; http://www.avalanche.org].	19
3.2	a) Above, the avalanche test site; b) below, a sketch of the instrumentation (CVA – Centro Valanghe Arabba) [Barbolini & Issler, 2005].	23
3.3	a) Above, the avalanche test site, b) below, a sketch of the instrumentation (SLF – Federal Institute of Snow and Avalanche Research of Davos) [Barbolini & Issler, 2005].	24
3.4	a) Above, the avalanche test site; b) below the instrumentation (ETNA – Cemagref de Grenoble) [Barbolini & Issler, 2005].	25
3.5	Example of granular deposit of an avalanche occurred in <i>Val di Lavina Granda</i> (near to Trento, Italy) [De Toni & Scotton, 2005].	26
3.6	Example of granular deposit of an avalanche occurred in <i>Val dei Spini</i> (<i>Val di Pejo</i> , Trentino Alto Adige Region, Italy) [De Toni & Scotton, 2005].	26
3.7	Università degli Studi di Pavia [Barbolini & Issler, 2005].	27
3.8	Cemagref of Grenoble [Faug, 2004].	27
3.9	University of Bristol [Hákonardóttir, 2004].	27
3.10	Norwegian University of Science and Technology [Norem & Brateng, 2005].	27
3.11	Models for the avalanche study [Barbolini et al., 2005].	30
4.1	Examples of avalanche bulletins: a) on the left, bulletin of the Arabba Avalanche Centre [http://www.arpa.veneto.it/csvdi]; b) on the right, bulletin of the Swiss Federal Institute for Snow and Avalanche of Davos [http://www.slf.ch].	37
4.2	Example of CLPV with its legend [http://www.arpa.veneto.it/csvdi].	38
4.3	Examples of hazard maps (high hazard zones are portrayed in red, moderate ones in blue and low ones in yellow): a) on the left, <i>Val Nigolaia</i> (Trentino Alto Adige Region, Italy) [Barbolini et al., 2003]; b) on the right, <i>Val dei Spini</i> (Trentino Alto Adige Region, Italy)	40

	[Scotton et al., 2006].	
4.4	Control by restrictions: a) road warning sign and closure systems; b) traffic light systems [http://cagem.bayindirlik.gov.tr; Somnavilla, 2006; McClung & Schaerer, 1996].	42
4.5	Control by compaction [McClung & Schaerer, 1996].	43
4.6	Control by explosive: a) hand charges; b) avalancheur; c) mortar; d) CaTEx; e) GazEx; f) Avalhex; g) helicopter charges [http://cagem.bayindirlik.gov.tr; http://www.anena.org; Somnavilla, 2006; http://avalancheblast.com/english/indexe.htm].	45
4.7	Active and passive defence structures [McClung & Schaerer, 1996].	46
4.8	a) Reforestation; b) earth terrace [http://cagem.bayindirlik.gov.tr; Frutiger & Martinelli, 1983].	46
4.9	Snow supporting or retention structures: a) snow bridges; b) snow rakes; c) snow nets; d) tripods; e) snow umbrellas; f) pilings; g) snow grippers [http://cagem.bayindirlik.gov.tr; http://www.arpa.veneto.it/csvdi; http://www.incofil.com].	49
4.10	Snow fences or redistribution structures: a) wind baffles; b) snow wind fences; c) wind panels; d) jet-roof [http://cagem.bayindirlik.gov.tr; http://www.arpa.veneto.it/csvdi; McClung et Schaerer, 1996].	50
4.11	The principals defence passive structures [Ancy, 1998].	51
4.12	a) Guiding structures; b) deflecting dams [http://cagem.bayindirlik.gov.tr; Bezzi, 2004].	52
4.13	Impact forces on defecting dam [McClung & Schaerer, 1996].	53
4.14	Example of defecting dams: on the left, open avalanche; on the right, channelled avalanche [Mears, 1981].	53
4.15	Schematic figure to calculate the height of to deflecting dam: H_d , design maximal height, H_d , snow pack depth, H_d , avalanche flow height H_d , uplift height [McClung & Schaerer, 1996].	54
4.16	Schematic figure deflecting dam showing the x,y,z- and ξ,η,ζ -coordinate systems the deflecting angle, φ , the slope of the terrain, ψ , and the angle between the upper dam side and the terrain, α [Domaas & Harbitz, 1998].	54
4.17	a) avalanche natural channel above the guiding structure; b) cross section of the guiding structure [Mears, 1981].	54
4.18	Impact forces on a protecting deflecting dam [Menegus & Soranzo, 1986].	55
4.19	Impact forces on a curve deflecting dam [Mears, 1981].	58
4.20	Canton of Valais, Switzerland [Frutiger & Martinelli, 1983].	58
4.21	Disentis, Canton of Grisons, Switzerland [http://cemadoc.cemagref.fr].	58
4.22	Nautagrovi, Gudvangen, Norway [Barbolini & Issler, 2005].	59
4.23	Pampeago, Val di Fiemme, Italy [Rossi, 2004].	59
4.24	Two views of Flateyri, Iceland [Barbolini, 2005].	59
4.25	Chamonix, Haute-Savoie, France [http://cemadoc.cemagref.fr].	59
4.26	Langageiti, Gudvangen, Norway [Barbolini, 2005].	59
4.27	Brun, Seyoisfjorour, Iceland [http://cemadoc.cemagref.fr].	59
4.28	Ytra-Strengsgil, Siglufjörður, Iceland [http://www.orion.is/snow2008].	59
4.29	Seljalandshverfi, Isafjordur, Iceland [http://www.orion.is/snow2008].	60
4.30	Funi, Isafjordur, Iceland [http://www.orion.is/snow2008].	60
4.31	Steinbichele, Krößbach, Austria [Höller, 2007].	60
4.32	Oberwald, Canton of Valais [Fraser, 1970].	60

4.33	Retarding or breaking mounds: a) retarding cone-shaped structures; b) retarding tooth-shaped structures [http://cagem.bayindirlik.gov.tr ; Frutiger & Martinelli, 1983].	61
4.34	Schematic figure of retarding mounds to reduce avalanche deposit stopping distance and flow depth [Mears, 1981]	62
4.35	Alpogli-Wilerhorn, Canton of Valais, Switzerland [Frutiger & Martinelli, 1983].	62
4.36	Retarding mounds in the accumulation zone [McClung & Schaerer, 1996].	62
4.37	Schematic figure of retarding mounds [Sommavilla, 2006].	62
4.38	Diagram to the measurement of retarding structures [Menegus & Soranzo, 1986].	63
4.39	A schematic diagram of a jet of length, L , with upstream flow thickness, h , and jet thickness, h_j . The jet is deflected at an angle, β , over a mound or a dam of height, H , positioned in a terrain with inclination ψ . The upstream mound face is inclined at an angle α with respect to the slope. u_0 , u_1 , u_2 , u_3 and u_4 are the speed at different locations in the path [Hákonardóttir et al., 2003].	64
4.40	Mattstock, Canton of St. Gallen, Switzerland [Mears, 1981].	65
4.41	Innsbruck, Austria [McClung & Schaerer, 1996].	65
4.42	Gully, Uttar Pradesh, India [Rao, 1985].	65
4.43	Rogers Pass, British Columbia [Frutiger & Martinelli, 1983].	65
4.44	Austria [http://www.kfunigraz.ac.at].	65
4.45	Austria [http://www.kfunigraz.ac.at].	65
4.46	Arzleralm, Austria [Frutiger & Martinelli, 1983].	66
4.47	Andermatt, Canton of Uri, Switzerland [Mears, 1981].	66
4.48	Valtorta, Valle Stabina, Italy [Barbolini, 2005].	66
4.49	Canton of Uri, Switzerland [http://cemadoc.cemagref.fr].	66
4.50	Catching dams: a) arresting walls; b) catching dams; c) breaking dams [http://cagem.bayindirlik.gov.tr ; McClung & Schaerer, 1996; http://cemadoc.cemagref.fr ; Pittracher, 2008].	68
4.51	Scheme figure of the snow storage space above a catching dam: h_s is the thickness of snow and previous avalanche deposits on the ground on the upstream side of the dam before an avalanche hits the dam; h_v is the vertical height of the upstream dam side. The figure is adapted from Margreth (2004) [Jóhannesson et al., 2008].	68
4.52	Catching dam: a) above, accumulate area; b) below, project height and velocity [Mears, 1981].	69
4.53	Impact forces on a protecting catching dam [Menegus & Soranzo, 1986].	70
4.54	Bethel, Colorado [Mears, 1981].	71
4.55	Larche, Alpes-Maritimes, France [http://cemadoc.cemagref.fr].	71
4.56	Galtür, Paznaun valley, Tirol, Austria [SATSIE Project, 2006].	72
4.57	Vorarberg, Austria [http://cemadoc.cemagref.fr].	72
4.58	Bleie, Ullensvang, Norway [http://cemadoc.cemagref.fr].	72
4.59	Seydisfjordu, Iceland [http://www.orion.is/snow2008].	72
4.60	Direct protection structures: a) building reinforcement techniques; b) reinforcement techniques for structures; c) protecting wedges or splitters; d) roofing; e) avalanche tunnels [http://cagem.bayindirlik.gov.tr ; Sommavilla, 2006; McClung & Schaerer, 1996].	74
4.61	Impact forces on a protecting wedge [Menegus & Soranzo, 1986].	75

4.62	Impact forces on a protecting wedge [Mears, 1981].	75
4.63	Typical houses of the Vanoise, France [Givry & Perfettini, 2004].	76
4.64	Example of building reinforcement techniques [Menegus & Soranzo, 1986].	77
4.65	Bonneval-sur-Arc, Savoie, France [http://cemadoc.cemagref.fr].	77
4.66	Peisey Nancroix, Savoie, France [http://cemadoc.cemagref.fr].	77
4.67	Galtür-Paznauntal, Austria [Höller, 2007].	78
4.68	Barèges, Hautes-Pyrénées, France [Givry & Perfettini, 2004].	78
4.69	Réalp, Canton of Uri, Switzerland [http://cemadoc.cemagref.fr].	78
4.70	Vallorcine, Haute-Savoie, France [Givry & Perfettini, 2004].	78
4.71	Mogno, Canton of Ticino, Switzerland [Givry & Perfettini, 2004].	78
4.72	Rosuel, Savoie, France [Givry & Perfettini, 2004].	78
4.73	Méribel, Savoie, France [http://cemadoc.cemagref.fr].	78
4.74	Larens, Alpes-de-Haute-Provence, France [http://cemadoc.cemagref.fr].	79
4.75	Fljotsdalslinur, Fljotsdalur valley, Iceland [http://www.orion.is/snow2008].	79
4.76	Val di Isère, Savoie, France [Givry & Perfettini, 2004].	79
4.77	Val di Isère, Savoie, France [Givry & Perfettini, 2004].	79
4.78	Fljótsdalur, Iceland [Hákonardóttir et al., 2008].	80
4.79	Ísafjörður, Iceland [http://www.orion.is/snow2008].	80
4.80	Passy, Haute-Savoie, France [Givry & Perfettini, 2004].	80
4.81	St.-Hilaire-du-Touvet, Savoie, France [http://cemadoc.cemagref.fr].	80
4.82	Avalanche tunnels [McClung & Schaerer, 1996].	81
4.83	Schematic figure of avalanche tunnel [Sommavilla, 2006].	81
4.84	Calculation of impact forces on an avalanche tunnel: a) on the left, the first method; b) on the right, the second method [Menegus & Soranzo, 1986].	82
4.85	Val d'Isère, Savoie, France [http://cemadoc.cemagref.fr].	85
4.86	Cohennoz, Savoie, France [http://cemadoc.cemagref.fr].	85
4.87	Isafjordur, Bolungarvik, Iceland [http://www.orion.is/snow2008].	85
4.88	Alpes-de-Haute-Provence, France [http://cemadoc.cemagref.fr].	85
4.89	Pampeago, Val di Fiemme, Italy [Rossi, 2004].	86
4.90	Großer Gröber, Pfafflar, Austria [Höller, 2007].	86
4.91	Schematic figure of a catching dam with retarding mounds [Margreth, 2004].	86
4.92	Tacconnaz, France [http://cemadoc.cemagref.fr].	87
4.93	Arzlernalm, Innsbruck, Austria [Höller, 2007].	87
4.94	Gotthard Pass, Switzerland [Ammann, 2008].	87
4.95	Neskaupstaður, Iceland [Hákonardóttir et al., 2008].	87
4.96	Active and passive defence structures at Davos, Canton of Grisons, Switzerland [McClung & Schaerer, 1996].	88
5.1	a) On the left, a lateral view of the experiment set-up; b) on the right, a view of the flume and its support structure.	90

5.2	The feeding box.	90
5.3	The flume.	90
5.4	Two views of the lower plane with the glass paper white coloured sheet.	90
5.5	Lateral view of the experimental set-up.	91
5.6	Planimetry of the experimental set-up (measures in cm).	91
5.7	a) On the left, the instrumentation on the channel; b) on the right, the instrumentation on the lower plane.	92
5.8	The video camera I.	92
5.9	Two views of the video camera I.	92
5.10	The measuring section of the preliminary test. The measuring section is fixed in 91-93 cm by the feeding-box (section 0 cm).	93
5.11	Two views of the feeding box with 10 kg of granular material.	93
5.12	The video camera II.	93
5.13	Two views of the video camera II.	94
5.14	The laserlyte alignment system.	94
5.15	The technical sheet of the laserlyte alignment system.	94
5.16	Two views of the laserlyte alignment system.	95
5.17	The video projector.	95
5.18	Two views of the video projector.	95
5.19	a), b), c), d) The images of the fringes with the phase shift of $0, \pi/2, \pi, 3\pi/2$.	95
5.20	The video camera III.	96
5.21	Two views of the video camera III.	96
5.22	Deposit photo examples.	96
5.23	A mixture of glass beads.	97
5.24	Two boards of wood.	98
5.25	White and black chess paper panel.	98
5.26	Four white boards of wood.	98
5.27	A sequence of frames obtained by the lateral video camera (video camera I) [Test 00 – 22/11/07].	99
5.28	A sequence of frames obtained by the frontal video camera (video camera II) [Test 00 – 22/11/07].	99
5.29	Flow depth in time at the measuring section (Fig. 5.10) [Test 00 – 22/11/07].	99
5.30	Front velocity in time along the channel [Test 00 – 22/11/07].	99
5.31	Two views of a preliminary test deposit [Test 00 – 22/11/07].	100
5.32	Scheme of the two measurements techniques: the Laser Line Technique on the channel and the Fringe Analysis Technique on the lower plane [Faug].	100
5.33	Scheme of the laser line.	101
5.34	a) On the left, view of the channel with the ruler positioned in the Centre of the channel; b) on the right, <i>Reference image – Calibration in the plane (x,y)</i> , ruler image.	101
5.35	a) On the left, view of the channel with the laser line in the Centre of the channel; b) on the right, <i>Reference image – Calibration along z</i> , channel plane image ($z = 0$ cm).	102

5.36	View of the laser line with the displacement due to one board taken with the video camera (video camera II), <i>Object image n°1 – Calibration along z</i> , board image ($z = 1$ cm).	102
5.37	View of the laser line with the displacement due to two boards superimposed, taken with the video camera (video camera II), <i>Object image n°2 – Calibration along z</i> , two boards image ($z = 2$ cm).	102
5.38	<i>Reference Images</i> : a) <i>Calibration in the plane (x,y)</i> , ruler image; b) <i>Calibration along z</i> , channel plane image ($z = 0$ cm).	103
5.39	<i>Object images</i> : a) <i>n°1 – Calibration along z</i> , board image ($z = 1$ cm); b) <i>n°2 – Calibration along z</i> , two board image ($z = 2$ cm);	103
5.40	<i>Test object images</i> – A sequence of frames taken by the frontal video camera (video camera II).	103
5.41	Fringe projection system and numerical 3D technique [Vincent, 2003].	105
5.42	a) On the left, view of the white and black chess paper panel; b) on the right, <i>Reference image – Calibration in the plane (x,y)</i> , white and black chess paper panel image.	108
5.43	a) On the left, view of the lower plane with the fringes projected; b)c)d)e) below, four images taken with the video camera (video camera III), <i>Reference images – Calibration along z</i> , lower plane images ($z = 0$) with the phase shift of $0, \pi/2, \pi, 3\pi/2$.	108
5.44	a) On the left, view of the lower plane with the fringes projected and the woods boards positioned in the Centre of plane; b)c)d)e) below, four images taken with the video camera (video camera III), <i>Object images – Calibration along z</i> , four boards images ($z = 0,9 ; 1,9 ; 3,0 ; 4,0$) with the phase shift of $0, \pi/2, \pi, 3\pi/2$.	108
5.45	<i>Reference image – Calibration in the plane (x,y)</i> , the white and black chess paper panel image.	110
5.46	b), c) d) e) <i>Reference images – Calibration along z</i> , the lower plane images with the phase shift of $0, \pi/2, \pi, 3\pi/2$.	110
5.47	b), c) d) e) <i>Object images – Calibration along z</i> , images of the boards with the phase shift of $0, \pi/2, \pi, 3\pi/2$.	111
5.48	b), c) d) e) <i>Test object images</i> , images of the deposit with the phase shift of $0, \pi/2, \pi, 3\pi/2$.	111
5.49	Effect of the mass ratio on the mean values of front velocity and of flow depth on the channel.	113
5.50	Effect of the mass ratio on the values of Froude Number.	114
5.51	a), b), c), d) Images of deposit with the phase shift of $0, \pi/2, \pi, 3\pi/2$.	114
5.52	Example of a deposit: the colours represent the depth of the granular mass ranging from high values (red) to low values (blue) (measures in mm).	114
5.53	Effect of the mass ratio on the values of deposit stopping distance and width.	115
5.54	Example of the longitudinal profile of the deposit (mass ratio = 0,00%) [Test 08 – 23/11/07].	116
5.55	Effect of the mass ratio on maximum values of the deposit depth.	116
5.56	Deposit shapes with the variation of mass ratio.	117
6.1	a) On the left, a view of the flume and its support structure; b) on the right, a lateral view of the experiment set-up.	120
6.2	The feeding box.	120
6.3	The flume.	120
6.4	Two views of the lower plane.	120
6.5	Lateral view of the experimental set-up.	121
6.6	Vertical view of the experimental set-up (measures in cm).	121

6.7	The instrumentation on the channel and on the lower plane	122
6.8	The video camera I.	122
6.9	a) On the left, the feeding box with 3 kg of granular material; b) on the right, the feeding box with 7 kg of granular material.	122
6.10	The load cell I – impact force on the rear structure (channel CH3 of the Spider8).	123
6.11	The load cell II – impact force on the front structure (channel CH0 of the Spider8).	123
6.12	The technical sheets of the load cells.	123
6.13	a) On the left, the protected load cell installed on the support under the upper plane that measured the impact force against the rear structure; b) on the right, the non-protected load cell that measured the impact force against the front structure.	124
6.14	The acquisition data system.	124
6.15	The technical sheets of the acquisition data system.	124
6.16	a) On the left, scheme of the acquisition system; b) on the right, posterior view of the Spider8 connected with the PC.	125
6.17	The video camera I.	125
6.18	The measuring section of the tests. The measuring section is fixed at 108 cm from the feeding box (section 0 cm).	125
6.19	The video camera II.	126
6.20	The monitor.	126
6.21	The photo camera.	126
6.22	Deposits photo examples with different types of retarding structures: a) elliptical cone-shaped; b) tooth-shaped structures; c) circular cone-shaped structures.	126
6.23	The retarding structures used in the experiments: a) above, the tooth-shaped and the circular cone-shaped structures; b) below, three elliptical cone-shaped structures used, respectively, at the inclinations of 30°, 27° and 24°.	127
6.24	a) On the left, a vertical and lateral view of a mound, carried out in a lot of valleys of <i>Trentino Alto Adige</i> region (Italy); b) on the right, scheme of the isosceles cone carried out in nylon. The grey coloured part represents the mound model that will be used for the experiments.	128
6.25	Elliptical base cones (measures in cm).	128
6.26	Elliptical base cones – 30° (measures in cm).	129
6.27	Elliptical base cones – 27° (measures in cm).	129
6.28	Elliptical base cones – 24° (measures in cm).	130
6.29	Circular base cones (measures in cm).	130
6.30	Tooth-shaped structures (measures in cm).	131
6.31	The linear guide.	131
6.32	The T-shaped support.	131
6.33	a) On the left, one of the T-shaped support with an example of retarding structure; b) on the right, scheme with the transmission of impact force to the load cell.	132
6.34	The technical sheets of the linear guide.	132
6.35	a) On the left, a view from below of the support plate of the three T-supports; b) on the right, a view from above.	132
6.36	Two views of the support plate with the three T-shaped supports below the upper plane.	133

6.37	a) On the left, a view from above of the retarding structures system; b) on the right scheme of the retarding structures: the rear structures forms an angle θ with the longitudinal flow direction.	133
6.38	A view from above of the upper plane with the retarding structures (measures in cm).	133
6.39	The T-shaped support used to transfer the force acting on the slowing down elements (measures in cm).	134
6.40	A view from above of the upper plane with the support (measures in cm).	134
6.41	The synthetic zeolite.	135
6.42	a) On the left, the experimental set-up used to perform the calibration of the load cells; b) on the right, the on site calibration of the force measurement system.	136
6.43	Example of calibration of the load cell on the front element (CH0) [Test 03_EC_26_3_24].	136
6.44	Example of calibration of the load cell on the rear elements (CH3) [Test 03_EC_26_3_24].	137
6.45	A sequence of frames obtained by the lateral video camera (video camera I).	137
6.46	A sequence of frames obtained by the frontal video camera (video camera II).	137
6.47	Definition of impact area for the cone-shaped (on left) and for the tooth-shaped structures (on right) used in the calculus of the dimensionless impact force.	138
6.48	Example of the acquired impact forces raw data (in terms of voltage) against front element (CH0) and rear elements (CH3) [Test 03_EC_26_3_24].	138
6.49	Scheme showing the physical parameters used to define the longitudinal and the cross-sectional efficiency of the retarding elements.	139
6.50	Example of data sheet realised for each experimental test [Test 03_EC_26_3_24].	141
6.51	Example of the flow depth in time at the measuring section in the channel [Test 03_EC_26_3_24].	142
6.52	Example of the front velocity in time along the channel and after the impact against the structures [Test 03_EC_26_3_24].	142
6.53	The Froude numbers of the events generated at the laboratory in the various experimental conditions.	143
6.54	A sequence of frames taken by the frontal video-camera (time interval 0,04 s) during the impact of a granular flow against a system of three tooth-shaped structures. The opening angle is equal to 26° .	144
6.55	A sequence of frames taken by the frontal video-camera (time interval 0,04 s) during the impact of a granular flow against a system of three tooth-shaped structures. The opening angle is equal to 35° .	144
6.56	Scheme of types of impact of a three-phase mixture [Armanini & Scotton, 1993].	144
6.57	Dimensionless impact force against retarding elements having the shape of elliptical base cones at various inclination angles and with various mixture weights.	144
6.58	Dimensionless impact force against retarding elements having the shape of circular base cones at various inclination angles and with various mixture weights.	145
6.59	Dimensionless impact force against retarding elements having a tooth-shaped structure, at various inclinations and with various mixture weights.	145
6.60	The dimensionless force measured and calculated following the model for the front elliptical cone.	146
6.61	The non-dimensional force measured and calculated following the model for the front circular cone.	146
6.62	The non-dimensional force measured and calculated following the model for the front	147

	tooth-shaped structure.	
6.63	Dimensionless impact force against rear retarding elements which have the shape of elliptical base cones positioned with various inclination angles, mixture weight and opening angles.	147
6.64	Dimensionless impact force against rear retarding elements which have the shape of circular base cones positioned with various inclination angles, mixture weight and opening angles.	148
6.65	Dimensionless impact force against rear retarding elements which have the shape of tooth-shaped structures with various inclination angles, mixture weight and opening angles.	148
6.66	Behaviour of the mean value of dimensionless impact force for the rear retarding elements when the opening angle varies from 26° to 45°.	149
6.67	A sequence of frames taken by the frontal video camera during five different events at the instant of the impact against a system of three elliptical cones. The opening angles are, from the left to the right, 26°, 30°, 35°, 40° 45°.	149
6.68	Behaviour of the mean value of deposit stopping distance and width when the opening angle varies from 26° to 45°.	151
6.69	Deposit shapes: upper plane tilting 24°, elliptical base cones, granular material weight of 3 kg and the opening angle of rear structures from 26° to 45°.	151
6.70	Deposit shapes: upper plane tilting 27°, elliptical base cones, granular material weight of 3 kg and the opening angle of rear structures from 26° to 45°.	152
6.71	Deposit shapes: upper plane tilting of 30°, elliptical base cones, granular material weight of 3 kg and the opening angle of rear structures from 26° to 45°.	152
6.72	Deposit shapes: upper plane tilting of 24°, circular base cones, granular material weight of 3 kg and the opening angle of rear structures from 26° to 45°.	153
6.73	Deposit shapes: upper plane tilting of 27°, circular base cones, granular material weight of 3 kg and the opening angle of rear works from 26° to 45°.	153
6.74	Deposit shapes: upper plane tilting of 30°, circular base cones, granular material weight of 3 kg and the opening angle of rear structures from 26° to 45°.	154
6.75	Deposit shapes: upper plane tilting of 24°, tooth-shape structures, granular material weight of 3 kg and the opening angle of rear structures from 26° to 45°.	154
6.76	Deposit shapes: upper plane tilting of 27°, tooth-shape structures, granular material weight of 3 kg and the opening angle of rear structures from 26° to 45°.	155
6.77	Deposit shapes: upper plane tilting of 30°, tooth-shape structures, granular material weight of 3 kg and the opening angle of rear structures from 26° to 45°.	155
6.78	Behaviour of the mean value of cross-sectional and longitudinal efficiency when the opening angle varies from 26° to 45°.	156
6.79	Relationship between mean values of longitudinal and cross-sectional efficiency for the various type of retarding structure systems.	156
7.1	Geographical setting of the <i>Val dei Spini</i> [Scotton et al., 2002].	160
7.2	IGM map extract: the <i>Val dei Spini</i> catchments (scale 1:25.000) [http://www.pcn.minambiente.it]	160
7.3	Scenic-view of the study site with the <i>Val dei Spini</i> catchments [Provincia Autonoma di Trento].	161
7.4	The geological map of the <i>Val dei Spini</i> catchments (scale 1:25.000) [Martin et al., 2001].	162
7.5	The four main channels of the <i>Val dei Spini</i> [Scotton et al., 2006].	163
7.6	The slope map of the <i>Val dei Spini</i> [Scotton et al., 2006].	164

7.7	The exposure map of the <i>Val dei Spini</i> [Scotton et al., 2006].	164
7.8	Vegetation in the <i>Val dei Spini</i> : a) in the accumulation zone; b)c) in the flowing zone; d) in the detachments zone [Scotton et al., 2006].	165
7.9	Monthly total precipitations values in three meteorological stations: Station of <i>Cogolo Pont</i> (1185 m a.s.l.), <i>Pejo</i> (1565 m a.s.l.), <i>Pian Palù</i> (1795 m a.s.l.). The data cover the period from 1978 to 2008.	167
7.10	Mean air temperature values (T_a) and maximum/minimum air temperature values (T_{\min} , T_{\max}) at the meteorological station of <i>Pejo-Tarlenta</i> (2010 m a.s.l.). The data cover the period from 1978 to 2008.	168
7.11	a) Above, wind type and activity (VQ1); b) above, localisation snow avalanche (VQ2) at the meteorological station of <i>Pejo-Tarlenta</i> (2010 m a.s.l.). The data cover the period from 1978 to 2008.	169
7.12	Maximum and mean snowpack depth values (HS) at the meteorological station of <i>Pejo-Tarlenta</i> (2010 m a.s.l.).	169
7.13	Maximum and mean fresh snow depth values (HN) at the meteorological station of <i>Pejo-Tarlenta</i> (2010 m a.s.l.).	170
7.14	Monthly maximum fresh snow depth values (HN) at the meteorological station of <i>Pejo-Tarlenta</i> (2010 m a.s.l.).	170
7.15	Two views of the snow nets in the <i>Val dei Spini</i> [Scotton et al., 2006].	172
7.16	Project for the realisation of active defence structure [Provincia Autonoma di Trento, 2003]	173
7.17	The project area [Provincia Autonoma di Trento, 2003].	173
7.18	CLPV, map of avalanche probable localisation of the <i>Val dei Spini</i> [Provincia Autonoma di Trento].	173
7.19	Model grid [De Toni et al., 2005].	177
7.20	Discharge flux across grid boundaries [FLO-2D, 2006].	177
7.21	Initial mass position example.	178
7.22	Inflow hydrograph example [http://water.me.vccs.edu].	178
7.23	Shear stress as function of shear rate for fluid deformation models [FLO-2D, 2006].	179
7.24	Absolute and curvilinear coordinates systems [De Toni et al., 2004].	180
7.25	Channel extension over several grid elements [FLO-2D, 2006].	180
7.26	Avalanche event n° 1 – Channel 1 – February 27 th 1998: input hydrograph for FLO-2D.	183
7.27	Avalanche event n°1 – Channel 1 – February 27 th 1998: a) SnowScotton simulation [Scotton et al., 2006]; b) FLO-2D simulation n°1; c) FLO-2D simulation n°2.	184
7.28	Avalanche event n°2 – Channel 4 – March 13 th 1972: input hydrograph for FLO-2D.	185
7.29	Avalanche event n°2 – Channel 4 – March 13 th 1972: a) SnowScotton simulation [Scotton et al., 2006]; b) FLO-2D simulation n°1; c) FLO-2D simulation n°2; d) FLO-2D simulation n°3; e) FLO-2D simulation n°4; f) FLO-2D simulation n°5.	187

List of Tables

2.1	Different types of metamorphism.	8
2.2	Major causes of snow avalanches [Ancy, 1998].	10
2.3	Factors used for classification of avalanches.	11
2.4	Comparison between flowing and powder avalanches – physical parameters.	11
3.1	Estimation of the accumulate frequency [Barbolini et al., 2005].	20
3.2	MOM and ML parameters in the FDP.	21
3.3	MOM and ML parameters in the LogNormal.	22
3.4	Statistical models.	30
3.5	Dynamic models.	31
4.1	European avalanche hazard scale [http://www.arpa.veneto.it/csvdi].	35
4.2	Definitions for the interpretation of the hazard scale [AINEVA, 2004].	36
4.3	High hazard zone features [Barbolini et al., 2005].	40
4.4	Moderate hazard zone features [Barbolini et al., 2005].	40
4.5	Low hazard zone features [Barbolini et al., 2005].	40
4.6	Study activity about the hazard avalanche zoning.	41
5.1	Geometrical characteristics experimental set-up.	89
5.2	Physical and mechanical material characteristics.	97
5.3	List of the preliminary tests and the tests.	112
5.4	Mean values of flow depth and mean front velocity in the channel for a mass ratio between 0,00% to 65,00%.	113
5.5	Values of Froude Number for a mass ratio between 0,00% to 65,00%.	113
5.6	Maximum values of deposit depth, stopping distance and width for a mass ratio between 0,00% to 65,00%.	115
6.1	Geometrical characteristics experimental set-up.	119
6.2	Geometrical characteristics of the retarding structures.	127
6.3	Physical and mechanical material characteristics.	135
6.4	List of the tests.	140
6.5	Maximum values of the flow depth on the channel.	142
6.6	Maximum values of the front velocity on the channel.	142
6.7	Maximum values of the deposit stopping distance.	150
6.8	Maximum values of the deposit width.	150
7.1	Climatic meteorological measurement stations [http://www.meteotrentino.it/].	166
7.2	Snow-meteorological measurements station [http://www.meteotrentino.it/].	167
7.3	Snow maximal depths values at the meteorological station of <i>Pejo-Tarlenta</i> . The data cover the period from 1981 to 2008.	171
7.4	Maximal values of snow depth on three consecutive depth realised with the statistical	171

distributions of Gumbel and Lognormal for the $T_r = 30, 50, 100, 300$ years.	
7.5 Historical avalanche events.	174
7.6 Deposits dimensional features observed (1997/98 – 1998/99) [Scotton et al., 2002].	176
7.7 Comparison between the two numerical-mathematical models.	177
7.8 Avalanche event n°1 – Channel 1 – February 27 th 1998.	183
7.9 Avalanche event n°2 – Channel 4 – March 13 th 1972.	185

Chapter 1

INTRODUCTION

In the European Alps expanding settlements and increasing mobility due to tourism lead to a growing number of constructions in terrain threatened by avalanches. Measures have to be taken in order to reduce avalanche risk: avalanche hazard mapping as a basis for land use planning is one of the most effective measures to reduce or even avoid avalanche exposure.

In many situations, technical measures such as supporting structures and deflecting dams, or short-term measures such as avalanche forecasting, artificial avalanche release or evacuation can be put into practice to reduce the avalanche risk to an acceptable level. It is important to evaluate the different measures within the frame of a risk management procedure [Ammann & Fohn, 1999].

1.1 Snow avalanche defence

Several possibilities of classification exist for the large variety of avalanche risk reducing measures. The most frequently used is a sub-division into short-term and long-term protection measures [Salm et al., 1990]:

- 1) short-term protection measures:
 - avalanche forecasting, warning;
 - artificial release of avalanches;
 - closure of roads and railways;
 - evacuation of people and cattle;

- 2) long-term protection measures:
 - hazard mapping, land use planning;
 - construction measures;
 - supporting structures (starting zone of avalanches);
 - deviation dams (avalanche path);
 - snow sheds (roads, railways crossing avalanche path);
 - retaining dams (deposition zone of avalanches);
 - retarding constructions (deposition zone of avalanches);
 - silvicultural measures;
 - reforestation, combined with technical measures.

1.2 Avalanche forecasting

The avalanche hazard forecasting and the subsequent measures such as evacuation of people in exposed settlements, the closing of roads and railway lines and the artificial release of avalanches under controlled conditions are called short-term measures.

Efficient use of these measures need a co-operation involving all national, regional and local security commissions and national avalanche awareness programmes. All Alpine countries operate national or regional avalanche warning centres, which supply avalanche forecast on a daily basis. With the introduction of the European avalanche hazard scale in 1993 a common

language to describe the snow cover stability and the probability of an avalanche release has been found.

Bulletins represent an important tool for all local and regional security commissions in their risk management processes, to close a road, to evacuate people or to order the artificial release of potential avalanches [Ammann & Fohn, 1999].

1.3 Avalanche hazard mapping

Hazard maps serve as basic documents for avalanche risk evaluation, especially with concern for land-use planning. Dangerous zones were designated according to disastrous events that had already occurred in a more qualitative way, without considering climatic factors or quantitative avalanche calculations. In the course of time methods have been improved and avalanche models introduced to calculate the dynamic behaviour. In recent years numerical simulations, GIS and DTM tools have led to substantial improvements [Ammann & Fohn, 1999].

Two parameters were chosen to quantify the potential hazard for a given site [Barbolini, 2005]:

- expected frequency of an avalanche reaching a given site (frequency is normally expressed by the return period);
- intensity of an avalanche (intensity is expressed by the avalanche pressure exerted on a wall of a building. As this pressure is assumed to increase with the square of speed and proportional to density, the kinetic energy of snow masses is also included).

To be able to distinguish variable hazard intensities and run-out scenarios, several hazard zones are defined.

The elaboration of hazard maps must strictly follow scientific criteria and methods including expert knowledge. The aim is that of determining the most catastrophic type of avalanche on a reliable basis. Field visits to assess the avalanche terrain, the examination of the avalanche register as a map with all known avalanches in history (including their extent and date), additional information from competent local people or from old chronicles, the checking of local climatic conditions and dynamic avalanche calculations are important tools. The dynamic calculations are used for [Ammann & Fohn, 1999]:

- predicting an extreme event, probably not registered in a register;
- delimiting the hazard zones for the different return periods;
- calculating run-out distances and pressures as a function of avalanche frequency.

The use of physical-numerical-mathematical models requires a careful estimation of its input parameters, such as rheology parameters or avalanche size. To check sensitivity, calculations have to be made with different input parameters. Critical assessments of the results are important. It has to be pointed out that dynamic calculations are just one part of hazard assessment.

In recent years, many such dynamic calculation methods have been proposed, some of which are constantly used by practitioners [Salm et al., 1990].

Numerical methods have set new standards in the use of avalanche dynamics models [McClung & Schaerer, 1996]. User-friendly GIS and DTM tools are additional assets to complete and facilitate avalanche hazard mapping [Ammann & Fohn, 1999].

1.4 Technical defence measures

Technical, long-term avalanche defence measures are used in the starting zone to prevent the release of avalanches (supporting structures) and in the avalanche track and run-out zones (avalanche sheds, deflecting and catching dams) to reduce the damage of descending avalanches.

Wide application of supporting structures began after the severe avalanche winter of 1950/51 in Europe. The aim of supporting structures is to prevent the start of large avalanches or at least to limit snow motions to a harmless extent [Ammann & Fohn, 1999].

The first effect of supporting structures is to introduce an overall increase in the stability of the inclined snow cover. The acting snow-pack forces are redistributed, compressive reaction forces increase, shear forces -which determinate stability- decrease. The second effect consists in limiting the mass of snow put in motion and in retarding and catching it. The vertical height must correspond to the extreme snow depth with a return period of at least 100 years. The adopted snow height is a crucial point for the design to guarantee the effectiveness of supporting structures [Ammann & Fohn, 1999].

Deflecting and catching dams are relatively cheap compared to the supporting structures but need space and volume to be effective. Deflecting and catching dams are normally earth dams, sometimes combined with stone masonry to increase the slope-inclination on the side where impact occurs. The height of catching dams may reach 15 m – 20 m, depending on the avalanche velocity and the snow volume which is to be retained.

The mountain forest corresponds to the most effective and the cheapest protection for villages, roads and railways. The trees retain the snow, stabilise the snow-pack and prevent avalanche to start [Ammann & Fohn, 1999].

Rapid mass movements, such as snow avalanches, are often modelled thanks to small-scale laboratory experiments, using dry granular materials flowing down an inclined plane. The aim of this dissertation is to carry out small-scale laboratory tests in order to study some aspects of granular avalanches: properties of deposits (Chapter 5) and interactions with obstacles (Chapter 6).

For the realization of the earth mounds there is no such legislation as in the case of active protection structures. The Swiss Federal Institute for Research on Snow and Avalanche in 1961 had already realised engineering directives for the design, construction and maintenance of active structures. For earth mounds the design is left to the sensibility and experience of the designer.

The final part describes the possibility of the realization of a hazard map -for the avalanche of *Val dei Spini* (*Val di Pejo*, *Trentino Alto Adige* Region, Italy)- in accordance with the *Linee di indirizzo per la gestione del pericolo di valanghe nella pianificazione territoriale* [Barbolini et al., 2005], by using numerical-mathematical models (Chapter 7).

Chapter 2

SNOW AVALANCHES

Avalanches are falling masses of snow that can contain rocks, soil or ice. Snow avalanches can be listed in a classification of natural hazards -including rock avalanches, rockfall, landslides, debris flow and ice avalanches- known as mountain-slope hazards [McClung & Schaerer, 1996].

2.1 Snow and avalanches rheology

Snow is a porous material composed of crystals of ice and air, often in the presence of water in its liquid form. Ice volumetric concentration of snow ranges from 1% to 65%.

The rheology of the air-snow unit is extremely complex, because snow is a very active thermodynamic medium. At 0°C, at the water triple point, the three phases coexist. For small temperature variations around the triple point, important variations in the system composition must be expected. The mechanical behaviour thus depends strongly by the thermodynamic state and the history of the snowpack. Thermodynamic sensitivity of the air-snow unit explains the large variety of aspects of the avalanches, which can assume the shape of a powder cloud in the case of dry snow, the shape of a granular mass if the presence of water is not considerable and the shape of a saturated mass of water and snow in the case of very wet snow (water content superior to 15%).

The fundamental properties are sufficiently known and their importance is considerable in the study of avalanche triggering.

Snow avalanches present properties which are very different from snowpack.

In case of a dense snow avalanche the volumetric concentration in ice is considerable and the avalanche shows properties that are typical of granular flows. Powder snow avalanches present very low density.

Both kinds of snow avalanches show an intense erosion activity. Mass differences, between the detachment zone and the stopping zone, show that the initial mass can also triple.

A case often observed, and prevalent on the southern slopes of the Alps, relates to the granular or particulate avalanches. The formation of the snowballs is determined by the presence of water in its liquid form in the snow cover at the detachment area, but may also occur in the phase of flow. The material can be regarded as a granular medium, characterized by a non-uniform granulometric distribution (the dimension of the snowball can range from a mean value of some centimetres to one meter). Nevertheless, the analogy with a simple granular medium must be treated with precaution, because the water content influence and many thermodynamic aspects are still not well known.

The avalanche rheology is often simulated with the rheology of a granular mass, through definition of two fundamental physical parameters: the internal friction angle and the bed friction angle.

Avalanches form as soon as the forces due to gravity, fresh snow, an explosion or the additional weight of a skier, exceed the mechanical strength of the packed snow and ice. The problem is to know when this happens in order to give local authorities the possibility to decide when to close a road, evacuate a village or artificially release an avalanche to protect a ski track. Researchers therefore need to address questions concerning the forces and the strength inside the snowpack (Fig. 2.1).

Not surprisingly, the mechanical properties of snow are somewhat similar to the properties of ice. Both are viscous elastic materials that exhibit creep behaviour over time. In other words,

snow and ice deform continuously when loaded. However, the loading rate is a critical parameter, and avalanche experts are just as interested in the rate of snowfall as they are in the amount. Heavy snowfalls over a short period of time lead to a greater chance of avalanche triggering.

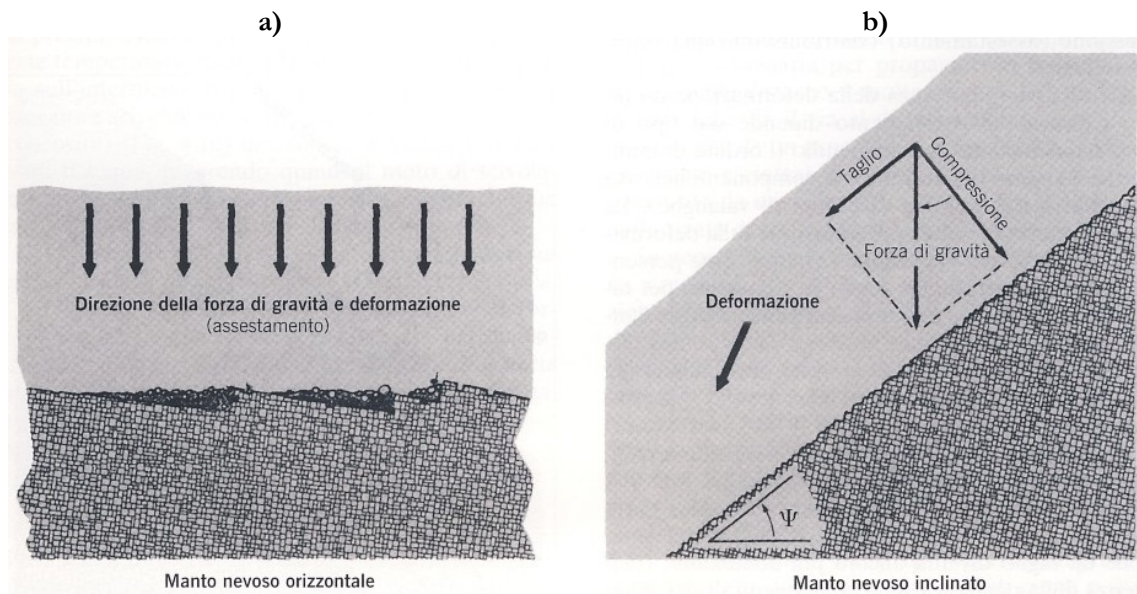


Fig. 2.1 – Deformation components of the snowpack: a) settlement (compressive deformation produces densification); b) shear deformation promotes failure [McClung & Schaerer, 1996].

Snow is a porous medium. It contains grains of ice that are arranged in a complicated interconnected lattice as well as air and, sometimes, water. Ice bonds exist among the grains that are responsible for resistance of snow cover under load.

During creep, the snowpack deforms with two main mechanisms: inter-granular sliding and straining. Experiments indicate that the sliding of the ice grains over each other -a frictional and irreversible process- dominates in new or low-density snow. Meanwhile, the viscous elastic straining of the granular ice chains, and in particular of the ice bonds, dominates in older and denser snow. As a chain is only as strong as its weakest link, the bonds between the grains are critical. However, the breaking of a single bond does not necessarily initiate a chain reaction that leads to an avalanche. On the contrary, new bonds can form under deformation that might even strengthen the snow cover.

The stresses in the ice bonds are some 50 to 100 times higher than the continuum stresses exerted on the snowpack as a whole because of their small cross-sectional area. The exact stress on the ice bonds depends on the micro-structural properties of the ice grains, such as their size and shape. And it is this problem that makes predicting the stability of the snowpack so difficult. Researchers must forecast how the micro-structural properties of the snow cover change over time. Attempts to accomplish this task are made with the help of numerical snowpack models.

2.2 Snow metamorphism

The single crystals of snow come in a myriad of shapes and sizes [Libbrecht, 2007]. These include a short column with its facet faces hollowed by competition for water vapour (f), a hexagonal plate (a), a stellar plate (c), a sectored plate (b), (d), a stellar dendrite (e), a hollow column (f), a cluster of needles (g), a capped column (h) and a capped bullet rosette (i) (Fig. 2.2).

The smallest simple prisms may be a few tenths of a millimetre, whereas the largest stellar dendrites may be 10 mm in diameter. All of these snow crystals were collected from natural snowfalls, but laboratory studies are discovering the reasons why such a variety of forms can all derive from the simple freezing of water vapour [Libbrecht, 2007].

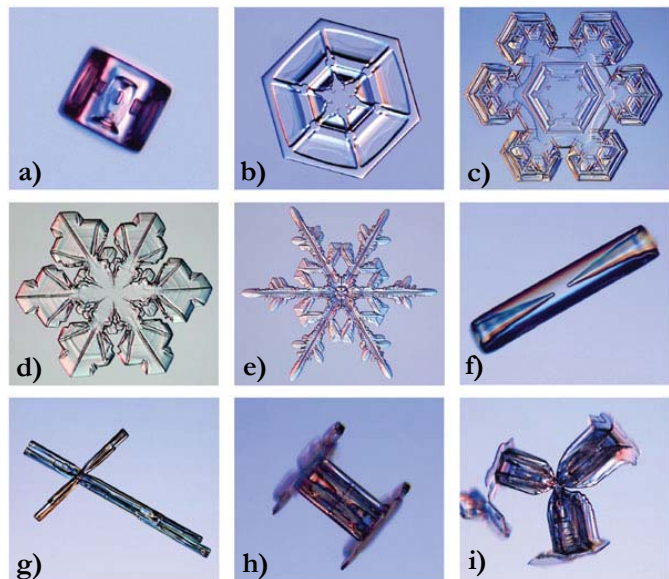


Fig. 2.2 – Different types of snow crystals:
a) simple prism; b)d) sectored plate; c) stellar plate;
e) stellar dendrite; f) hollow column; g) needle; h) capped
column; i) bullet rosette [<http://www.snowcrystals.com>].

The delicate and intricate structure of falling snowflakes does not last for long. The tiny branches of the crystal break as soon as the flake lands on the ground and is covered by fresh snow. This load deforms the crystalline structure, increasing the density of the new layer of snow (Fig. 2.3). Gravity is the obvious force driving the structural changes but there are other, more subtle, mechanisms at work that are just as powerful.

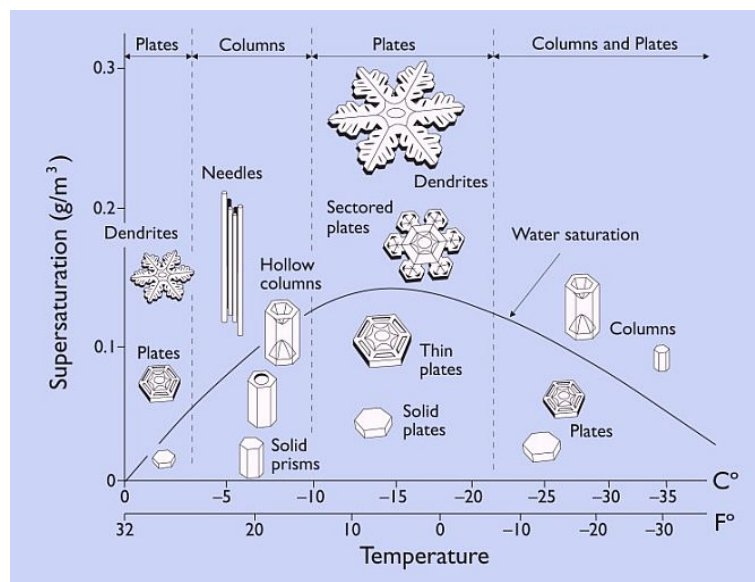


Fig. 2.3 – Transformation of the crystals at the variation of the temperature
[<http://www.snowcrystals.com>].

The heat flow from the ground is typically large enough to ensure that the temperature at the soil-snow interface is kept at freezing point, while the surface of the snow is normally below 0°C. This heat flow generates a corresponding water-vapour pressure difference, which leads to the onset of diffusion.

The sublimed water molecules in the warmer regions wander to the colder areas, where they deposit on the ice frame. In addition, water vapour can move freely throughout the porous system. The consequence of this transport is a localized change in the density and in the shape of the crystals, known as metamorphism (a term borrowed from geology). As a result, we often find a spectacular layer of “depth-hoar” - hollow cup-shaped ice crystals that grow up to a few millimetres in size. Depth-hoar crystals develop in a loose array that leads to a zone of weakness within the snowpack and are a major contributor to avalanche formation [McClung & Schaerer, 1996].

Metamorphism is often thought of as a rather slow process. However, since the structural changes in porous snow occur close to the melting point, metamorphism can happen quickly. Indeed, the changes may be visible within a day or so.

Ice grains nucleate and then grow in clouds that are below freezing point and where moisture is present. The form of the crystals form depends on the temperature and moisture content of the atmosphere they fall through.

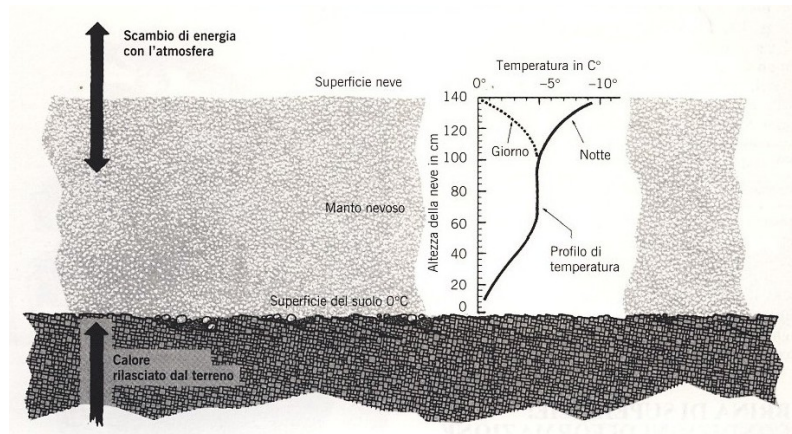


Fig. 2.4 – Illustration of the temperature variations in a snowpack. Diurnal variation occurs in the upper portion. A temperature gradient of 10°C/m is strong enough to produce facets in the snowpack [McClung & Schaerer, 1996].

Once snow falls to the ground it begins to change. Vapour pressure and temperature, acting over time, change the form of the crystals and the texture of the sedimentary layer of snow (Fig. 2.4). The metamorphism occurs rapidly in snow and changes the structural strength, permeability, thermal conductivity and density of the snow cover (Table 2.1).

Table 2.1 – Different types of metamorphism.					
Type of snowfall	Type of Metamorphism	T	Cause	Type of snowpack	Results
Dry snow	<u>Destructive metamorphism:</u> destroys crystal structure	$T \leq 0^\circ\text{C}$	temperature weak gradient ($< 5^\circ\text{C}/\text{cm}$) or equitemperature	rounded grains (diameter = 0,5 mm)	strong snowpack
	<u>Constructive metamorphism:</u> builds grains		temperature medium gradient ($6-19^\circ\text{C}/\text{m}$)	angular and facets grains	weak snowpack
			temperature elevated gradient ($> 20^\circ\text{C}/\text{m}$)	capped crystals or sharp corners crystals	depth frost
Wet snow	Fusion or regelation metamorphism	$T > 0^\circ\text{C}$		rounded grains (diameter > 1 mm)	spring snow or snowfield

2.3 Avalanche formation

The stability of snow cover depends on many parameters. We can distinguish the fixed parameters related to the avalanche path from the varying parameters, generally connected to weather conditions. Fixed parameters include:

Factors	Description	
Terrain	INCLINATION In most case, the average inclination of starting zones ranges from 27° to 50°.	
	SHAPE AND CURVATURE OF SLOPE The stress distribution within the snowpack and the variation in its depth depend on the longitudinal shape of the ground.	
	ASPECT In winter, shady slope receive little incoming radiations from the sun and conversely lose heat by long-wave radiation. It is generally observed that for these slopes, the snowpack is cold and tends to develop weak layers. In late winter and in spring, the temperature increase enhances stability of snowpacks on shady slopes and instability in sunny slopes.	
	ROUGHNESS Ground surface roughness is a factor very important in the anchorage of the snow cover to the ground. Dense forests or ground covered by large boulders generally limit the amount of snow that can be involved in the start of an avalanche. Otherwise, large and open slopes with smooth ground may favour avalanche release.	
Snowpack	SNOWPACK DEPTH The weight of the snow cover is an exciting factor very important. Snow cover on a slope tends to slide down the slope because of gravity. Conditions affecting stability include the gravitational force component of the snow and resisting forces, such as the frictional resistance of the slope or the anchoring effect of shrubs. In general, avalanches are caused when this balance is lost and when the forces exceed the resistance.	
	The stability of the resulting layer structure depends a great deal on the bonds between layers and their cohesion. Heterogeneous snowpack, made up of weak and stiff layers, are more suitable than homogeneous snowpacks.	HARDNESS
		LAYERING
		CRYSTAL FORMS
	FREE WATER CONTENT	
Weather	WIND VELOCITY AND DIRECTION It causes uneven snow redistribution; accelerate snow metamorphism, forms cornices, whose collapses may trigger avalanches. Influence of the wind is very diverse, either consolidating snow or wreaking it.	
	ATMOSPHERIC AND SNOW TEMPERATURES There is a relationship between atmospheric temperature and snow quality. In fact it determines the snow water content and the process of metamorphism.	
	PRECIPITATIONS AND LIQUID WATER CONTENT Most of the time, snowfall is the cause of avalanches. The hazard increases significantly with the increases in the depth of new snow. An accumulation of 30 cm/day may be sufficient to cause widespread avalanching. Generally, for dry snow, a small increase in the liquid water content does not significantly affect the mechanical properties of snow. However, heavy rain induces a rapid and noticeable increase in liquid water content, which results in a drop in the shear stress strength. This situations leads to widespread avalanche activity.	
Other factors	Increase in weight of snow cover because of snow dropping from cornices or snow covers.	
	Vibrations such as earthquake or the sound of gunfire.	

2.4 Avalanche path

An avalanche path is the terrain area where an avalanche occurs. It is composed of a starting zone, a track, and a run-out zone (Fig. 2.5).

[1] STARTING ZONE (ZONE OF ORIGIN) It is the area where the unstable snow falls and begins to move. The crown (or fracture line) of an avalanche defines the upper limit of the starting zone. Some avalanches have multiple starting zones which are well separated by ridges or forests, connected to a single track. Characteristics of a starting zone are slope inclination, exposure to wind and sun, forest cover, ground surface, altitude and crown and flank locations.

[2] TRACK (ZONE OF TRANSITION)

It is the slope below the starting zone that connects the starting zone to the zone where debris collects. While a well defined track is the major terrain feature for large avalanches, in avalanches with short running distances this is less determinant. Avalanche speed reaches its maximum value in the track, but speed variations are smallest there. Deposition in the track is not significant for very large events. Avalanche tracks have a variety of configurations but two main categories are recognized: open slope and channel. Open slopes have no lateral boundaries. Channels are gullies and other depressions. Long tracks often have mixed terrain. For example, a gully may widen into an open slope. Avalanches usually follow the fall line, but they are not always confined by lateral boundaries and can take unexpected paths and also meander from side to side in a gully. Big avalanches in log paths decelerate significantly when the slope angle decreases to 10° or less. Typical track slope angles are 15° - 30° .

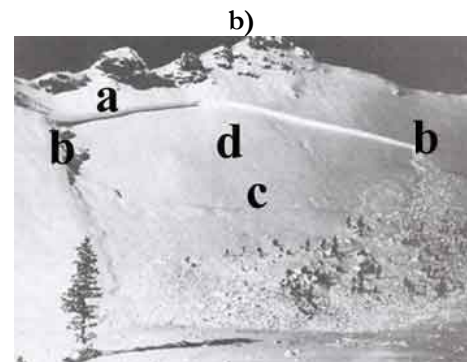
[3] RUN-OUT ZONE (ZONE OF DEPOSITION)

It is the area where deceleration is rapid, debris is deposited, and the avalanche stops. An abrupt change in slope angle can mark the transition between track and run-out zone but it is often not the case. Typical slope angles for this zone are 15° or less. The run-out zone can be wide bench, a talus slope, a valley bottom, the opposite side of a valley, or anywhere an avalanche stops. Due to slow speeds in the run-out zone, avalanches are sensitive to terrain variations there. This allows deflection by small obstacles. Forest cover cannot assure to stop avalanches but may retard them.

The tree zones can vary for individual avalanches within an avalanche path. Some avalanches may start low on a mountain with their starting zone in the track of larger avalanches. Similarly, small avalanches often run out in the track of larger avalanches.



**[1] STARTING ZONE;
[2] TRACK;
[3] RUN-OUT ZONE.**



**[a] CROWN;
[b] FLANKS;
[c] STAUCHWALL;
[d] BED SURFACE.**

**Fig. 2.5 – a), b) The avalanche path [<http://cagem.bayindirlik.gov.tr>;
<http://utahavalanchecenter.org>].**

2.5 Avalanche classification

Avalanches can be classified according to properties of snow layers, types of starting zones, occurring date (seasons), and terrain morphology (Table 2.3).

Type	Classification	Description
Release	NATURAL AVALANCHE	Snowpack features. Climatic and environmental factors
	ARTIFICIAL AVALANCHE	Artificial triggering with explosion.
Occurrence	LOOSE SNOW AVALANCHE	Avalanches that flow rapidly, spreading widely from a point normally small in scale.
	SLAB AVALANCHE	Avalanches that start to move suddenly over wide areas, normally large in scale.
Surface layer avalanche	SURFACE LAYER AVALANCHE	Slip surface exists within the snow cover.
	FULL-DEPTH AVALANCHE	Slip surface occurs on the ground surface.
Snow humidity	DRY SNOW AVALANCHE	Avalanches that contain no water.
	WET SNOW AVALANCHE	Avalanches that contain water.
Motion	FLOWING AVALANCHE	Avalanche that flows near to the ground (high bulk density).
	POWDER AVALANCHE	Avalanche that flows at low bulk density with large dimensions.
Ground features	UNCONFINED AVALANCHE	In large and open slope.
	CHANNELLED AVALANCHE	In an avalanche channel.

Very often an avalanche presents both a dense core of snow and an airborne cloud of powder. The following table, Table 2.4, presents the main characteristics of the two avalanche types.

Characteristics	Flowing avalanche	Powder avalanche
Velocity	30 – 40 m/s	70 – 80 m/s
Flow height	1 – 5 m	10 – 100 m
Density	300 – 600 kg/m ³	10 – 50 kg/m ³
Pressure	100 – 500 kPa	0,5 – 40 kPa
Friction	Granular collisions, basal friction	Turbulent drag, surface friction unimportant
Terrain	Avalanche often follows gullies	Terrain less important, follows steepest descent

In the run-out zone avalanches decelerate, however the dynamic pressure can reach values of some hundred thousand Pa [McClung & Schaerer, 1996].

In Fig. 2.6-Fig 2.7 slab avalanches, dry snow avalanches, powder avalanches and wet avalanches are presented.

SLAB AVALANCHES

Slab avalanches have different names according to moisture content of snow layers, slope cover (rock, soil or trees), and fracture depth. All of these types of avalanches have similar properties: snow temperatures are below 0°C but too close to 0°C, snow layers are divided into small parts during flow and deposited in a run-out zone with high density and their speeds are near to 20 km/h.

a) DRY SLAB AVALANCHES

This type of avalanche occurs when the weak layer of snow breaks, usually because too much weight has been added to the snowpack, too fast.



b) LOOSE SNOW AVALANCHES

Loose snow has little or no cohesion. Loose snow avalanches involve, initially, the snow near the surface. They are easily recognizable because they start from a point and form a triangular pattern. The initial sliding is triggered by a local loss of cohesion due to metamorphism or the effects of sun or rain. Often the initiation is near rocks, which cause locally high snow temperatures. If moisture content of snow is high due to rain or sun, the avalanche is called “wet loose avalanche”. Wet loose avalanches can be much bigger than dry ones. Grain geometry, temperature, cohesiveness and water content control the motion mechanisms of loose snow avalanches.



c) WET SLAB AVALANCHES

Wet slab avalanches are caused by three principal mechanisms:

- 1) loading by new precipitation (rain);
- 2) changes caused by a buried weak layer, due to water;
- 3) by water lubrication of a sliding surface, which may be partially or totally impermeable to water.

Sometimes, failure occurs along the whole snow cover and ground is visible after the avalanche. This type of avalanche is called “ground avalanche”.



Fig. 2.6 – a) Dry slab avalanche; b) loose snow avalanche; c) wet slab avalanche
[<http://cagem.bayindirlik.gov.tr>].

DRY SNOW AVALANCHES AND POWDER AVALANCHES

This kind of avalanches occurs when moisture content in the snow cover is low, density is near to 100 kg/m^3 or less, snow temperatures less than 0°C and snow depth more than 1 m. After avalanche starts a dust cloud containing snow and air rises.

a) DRY SNOW AVALANCHES

In this type of avalanche there is a core at the bottom of the avalanche. It is estimated that about one-third of the space in the core is filled with snow particles and about two-thirds is air. In the dust cloud, only about 1% of the space is filled with snow particles and 99% is air. Therefore the density is about 10 times higher in the core than in the dust cloud. Usually the depth of flow of the core is less than 5 m, but the depth of dust cloud can be tens of meters. Once the deposit comes to rest, the water on the particles' surfaces can freeze to fuse the particles together, producing a very hard deposit. Deceleration is rapid in run-out zone. Velocities range between 25 km/s and 100 km/h.



b) POWDER AVALANCHES

Powder avalanches are those in which a dense core at the bottom is absent. Any high-speed dry snow avalanche will have a powder or dust cloud associated with it and tends to make powder avalanches and dry flowing avalanches look similar. To distinguish between powder and dry snow avalanches, one must observe the deposit, the destructive effects, or flowing snow properties to determine the presence of a core. In a true powder avalanche, almost all of the material is suspended by turbulent eddies. They often form from falling ice (or sometimes by ice avalanches) from steep icefalls. Their speed sometimes may be more than that of dry snow avalanches.



WET AVALANCHES

c) WET AVALANCHES

Generally wet avalanches occur, at our latitude, at the end of March or beginning of Spring. In wet avalanches flowing of snow is similar to flow of mud due to high water content. Density of snow cover changes between 200 kg/m^3 and 600 kg/m^3 . Densities of saturated snow in slush deposits have been measured that exceed 1000 kg/m^3 due to the combination of water, ice, snow and entrained earth or rock material. Temperature of snow is 0°C . The prevalence for formation at high latitudes is partially due to the rapid onset of snowmelt in spring as the sun returns to provide direct, intense radiation to snow-packs that have been previously subjected to strong temperature gradients and a lack of solar radiation. Starting zone slope angles are in the range of 5° to 40° . The release is associated to a bed surface that is nearly impermeable to water. In most cases "depth hoar" is present at the base of the snow cover. Their speeds do not exceed 20 km/h.



Fig. 2.7 – a) Dry snow avalanche; b) powder avalanche; c) wet avalanche
[<http://cagem.bayindirlik.gov.tr>].

Chapter 3

AVALANCHES STUDY

The dynamics of snow avalanches is very complicated depending, among many other parameters, on the quality of the snow at the moment of triggering. The mass sometimes moves like a fluid, following the slope like a flow of water, and sometimes appears like a granular mass with properties of a moving granular mass. At times the dynamic is completely dominated by the air turbulence.

In the design of defence structures, the basic problem is that of being able to estimate, in a realistic way, the dynamic properties of such phenomena in order to calculate impact forces and run-out distances.

Physical parameters (velocity, discharge, flowing depth, etc.), that can be estimated from numerical models, very much depend on snow volume and properties and on the rheology of the moving mass (a function of the material and of the track properties). A proper representation of initial and boundary conditions is crucial.

Avalanche hazard maps are finally defined, nowadays, with the help of dynamical models. In order to obtain a reliable definition of the hazard maps a lot of work has to be done with the aim of acquiring knowledge of the initial conditions (fracture area and depth of sliding snow layers, quality of sliding snow), all dependent on the return period, and choosing adequate physical models to describe the flow regime (for instance, Bartelt & Gruber, 1997; Issler, 1998).

3.1 Data collection

Validation of physical models and numerical modelling are possible with field and laboratory data. Real progress will only be possible when field and laboratory data will be available covering all major parameters influencing avalanche dynamics.

3.1.1 Historical analysis

In an avalanche study it is very important to collect all the data necessary to understand the avalanche events that occur in a specific site.

Analysis of the avalanche register. The avalanche register is certainly the principal information source concerning avalanche events in the past. The principal information that can be obtained concerns: the events date, the stopping distance, the avalanche extension in the deposit zone, the damages caused to buildings or roads, the number of victims, the type of avalanche.

Chronicles of direct testimonies. The information obtained by people who have witnessed an avalanche event is very important, even if difficult to certify. Witnesses can furthermore provide photographic material.

Photo-interpretation and analysis of the topographic maps. Aerial photos can provide a general vision of the possible extent of the avalanche site, a first idea of the possible profiles followed by the avalanches, and can help to understand the modification of morphology of the detachment zones in time.

The topographic maps contain further information concerning the slopes of the path and help detachment zone definition. The use of a Geographic Informative Systems (GIS) makes this analysis easier.

3.1.2 Field measurements

One of the most important operations for an expert who must elaborate an avalanche hazard map is to perform a field analysis, in order to understand the zone morphology.

The vegetation is the most explicit indicator to identify a zone subject to avalanches with greater or less frequency. Normally in the zones interested by avalanches vegetation is exposed to strong solicitations, so it does not have the time to grow, and it is more likely to find shrub. A science which can help in the definition of the frequency of the avalanches in a avalanche path is dendrology, which allows to identify the age of the trees and possible damage made by an avalanche.

During a field work, the expert also analyses the type of substratum which determines the friction which is produced between avalanche and ground.

Besides, on field it is possible to locate -with a good margin of precision- rock jumps or morphological changes in the ground that are often not recognizable on maps or in aerial photos.

In Fig. 3.1 field measurements and tests for the snow cover are presented.

FIELD MEASUREMENTS AND TESTS

a) METEOROLOGICAL STATION

In a meteorological station, air temperature, cloudiness, wind direction and speed, fresh and total snow depth, sun radiation, and other parameters, are measured.



b) RAM PROFILE

The ram profile is a record of a hardness index concerning a vertical section of the snowpack. With this method a steel cylindrical tool called ram penetrometer, which consists of three parts, is used. The ram penetrometer can be used for studying variations in snow hardness related to depth. This test is based on dropping a number of weights and measuring the distance travelled through the snow by using a ram. This test has been developed in Switzerland.



c) SNOW PROFILE

A snow profile is a record of layer sequences and of individual layer properties. It is obtained by digging a pit and observing the snow layers. It is used on a small test slope which faces the same direction and has the same inclination. To perform this test a snow shovel, a wood meter, a crystal card, thermometer and a snow profile form are necessary. With this method, it is possible to register: thickness, hardness (by using hands), moisture content, density, crystal types and temperatures of snow layers.



d) SHOVEL SHEAR TEST

The principal objective of the shovel shear test is to locate weak layers and interfaces. The test is prepared by cutting a vertical column of snow to a depth below suspected weak layers. The shovel is inserted into the back cut. A force is applied in the down slope direction by holding the shovel handle with both hands and pulling. The column shears in a smooth plane when a weak layer exists. When no weak layers are present, the column usually breaks obliquely at the lower end of the back cut. This process is continued down to the ground.



e) SHEAR FRAME TEST

The shear frame test is used to measure the shear strength of weak snow layers that have been identified by another test. The equipment required is a shear frame and a dynamometer. A shear frame is a rectangular metal frame with thin cutting edges and crossbars. Shear frame index and normal pressure exerted above and perpendicular to the weak layer allow the calculation of an effective friction coefficient called "stability factor".



f) COMPRESSION TEST

First one has to isolate a 30 cm by 30 cm column of snow deep enough to expose potential weak layers on the smooth walls of the column. Then it is necessary to put the snow shovel on the top of the column surface and to tap on the shovel with variable force. During this process, developing failures are observed. If during tapping the upper part of the column slides off, or crushes so that it no longer "evenly" supports further tapping on the column, remove the damaged part of the column, level the new top of the column and continue tapping.



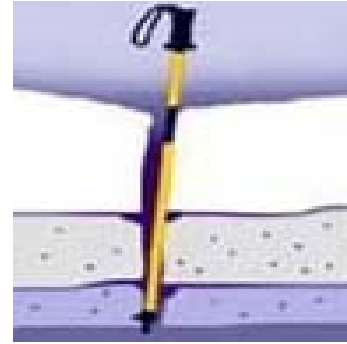
g) RUTSCHBLOCK TEST

In this test a block of snow is loaded by a person in several stages. On a slope (an inclination of at least 30° is preferred), a rectangular block of snow is exposed by shovelling a vertical (plumb) trench in front and two narrow trenches at the sides. The block should be about 1.5 m wide in the down slope direction, and 2 m wide. Side trenches may be 50 cm wide or less. Back side of block can be cut with a snow saw or a rope tied to ski poles.



h) PROBING TEST

Probing is used to check the structure of the snowpack at numerous locations during travel, climbing, and skiing with ski poles, avalanche probes and ice axes. Probing is used to check the relative hardness of the snow layers, to detect weakness, and to determine the depth of weak layers from the surface. Probing the ground also allows depth determination for studying snow distribution. If a ski pole is utilised, one has to push the pole with the basket end into the snow at a right angle to the snow surface as deep as possible.



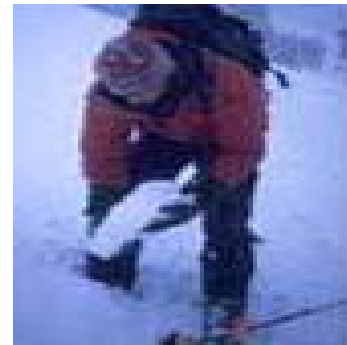
i) STUFFBLOCK TEST

In this test an isolated column in a snow pit is stressed by dropping a nylon stuff sack with a known mass onto the column from various heights until the weak layer fails.



l) SKI SHEAR TEST

This is basically the same as the shovel shear test but you completely isolate the column, then insert a ski behind the column and pull on the ski. Results are hard to interpret and subjective.



m) HAND SHEAR TEST

This is a quick way to test how well the surface snow is bonded to the underlying snow. It is possible to determine fresh snow instabilities and shallow weak layers. This determination is limited to only shallow layers.



n) TEST SLOPES

First one has to find a small, steep slope -where the consequences of a slide are small. One simply jumps on the slope to see how it responds. Interpretation of results is easy and quick but it may be dangerous if done on dangerous slopes.

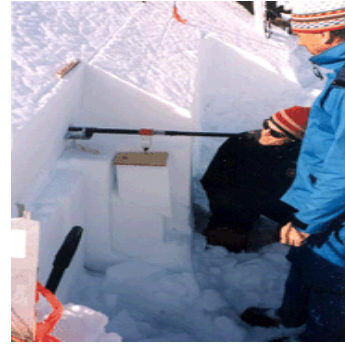
o) TILT BOARD TEST

The tilt board is used to locate weak layers in soft and very soft snow close to the surface in flat weather observation sites. The observation is inconvenient for testing snow layers deeper than about 40 cm.



p) LOADED COLUMN TEST

This is mostly an avalanche forecaster's snow pit test which can estimate how much additional snow will trigger an avalanche. The test is also quantifiable. First, on a slope of at least 30°, one has to completely isolate a column -no matter how big. Then one has to cut blocks of snow the same size as the top of the column and carefully stack them on top of the column until it fails. Quantification comes through estimating the density of the added snow. The test does not suffer any of the difficulties in interpretation like the shovel shear test, but it does take more time.



q) CORNICE TEST

Cornices are the “bombs” of the backcountry. Simply, one has to find a cornice which weighs significantly more than a person and knock it down the slope. The smaller the cornice, the less effective the test. This test is probably the best test of a slope without using explosive charges and it is easy to interpret. It is very dangerous if done improperly, and cornices are not always available.



Fig. 3.1 – a) Meteorological station; b) ram profile; c) snow profile; d) shovel shear test; e) shear frame test; f) compression test; g) rutschblock test; h) probing test; i) stuffblock test; l) ski shear test; m) hand shear test; n) test slopes; o) tilt board test; p) loaded column test; q) cornice test [Tremper, 1994; <http://cagem.bayindirlik.gov.tr>; <http://www.avalanche.org>].

3.1.3 Statistical analysis of snow-meteorological data

The required extreme snow depth can be calculated statistically .

Probability density function or FDP. Probability distributions are typically defined in terms of the probability density function. The mathematical definition of a probability function, $p(x)$, is a function that satisfies the following properties.

- 1) The probability that x can take a specific value is $p(x)$;
- 2) $p(x)$ is non-negative for all real x ;
- 3) The sum of $p(x)$ over all possible values of x is 1, that is $\sum_j p_j = 1$, where j represents all possible values that x can have and p_j is the probability at x_j .

Moments. If we consider a data set x_i with $i = 1, \dots, n$, we calculate the moment of first order – mean, it is simply the arithmetic mean of the values in the set, obtained by summing the values and dividing by the number of values; the moment of second order, the variance, that is the arithmetic average of the squared differences between the values and the mean; and the standard deviation, that is the square root of the variance:

$$M_k = \frac{1}{n} \sum_{i=1}^n (x_i - x_0)^k$$

Moment of order k;

$$\mu_x = \frac{1}{n} \sum_{i=1}^n x_i = M_1$$

Mean or moment of order 1;

$$\sigma_x = \frac{1}{n} \sum_{i=1}^n (x_i - x_0)^2 = \frac{1}{n-1} \sum_{i=1}^n (x_i - \mu_x)^2 = M_2$$

Variance or moment of order 2.

Annual maximum series (AMS). For analyzing extreme avalanche events for a specific return period, it is possible to use the cumulative distribution function (CDF) and the probability density function (PDF):

$$F(x) = P(X \leq x)$$

CDF, cumulative distribution function;

$$f(x) = \frac{dF}{dx}$$

PDF, probability density function;

$$T_r = \frac{1}{1 - F(x)}$$

Return period.

The cumulative distribution function is defined as $F(x) = 1 - \frac{1}{T_r}$ and, in case of a sample, as in Table 3.1.

Table 3.1 – Estimation of the accumulate frequency [Barbolini et al., 2005].			
Weibull	Cunnane	Hazen	Gringorten
$F(x_i) = \frac{i}{n+1}$	$F(x_i) = \frac{i-0,4}{n+0,2}$	$F(x_i) = \frac{i-0,5}{n}$	$F(x_i) = \frac{i-0,44}{n+0,12}$

Distribution and parameters estimation methods. The method of moments equates sample moments to parameter estimates. The method of maximum likelihood begins with the mathematical expression known as a likelihood function of the sample data. Loosely speaking, the likelihood of a set of data is the probability of obtaining that particular set of data given the chosen probability model. This expression contains the unknown parameters. Those values of the parameters that maximize the sample likelihood are known as the maximum likelihood estimates.

1) FDP of Gumbel, EV1 (α, u).

$$F(x) = e^{-e^{-\alpha(x-u)}}$$

CDF, cumulative distribution function;

$$f(x) = \alpha e^{-e^{-\alpha(x-u)}} e^{-\alpha(x-u)}$$

PDF, probability density function;

$$y_i = \alpha(x_i - u)$$

Reduced variable.

Table 3.2 – MOM and ML parameters in the FDP.	
Method of moments (MOM)	Method of maximum likelihood (ML)
$\begin{cases} \mu_y = \alpha \mu_x - u \\ \sigma_y = \alpha \sigma_x \end{cases}$	$\begin{cases} \frac{1}{\alpha} - \mu_x + \frac{1}{n} \sum_{i=1}^n x_i e^{-\alpha(x_i-u)} = 0 \\ n - \sum_{i=1}^n e^{-\alpha(x_i-u)} = 0 \end{cases}$
$\begin{cases} \mu_x = \frac{\mu_y}{\alpha} + u = \frac{0,577}{\alpha} + u \\ \sigma_x = \frac{\sigma_y}{\alpha} = \frac{1,283}{\alpha} \end{cases}$	$\begin{cases} \frac{1}{\alpha} = \mu_x - \frac{\sum_{i=1}^n x_i e^{-\alpha x_i}}{\sum_{i=1}^n e^{-\alpha x_i}} \\ u = \frac{1}{\alpha} \ln \frac{n}{\sum_{i=1}^n e^{-\alpha x_i}} \end{cases}$
$\begin{cases} \alpha = \frac{1,283}{\sigma_x} \\ u = \mu_x - \frac{0,577}{\alpha} = \mu_x - 0,45 \sigma_x \end{cases}$	

$$x(T_r) = u - \frac{1}{\alpha} \ln \left(-\ln \left(1 - \frac{1}{T_r} \right) \right)$$

Extreme value.

2) FDP LogNormal, LN (μ_L, σ_L).

$$F(x) = \frac{1}{\sqrt{2\pi} \sigma_L} \int_0^x \frac{1}{\xi} \exp \left[-\frac{1}{2} \left(\frac{\ln \xi - \mu_L}{\sigma_L} \right)^2 \right] d\xi$$

CDF, cumulative distribution function;

$$f(x) = \frac{1}{x \sqrt{2\pi} \sigma_L} \exp \left[-\frac{1}{2} \left(\frac{\ln x - \mu_L}{\sigma_L} \right)^2 \right]$$

PDF, probability density function;

$$L_i = \ln x_i$$

$$y_i = \frac{\ln x_i - \mu_L}{\sigma_L}$$

Reduced variable.

Table 3.3 – MOM and ML parameters in the LogNormal.	
Method of moments (MOM)	Method of maximum likelihood (ML)
$\left\{ \begin{array}{l} \mu_L = \ln \mu_x - \frac{1}{2} \ln \left(1 + \frac{\sigma_x^2}{\mu_x^2} \right) = \ln \mu_x - \frac{1}{2} \sigma_L^2 \\ \sigma_L = \sqrt{\ln \left(1 + \frac{\sigma_x^2}{\mu_x^2} \right)} \end{array} \right.$	$\left\{ \begin{array}{l} \mu_L = \frac{1}{n} \sum_{i=1}^n L_i \\ \sigma_L = \sqrt{\frac{\sum_{i=1}^n (L_i - \mu_L)^2}{n}} \end{array} \right.$

$$x(T_r) = e^{(\mu_L + z(T_r)\sigma_L)}$$

Extreme value.

Pearson Test or chi-square test. It is the best-known of several chi-square tests – statistical procedures whose results are evaluated by reference to the chi-square distribution.

The first step in the chi-square test is to calculate the chi-square statistic. The chi-square statistic is calculated by finding the difference between each observed and theoretical frequency for each possible outcome, squaring them, dividing each by the theoretical frequency, and obtaining the sum of the results:

$$\chi_c^2 = \sum_{i=1}^k \frac{(N_i - N_p)^2}{N_p}$$

χ_c^2 test statistic that asymptotically approaches a χ^2 distribution;

N_i observed frequency;

N_p theoretical frequency;

k number of possible outcomes of each event.

3.1.4 Monitoring systems

An overview of three avalanche test sites in Western Europe that were operational in recent years is given: Monte Pizzac in Italy, the Vallée de la Sionne in Switzerland and the Col du Lautaret in France (Fig. 3.2-Fig. 3.4). The geographical location, the avalanche path and the typical avalanches occurring at the site are described.

In the monitoring systems an essential element of a quantitative risk assessment is the impact pressure to be expected at a given location in the run-out zone. A distinction is made between sites where avalanches are released artificially during manned experiments, and sites with unattended measurements on spontaneous avalanches. On the basis of this information, a comparative analysis assesses the potential of these sites for various types of experiments, ranging from practical studies of impact forces to the validation of dynamic models of avalanche motion and to detailed studies of the physical processes inside avalanches [Barbolini & Issler, 2005].

3.1.3.1 Monte Pizzac – Italy

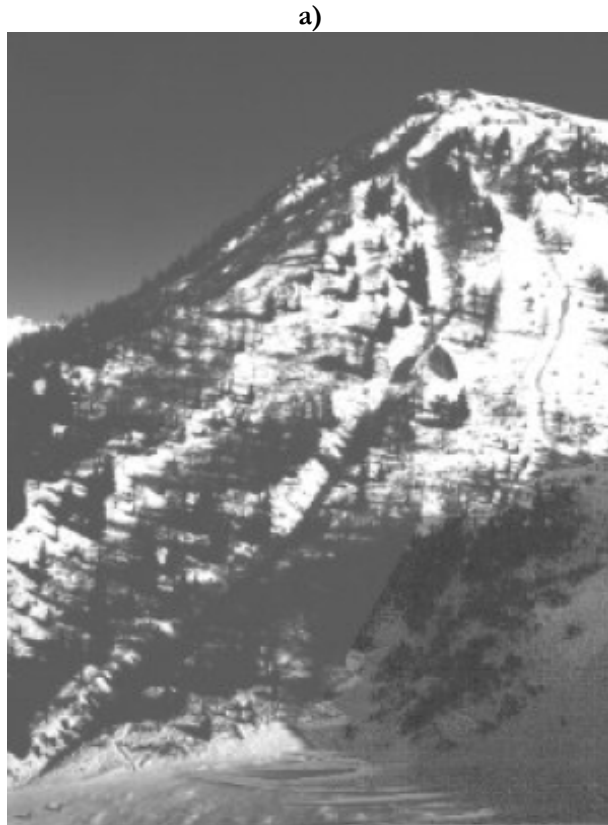
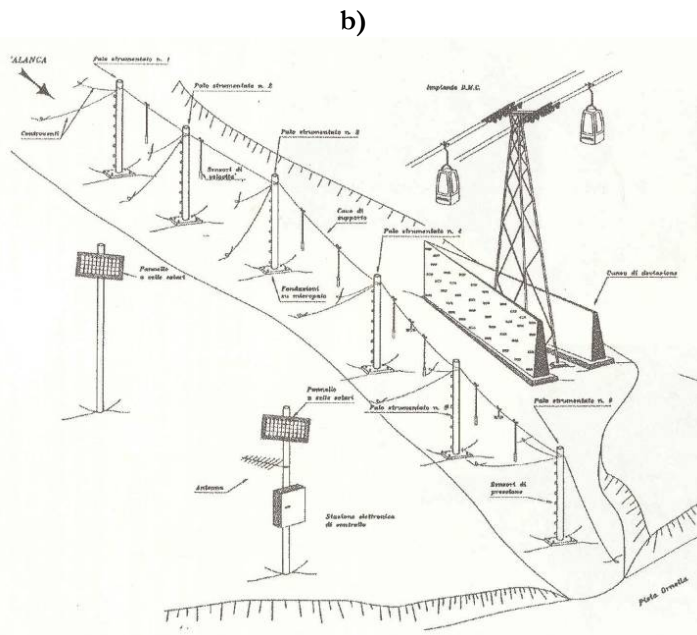


Fig. 3.2 – a) Above, the avalanche test site;
b) below, a sketch of the instrumentation
(CVA – Arabba Avalanche Centre)
[Barbolini & Issler, 2005].



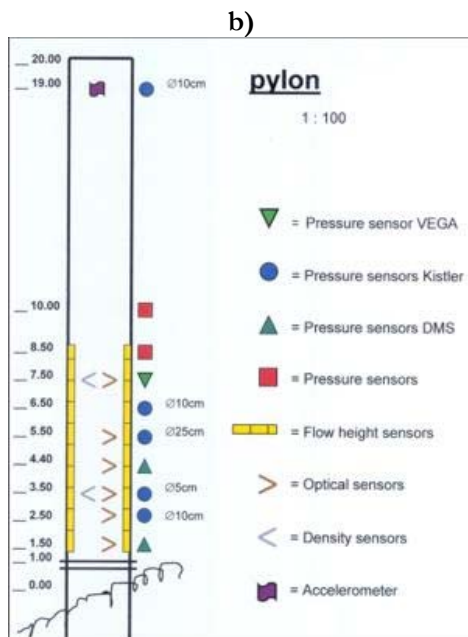
GEOGRAPHICAL SETTING	
MOUNTAIN	Monte Pizzac
ELEVATION	22181 m s.l.m.
COMMUNE	Livinallongo del Col di Lana Belluno
PROVINCE	Trentino Alto Adige
REGION	Italy
COUNTRY	
TEST SITE FEATURES	
INSTALLATION YEAR	1993
PURPOSE	Investigation of the dynamic parameters of avalanches (pressure, snow depth, front speed). Analysis of impact pressures against obstacle. Mass balance experiments.
RELEASE	Natural and Artificial Catex
QUANTITY MEASURED	Pressure profile Pressure on small wedge-shaped obstacle Depth profile Front velocity Flow height Mass balance

AVALANCHE FEATURES	
TYPE	Dry or wet dense flow avalanches
NUMBER OF PATHS	1
DETACHMENT ELEVATION	2200 m s.l.m.
ACCUMULATION ELEVATION	1745 m s.l.m.
LENGTH AVALANCHE PATH	836 m
MONITORED LENGTH	418 m
SLOPE	31°
VOLUME	2000 m ³
VELOCITY MAX	20 m/s
FREQUENCY	2-3 per year

3.1.3.2 Vallée de la Sionne – Switzerland



Fig. 3.3 – a) Above, the avalanche test site,
b) below, a sketch of the instrumentation
(SLF – Federal Institute of Snow and Avalanche
Research of Davos)
[Barbolini & Issler, 2005].



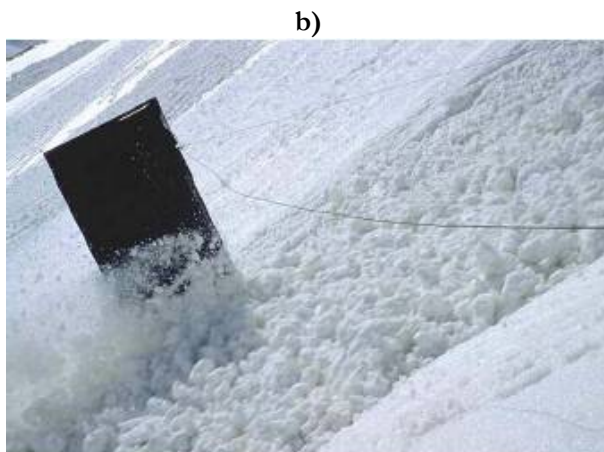
GEOGRAPHICAL SETTING	
MOUNTAIN	Crêta Besse
ELEVATION COMMUNE	2700 m s.l.m.
DEPARTMENT	Arbaz
CANTON	Sion
COUNTRY	Valois Switzerland
TEST SITE FEATURES	
INSTALLATION YEAR	1997
PURPOSE	Studies of basic processes in avalanches (flow regimes, snow entrainment and deposition). Determination of avalanche forces on structures.
RELEASE	Natural and artificial Helicopter, mortar
QUANTITY MEASURED	Impact pressures on ovalshaped pylon, narrow wedge and small wall Front velocity Velocity profile Density Flow depth Front velocity Flow height Mass balance

AVALANCHE FEATURES	
TYPE	Dry mixed avalanches, often with a strongly developed powder-snow part. Wet dense flow avalanches, in early and late winter.
NUMBER OF PATHS	2
<u>PATH N°1</u>	
DETACHMENT ELEVATION	2300 m s.l.m.
ACCUMULATION ELEVATION	1800 m s.l.m.
LENGTH AVALANCHE PATH	400 m
MONITORED LENGHT	2,5 km
SLOPE	35°-40°
VOLUME	
VELOCITY MAX	70 m/s
FREQUENCY	

3.1.3.3 Col du Lautaret – France



Fig. 3.4 – a) Above, the avalanche test site;
b) below the instrumentation
(ETNA – Cemagref de Grenoble)
[Barbolini & Issler, 2005].



GEOGRAPHICAL SETTING	
MOUNTAIN	Crête de Chaillol
ELEVATION COMMUNE	2600 m s.l.m.
DEPARTMENT	Hautes-Alpes
REGION	Provence-Alpes-Côte d'Azur
COUNTRY	France
TEST SITE FEATURES	
INSTALLATION YEAR	1973
PURPOSE	1) Study of snow avalanche dynamics ; 2) Study of artificial release technique.
RELEASE	Catex (1975-1985) GazEx (1998) Avalhecix (1999)
QUANTITY MEASURED	Impact pressure Front velocity Density

AVALANCHE FEATURES	
TYPE	Dense, wet to dry, sometimes with powder part..
NUMBER OF PATHS	7
<i><u>PATH N°2</u></i>	
DETACHMENT ELEVATION	2600 m s.l.m.
ACCUMULATION ELEVATION	2100 m s.l.m.
LENGTH AVALANCHE PATH	
RUN-OUT DISTANCE	500-800 m
SLOPE	36°
VOLUME	500-10.000 m ³
VELOCITY MAX	10-30 m/s
FREQUENCY	3-4 per year

3.2 Experimental analysis

In this dissertation two experimental analyses are presented:

- 1) experimental analysis on the characterization of avalanche deposits;
- 2) experimental analysis on retarding cone-shaped and tooth-shaped structures.

Experimental analysis on the characterization of avalanche deposits. Much field evidence proves that dense snow avalanches, after a first phase of granulation, move downstream and stop in almost the same way as granular materials (Fig. 3.5-Fig. 3.6).

Recent detailed measurements [Rognon, 2006], made in a large scale channel using real snow, evidenced a thin layer -just above the base- made of granular snow, as a result of granulation. Most of the velocity occurs in this layer while the upper mass moves almost undisturbed.

Due to the above observations dense snow avalanches are often modelled adopting small-scale laboratory experiments, using dry granular materials.

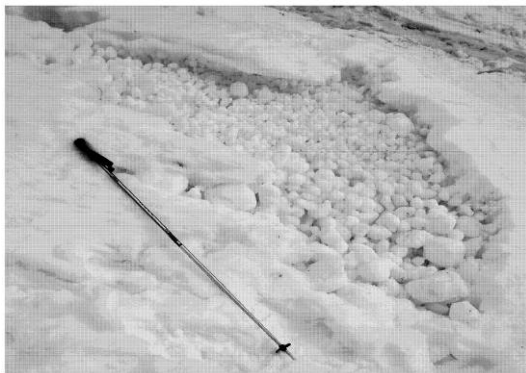


Fig. 3.5 – Example of granular deposit of an avalanche occurred in *Val di Lavina Granda* (near to Trento, Italy) [De Toni & Scotton, 2005].



Fig. 3.6 – Example of granular deposit of an avalanche occurred in *Val dei Spini* (*Val di Pejo, Trentino Alto Adige Region, Italy*) [De Toni & Scotton, 2005].

Starting from field observations showing several similarities with granular flows, we chose to represent a dense and dry snow avalanche with a non-cohesive granular material. Many experimental investigations on reduced models studied dense snow avalanches dynamics with granular materials: for example sand [Chu et al., 1995], beads [Hutter et al., 1995] and ping-pong balls [Keller et al., 1998].

Experimental analysis on retarding cone-shaped and tooth-shaped structures. The first earth mounds for protecting roads were constructed in Norway in 1975. Their use was based on ideas and experiences made in Switzerland and Rogers Pass in Canada. The design and location of the earth mounds up to now are partly based on a trial and error basis, and partly on measures to dissipate energy on water flume. A Norwegian handbook recommending design and location of this type of works was published [Norem, 1995], and some studies on evaluating the effect of snow avalanche retarding measures were carried out in the following years [Larsen & Norem, 1996; Hammersland et al., 2000].

Today braking or retarding mounds are widely used for protection against dense snow avalanches. The design of such mounds is in most cases based on the subjective conviction of avalanche experts. Furthermore, there are no accepted methods for estimating the retarding effect of avalanche mounds in a quantitative way. Therefore, the design of protection structures in the run-out zone of avalanches is very empirical.

Experiments on full-scale avalanches are expensive, dangerous and highly dependent on weather conditions. For these reasons, experiments on smaller scales are useful to study natural snow avalanche dynamics.

The problem can be faced studying the effect of the presence of the retarding structures in terms of energy dissipation of the moving mass and analysing the impact against the retarding elements. This second point of view is adopted in this research.

A way to protect areas against dense snow avalanches is to dissipate energy using passive defence structures such as dams or retarding mounds, thereby reducing the run-out distance of the avalanche. The question therefore arises of how a given avalanche flow changes in terms of its run-out distance.

A number of chute experiments at different scales and with different types of granular materials have recently been performed (Fig. 3.7-Fig. 3.10) in order to shed light on the dynamics of avalanche flow over and around braking mounds and catching dams and to estimate the retarding effect of the mounds [Woods & Hogg, 1999; Faug, 2004; Hákonardóttir, 2004; Norem & Brateng, 2005].



Fig. 3.7 – Università degli Studi di Pavia [Barbolini & Issler, 2005].



Fig. 3.8 – Cemagref of Grenoble [Faug, 2004].



Fig. 3.9 – University of Bristol [Hákonardóttir, 2004].

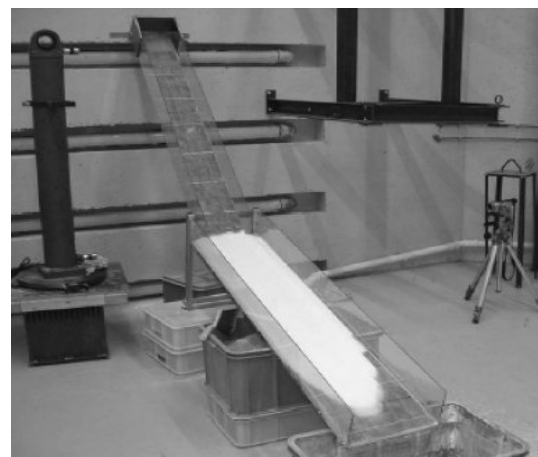


Fig. 3.10 – Norwegian University of Science and Technology [Norem & Brateng, 2005].

Some of these experiments were carried out as a part of the projecting of avalanche protection measures for the town of Neskaupstaður in eastern Iceland [Tomasson et al., 1998], and the town of Taconnaz in the French Alps [Berthet-Rambaud et al., 2005]. The analyses of

damage generated by snow avalanches can be very valuable to improve knowledge of avalanche pressure against a structure [Margreth & Ammann, 2003].

There are some other studies that present the effects of the avalanches against obstacles: one, using a reduced model, investigates granular avalanches interacting with a stopping dam [Chu et al., 1995]; another studies -numerically- the effect of variation of the structure height on the reduction of the dynamic pressure [Naaim, 1998]; a third compares experimental and numerical results using a granular flow interacting with a tetrahedral wedge [Tai et al., 2001].

The experiments may be used to identify certain types of behaviour, which do not strongly depend on scale or material properties, and which may be exploited in the designing of avalanche protection measures. The experiments, thus, provide useful indications for designers of retarding structures for snow avalanches in the absence of data from experiments on larger scales and measurements of natural avalanches.

3.2.1 Models theory

To describe a physical phenomenon, the first step is to establish which parameters can be judged important for it, and, subsequently, to establish the functional relations between these parameters.

The dimensional analysis is a procedure to combine the variables of a physical phenomenon so as to create some non dimensional products. Two big advantages are obtained in this way:

- 1) the number of the variables is reduced;
- 2) the obtained equations are dimensionally homogeneous.

A set of non-dimensional products is complete when every product of the set is independent from the others and all the other possible products which can be formed with the variables involved can be expressed in a monomial form.

Once a complete set of non dimensional products is identified, the physical phenomenon is completely described by these variable fundamental functional relations.

The number of non dimensional products which can be expressed, from a set of variables, is defined by the theorem of Buckingham, according to which in an equation dimensionally homogeneous with n variables, the number of non-dimensional products that it is possible to express is $(n - r)$ where r it is the number of the fundamental dimensions of the variables. The theorem assures that a homogeneous equation in the form:

$$x_1 = f(x_2, \dots, x_n)$$

can be transformed into an equation in non dimensional terms of the type:

$$\Pi_1 = f(\Pi_2, \dots, \Pi_n)$$

The physical modelling of the natural phenomena is carried out, in general, following the theory of the similarity which makes it possible to reproduce the real phenomenon in a dynamic small-scale model. For the correct reproduction of the phenomenon the knowledge of the significant physical parameters is necessary. The possibility of obtaining a model in a reduced scale often implies determining limits in dimensions of the model and the choice of the materials used to simulate the real materials. A scale ratio which represents the relation between the value in the prototype and the value in the model is associated to each parameter of the physical phenomenon:

$$N = \frac{X_p}{X_m}$$

X_p value in the prototype;

X_m value in the model.

According to the type of the physical magnitudes reproduced in the model, three types of similarity are defined: geometrical, cinematic and dynamic.

The phenomenon of avalanches is very complex; its complete description depends on many physical parameters of thermo-fluid-dynamics origin. The difficulty in the definition of the initial and boundary conditions contributes, decisively, in increasing the limits in the knowledge of the real phenomena. For these reasons physical simulations are carried out to try and describe the fundamental aspects of the phenomenon.

In each dynamic phenomenon, inertia force, which is balanced by other forces, is present - for example, gravitational or viscous forces. Froude and Reynolds similarity criteria (more known) are used when gravitational forces or viscous forces are prevalent, respectively.

3.2.2 Froude Number

The number of Froude is a non dimensional number which is the square root of the relation between the inertial forces and the gravitational forces acting on an element of volume in the motion field (or also the ratio between kinetic energy and potential energy). With reference to a dense snow avalanche flowing along an open slope with homogenous density, the Froude Number can be written as [Jóhannesson & Hákonardóttir, 2003]:

$$F_r = \frac{v}{\sqrt{g \cos \phi \cdot h}}$$

v [m/s]	velocity;
g [m/s ²]	gravitational acceleration;
h [m]	flow depth;
ϕ [°]	slope.

The criterion of similarity of Froude consists in preserving this number in the passage from the prototype to the model. This criterion allows to describe all the phenomena in which the gravitational forces result prevalent compared to the other ones (for example, the viscous forces). The criterion of similarity offers, moreover, the rules to transform the values of the parameters measured in the model into the values of the same parameters in the prototype.

3.3 Numerical-mathematical analysis

In the past, many models have been used to describe the behaviour of dense snow avalanches [Voellmy, 1955; Perla et al., 1980; Dent & Lang, 1983; Norem et al., 1989; Savage & Hutter, 1989; Naaim & Ancey, 1992]. Since snow avalanches are very destructive and cannot be controlled, it is very difficult to fully test these models experimentally. Direct measurements on avalanches do exist [Dent et al., 1998] but are rare and must be completed by “laboratory experiments” to study the rheology of snow [Nishimura & Maeno, 1989; Cassassa et al., 1991; Kern et al., 2004].

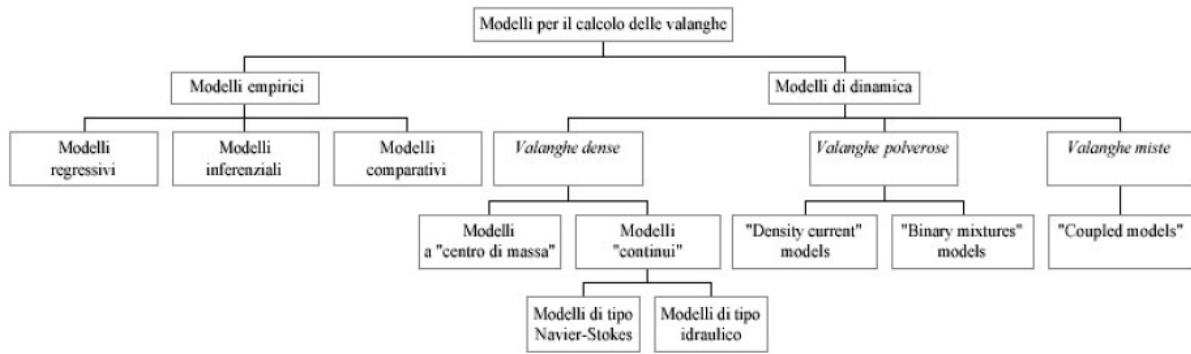


Fig. 3.11 – Models for the avalanche study [Barbolini et al., 2005].

Numerical models allow the simulation of the avalanche events with more detail respect to laboratory models. Their application, for example, permits to evaluate the velocities and the form of the deposits. The areas with different hazard degree for an assigned return time, the detachment height and the dynamic parameters can properly be defined with the mathematical model.

The models are subdivided in statistical and dynamical models (Fig. 3.11).

3.3.1 Avalanche statistical models

Statistical models estimate extreme run-out distances for simple topographies, based on a sample of avalanche observations. All these methods rely on the correlations existing between the run-out distance and the topographic parameters. They assume that the longitudinal profile of the avalanche path governs avalanche dynamics.

Although they permit the estimation of the probable extent of extreme avalanches, they do not provide any information on velocities and impact pressures. The most important models are (Table 3.4):

Table 3.4 – Statistical models.	
Regressive models:	
BOVIS & MEARS	[Bovis & Mears, 1976]
LIED & BAKKEHØI	[Lied & Bakkehøi, 1980]
Interferential models:	
MCCLUNG & LIED	[McClung & Lied, 1987]
BARBOLINI & CAPPABIANCA	[Barbolini & Cappabianca, 2002]
Comparative models:	
BAKKEHØI & NOREM	[Bakkehøi & Norem, 1993]
KEYLOCK – MCCLUNG – MAGNUSSON	[Keylock et al., 1999]

3.3.2 Dense avalanche dynamic models

Dynamic models aim to describe the avalanche movement along its path, calculating the fundamental dynamic variables for the definition of the hazard areas, such as stopping distance and impact pressure.

A sensitivity analysis of the most common models used in practice was carried out by Barbolini et al. (2000).

In Table 3.5 the most important models are presented.

Table 3.5 – Dynamic models.	
Mass point models:	
COULOMB	
<ul style="list-style-type: none"> MOTION EQUATION: $\frac{dv}{dt} = g(\text{sen } \psi - \mu \cos \psi)$ <p> <i>v</i> avalanche velocity; <i>v</i>₀ avalanche velocity at the starting zone; <i>g</i> gravitational acceleration; <i>ψ</i> angle of track avalanche slope; <i>μ</i> Coulomb friction coefficient. </p>	Avalanche velocity: $v = \sqrt{v_0^2 + 2g(\text{sen } \psi - \mu \cos \psi)s}$
	Stopping distance: $s = \frac{v_0^2}{2g(\text{sen } \psi - \mu \cos \psi)}$
VOELLMY	[Voellmy, 1955]
<ul style="list-style-type: none"> MOTION EQUATION: $\frac{dv}{dt} = g \left(\frac{\gamma - \gamma_a}{\gamma} \right) (\text{sen } \psi - \mu \cos \psi) - \frac{g}{\xi \cdot h} v^2$ <p> <i>v</i> avalanche velocity; <i>v</i>₀ avalanche velocity at the starting zone; <i>g</i> gravitational acceleration; <i>γ</i> snow density; <i>γ</i>_a air density = 1,25 kg/m³; <i>ψ</i> angle of track avalanche slope; <i>ψ</i>₀ angle of track avalanche slope at the starting zone; <i>μ</i> Coulomb friction coefficient; <i>ξ</i> turbulent friction coefficient; <i>h</i> snow depth. </p>	Avalanche velocity: $v_{max} = \sqrt{\xi \cdot h \left(\frac{\gamma - \gamma_a}{\gamma} \right) (\text{sen } \psi - \mu \cos \psi)}$
	Stopping distance: $s = \frac{\xi \cdot h}{2g} \ln \left(1 - \frac{v_0^2}{\xi \cdot h (\text{sen } \psi - \mu \cos \psi)} \right)$
PERLA – CHENG – MCCLUNG “PCM MODEL”	[Perla et al., 1980]
<ul style="list-style-type: none"> MOTION EQUATION: $\frac{dv}{dt} = g(\text{sen } \psi - \mu \cos \psi) - \frac{D}{M} v^2$ <p> <i>v</i> avalanche velocity; <i>v</i>₀ avalanche velocity at the starting zone; <i>g</i> gravitational acceleration; <i>ψ</i> angle of track avalanche slope; <i>μ</i> Coulomb friction coefficient; <i>D</i> friction coefficient; <i>M</i> avalanche mass. </p>	Avalanche velocity: $v_{max} = \sqrt{\frac{M}{D} g(\text{sen } \psi - \mu \cos \psi)}$
	Stopping distance: $s = \frac{M}{2D} \ln \left(1 - \frac{v_0^2}{\frac{M}{D} g(\text{sen } \psi - \mu \cos \psi)} \right)$

LANG – NAKAMURA – DENT – MARTINELLI “LANG MODEL”	[Lang et al., 1985]
<ul style="list-style-type: none"> MOTION EQUATION: $\frac{dv}{dt} = g(\sin\psi - \mu \cos\psi) - \frac{\nu}{h^2} v^2$ <p> <i>v</i> avalanche velocity; <i>v</i>₀ avalanche velocity at the starting zone; <i>g</i> gravitational acceleration; <i>ψ</i> angle of track avalanche slope; <i>μ</i> Coulomb friction coefficient; <i>ν</i> viscosity turbulent coefficient; <i>h</i> snow depth. </p>	<p>Avalanche velocity:</p> $v_{max} = \sqrt{\frac{h^2}{\nu} g(\sin\psi - \mu \cos\psi)}$ <hr/> <p>Stopping distance:</p> $s = \frac{h^2}{2\nu} \ln \left(1 - \frac{v_0^2}{\frac{h^2}{\nu} g(\sin\psi - \mu \cos\psi)} \right)$
VOELLMY – SALM – GLUBLER “VOELLMY – SALM MODEL”	[Salm et al., 1990]
<ul style="list-style-type: none"> MOTION EQUATION: $\frac{dv}{dt} = g(\sin\psi - \mu \cos\psi) - \frac{g}{\xi \cdot h} v^2$ <p> <i>v</i> avalanche velocity; <i>v</i>_p avalanche velocity of the characteristic point P (<i>tgψ = μ</i>); <i>g</i> gravitational acceleration; <i>ψ</i> angle of track avalanche slope; <i>μ</i> Coulomb friction coefficient; <i>ξ</i> turbulent friction coefficient; <i>h</i> snow depth. </p>	<p>Avalanche velocity:</p> $v_{max} = \sqrt{\xi \cdot h(\sin\psi - \mu \cos\psi)}$ <hr/> <p>Stopping distance:</p> $s = \frac{\xi \cdot h}{2g} \ln \left(1 - \frac{v_p^2}{\xi \cdot h(\sin\psi - \mu \cos\psi)} \right)$

Continuous-flow models:	
LANG – DAWSON – MARTINELLI “AVALNCH”	[Lang et al., 1979]
<ul style="list-style-type: none"> GOVERNING EQUATIONS: <p>Mass balance:</p> $\frac{\partial u}{\partial x} + \frac{\partial v}{\partial y} = 0$ <p>Momentum balances:</p> $\begin{cases} \frac{\partial u}{\partial t} + \frac{\partial u^2}{\partial x} + \frac{\partial(uv)}{\partial y} = g \sin\psi - \frac{1}{\rho} \frac{\partial p}{\partial x} + \nu \nabla^2 u \\ \frac{\partial v}{\partial t} + \frac{\partial(uv)}{\partial x} + \frac{\partial v^2}{\partial y} = g \cos\psi - \frac{1}{\rho} \frac{\partial p}{\partial y} + \nu \nabla^2 v \end{cases}$	<p>(<i>x, y</i>) coordinates system; <i>u, v</i> avalanche velocity components; <i>h</i> avalanche depth; <i>g</i> gravitational acceleration; <i>ψ</i> slope angle; <i>ρ</i> snow density; <i>p</i> pressure; <i>ν</i> cinematic viscosity.</p>

SAVAGE & HUTTER "SH MODEL"	[Savage & Hutter, 1989]
<p>• GOVERNING EQUATIONS:</p> <p>Mass balance:</p> $\frac{\partial h}{\partial t} + \frac{\partial(hu)}{\partial x} + \frac{\partial(hv)}{\partial y} = 0$ <p>Momentum balances:</p> $\begin{cases} \frac{\partial(hu)}{\partial t} + \frac{\partial(hu^2)}{\partial x} + \frac{\partial(huv)}{\partial y} = hs_x - \frac{\partial}{\partial x} \left(\frac{\beta_x h^2}{2} \right) \\ \frac{\partial(hv)}{\partial t} + \frac{\partial(huv)}{\partial x} + \frac{\partial(hv^2)}{\partial y} = hs_y - \frac{\partial}{\partial y} \left(\frac{\beta_y h^2}{2} \right) \end{cases}$	<p>(x, y) coordinates system;</p> <p>h avalanche depth;</p> <p>u, v depth-averaged velocity components;</p> <p>$\beta_x = \varepsilon g_x K_x$ normal pressure in x-direction;</p> <p>$\beta_y = \varepsilon g_y K_y$ normal pressure in y-directions;</p> <p>ε aspect ratio of the height to the horizontal extend of the avalanche;</p> <p>s_x net driving acceleration in the down-slope direction;</p> <p>s_y net driving acceleration in the cross-slope direction;</p> <p>$K_x = 2 \sec^2 \phi \left(I \mp \sqrt{1 - \frac{\cos^2 \phi}{\cos^2 \delta}} \right) - I$ down-slope earth pressure coefficient;</p> <p>$K_y = \frac{I}{2} \left(K_x + I \mp \sqrt{(K_x - I)^2 + 4 \tan^2 \delta} \right)$ cross-slope earth pressure coefficient;</p> <p>ϕ internal friction angle;</p> <p>δ bed friction angle.</p>
NAAIM & ANCEY "MN-2D MODEL"	[Naaïm & Ancey, 1992]
<p>• GOVERNING EQUATIONS:</p> <p>Mass balance:</p> $\frac{\partial h}{\partial t} + \frac{\partial(hu)}{\partial x} + \frac{\partial(hv)}{\partial y} = 0$ <p>Momentum balances:</p> $\begin{cases} \frac{\partial(hu)}{\partial t} + \frac{\partial(hu^2)}{\partial x} + \frac{\partial(huv)}{\partial y} = \\ - \frac{\partial}{\partial x} \left(\frac{1}{2} k \cdot g \cos \psi \cdot h \right) - gh \cos \psi_x - \frac{u}{ u } \frac{\tau}{\rho} \\ \frac{\partial(hv)}{\partial t} + \frac{\partial(huv)}{\partial x} + \frac{\partial(hv^2)}{\partial y} = \\ - \frac{\partial}{\partial y} \left(\frac{1}{2} k \cdot g \cos \psi \cdot h \right) - gh \cos \psi_y - \frac{v}{ v } \frac{\tau}{\rho} \end{cases}$	<p>(x, y) coordinates system;</p> <p>h avalanche depth;</p> <p>u, v depth-averaged velocity components;</p> <p>g gravitational acceleration;</p> <p>ψ_x, ψ_y slope angles in the x and y directions;</p> <p>k active-passive pressure coefficient;</p> <p>τ friction term;</p> <p>ρ snow density.</p>

NATALE – NETTUNO – SAVI “VARA-1D MODEL”	[Natale et al., 1994]
<ul style="list-style-type: none"> GOVERNING EQUATIONS: <p>Mass balance:</p> $\frac{\partial h}{\partial t} + \frac{\partial(hu)}{\partial x} = 0$ <p>Momentum balance:</p> $\frac{\partial(hu)}{\partial t} + \frac{\partial(hu^2)}{\partial x} = gh \sin \psi +$ $- gh \cos \psi \left(\frac{\partial h}{\partial x} + \frac{u}{ u } J \right)$	<p>x vertical axis;</p> <p>h avalanche depth;</p> <p>u depth-averaged velocity;</p> <p>g gravitational acceleration;</p> <p>ψ slope angle;</p> <p>μ Coulomb friction coefficient;</p> <p>$J = \mu + n^2 \frac{ u ^2}{h}$ dynamic friction coefficient;</p> <p>$n^2 = 1 / \xi$ internal friction coefficient (ξ turbulent friction coefficient of the Voellmy Model).</p>
SARTORIS & BARTELT “AVAL-1D MODEL”	[Sartoris & Bartelt, 1997]
<ul style="list-style-type: none"> GOVERNING EQUATIONS: <p>Mass balance:</p> $\frac{\partial h}{\partial t} + \frac{\partial(hu)}{\partial x} = 0$ <p>Momentum balance:</p> $\frac{\partial(hu)}{\partial t} + \frac{\partial(hu^2)}{\partial x} = gh \sin \psi +$ $- \frac{\partial}{\partial x} \left(\lambda g \cos \psi \frac{h^2}{2} \right) - gh \left[\mu \cos \psi + \frac{u^2}{\xi \cdot h} \right] \text{sgn}(u)$	<p>x vertical axis;</p> <p>h avalanche depth;</p> <p>u depth-averaged velocity;</p> <p>λ active-passive pressure coefficient;</p> <p>g gravitational acceleration;</p> <p>ψ slope angle;</p> <p>μ Coulomb friction coefficient;</p> <p>ξ turbulent friction coefficient.</p>

Today, the primary motivation for models concerning avalanche dynamics is avalanche hazard mapping. Essential, however, is to calibrate them on the basis of numerous field observations (different topography and climate, involved mass). Without this, a model can never be a credible one [Salm, 2004].

Chapter 4

HAZARD MAPS AND PASSIVE DEFENCE STRUCTURES

4.1 Avalanche hazard zoning

In Alpine regions snow avalanches are a severe threat for human settlements, activities, and infrastructures. Snow avalanche hazard is the probability of occurrence of avalanche events with defined properties and in a defined return period. In the bulletins, the information has to be relating to a specific real situation (type of ground, type of avalanche, presence of material goods).






4.1.1 European avalanche hazard scale

The use of numerical indexes or describers for the definition of avalanche hazard in forecasting bulletins is a usual procedure, consolidated in all countries. In fact, the hazard scale is a support tool to identify an avalanche situation and is also a help for the users in order to have a correct idea of the hazard.

In April 1993 people responsible for the Avalanche European Services finally came to an agreement for the use of a unified avalanche hazard scale. The new scale, which includes 5 hazard degrees, is used in Austria, France, Germany, Italy, Scotland, Spain and Switzerland.

Three sections compose the European avalanche hazard scale: hazard scale, avalanche trigger and avalanche detachment probability (Table 4.1-Table 4.2).

Table 4.1 – European avalanche hazard scale [<http://www.arpa.veneto.it/csvdi>].

	Hazard levels	Avalanche trigger	Avalanche probability
	LOW	The snow pack is generally well bonded and stable.	Triggering is possible only with high additional loads on very steep slopes. Only a few small natural avalanches (sluffs) are possible.
	MODERATE	The snow pack is moderately bonded on some steep slopes, otherwise generally well bonded.	Triggering is possible with high additional loads, particularly on the steep slopes indicated in the bulletin. Large natural avalanches are not likely.
	CONSIDERABLE	The snow pack is moderately to weakly bond on many steep slopes.	Triggering is possible, sometimes even with low additional loads. The bulletin may indicate many slopes, which are particularly affected. In certain conditions, medium and -occasionally- large sized natural avalanches may occur.
	HIGH	The snow pack is weakly bonded in most places.	Triggering is probable even with low additional loads on many steep slopes. In some conditions, frequent medium or large avalanches are likely.
	VERY HIGH	The snow pack is generally weakly bonded and largely unstable.	Numerous large natural avalanches are likely, even on moderately steep terrain.

The scale is based on the following principles:

- a single adjective summarizes all the particularities of the degree (low, moderate, considerable, high, very high);
- the scale goes from 1 to 5, as the hazard increases;
- the scale is not linear. Degree 3, which is the median degree of the scale, does not represent the average hazard, but a critic situation (above all for the mountaineer skiers);
- the scale gradation is based on the increase of the extent of the areas of weakness of the snowpack;
- the probability of detachment of avalanches can be increased in a considerable way by an outside overload; less is the degree of snowpack consolidation, minor is the overload that is sufficient to produce a detachment.

The detachments are divided in:

- spontaneous detachment: detachment that occurs without the intervention of man;
- caused detachment: detachment that is provoked (overloading, explosives);
- detachment caused by strong overload: compact group of skiers, snow cats;
- weak overload: individual skier, excursionist.

Classification	Size class	Slopes	Length	Volume
		[°]	[m]	[m ³]
Steep slopes	low steep slopes	< 30		
	steep slopes	30 – 35		
	very steep slopes	35 – 40		
	extreme steep slopes	> 40		
Avalanche dimension	slide	Shifting of the snow without hazard of burial.	< 50	< 100
	small avalanches	It stops on a steep slope.	< 100	< 1000
	mean avalanches	It reaches the foot of a steep slope.	< 1000	< 10.000
	big avalanches	On grounds to reduced inclination for a distance higher than 50 m and it can reach the valley fund.	> 1000	> 10.000

The entity of the sufficient overload which determines a detachment should be defined statistically. However, considering that hazard degree provides information concerning the amount of hazardous slopes in a determinate zone, nothing is said about their localisation, which is shown in detail in the bulletin.

4.1.2 Snow-meteorological bulletins

The snow-meteorological bulletin or avalanche bulletin (Fig. 4.1) is the tool which supplies a synthetic report of the snow and the snowpack situation and evidences the avalanche hazard in a determinate territory. It is based on forecasts of the meteorological situation and recording of the evolution of the snowpack.

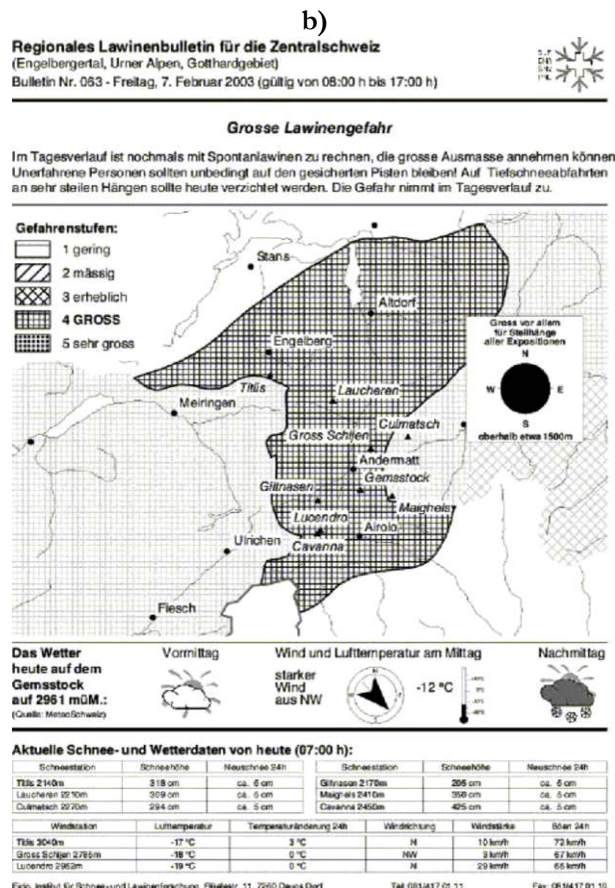
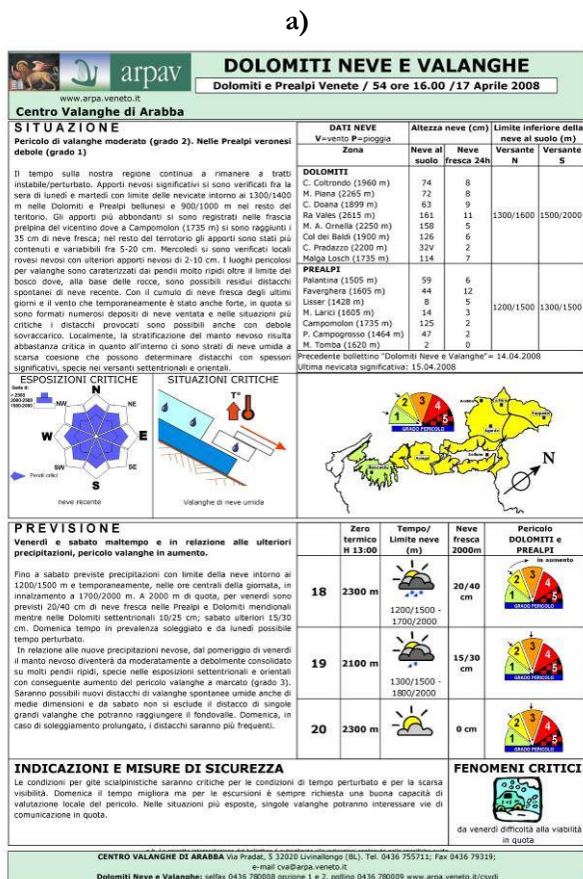


Fig. 4.1 – Examples of avalanche bulletins: a) on the left, bulletin of the Arabba Avalanche Centre [http://www.arpa.veneto.it/csvdi]; b) on the right, bulletin of the Swiss Federal Institute for Snow and Avalanche of Davos [http://www.slf.ch].

The bulletins are realised and diffused by the various Alpine Regions and Provinces. They are different but present some common contents:

- snow covering: snow depth at certain heights, snow distribution on the slopes, amount of fresh snow;
- snow section: with information on the structural characteristics of the snowpack, such as consistency, expected evolution and signs of elements capable of triggering avalanche events (deposits brought by wind, fresh snow, weak layers inside the snowpack);
- information concerning the hazard at the moment of emission of the bulletin;
- meteorological section: forecast, in terms of cloudiness and meteoric events, for a period of validity from 24-48 hours to 72 hours.

The series of data come from:

- a net of snow-meteorological automatic stations placed in the most representative sites of the alpine arc, which provides real time data on temperature, intensity and direction of the wind, height of the snow, humidity, solar radiation;
- a net of snow fields from which surveyors transmit -daily- detailed information regarding the conditions of the snowpack and descriptions of avalanche activity during the last 24 hours;
- a net of snow fields where profiles of the snowpack were executed (penetrometric test and analysis of the layers). Various stability tests may then be also made. Data concerning the constructed field structures are provided on a weekly basis by the various centres, whose average number ranges between 60-70 [Cagnati, 1999].

4.1.3 Maps of avalanche probable localisation

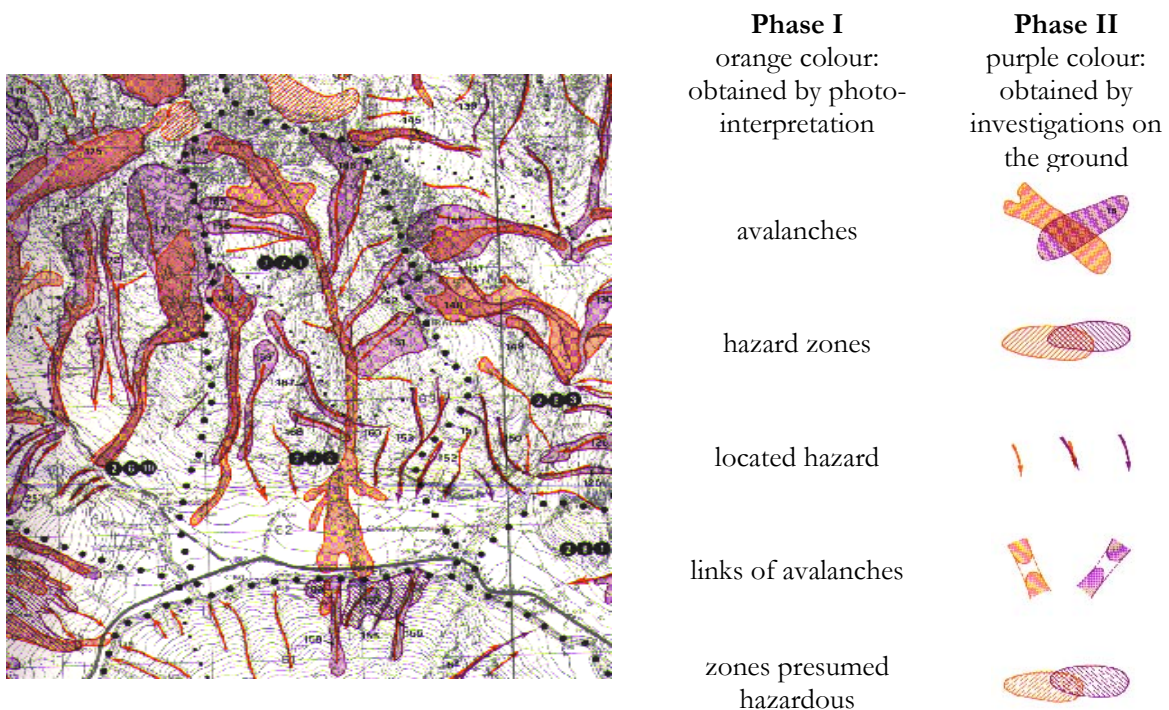


Fig. 4.2 – Example of CLPV with its legend [<http://www.arpa.veneto.it/csvdi>].

The avalanches probable localisation map, CLPV, is a thematic map (Fig. 4.2) -in scale 1:25000- of avalanche sites identified both through historical data and territorial analysis, starting from photogrammetric data.

This kind of map does not give information concerning dynamic characteristics (velocity, pressure and flow depth) and frequency of the events.

The CLPV represents a useful informative document, mainly for consultation, because it allows an immediate and widespread acquisition of avalanche information in a determinate territorial context.

4.1.4 Italian law references

National and regional regulation on avalanche hazard prevention basically considers: the characterization of the phenomenon and the individuation of the zones potentially interested.

In Italy the following national law regarding avalanches exists: *Decreto del Ministero delle Infrastrutture e dei trasporti del 5 dicembre 2003, n. 392 (Regolamento concernente modifica dell'articolo 7 del decreto del Ministro dei trasporti e della navigazione 4 agosto 1998, n. 400, recante norme per le funicolari aeree e terrestri in servizio pubblico destinati al trasporto di persone)*. Art. 1 of this decree refers to local law.

The law on Civil Protection grants institutions a Civil Protection Committee, directed by the Mayor, who is responsible for the management of emergencies.

In a few Regions and Provinces however there is a more specific legislation which foresees the possibility of forming specific local avalanche committees in the municipalities. These have to verify the snowpack stability and offer the Mayor and other responsible figures important technical opinions for rapid evaluation of avalanche hazard and possible prevention measures. Such committees are constituted by experts -in the area- in problems related to snow and avalanches.

Town plans regarding the avalanche phenomena do not exist on a unified scale in Italy, and at a regional level the territorial problems are also faced in a heterogeneously (at least in the Alpine area).

In order to supply a few general indications, the meeting of the Presidents of the areas adhering to the AINEVA (Inter-Regional Snow and Avalanches Association), recently approved the following documents:

- *Linee di indirizzo per la gestione del pericolo di valanghe nella pianificazione territoriale (Documento approvato dall'Assemblea AINEVA, 23/02/01);*
- *Criteri per la perimetrazione e l'utilizzo delle aree soggette al pericolo di valanghe (Documento approvato dall'Assemblea AINEVA il 19/06/02) e Appendice di chiarificazione (Documento approvato dal Comitato Tecnico Direttivo AINEVA, 06/07/05).*

Such documents aim to harmonize and address Regions and Provinces in the elaboration of technical and normative tools necessary to guarantee an effective activity of prevention of avalanche hazard in settlements and infrastructures.

One of the important aspects is the individuation of the zones subject to avalanches. Four different degrees of exposure to the hazard are distinguished (high, moderate, low and null) and are represented with various colours: red, blue, yellow and white (in a decreasing order of hazard).

The Regional Territorial Coordination Plan (PTRC), adopted by the Veneto Region, foresees that *“in the formation of general town planning tools and in the revision of the existing ones, the competent authorities proceed to formulate choices on the basis of the avalanche probable localisation map. It constitutes the document of reference necessary for the choices concerning planning and management of the interested territories, and for the design of the defence structures in hazardous situations”* (art. 8 of the *Norme Attuative “Prescrizioni per le zone soggette a pericolo di valanghe”*).

4.1.5 Avalanche hazard zones and hazard maps

In the PZEV -the avalanche hazard exposure zones plans- the evaluation of the hazard is fixed through mathematical parameters, which quantify velocity and flow height, transmitted pressures and stopping distances of the avalanches. The definition of their maximum extent does not necessarily correspond to the extension described in the CLPV. In the stopping zone some areas are identified and characterized by strong hazard (red colour), weak hazard (blue colour) and -presumably- null hazard (white colour). A yellow zone is also expected, with particular characteristics. Town planning prescriptions are fixed for each of the identified zones (Fig. 4.3).

To define the degree of exposure of a certain portion of territory, frequency and intensity of the expected avalanche events are utilised, expressed through [Barbolini et al., 2005]:

- the avalanche return period - the average number of years between two events of the same intensity;
- the avalanche pressure - the forces per unit of surface exercised by the avalanche on a flat obstacle of big dimensions disposed perpendicularly to the trajectory of the advancing mass of snow. The pressure can be determined with reference to both the dynamic and static components of the solicitation.

The maps of the grounds subject to avalanche hazard identify areas of the territory interested by avalanches of different intensity. They have usually been large scale maps (from 1:5.000 to 1:1.000) which identify the avalanche site and in particular -through dynamic studies- its expansion in the accumulation zone.

This has proven to be most useful in defining these zones in terms of avalanche frequency and dynamic pressure, thus defining magnitude/frequency distribution in the run-out zones.

Red (high hazard) zone. This zone (Table 4.3) includes areas exposed to frequent and/or large powerful avalanches. New buildings are not generally permitted in the red zone.

Table 4.3 – High hazard zone features [Barbolini et al., 2005]:		
Frequent avalanches	Return period	< 30 years
	Pressure	≥ 3 kPa
Rare avalanches	Return period	$30 < T_r < 100$ years
	Pressure	≥ 15 kPa

Blue (moderate hazard) zone. This zone (Table 4.4) includes avalanches that are either small or not frequent. New buildings are generally permitted in the blue zone, but there are many restrictions.

Table 4.4 – Moderate hazard zone features [Barbolini et al., 2005].		
Frequent avalanches	Return period	< 30 years
	Pressure	≤ 3 kPa
Rare avalanches	Return period	$30 < T_r < 100$ years
	Pressure	$3 \text{ kPa} \leq P \leq 15 \text{ kPa}$

Yellow (low hazard) zone. This optional zone (Table 4.5) is not always used. It defines avalanches which are very rare. In the yellow zone new buildings are permitted, with some restrictions.

Table 4.5 – Low hazard zone features [Barbolini et al., 2005].		
Rare avalanches	Return period	< 100 years
	Pressure	≤ 3 kPa
Extreme avalanches	Return period	$100 < T_r < 300$ years
	Pressure	

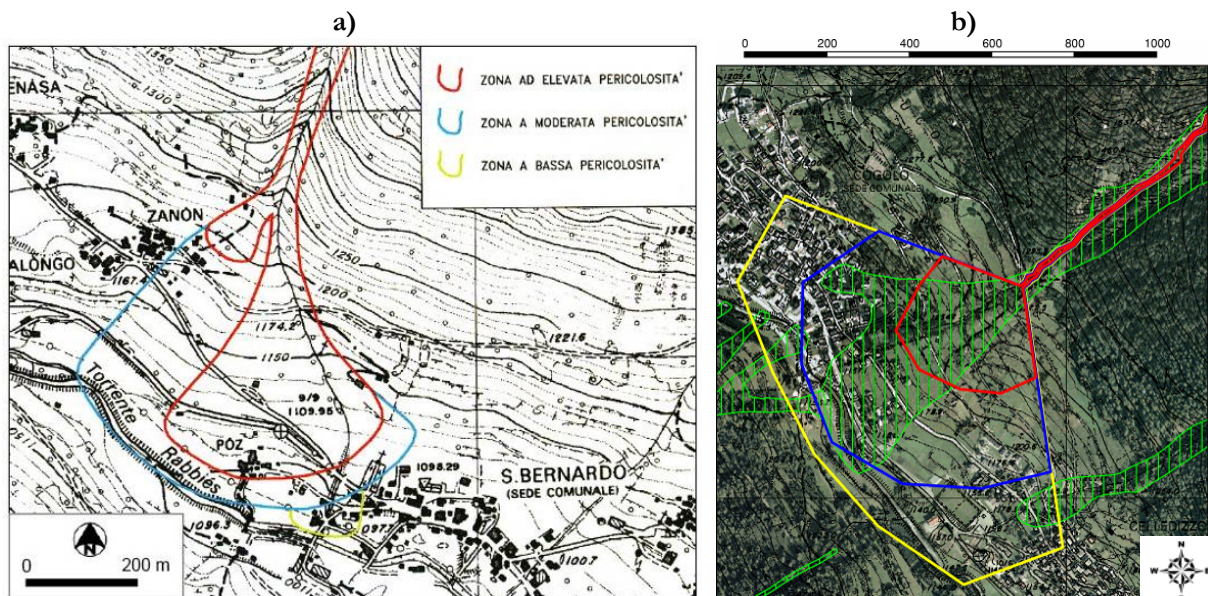


Fig. 4.3 – Examples of hazard maps (high hazard zones are portrayed in red, moderate ones in blue and low ones in yellow):
a) on the left, Val Nigolaia (Trentino Alto Adige Region, Italy) [Barbolini et al., 2003];
b) on the right, Val dei Spini (Trentino Alto Adige Region, Italy) [Scotton et al., 2006].

In the various European countries avalanche hazard levels are defined in different ways. However, some fundamental operations in the procedures for the drafting of hazard maps are similarly developed in all the countries (Table 4.6).

Field analyses represent an essential activity that supports all the study phases, from the preliminary cognitive activities (collection and elaboration data) to the calculation of dynamics and the final realisation of the hazard map. The maps require a detailed topographic base map and extensive on-site field investigations. The degree of accuracy of these maps corresponds to the maximum level possibly obtained from detailed analysis of a large avalanche path.

For the preparation of avalanche maps (for planning aims), generally the following points should be taken into account [Mears, 1991]:

- the size of the run-out zone should be related to the size of the starting zone and the elevation and climate of the mountain area;
- the shape and length of the run-out zone, considering all types of possible avalanches over a long time period;
- the dynamics and sequences of slab releases from the starting zone and how they combine, as this strongly affects avalanche size. This is especially important in paths with complex or multiple starting zones;
- vegetation damage may offer good indications concerning past events but does not necessarily show the size of an avalanche.

Study activity diagram		Type of maps	
1. Data collection	Existing studies of the avalanche site		
	Avalanche preliminary analysis	Geographical setting	IGM map
		Geological setting	Geological map
		Lithological setting	Lithological map
		Geomorphological setting	DTM
			Geomorphological map
			Slope map
			Exposure map
	Forestal setting	Soil use map	
	Avalanche protection structures	Avalanche structures localisation map	
	Historical analysis of the avalanche events	Historical avalanche events	CLPV, map of avalanche probable localisation
		Direct testimonies, historical documents	
		Public and private office data	
		Statistical analysis of historical data	
	Photo interpretation		
	Surveys on the avalanche site and topographical measurements		
	Preliminary zoning of avalanche		
	Climatic setting	Precipitations	
		Temperature	
		Wind	
Snow depth			
2. Data analysis	Statistical analysis of snow-meteorological data	DH3gg fresh snow depth on 3 consecutive days	
		HS, snow pack depth	
		HN, fresh snow depth	
		Wind (direction and intensity)	
		Detaching heights with $Tr = 30, 100, 300$ years	
3. Mathematical modelling	Mathematical models calibration		
	Numerical simulations		
4. Realisation of the PZEV			

SNOW COMPACTION

In the detachment zone use of mechanical means is not possible. The compacting can therefore be done with skis or feet.



Fig. 4.5 – Control by compaction [McClung & Schaerer, 1996].

Control by explosive. Small avalanches may be triggered manually by disturbing snow up the possible avalanche path. However, the most common method is the use of explosives (Fig. 4.6). Explosives may be launched manually or by shelling. Each method has its advantages and disadvantages. Explosive control has proved to be effective in areas with easy access to avalanche starting areas and where minor avalanches can be tolerated. It is not acceptable, however, in areas with human settlements and where there is even a small probability of a larger avalanche.

a) HAND CHARGES

These are very cheap and can be used everywhere. Hand charges are used more frequently than other methods, but the blasters should be well-trained experts. Disadvantages are due to transportation difficulties in bad weather conditions, necessary experience during preparation and the limited amount of explosive that may be used.



b) AVALANCHEUR

The principle of the avalancheur is that of cannon projecting an explosive load. The cannon is a pneumatic pitcher (the violent relaxation of an inert gas - nitrogen), put under pressure to then launch the load. The range of the avalancheur is in function of the pressure of nitrogen in the spherical reservoir of 45 litres (from 5 to 30 bars). This can attain 2000 m and a difference in level of 600 m. The load is an arrow containing a liquid explosive, Nitroroc N 4-24, obtained by blending two non-explosive liquids separately.



c) MORTAR

Mortar use is widespread and gives successful results, but the cost and storage of projectiles can create problems. The system should be used by experts. Legal procedures and blasting effects on the ground surface must be taken into consideration.



d) CATEx

(Cable Transporters Explosives)

CaTEEx is a system to trigger artificial avalanches by blasting TNT explosive carried by a cableway to the top -and safe- part of an avalanche path. This system has to be used by experts. Explosives must be stored in a safe place and legal procedures have to be considered. Application of this system in our country seems difficult.



e) GAZEx

(Gaseous Explosives)

The GazEx system uses an oxygen and propane gas mixture. Blasting of this mixture on the snow cover provides high blasting pressure and the triggering of an artificial avalanche. Blasting is controlled by a computer that is located in a safe place far from blast heads. This may be applied in any condition and operation costs are low.



f) AVALHEX

A rubber balloon filled with a hydrogen and oxygen mixture with a 4 m³ volume is blasted using an electronic detonator. This method is called Avalhair. After max. 120 sec., the blast occurs with an effect that equals exploding 3,5 kg of TNT. This system is remote controlled, safe and cheap but is still being tested.



g) HELICOPTER CHARGES

A helicopter can be used to transport explosives and artificers: artificers can launch grenades from the helicopter at a height of 5-10 m above the snowpack. Alternatively, it can carry a balloon full of hydrogen and oxygen which is programmed to explode. This system is limited by weather conditions - in the presence of a strong snowfall the helicopter cannot take off.



Fig. 4.6 – Control by explosive: a) hand charges; b) avalancheur; c) mortar; d) CaTE_x; e) GazEx; f) Avalhex; g) helicopter charges [http://cagem.bayindirlik.gov.tr; http://www.anena.org; Sommavilla, 2006; http://avalancheblast.com/english/indexe.htm].

4.2.2. Permanent protection: active defence structures

Active defence to reduce the conditions for the formation of avalanches and contribute in stabilizing the snowpack in the detachment zone consists in three types of intervention.

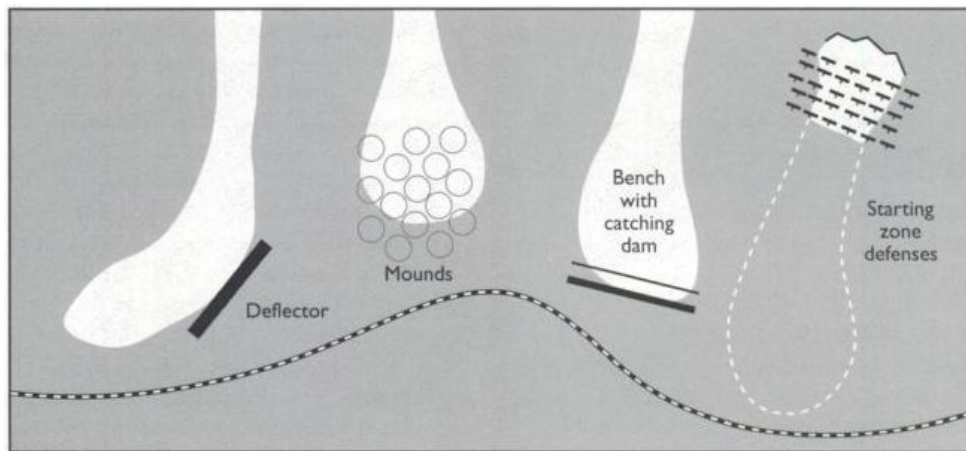


Fig. 4.7 – Active and passive defence structures [McClung & Schaerer, 1996].

Reforestation and earth terrace. A possibility of intervention is that of modifying the soil, through reforestation or the creation of earth terraces, with the aim of increasing the roughness and breaks the snow flow (Fig. 4.8).

a) REFORESTATION

To realize a reforestation procedure, soil should be of sufficient depth and suitable for planting. If this system is used with snow fences or snow-nets, trees can growth without snow load until the snow fences naturally wear out.



b) EARTH TERRACE

This method is generally used for prevention structures, which are far from settlements. In terraces, the top of the steps is hardened and trees are then planted in.. Steps are supported by walls designed perpendicular to the slope. This method does not give satisfactory results.



Slope inclination [°]	Interval of terraces [cm]
28 – 35	140 – 120
35 – 40	120 – 100
40 – 45	100 – 80



Fig. 4.8 – a) Reforestation; b) earth terrace
[<http://cagem.bayindirlik.gov.tr>;
Frutiger & Martinelli, 1983].

Snow supporting or retention structures. The function of this type of structure is to hold back the snowpack. Wood or steel structures are arranged in several parallel lines in the detachment zone. They are subdivided into rigid structures and flexible structures (Fig. 4.9). Rigid structures are avalanche snow bridges, and snow racks. Flexible structures are snow nets. The choice of the proper structures depends on the objects to protect and the type of the terrain. They are used in the starting zone of probable avalanche paths.

a) SNOW BRIDGES

These are made of wood, concrete, aluminium or steel. They are very expensive but supply best result along the 100 years of their economic cycle. Wooden ones serve for 20 to 40 years. In spite of these disadvantages, they can easily be used for safeguarding settlements against avalanches. They can be destroyed by corrosion, snow load and rock fall if badly designed. They are designed according to the kind of the material, situation, length and sizes. Snow bridges are fastened to the slope on the upslope side by tension anchors and on the down slope by compression anchors.



b) SNOW RAKES

These structures are made of crossbeams that are almost perpendicular to the slope.



c) SNOW NETS

These are flexible snow supporting structures for avalanche control, constructed of steel or nylon cables or straps held by steel poles, supplied with anchoring devices. They are installed in the upper parts of potential avalanche paths to prevent snow from starting to turn into an avalanche, or to retard the slide. Snow fences may at first seem similar to snow bridges, but they act differently. Snow fences are built vertically and accumulate snow on their downwind side, while snow bridges are slanted or horizontal and hold the snow on their topside.



d) TRIPODS

Tripods produced from tree logs and used on slopes with a slope inclination of less than 37°. They can be used with pilings, but they are not done guarantee preventing avalanches - pilings are not useful for safeguarding of settlements.



e) SNOW UMBRELLAS

This is a stabile structure, recommended for the areas where compact rock is not reachable and where the height of the snow does not exceed 3 m.



f) PILINGS

These are logs with diameters that vary from 10 to 20 cm and a length above the ground that goes from 30 to 200 cm.. They are planted in a chessboard formation. Digging intervals decrease with increasing slope inclination and snow depth. The buried part of the log must be in a ratio of 1:2 in relation to the unburied part. Minimum depth for the buried part is 60 cm in hard ground and 80-100 cm in loose ground. They are not safe enough and not useful for the safeguarding of settlements. Wide area applications sometimes are very expensive.



g) SNOW GRIPPERS

Snow grippers exploit the turbulence produced by wind, which brings to the shattering of the snow in blocks and to the compacting of the snow. They heat up with the solar irradiation and spread the accumulated heat in the surrounding environment.



Fig. 4.9 – Snow supporting or retention structures: a) snow bridges; b) snow rakes; c) snow nets; d) tripods; e) snow umbrellas; f) pilings; g) snow grippers [<http://cagem.bayindirlik.gov.tr>; <http://www.arpa.veneto.it/csvdi>; <http://www.incofil.com>].

Snow fences or redistribution structures. These structures contrast the snow transported by the wind with wind baffles and fences that modify the wind flow, limiting the formation of frames in critical points (Fig. 4.10).

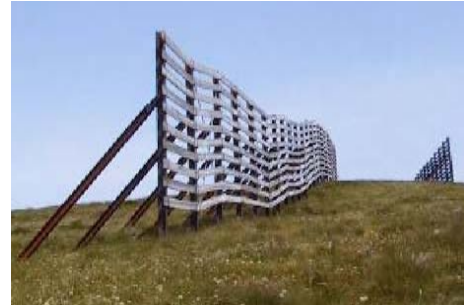
a) WIND BAFFLES

Very similar to wind panels, these are placed at intervals between structure units. They control snow distribution on the crest better than wide panels.



b) SNOW WIND FENCES

These structures control the wind transportation and accumulation of snow where this occurs. Thus accumulation of snow can be avoided in hazardous places. Cornice formation can also be avoided by using this structure. They supply best results by using another preventive structure along with it. A snow fence is a structure used to force the drifting of snow to a predetermined place. Snow fences are primarily employed to minimize the amount of snowdrift on roadways. In rural areas, farmers and ranchers may use temporary snow fences to create large drifts in basins for a ready supply of water in the spring.



c) WIND PANELS

These are used for controlling snow accumulation. Their difference from snow bridges is that there is no interval between units of material. They can be different in length.



d) JET-ROOF

Its role is similar to that of snow (wind) fences but this structure is used to reduce wind velocity and accumulate the snow at a lower level than the crest. It can avoid cornice formation and is not expensive.



Fig. 4.10 – Snow fences or redistribution structures: a) wind baffles; b) snow wind fences; c) wind panels; d) jet-roof [http://cagem.bayindirlik.gov.tr; http://www.arpa.veneto.it/csvdi; McClung & Schaerer, 1996].

4.2.3. Permanent protection: passive defence structures

Passive techniques amount to slowing down, stopping, and diverting the moving snow and preventing it from moving, either completely or in big masses. Passive techniques involve building various structures and some other approaches. Passive defence consists in structures positioned along the path or the run-out zone where the avalanche is in movement. The principal typologies are (Fig. 4.11):

- **snow deflecting structures:** these have the function of changing the flow direction of the loose avalanches with the aim of protecting definite structures or dividing the mass of the avalanche into little parts more easily;
- **snow retarding structures:** these support the deceleration of the snow in movement, causing lateral expansion;
- **direct protection structures:** directed protection of roads (avalanche tunnels) or buildings (protecting wedges);
- **snow catching structures:** these are used to block an avalanche in movement or to retard the velocity and reduce the stopping distance.

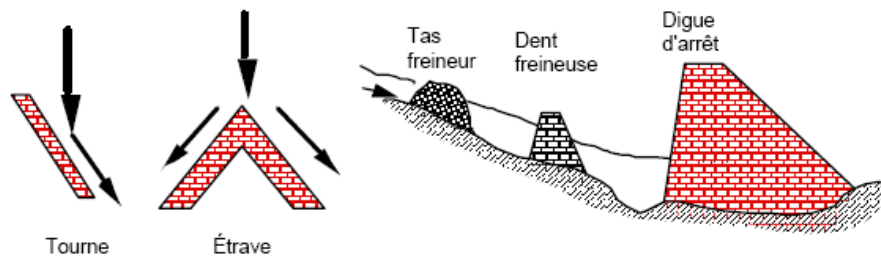


Fig. 4.11 – The principal defence passive structures [Ancey, 1998].

Passive defence structures present a series of advantages:

- they are built, generally, not at high levels and on slopes that are not very steep, where the use of operators is possible;
- the materials are of easy to find and are limited in cost;
- protection is aimed.

Instead, its disadvantages or limits are:

- the structures necessarily have to face solicitations and often assume big dimensions;
- variability of the dynamic parameters, because of the difficulty in determining the initial conditions and the boundary conditions;
- it is not possible to build these structures with slope inclinations above 40%, because they can be surmounted by the avalanche;
- protection in case of powder avalanches is low, because such avalanches can develop heights of 25-50 m, while the passive defence works seldom exceed 10 m [Cresta, 1991].

4.2.3.1. Deflecting dams

Deflecting dams are designed when an avalanche can be deflected in an area without human settlements (Fig. 4.12). These dams can be lower in height because it is assumed that there is not direct impact [Höller, 2007].

These structures can be almost built parallel to the direction of the flow of the avalanche, so as to deflect it into natural channels along the slope [McClung & Schaerer, 1996].

a) GUIDING STRUCTURES

The guiding structures try to prevent propagation.



b) DEFLECTING DAMS

The main aim of deflecting walls is divert the avalanche flow in the desired direction. They can be made of concrete, dry stone, masonry wall and soil or a mixture of all these. It must be remarked that these structures are not effective against big powder avalanches. Long-term mean maximum snow depth and maximum avalanche flow depth used are in calculation of height and length of these walls.



Fig. 4.12 – a) Guiding structures; b) deflecting dams
[<http://cagem.bayindirlik.gov.tr>; Bezzi, 2004].

Structure description. Most deviation works are realized by building earth embankments reinforced with concrete walls. These structures usually have a height from 6 to 12 m, even if some can reach 20 m. The cost of the investment is reasonable when it is possible to use the traceable material on the site.

Powder avalanches are generally too fast to be able to be deviated and it is probable that they may slide over the deviation structures.

Diversion dams or deflection dams can be located to deflect a flowing avalanche in a desired direction, away from the installations that are to be protected (Fig. 4.13-Fig. 4.14). The angle between the dam and direction of the avalanche is kept below 20°. The side of the dam facing the avalanche is as steep as possible in order to produce good deflecting effects. These structures are found to be most effective on lower track slopes (20°).

The maximum efficiency of these types of structures is obtained in the accumulation zones and along the lower part of the slopes where the inclination is between 12° and 20° . On slopes with more than 20° , avalanches always assume velocities which are sufficient to step over the deviation structures. On slopes with an inclination of less than 12° , also avalanches of big dimensions tend to deposit big part of their mass. Such deposits strongly reduce the total efficiency of the structure because they decrease its necessary height. The deposition and the surmounting create problems for the designing of all structures meant for the lower parts of the path and for the accumulation zone, including the blocking, slowing down and direct protection structures [Mears, 1981].

Precise directives regarding the optimum slope of the ground on which the structures could preferably be arranged are not possible. In fact, avalanches of small dimensions usually begin to slow down and deposit on steeper slopes, between 15° and 25° . In these cases, the structures can be built also on greater slopes with an inclination of 20° . On the contrary, if the avalanches reach very extensive dimensions the slowing down and the deposit can start on slopes of 15° .

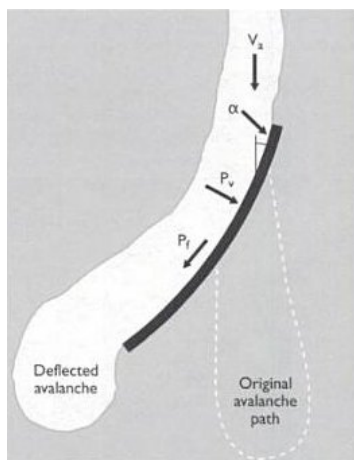


Fig. 4.13 – Impact forces on deflecting dam [McClung & Schaerer, 1996].

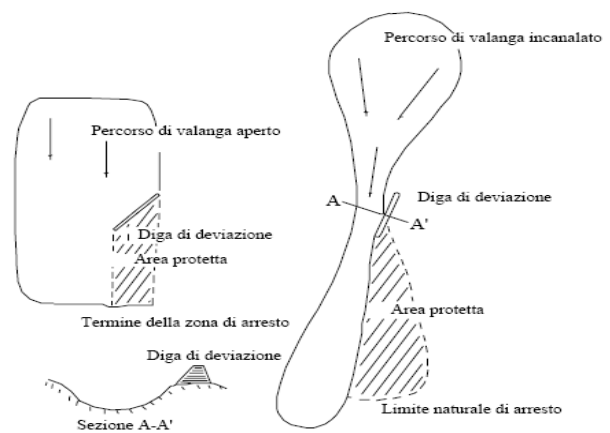


Fig. 4.14 – Example of deflecting dams: on the left, open avalanche; on the right, channelled avalanche [Mears, 1981].

If avalanches -with smaller dimensions than those designed- deposit snow against the structures, opportune maintenance plans have to be realized to arrange its removal and assure an optimum degree of efficiency of the structure. In the case of canalized avalanches a much wider territory surface can be protected.

The principal deflecting structures may be of a straight kind or curved kind. Both types substantially consist of earth embankments possibly lined with material which can resist impacts, and the choice of the type of structure essentially depends on the morphological characteristics of the slope [Mears, 1981].

Structure projecting. During the designing it is necessary to keep present that the snow mass must be deviated towards zones where damage is not caused.

The necessary height of the structure is calculated measuring the channel depth, the area of the transverse section and by calculating the snow discharge that can flow down the natural section (Fig. 4.15). For the effective success of the intervention the real discharge of the expected avalanche must be less than the calculated discharge, without considering the height of the structure; this, in fact, must contain only the natural amount of snow that tends to flow out of the natural channel, caused by the deviation.

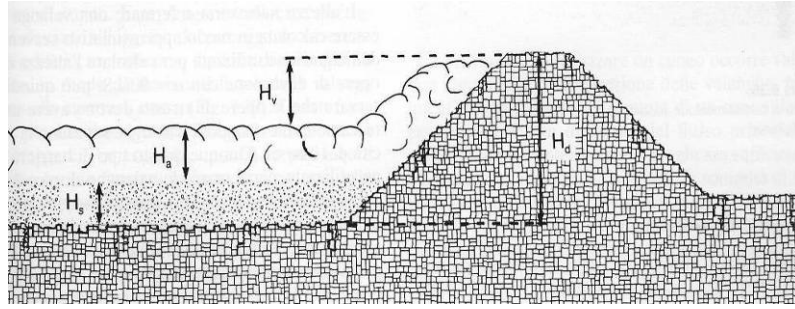


Fig. 4.15 – Schematic figure to calculate the height of to deflecting dam: H_d , design maximal height, H_d , snow pack depth, H_a , avalanche flow height H_d , uplift height [McClung & Schaerer, 1996].

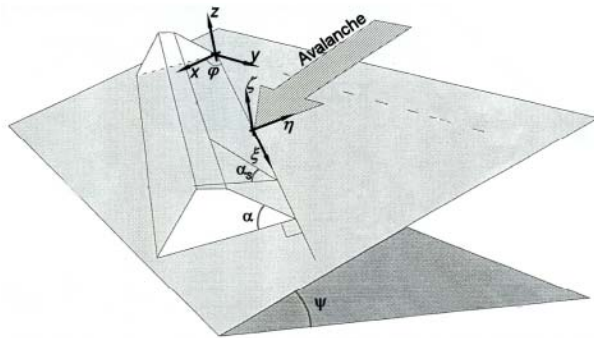


Fig. 4.16 – Schematic figure of a deflecting dam showing: the x,y,z- and ξ,η,ζ -coordinate systems, the deflecting angle, φ , the slope of the terrain, ψ , and the angle between the upper dam side and the terrain, α [Domaas & Harbitz, 1998].

The structure must also allow a gradual deviation of the avalanche; otherwise this could be able to step over the barrier. The angle between the direction of an avalanche and the structure should never exceed 20° (max. 30°) (Fig. 4.16).

The walls must be planned to resist shear and normal impact but these often result inefficient if the avalanche is of a powder kind - there is a good probability that this type of avalanche be able to clear the obstacle [McClung & Schaerer, 1996].

Guiding structures. The guiding structures do not have the aim of modifying the direction of the avalanche but that of trying to prevent side propagation. The necessary height of the structures depends by the flow height, the transverse section area and the hydraulic ray of the avalanche (Fig. 4.17).

To calculate the height of the wall guides h , of a rectangular channel, the continuity equation is applied [Mears, 1981]:

$$v_1 F_1 = v_u F_u$$

$$R_1 (sen \alpha_1 - \mu cos \alpha_1) F_1^2 = R_u (sen \alpha_u - \mu cos \alpha_u) F_u^2$$

$$R_1 F_1^2 = \frac{sen \alpha_u - \mu cos \alpha_u}{sen \alpha_1 - \mu cos \alpha_1} R_u F_u^2$$

$$\frac{bh}{2(h+b)} (bh)^2 = \frac{sen \alpha_u - \mu cos \alpha_u}{sen \alpha_1 - \mu cos \alpha_1} R_u F_u^2$$

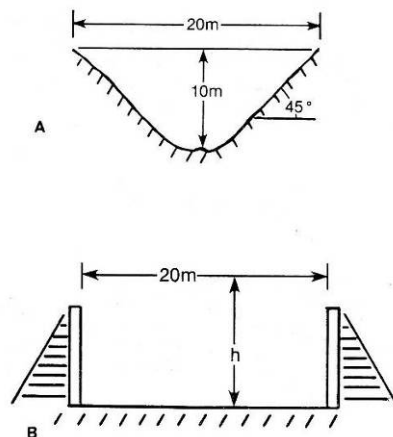


Fig. 4.17 – a) avalanche natural channel above the guiding structure; b) cross section of the guiding structure [Mears, 1981].

$\left\{ \begin{array}{l} R_1 = \frac{bh}{2(h+b)} \\ R_u \end{array} \right.$	[m]	hydraulic ray of the inferior channel (rectangular section);
	[m]	hydraulic ray of the superior channel;
b	[m]	guiding channel length;
h	[m]	guiding channel height;
$\left\{ \begin{array}{l} F_1 = (bh)^2 \\ F_u \end{array} \right.$	[m ²]	cross section area of the inferior channel;
	[m ²]	cross section area of the superior channel;
$\left\{ \begin{array}{l} \alpha_1 \\ \alpha_u \end{array} \right.$	[°]	inclination of the inferior channel;
	[°]	inclination of the superior channel;
μ	[-]	sliding friction coefficient.

Straight deflecting dams. Because of the conservation of the quantity of motion, when the avalanche runs down the deflecting dam there is an increase of the flow height, said uplift height, near the structure [Mears, 1981]:

$$H = h_0 + h' + h = h_0 + h' + \frac{(v \text{sen } \phi)^2}{2g}$$

H	[m]	design maximal height;
h_0	[m]	snow pack depth/the thickness of snow and previous avalanche deposits on the ground;
h'	[m]	avalanche flow height/the thickness of the flowing dense core;
$h = \frac{(v \text{sen } \phi)^2}{2g}$	[m]	uplift height/the contributions of the velocity of the avalanche;
v	[m/s]	design avalanche velocity;
ϕ	[°]	deflection angle;
g	[m/s ²]	gravity acceleration.

When $\phi = 0^\circ$ there is no deviation and the wall behaves like a guiding structure. If $\phi = 90^\circ$, instead, the wall behaves like a catching dam. Since the projected height of the structure increases both with the velocity and with the deviation angle, it is always better keeping a value of ϕ low.

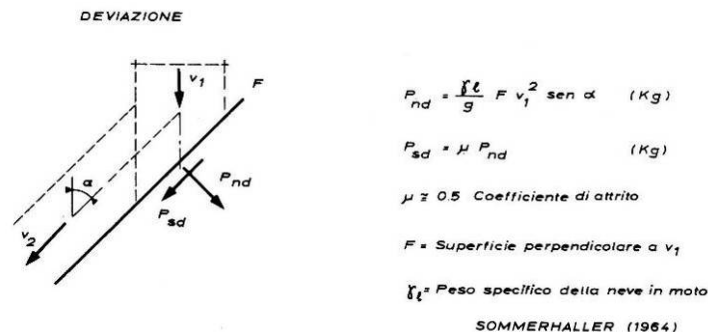


Fig. 4.18 – Impact forces on a protecting deflecting dam [Menegus & Soranzo, 1986].

Because of the impact of the avalanche against the deflecting dam, there is a change in the quantity of motion which produces deviation forces between the dam and the avalanche. The

entity of such forces depends on velocity, avalanche density, deviation angle and surface involved in the impact.

The specific deflection force (force per surface unit) (Fig. 4.18) can be defined in terms of perpendicular components: normal, shear and uplift. For a vertical deflecting wall, the normal pressure is calculated as [Mears, 1981]:

$$P_{dn} = \rho(v \sin \phi)^2 = \frac{\gamma}{g} F \sin \phi$$

P_{dn}	[kg/m ²]	deflection force normal component;
ρ	[kg/m ³]	avalanche density;
v	[m/s]	design avalanche velocity;
ϕ	[°]	deflection angle;
γ	[kg/ m ³]	avalanche volume weight;
F	[m ²]	surface perpendicular to v ;
g	[m/s ²]	gravity acceleration;
$\left\{ \begin{array}{l} P_{ds} = \mu P_{dn} \\ P_{dv} = \mu P_{dn} \end{array} \right.$	[kg/m ²]	deflection force shear component;
	[kg/m ²]	deflection force uplift component;
μ	[-]	friction coefficient: $\mu = 0.5$.

For $\phi = 90^\circ$, one obtains $P_{dn} = \rho v^2$, that is the expression of the impact of the fluids on a surface perpendicular to the direction of flow.

The total dynamic force on a wall is the sum of all the specific deflecting forces multiplied by the areas on which these specific forces act.

The impact will not concern a whole wall, because a certain distance is necessary before the avalanche reaches the maximum height. Since this distance is not known, it is supposed that the impact area is the projected height multiplied by the wall length.

Normal total force per unit of wall length, keeping also in account the hydrostatic pressure of the avalanche, turns out [Mears, 1981]:

$F_n = P_{dn} H + \frac{\rho g H^2}{2}$	[kg/m]	normal force for dam unit length;
P_{dn}	[kg/m ²]	deflection force normal component;
H	[m]	design maximal height;
$\frac{\rho g H^2}{2}$	[kg/m]	hydrostatic force for dam unit length;
ρ	[kg/m ³]	avalanche density;
g	[m/s ²]	gravity acceleration;
$\left\{ \begin{array}{l} F_s = \mu F_n \\ F_v = \mu F_n \end{array} \right.$	[kg/m]	shear force for dam unit length;
	[kg/m]	uplift force for dam unit length.
μ	[-]	friction coefficient: $\mu = 0.5$.

This expression is an estimate in excess because it does not consider the shear force of the snow, which however cannot be exactly calculated in advance. In the designing phase a null shear force is presumed.

Curved deflecting dams. A curved deflecting dam has the advantage of allowing a gradual phase of deviation of the snow mass in motion, if compared to the previous case.

The height of a projected curved wall (Fig. 4.19) is calculated in the same way as a straight wall [Mears, 1981]:

$$H = h_0 + h' + h = h_0 + h' + \frac{v^2 W}{gR}$$

H	[m]	design maximum height;
h_0	[m]	snow pack depth;
h'	[m]	avalanche flow height;
$h = \frac{v^2 W}{gR}$	[m]	uplift height;
v	[m/s]	design avalanche velocity;
W	[m]	avalanche width in the channel curve section;
g	[m/s ²]	gravity acceleration;
R	[m]	deflection circle ray.

The deviation force is the sum of its components [Mears, 1981]:

$$\bar{F} = \sqrt{F_x^2 + F_y^2} \quad [\text{kg}] \quad \text{deflection dynamic force;}$$

$$\left\{ \begin{array}{l} F_x = \rho Q (v_{2x} - v_{1x}) \\ F_y = \rho Q (v_{2y} - v_{1y}) \end{array} \right. \quad \left\{ \begin{array}{l} v_{2x} = v_2 \cos \delta = v_1 \cos \delta \\ v_{1x} = v_1 \cos \theta = v_1 \\ v_{2y} = v_2 \sin \delta \\ v_{1y} = v_1 \sin \theta = 0 \end{array} \right.$$

Q	[m ³ /s]	avalanche discharge;
v_1	[m/s]	design avalanche velocity before the impact with the dam;
v_2	[m/s]	design avalanche velocity after the impact with the dam;
δ	[°]	maximal avalanche deflection.

It is possible to assume $v_1 = v_2$ if the work length is very little in comparison to the stopping distance.

Actually, simultaneously to the impact, some friction forces will be activated with snow tending to deposit against the structure. The discharge will, therefore, decrease because of the deposits, and the above expression -based on the conservation of the quantity of motion- will not be applicable any more, if not only in an approximate form. Besides the dynamic forces, a normal “hydrostatic” force also exists, which can be expressed as [Mears, 1981]:

$$F_n = \frac{\rho g H^2}{2} L \quad [\text{kg}] \quad \text{hydrostatic normal force;}$$

$$\rho \quad [\text{kg/m}^3] \quad \text{avalanche density;}$$

g	[m/s ²]	gravity acceleration;
H	[m]	design maximal height;
$L = \frac{\delta}{360} 2\pi R$	[m]	length design;
δ	[°]	maximal avalanche deflection;
R	[m]	deflected path ray.

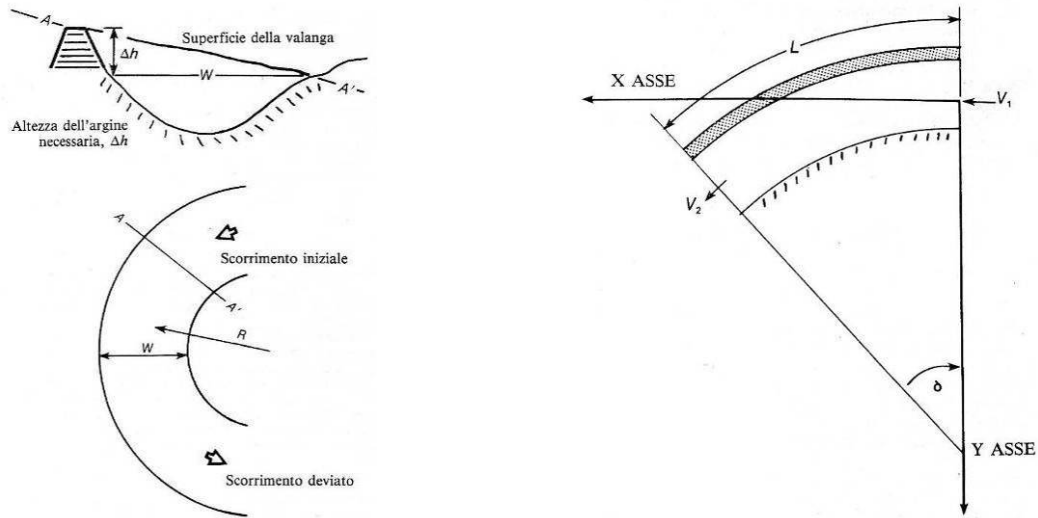


Fig. 4.19 – Impact forces on a curved deflecting dam [Mears, 1981].

The total force on the curved surface of the wall is the sum of the “hydrostatic” force and the dynamic deviation force.

Generally, earth walls are more economic, even if the volumes necessary for their construction are considerable. In function of the available space along the versant, a same area can be protected both by a short and high wall with an important deviation angle, or by a long and low wall with a smaller deviation angle.

In Fig. 4.20-Fig. 4.32 some example of deflecting dams are presented.

DEFLECTING DAMS



Fig. 4.20 – Canton of Valais, Switzerland [Frutiger & Martinelli, 1983].



Fig. 4.21 – Disentis, Canton of Grisons, Switzerland [<http://cemadoc.cemagref.fr>].



Fig. 4.22 – Nautagrovi, Gudvangen, Norway [Barbolini & Issler, 2005].



Fig. 4.23 – Pampeago, Val di Fiemme, Italy [Rossi, 2004].



Fig. 4.24 – Two views of Flateyri, Iceland [Barbolini, 2005].



Fig. 4.25 – Chamonix, Haute-Savoie, France [<http://cemadoc.cemagref.fr>].



Fig. 4.26 – Langageiti, Gudvangen, Norway [Barbolini, 2005].



Fig. 4.27 – Brun, Seyoisfjorour, Iceland [<http://cemadoc.cemagref.fr>].



Fig. 4.28 – Ytra-Strengsgil, Siglufjörður, Iceland [<http://www.orion.is/snow2008>].



Fig. 4.29 – Seljalandshverfi, Isafjordur, Iceland
[<http://www.orion.is/snow2008>].



Fig. 4.30 – Funi, Isafjordur, Iceland
[<http://www.orion.is/snow2008>].



Fig. 4.31 – Steinbichele, Kröbzbach, Austria
[Höller, 2007].



Fig. 4.32 – Oberwald, Canton of Valais, Switzerland
[Fraser, 1970].

4.2.3.2. Retarding or braking mounds

The aim of the slowing down and breaking structures (Fig. 4.33) -placed in the accumulation zone- is that of reducing the stopping distance of dense snow avalanches, increasing friction conditions, increasing the internal friction of the snow mass and the snow-ground friction, during the flowing phase [Mears, 1981]. This is possible by arranging some obstacles along the path in order to cause side propagation of the snow mass and decrease the flow height, allowing an increase in the area of expansion and a reduction of the flow velocity caused by energy loss [McClung & Schaerer, 1996].

a) RETARDING CONES-SHAPED STRUCTURES

Retarding cones are structures which decrease the avalanche velocity and run-out length. Retarding cones are made of a mixture of soil and rocks or just rocks.



b) RETARDING TOOTH-SHAPED STRUCTURES

Retarding tooth-shaped structures decrease the avalanche velocity and run-out length. Retarding tooth-shaped obstacles are made of concrete.



Fig. 4.33 – Retarding or braking mounds: a) retarding cone-shaped structures; b) retarding tooth-shaped structures [<http://cagem.bayindirlik.gov.tr>; Frutiger & Martinelli, 1983].

Structure description. There are no basic design guidelines for braking mounds capable of retarding snow avalanches, although they are widely used as a part of avalanche protection measures. Laboratory experiments have been performed during recent years in order to reveal the dynamics of an avalanche flow over and around braking mounds and to estimate the retarding effect of the mounds. The experiments and the design criteria for braking mounds are described by Hákonardóttir (2004), Jóhannesson and Hákonardóttir (2003) and Hákonardóttir et al. (2003) (Fig. 4.39).

The slowing down structures are mostly efficient if they are positioned in places near areas in which the avalanches tend to slow down in a natural way.

These structures are placed in the run-out zone on relatively flat slopes with the object of reducing avalanche velocity and shortening the avalanche path by increasing ground friction and modifying flow characteristics. These mounds are designed to absorb energy from the avalanche and to stop it before it reaches the area needing protection. These are placed in rows and alternately spaced. Experience evidences that two or more rows of mounds are required to control avalanches (Fig. 4.34-Fig. 4.35). The base of one should almost meet the base of the other. The width of the avalanche path should be completely covered by the mounds.

For dense snow avalanches the maximum efficiency of such structures is on slopes with less than 20° , which corresponds to the natural accumulation zones of avalanches of small or average-size dimensions. If the snow is dry the avalanche is much faster, so these structures result to be efficient only on slopes with less than 15° .

For powder snow avalanches, because of the high velocities and the big flow heights, these types of structures are not suitable since they should be as high as the snow cloud to be effective.

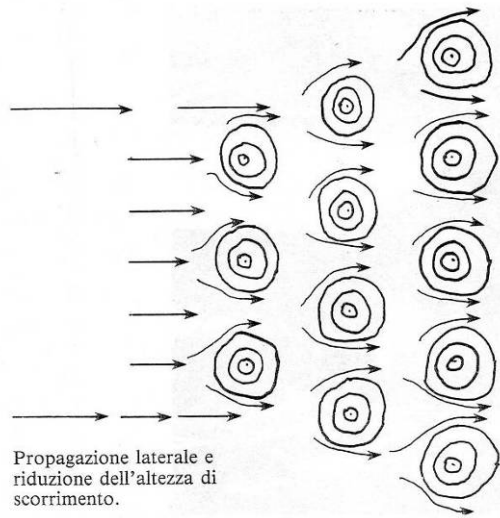


Fig. 4.34 – Scheme of retarding mounds to reduce avalanche deposit stopping distance and flow depth [Mears, 1981].

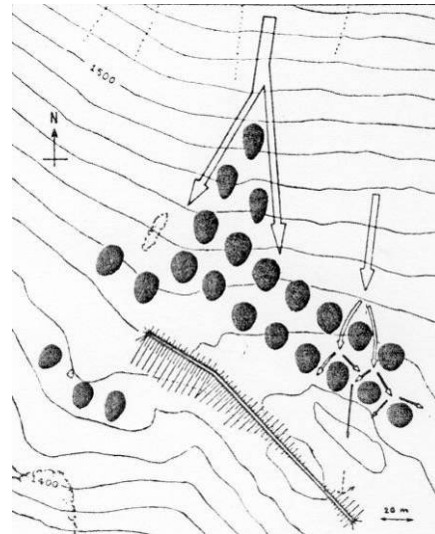


Fig. 4.35 – Alpogli-Wilerhorn, Canton of Valais, Switzerland [Frutiger & Martinelli, 1983].

Since the retarding structures have the purpose to propagate the flow down the sides, their best location is in open areas, rather than bordered ones; the best solution is that of structures disposed in chessboard formation (Fig. 4.36-Fig. 4.37). This way the snow flow -deviated and pushed laterally- is brought to run through chosen channels. The increase of the side friction then causes the reduction of the flow height.



Fig. 4.36 – Retarding mounds in the accumulation zone [McClung & Schaerer, 1996].

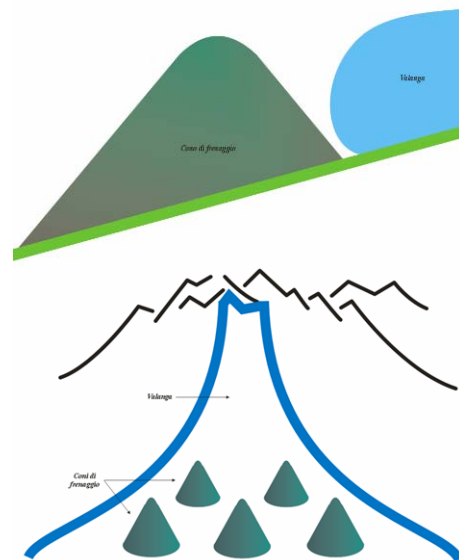


Fig. 4.37 – Schematic figure of retarding mounds [Somavilla, 2006].

It is then important to consider the phenomena of a large amount of minor avalanches that -even if they don't produce damage- often tend to stop on these structures, reducing their real

height and decreasing the efficiency of the defence system conceived for bigger avalanches [Mears, 1981].

In order to avoid the phenomena of erosion it can be useful to plant bushes and grass near the mounds [McClung & Schaerer, 1996].

However, an important advantage of these structures is that a wide excavation is not required in the installation zone, thus allowing to preserve the natural surface of the soil. They can also be positioned in a specific way to allow easy access for the removal of the snow, if this becomes necessary [Mears, 1981].

Two fundamental types of slowing down structures are the mounds made of earth or stone and the tooth-shaped structures made of concrete.

Structure project. For design it is possible to refer to the following diagram (Fig. 4.38), in which the width of the mound base at the top a is obtained in function of the structure height, assuming a resistance to the motion of the avalanche of 10 t/m^2 .

Three curves, corresponding to three cohesions c of the obstacle material, are presented, for an angle of ground friction of 30° .

The linear interpolation is admitted for intermediate cohesions.

The value of a is obtained assuming a security coefficient of $F = 1.5$.

The diagram may be used in the case of horizontal ground, while for structures on inclined versants it is necessary to keep in mind that the weight component of the structure decreases with the augmenting of slope inclination [Menegus & Soranzo, 1986].

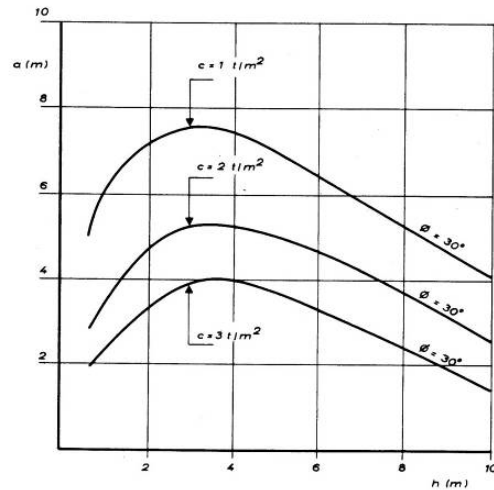
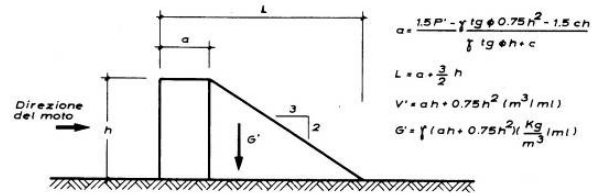


Fig. 4.38 – Diagram for the measurement of retarding structures [Menegus & Soranzo, 1986].

$$a = \frac{1.5 P' - \gamma tg \phi 0.75 h^2 - 1.5 ch}{\gamma tg \phi h + c} \quad [\text{m}] \quad \text{mound base width at the top;}$$

$$P' = G' tg \phi + cL = \gamma (ah + 0.75h^2) \gamma tg \phi + cL \quad [\text{kgm/m}^3] \quad \text{mounds resistance limit force;}$$

$$G' = \gamma V' \quad [\text{kgm/m}^3] \quad \text{mounds weight;}$$

$$\gamma \quad [\text{kg/m}^3] \quad \text{volume weight;}$$

$$V' = ah + 0.75h^2 \quad [\text{m}^3/\text{m}] \quad \text{volume;}$$

$$\phi \quad [^\circ] \quad \text{frictional angle of mounds material;}$$

$$c \quad [\text{t/m}^2] \quad \text{cohesion;}$$

$$L = a + \frac{3}{2} h \quad [\text{m}] \quad \text{mound total base length;}$$

$$h \quad [\text{m}] \quad \text{mound height.}$$

As for the other types of defence structures, these are positioned in the lower part of the path and in the stopping zone - also for the slowing down structures the parameters which must necessarily be assumed are the snow velocity, the flow height and the flow density. The projected

height H of the structure should be the same or higher than the sum of the snow pack depth h_0 and the avalanche flow height h' [Mears, 1981]:

$H \geq h_0 + h'$	[m]	maximum structure height;
h_0	[m]	snow pack depth;
h'	[m]	avalanche flow height.

High-velocity avalanches tend to step over the works upstream, but this is not a big problem because the effects of both the increased side friction and the forced lateral propagation will bring the velocity of the avalanche to decrease downstream. Positioning the structures in several rows permits to have the avalanche propagated laterally, reducing the flow height, increasing the side friction and forcing the avalanche to run through a series of channels.

The planning difficulties for such structures reside in the determination of the dynamic parameters and the characteristics of the interaction with the structure.

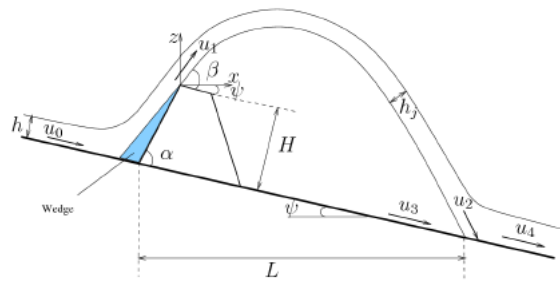


Fig. 4.39 – A schematic diagram of a jet of length, L , with upstream flow thickness, h , and jet thickness, h_j . The jet is deflected at an angle, β , over a mound or a dam of height, H , positioned on a terrain with inclination ψ . The upstream mound face is inclined at an angle α with respect to the slope. u_0 , u_1 , u_2 , u_3 and u_4 are the speed at different locations in the path [Hákonardóttir et al., 2003].

Retarding cone-shaped structures. These are cone-shaped structures, with a height of 8-12 m and made of filling material (*Trentino Alto Adige* Region, Italy).

Earth mounds, made of traceable material found on site, are an economic and widely used type of barrier, but rocks or cement blocks can also be used where possible. The mounds are suitable for a ground with an inclination not greater than 15-20° and are to be positioned near the accumulation zone.

To reach a certain degree of efficiency it is necessary to have at least two rows of mounds in an chessboard formation, with a variable height of 5-8 m [McClung & Schaerer, 1996].

The mound has a conic form and variable dimensions in function of the local morphological characteristics and the typology of the avalanche. Its structure and its height must be determined so as to resist the impact of the avalanche.

The section is generally constituted by a core in boulders of a trapezoidal form with thickness at the top of 1,5 m and an inclination not superior to 45°. The core is then covered with filling material, arranging the material so as to form a conic shape, and covered with boulders upstream to improve stability. These are not very expensive structures because they are made with filling material found on the site.

Downstream, the section presents a thick layer of well compacted vegetal ground where bushes are planted - a suitable reforestation with local bushes with the aim of masking the mound (its dimensions are always rather big). Another important aspect is the distance between the structures, which must be able to avoid obstruction of the passage downstream, between the rows of structures.

The mounds are usually linked with other structures realized at a higher level or realized on terraces (of a width of 4-5 m), or snow nets and bridges, or deflecting works.

The disadvantages of this type of structure are due to the big excavations before construction and the wide base area which at times makes the removal of the snow deposited between the mounds difficult.

In Fig. 4.40-Fig. 4.45 some example of cone-shaped structures are presented.

RETARDING CONE-SHAPED STRUCTURES



Fig. 4.40 – Mattstock, Canton of St. Gallen, Switzerland [Mears, 1981].

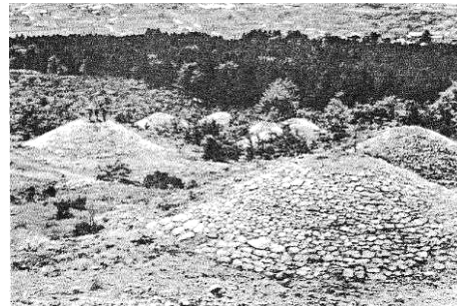


Fig. 4.41 – Innsbruck, Austria [McClung & Schaerer, 1996].



Fig. 4.42 – Gully, Uttar Pradesh, India [Rao, 1985].



Fig. 4.43 – Rogers Pass, British Columbia [Frutiger & Martinelli, 1983].



Fig. 4.44 – Austria
[<http://www.kfunigraz.ac.at>].



Fig. 4.45 – Austria
[<http://www.kfunigraz.ac.at>].

Retarding tooth-shaped structures. These are another example of braking mounds and, like the cones, have the aim of decelerating and deflecting moving snow. However, they are not built of earth but are prevalently realized in concrete; they are therefore more expensive. Then they do not need of a big excavation. The tooth-shaped structures are planned with an opportunely dimensioned massive structure and vertical walls to dissipate the energy, to reduce the velocity and to retard the avalanche as soon as possible. The use of the mounds is often preferred.

They have a trapezoidal or rectangular structure, with height of 5-10 m (*Trentino Alto Adige* Region, Italy), usually the face of mountain is inclined of 90° on the horizontal and introduces a rectangular or square section.

Like the mounds, also the tooth-shaped structures are generally arranged in chessboard formation and the distance between them it must be such allow an easy access to remove of the deposited material.

At times, both the typologies of works are built in the same place, to guarantee a greater braking action.

In Fig. 4.46-Fig. 4.49 some example of tooth-shaped structures are presented.

RETARDING TOOTH-SHAPED STRUCTURES

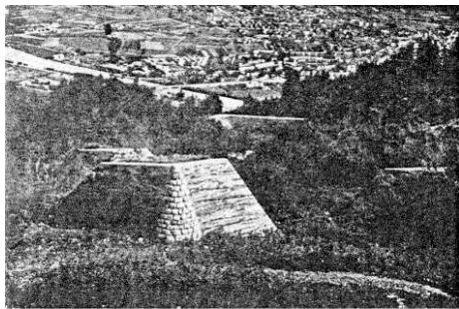


Fig. 4.46 – Arzlertal, Austria [Frutiger & Martinelli, 1983].

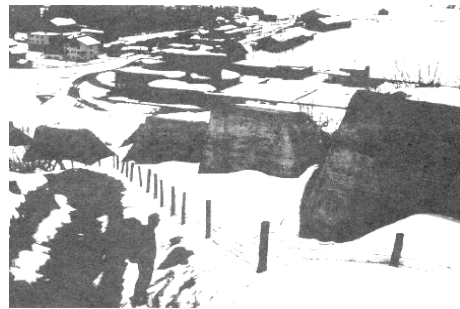


Fig. 4.47 – Andermatt, Canton of Uri, Switzerland [Mears, 1981].



Fig. 4.48 – Valtorta, Valle Stabina, Italy [Barbolini, 2005].



Fig. 4.49 – Canton of Uri, Switzerland [<http://cemadoc.cemagref.fr>].

4.2.3.3. Catching dams

Catching dams (Fig. 4.49) are used to slow or to stop avalanches [McClung & Schaerer, 1996]. They are built perpendicular to the direction of the avalanche and are breaking barriers designed to reduce the energy of a moving avalanche and halt its advance. These are more efficient against avalanches of wet, heavy snow rather than those of fast moving dry snow. As the height of catching dams increases with the square of avalanche velocity, this method can be used only for slower avalanches.

Aim of the interception structures is to block the loose avalanches and the lower sections of powder avalanches and avalanches of the mixed type. The superior cloud will seldom be able to be stopped, thus defining the lower limit (depth) of the project avalanche. In many cases it can be possible to block only a certain amount of the mass in movement, allowing the fastest powder part -less dense- to step over the structure and continue flowing in the accumulation zone. The structures placed downstream are possibly exposed to this “wind” of powder snow and will have to be adequately designed to resist to the impact [Mears, 1981].

a) ARRESTING WALLS

These are constructed in the stopping zone of avalanches. Angle of avalanche and height of the wall are very important. If avalanche velocity is high, these types of walls are inadaptable.



b) CATCHING DAMS

These are built where the avalanche velocity is not high (close to the starting zone or the stopping zone). Suitable land is required for the construction of these dams, which are backfilled, rock filled or constructed using concrete with steel supports.



c) BREAKING DAMS



Fig. 4.50 – Catching dams: a) arresting walls; b) catching dams; c) breaking dams
[<http://cagem.bayindirlik.gov.tr>; McClung & Schaerer, 1996;
<http://cemadoc.cemagref.fr>; Pittracher, 2008].

Structure description. The slowing down phase for avalanches of big dimensions starts when the slope assumes a inclination near 15° to 20° , and the interception structures will result more efficient if positioned in zones with less inclination.

For all the types of structures, the storage volume to contain the avalanche can be calculated considering that [McClung & Schaerer, 1996]:

- the width of the drain depends on the surface of available ground (they usually have values of 2-5 m);
- the snow density of the deposit can be assumed equal at 250 kg/m^3 for dry snow and at 400 kg/m^3 for wet snow;
- the surface angle of the snow deposit changes between 10° - 25° , according to the characteristics of the deposit;
- the efficiency of the drain can be restored by periodically removing the accumulated snow.

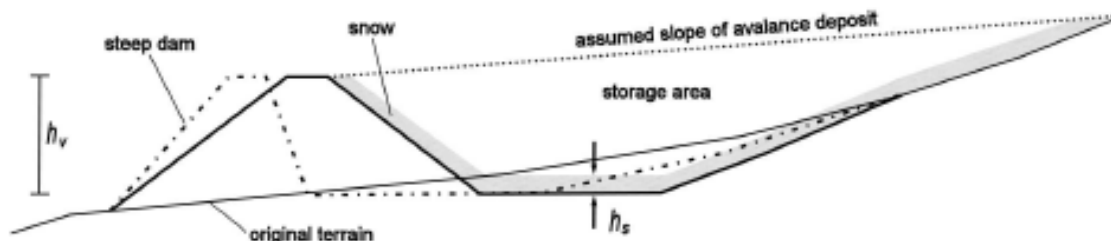


Fig. 4.51 – Scheme figure of the snow storage space above a catching dam: h_s is the thickness of snow and previous avalanche deposits on the ground on the upstream side of the dam before an avalanche hits the dam; h_v is the vertical height of the upstream dam side. The figure is adapted from Margreth (2004) [Jóhannesson et al., 2008].

Also in the case of this typology of structure it is necessary to place a lot of attention on the frequency of the least events: if the site in question was subject to numerous and little detachments, the catching structures could be easily obstructed by the snow, with a significant decrease in storage capacity height (Fig. 4.51). This can also bring the structures themselves to act as ramps for the next avalanches -if characterized by high velocity; these can become powder avalanches and cause an increase in the stopping distance.

The best position for the structures is next to the accumulation zone, where avalanches of modest dimensions are seldom able to arrive.

Structure project. Traditional design methods for avalanche dams are described by Salm et al. (1990), Margreth (2004), Norem (1994) and Lied & Kristersen (2003).

Several methods have been used to design avalanche dams, based on simple point mass considerations pioneered by Voellmy (1955) and widely used in Alpine countries (Salm et al., 1990), a description of the dynamics of the leading edge of the avalanche (Chu et al., 1995) and numerical computations of the trajectory of a point mass upstream facing the sloping side of the dam (Irgens et al., 1998).

For each dam height a sufficient storage capacity volume for the accumulated snow must be foreseen, positioned upstream.

A good design criterion is to assume the snow mass deposited upstream -regarding a single avalanche event- as equal to the mass freed in the detachment zone. It would be necessary to suppose [Mears, 1981]:

$\rho_l = 2\rho_0$	[kg/m ³]	deposit average density in the dam;
ρ_0	[kg/m ³]	flow snow average density.

An estimate of the maximum storage capacity necessary for the snow accumulated must foresee that this be half of the volume in the detachment zone (Fig. 4.52). This evaluation goes in favour of security, as it does not consider the volume of snow deposited along the avalanche path before the avalanche reaches the structure.

However, this estimate does not consider that the storage area can be subject to more than one avalanche event during the same winter.

A reduction of the avalanche velocity is possible if the dam is surmounted, since a part of the kinetic force of the avalanche is lost during the overwhelming of the dam.

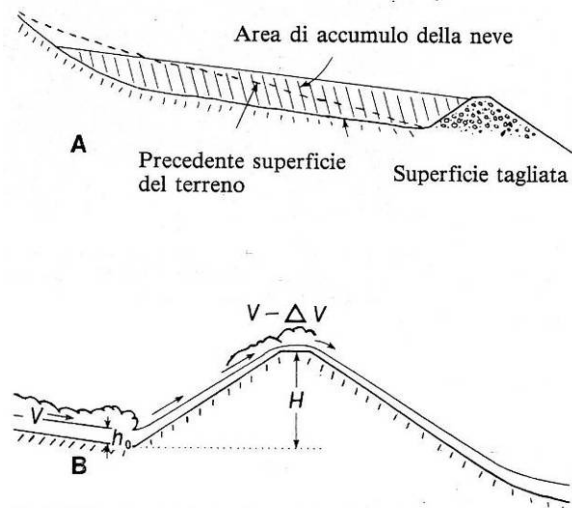


Fig. 4.52 – Catching dam: a) above, accumulate area; b) below, project height and velocity [Mears, 1981].

The velocity reduction can be evaluated as [Mears, 1981]:

$\Delta v = \sqrt{2g(H-h_0)(1+\mu\cos\theta)}$	[m/s]	design avalanche velocity variation;
g	[m/s ²]	gravity acceleration;
H	[m]	design maximal height;
h_0	[m]	snow pack depth;
μ	[-]	friction coefficient;
θ	[°]	dam lateral inclination.

Considering this loss in velocity, the real stopping distance can then be recalculated. The flow height after catching can also remain unvaried, even though a reduction of the velocity occurs.

Straight interception walls. If the catching dam is equipped with a vertical wall, the calculation of the impact forces can be made the same way as in the case of deviation structures

(fig. 4.53). It should in fact be supposed that all the snow is blocked or deviated of $\phi = 90^\circ$, in order to use the following expression to calculate the structure height [Mears, 1981]:

$$H = h_0 + h' + h = h_0 + h' + \frac{v^2}{2g}$$

H	[m]	design maximum height;
h_0	[m]	snow pack depth;
h'	[m]	avalanche flow height;
$h = \frac{v^2}{2g}$	[m]	uplift height;
v	[m/s]	design avalanche velocity;
g	[m/s ²]	gravity acceleration.

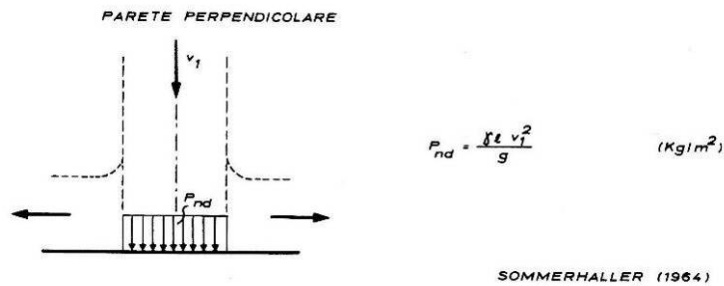


Fig. 4.53 – Impact forces on a protecting catching dam [Menegus & Soranzo, 1986].

and the following expression for the calculation of the specific deflection force [Mears, 1981]:

$$P_{dn} = \rho v^2 = \frac{\gamma v^2}{g}$$

P_{dn}	[kg/m ²]	deflection force normal component;
ρ	[kg/m ³]	avalanche density;
v	[m/s]	design avalanche velocity;
γ	[kg/m ³]	avalanche volume weight;
g	[m/s ²]	gravity acceleration;
$\left\{ \begin{array}{l} P_{ds} = \mu P_{dn} \\ P_{dv} = \mu P_{dn} \end{array} \right.$	[kg/m ²]	deflection force shear component;
	[kg/m ²]	deflection force uplift component;
μ	[-]	friction coefficient: $\mu = 0.5$.

Curved interception walls. The structure height can be determined with knowledge of the avalanche design velocity, the flow height and the snow pack depth near the structure [Mears, 1981]:

$$H = h_0 + h' + h = h_0 + h' + \frac{v^2}{2g}$$

H	[m]	design maximum height;
h_0	[m]	snow pack depth;
h'	[m]	avalanche flow height;
$h = \frac{v^2}{2g}$	[m]	uplift height;
v	[m/s]	design avalanche velocity;
g	[m/s ²]	gravity acceleration.

This equation provides the superior limit of the design height. For the structures made of earth with side slopes of θ degrees, the expression of the design height becomes:

$$H = h_0 + h' + h = h_0 + h' + \frac{v^2}{2g}(1 + \mu \cot g\theta)$$

H	[m]	design maximum height;
h_0	[m]	snow pack depth;
h'	[m]	avalanche flow height;
$h = \frac{v^2}{2g}(1 + \mu \cot g\theta)$	[m]	uplift height;
v	[m/s]	avalanche velocity;
g	[m/s ²]	gravity acceleration;
μ	[-]	friction coefficient;
θ	[°]	dam lateral inclination.

The second type of equation gives lower values of design maximum height than the previous equation because it supposes that a certain quantity of energy of the avalanche is dissipated due to friction during the uplifting phase of the avalanche along the inclined side of the catching structure. [Mears, 1981].

In Fig. 4.54-Fig. 4.59 some example of catching dams are presented.

CATCHING DAMS



Fig. 4.54 – Bethel, Colorado
[Mears, 1981].



Fig. 4.55 – Larche, Alpes-Maritimes, France
[<http://cemadoc.cemagref.fr>].



Fig. 4.56 – Galtür, Paznaun valley, Tirol, Austria [SATSIE project].



Fig. 4.57 – Vorarberg, Austria [http://cemadoc.cemagref.fr].



Fig. 4.58 – Bleie, Ullensvang, Norway [http://cemadoc.cemagref.fr].



Fig. 4.59 – Seydisfjordu, Iceland [http://www.orion.is/snow2008].

4.2.3.4. Direct protection structures

If all the previous interventions result useless, or are economically inconvenient, the defence must be directly guaranteed by the same structure (Fig. 4.60).

a) BUILDING REINFORCEMENT TECHNIQUES

Buildings can be constructed in avalanche hazard zones with special permission, but particular building techniques must be applied..



b) REINFORCEMENT TECHNIQUES FOR STRUCTURES

Some prevention is necessary for prevention structures and energy poles on highways and -especially- on railways. This consists in covering the poles with steel belts or using concrete foundations, steel snow nets or walls.



c) PROTECTING WEDGES OR SPLITTERS

This is a kind of deflecting structure that splits the avalanche flow and creates two different flow directions. It is useful for the protection of small structures (house, poles, other small things). Avalanche flow should not be too high in the path where this structure is to be used.



d) ROOFING



e) AVALANCHE TUNNELS

These are constructed in order to avoid damage to cars or vehicles in highways and railways. They are generally made of concrete or steel and their top part inclines towards to valley. Some of them are constructed by digging the main rock. They are of an open or closed type, according to morphology and avalanche type.



Fig. 4.60 – Direct protection structures: a) building reinforcement techniques; b) reinforcement techniques for structures; c) protecting wedges or splitters; d) roofing; e) avalanche tunnels [<http://cagem.bayindirlik.gov.tr>; Somnavilla, 2006; McClung & Schaerer, 1996].

Structure description. For situations in which ground is impervious and avalanches occur frequently, the most economic solution is to protect in a direct and punctual way [Frutiger & Martinelli, 1983].

The most common type of direct protection structure is an avalanche tunnel for protection of communication channels. Other examples of direct protection structures are wedges and walls built upstream -with respect to the buildings- in zones subject to avalanche hazard.

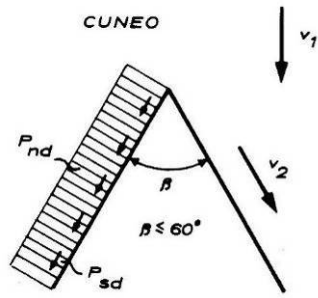
The construction of the defence structure is very often incorporated in the designs of the buildings to protect [Mears, 1981].

These structures assure complete protection, but their cost is very high and they are often only adopted when installation of other defence structures is impossible.

Like other types of structures, also for direct protection maximum efficiency is reached on slopes with an inclination between 15° and 20° .

Also in this case, before designing the structure, it is necessary to determine the natural characteristics of the project avalanche.

Structure project. Wedges do not permit total defence when powder avalanches are concerned. If high tension lines and pillars of ski plants must be defended, the wedge will only act as a deflecting structure for the dense avalanche component, while the superior part of the pillar will have to be designed to resist forces caused by the powder component [McClung & Schaerer, 1996].



$$P_{nd} = \frac{\gamma l v^2}{g} \text{sen}^2 (\beta / 2) \quad (\text{Kg/m}^2)$$

$$P_{sd} = \mu P_{nd} \quad (\text{Kg/m}^2)$$

SOMMERHALLER (1964)

Fig. 4.61 – Impact forces on a protecting wedge [Menegus & Soranzo, 1986].

The design forces on a vertical surface exposed to the impact of avalanches must be determined exactly in the same way as described for vertical, straight and deflecting walls.

The design height (fig. 4.62) is calculated by the equation [Mears, 1981]:

$$H = h_0 + h' + h = h_0 + h' + \frac{(v \text{sen} \phi)^2}{2g}$$

H [m] maximum height structure;

h_0 [m] snow pack depth;

h' [m] avalanche flow height;

$h = \frac{(v \text{sen} \phi)^2}{2g}$ [m] uplift height;

v [m/s] design avalanche velocity;

ϕ [°] deflection angle;

g [m/s²] gravity acceleration.

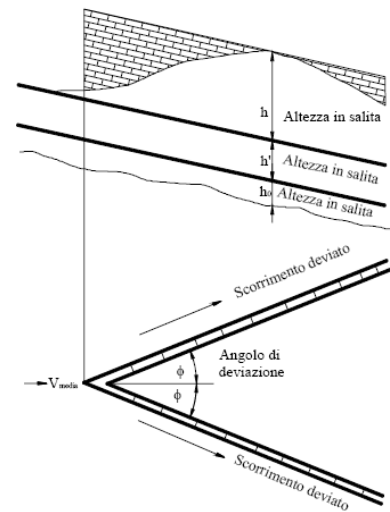


Fig. 4.62 – Impact forces on a protecting wedge [Mears, 1981].

The normal pressure is calculated as (fig. 4.61):

$$P_{dn} = \rho (v \text{sen} \phi)^2 = \frac{\gamma v^2}{g} \text{sen}^2 \phi$$

P_{dn} [N/m²] deflection force normal component;

ρ [kg/m³] avalanche density;

v [m/s] design avalanche velocity;

ϕ [°] deflection angle;

γ [kg/m³] avalanche volume weight;

g [m/s²] gravity acceleration;

$\left\{ \begin{array}{l} P_{ds} = \mu P_{dn} \\ P_{dv} = \mu P_{dn} \end{array} \right.$ [N/m²] deflection force shear component;

[N/m²] deflection force uplift component;

μ [-] friction coefficient: $\mu = 0.5$.

It is necessary to design the direct protection structures so that they be able to support the fluid-dynamic pressure of stagnation and the total pressure caused by the dense avalanche component (or both the types of pressure).

Computation of the stagnation pressure, when powder avalanches of high-velocity invest these structures, is [Mears, 1981]:

$$P_s = \frac{1}{2} \rho v^2 \quad [\text{N/m}^2] \quad \text{stagnation pressure;}$$

$$\rho \quad [\text{kg/m}^3] \quad \text{avalanche density;}$$

$$v \quad [\text{m/s}] \quad \text{design avalanche velocity.}$$

The total pressure, when the dense avalanche component invests a structure [Mears, 1981]:

$$P_f = K \rho v^2 \quad [\text{N/m}^2] \quad \text{stagnation pressure;}$$

$$K \quad [-] \quad \text{coefficient function of the avalanche and the direct structure form:}$$

$$\left\{ \begin{array}{l} K = 0.5 \quad \text{powder avalanches;} \\ K = 1.0 - 1.5 \quad \text{dense avalanches;} \end{array} \right.$$

$$\rho \quad [\text{kg/m}^3] \quad \text{avalanche density;}$$

$$v \quad [\text{m/s}] \quad \text{design avalanche velocity.}$$

Building reinforcement techniques. In designing direct protection structures it is necessary that these be able to support the stagnation fluid-dynamic pressure and the total pressure caused by the dense component [Mears, 1981].

Sometimes it is also possible to choose to build the defence structure inside the same element that is to be protected (Fig. 4.63-Fig. 4.64). For instance, a building can be built with a reinforcement wall in direction of the avalanches. Some solutions are defined for the defence of isolated buildings [Menegus & Soranzo, 1986].

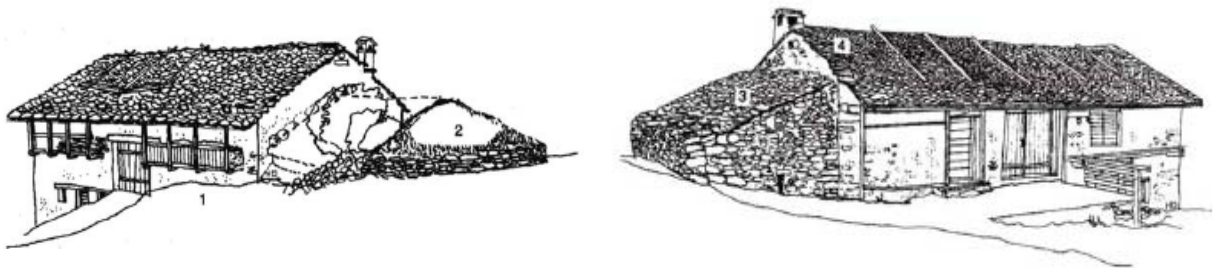


Fig. 4.63 – Typical houses of the Vanoise, France [Givry & Perfettini, 2004].

Buildings in avalanche hazard zones should consider:

- suitable geometric shapes to reduce effects of impact;
- additional effects of other elements (rocks, trees);
- reinforcement for extra static snow loads;
- safe positioning of doors, windows, balconies, gardens, parking areas (not on the side facing possible avalanches). If doors are necessary on the risky side, they must be very strong and an emergency exit must exist. Windows should be small, strong, with pull-down shutters;
- safe positioning of dining rooms, bedrooms and halls;
- construction of ditches or walls to reduce avalanche effects on gardens facing avalanches;
- avoiding to plant trees on the exposed side.

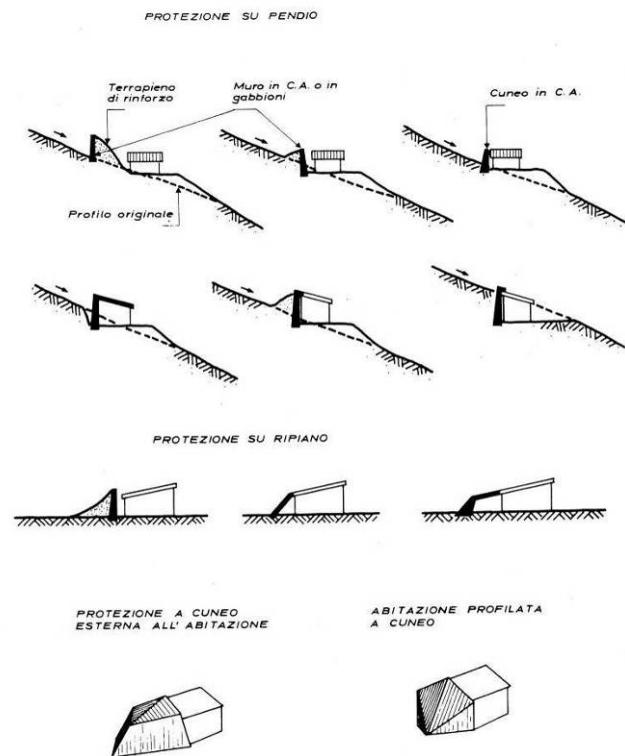


Fig. 4.64 – Example of building reinforcement techniques [Menegus & Soranzo, 1986].

For the defence of isolated structures, houses, trellises, plant lifting apparatus, a defence structure of a passive type -which generally assumes the form of a wedge-, can be convenient.

In Fig. 4.65-Fig. 4.77 some example of direct protection structures are presented.

DIRECT PROTECTION STRUCTURES



Fig. 4.65 – Bonneval-sur-Arc, Savoie, France [http://cemadoc.cemagref.fr].



Fig. 4.66 – Peisey Nancroix, Savoie, France [http://cemadoc.cemagref.fr].



Fig. 4.67 – Galtür-Paznauntal, Austria
[Höller, 2007].



Fig. 4.68 – Barèges, Hautes-Pyrénées, France
[Givry & Perfettini, 2004].



Fig. 4.69 – Réalp, Canton of Uri, Switzerland
[<http://cemadoc.cemagref.fr>].



Fig. 4.70 – Vallorcine, Haute-Savoie, France
[Givry & Perfettini, 2004].



Fig. 4.71 – Mogno, Canton of Ticino, Switzerland
[Givry & Perfettini, 2004].



Fig. 4.72 – Rosuel, Savoie, France
[Givry & Perfettini, 2004].



Fig. 4.73 – Méribel, Savoie, France
[<http://cemadoc.cemagref.fr>].



Fig. 4.74 – Larens, Alpes-de-Haute-Provence, France [<http://cemadoc.cemagref.fr>].



Fig. 4.75 – Fljotsdalslinur, Fljotsdalur valley, Iceland [<http://www.orion.is/snow2008>].



Fig. 4.76 – Val di Isère, Savoie, France [Givry & Perfettini, 2004].



Fig. 4.77 – Val di Isère, Savoie, France [Givry & Perfettini, 2004].



Protecting wedges. A particular type of direct defence structure is represented by wedges. These are barriers, walls or pillars of a wedge shape that are directly placed in front of the object to be protected in order to deflect the snow flow [McClung & Schaerer, 1996].

In the construction of a wedge, it is necessary to have particular attention for its the upstream versant - the tip of a wedge must always be oriented in the direction of the principal flow, while the sides must have an angular opening (usually not less of 60°) and sufficient length so as to avoid the snow mass to interfere with the structure. The height of these structures and the foreseen forces are calculated adopting a procedure such as the one adopted for the deviation works [Menegus & Soranzo, 1986].

In Fig. 4.78-Fig. 4.81 some example of protecting wedge are presented.

PROTECTING WEDGES



Fig. 4.78 – Fljótsdalur, Iceland
[Hákonardóttir et al., 2008].



Fig. 4.79 – Ísafjörður, Iceland
[<http://www.orion.it>].



Fig. 4.80 – Passy, Haute-Savoie, France
[Givry & Perfettini, 2004].



Fig. 4.81 – St.-Hilaire-du-Touvet, Savoie, France
[<http://cemadoc.cemagref.fr>].

Avalanche tunnels. These are deflecting structures which allow the snow masses to run beyond the structure to be protected, instead of beside it [Cresta, 1991].

The most frequent case of protection using tunnels is that regarding the protection of transport links (Fig. 4.82), especially roads and railway lines. It is not always possible to avoid the intersection of the avalanche paths and, when this becomes economically unsustainable, avalanche tunnels can be used [McClung & Schaerer, 1996].

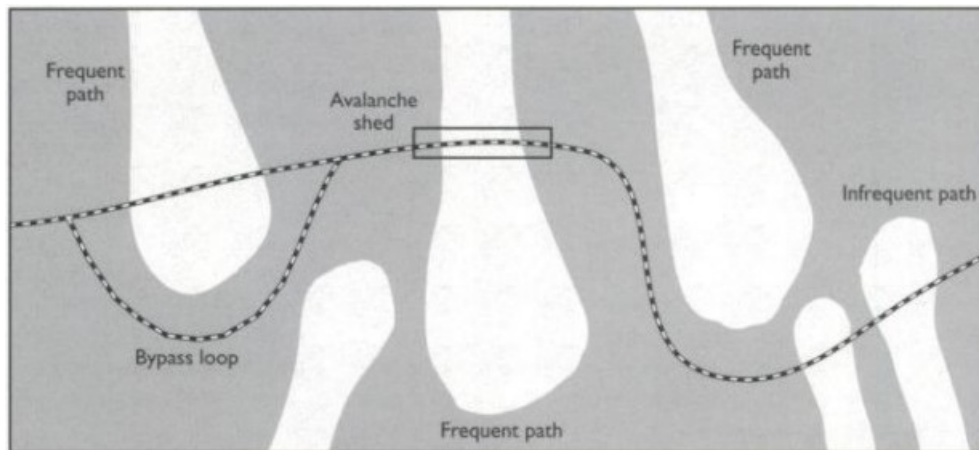


Fig. 4.82 – Avalanche tunnels [McClung & Schaerer, 1996].

Some useful rules for the location and designing of roads on the avalanche path can be:

- cross an avalanche slope at the beginning of the stopping zone;
- if possible, build the road on an embankment;
- avoid the deviations levelling the slope;
- realize wide and deep drains so as to be able to drain away avalanches of small dimensions [McClung & Schaerer, 1996].

The design of an avalanche tunnel obliges to solve several problems that arise, due to the morphology of the ground [Cresta, 1991].

The simplest solution consists in a series of coverings suitably planned to allow the snow to flow above the structure [McClung & Schaerer, 1996].

According to the entity of the structure, carrying structures in concrete, steel or wood can be used.

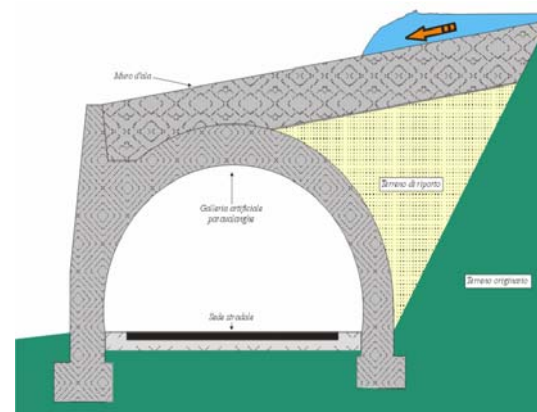


Fig. 4.83 – Scheme of an avalanche tunnel [Sommavilla, 2006].

The covering must have a greater slope than that of the versant, because a decrease of slope brings to slowing down the avalanche, with consequent increase in amount of snow deposited on the roof and relative side expansion, which can obstruct the two entrances. Besides, the structure must be sufficiently long enough to cover the extent of the flowing area (Fig. 4.83).

During the designing phase the importance of the consequences of freezing on foundations, walls and the road surface must be pointed out. Water must be drained through channels arranged on the avalanche slope that run through the tunnel (interior drainage).

Structure project. For the dimensioning of an avalanche tunnel the forces to examine are those of deviation and friction (the snow-coverage contact) [Mears, 1981].

For the calculation of the solicitations it is possible to adopt two methods (Fig. 4.84).

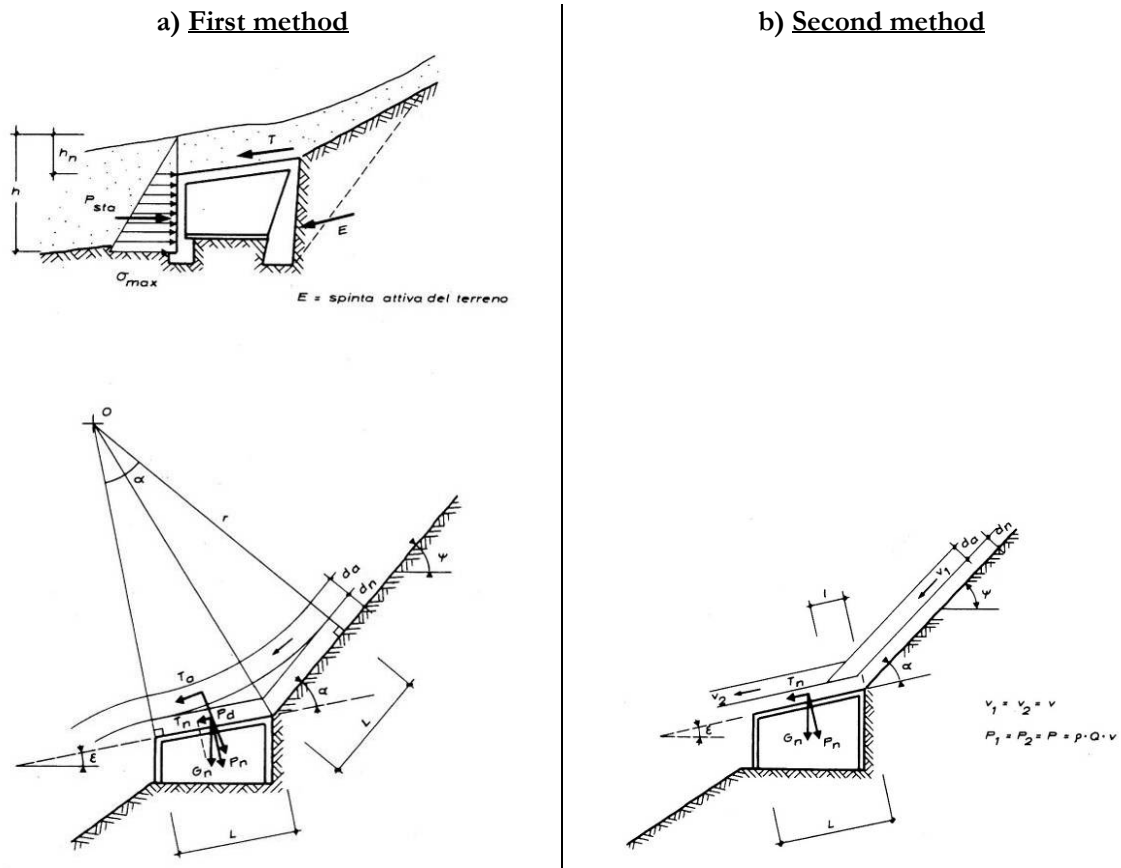


Fig. 4.84 – Calculation of impact forces on an avalanche tunnel:
a) on the left, first method; b) on the right, second method [Menegus & Soranzo, 1986].

First method. The avalanche is considered deflected from a distance upstream equal to that of the length of the tunnel roof. The mass in motion almost designs an arc of a circle. A centrifugal force is produced that is disposed partly on the ground and partly on the tunnel roof. The centrifugal force is expressed as [Menegus & Soranzo, 1986]:

$$P_{dn} = m \frac{v_a^2}{r} = \frac{\gamma_a}{g} d_a v_a^2 \operatorname{tg} \frac{\alpha}{2} \quad [\text{kg/m}] \text{ deflection force normal component;}$$

$$m = \frac{\gamma_a L d_a}{g} \quad [\text{kg}] \quad \text{avalanche flow mass;}$$

$$\gamma_a \quad [\text{kg/m}^3] \quad \text{avalanche volume weight:}$$

$$\left\{ \begin{array}{l} \gamma_a = 200 - 300 \text{ kg/m}^3 \text{ dry snow;} \\ \gamma_a = 400 - 500 \text{ kg/m}^3 \text{ wet snow;} \end{array} \right.$$

$$L = r \tan \frac{\alpha}{2} \quad [\text{m}] \quad \text{tunnel roof length;}$$

$$r = \frac{L}{\tan \frac{\alpha}{2}} \quad [\text{m}] \quad \text{deflection circle ray;}$$

α	[°]	deflection angle;
d_a	[m]	avalanche flow depth;
g	[m/s ²]	gravity acceleration;
v_a	[m/s]	design avalanche velocity near the tunnel.

The components of snow weight -normal and parallel to the roof- and the avalanche weight are easily obtained [Menegus & Soranzo, 1986]:

{	$G_n = \gamma_n d_n L$	[kg/m]	deposited snow weight;
	$P_{nn} = G_n \cos \beta = \gamma_n d_n L \cos \beta$	[kg/m]	deposited snow weight normal component;
	$P_{ns} = G_n \sin \beta = \gamma_n d_n L \sin \beta$	[kg/m]	deposited snow weight parallel component;
	γ_n	[kg/m ³]	snow volume weight;
	d_n	[m]	deposited snow depth;
	L	[m]	tunnel roof length;
	β	[°]	roof slope.

{	$G_a = \gamma_a d_a L$	[kg/m]	avalanche weight;
	$P_{an} = G_a \cos \beta = \gamma_a d_a L \cos \beta$	[kg/m]	avalanche weight normal component;
	$P_{as} = G_a \sin \beta = \gamma_a d_a L \sin \beta$	[kg/m]	avalanche weight parallel component;
	γ_a	[kg/m ³]	avalanche volume weight;
	d_a	[m]	avalanche flow height;
	L	[m]	tunnel roof length;
	β	[°]	roof slope.

Therefore the total normal and shear pressures are [Menegus & Soranzo, 1986]:

$$P_n = P_{nn} + P_{an} + P_{dn}$$

P_n	[kg/m]	snow mass total normal force;
P_{nn}	[kg/m]	deposited snow weight normal component;
P_{an}	[kg/m]	avalanche weight normal component;
P_{dn}	[kg/m]	deflection force normal component.

$$P_s = P_{ns} + P_{as} + P_{ds}$$

P_s	[kg/m]	snow mass total shear force;
P_{ns}	[kg/m]	deposited snow weight shear component;
$P_{as} = \mu P_{an}$	[kg/m]	avalanche weight shear component;
$P_{ds} = \mu P_{dn}$	[kg/m]	deflection force shear component;
μ	[-]	friction coefficient: $\mu = 0.5$.

$$P_s = P_{ns} + \mu(P_{an} + P_{dn}) = G_n \sin \beta + \mu(G_a \cos \beta + P_{dn})$$

Second method. The deviation takes place in correspondence of the tunnel roof. The conservation of the quantity of the motion is admitted with the relation [Menegus & Soranzo, 1986]:

$$P = P_1 = P_2 = \rho Qv = \rho Fv^2 = \frac{\gamma_a d_a v^2}{g} \quad [\text{kg/m}] \text{ quantity of the motion;}$$

ρ	[kg/m ³]	avalanche density;
$Q = Fv$	[m ³ /s]	avalanche discharge;
F	[m ²]	avalanche flow section;
$v = v_1 = v_2$	[m/s]	design avalanche velocity;
v_1	[m/s]	avalanche arrive velocity;
v_2	[m/s]	deviated design avalanche velocity;
γ_a	[kg/m ³]	avalanche volume weight;
d_a	[m]	avalanche flow height;
g	[m/s ²]	gravity acceleration.

The normal component of the deflection force is [Menegus & Soranzo, 1986]:

$$P_{dn} = P \text{sen} \alpha = \frac{\gamma_a d_a v^2}{g} \text{sen} \alpha \quad [\text{kg/m}] \quad \text{deflection force- normal component;}$$

P	[kg/m]	quantity of the motion;
α	[°]	deflection angle.

Since the deviation force principally acts on the mountain roof portion, it is assumed:

$$l = \frac{d_a}{\text{sen} \alpha} \quad [\text{m}] \quad \text{deflecting zone;}$$

$$d_a = l \text{sen} \alpha \quad [\text{m}] \quad \text{avalanche flow height;}$$

$$P_d = \frac{P_{dn}}{l} = \frac{\gamma_a v^2 \text{sen}^2 \alpha}{g} \quad [\text{kg/m}^2] \quad \text{deflection force.}$$

For the determination of the total pressure it is assumed that P_n is uniformly put on all the length obtaining [Menegus & Soranzo, 1986]:

$$P_n = P_{nn} + P_{an} + P_{dn}$$

P_n	[kg/m]	snow mass total normal force;
P_{nn}	[kg/m]	deposited snow weight normal component;
P_{an}	[kg/m]	avalanche weight normal component;
P_{dn}	[kg/m]	deflection force normal component.

$$P_s = P_{ns} + P_{as} + P_{ds}$$

P_s	[kg/m]	snow mass total shear force;
P_{ns}	[kg/m]	deposited snow weight shear component;
$P_{as} = \mu P_{an}$	[kg/m]	avalanche weight shear component;
$P_{ds} = \mu P_{dn}$	[kg/m]	deflection force shear component;
μ	[-]	friction coefficient: $\mu = 0.5$.
$P_s = P_{ns} + \mu(P_{an} + P_{dn}) = G_n \text{sen} \beta + \mu(P_{an} + P_{dn})$		

With the second method, deviation pressure for small deviation angles is twice that which is defined with the first method. It is still useful to observe that [Menegus & Soranzo, 1986]:

- limiting the deflecting angle of deviation between the tunnel roof and the slope upstream is necessary;
- deflecting the avalanche before the passage on the roof tunnel in order to increase the distance L as much as possible is opportune ;
- the tunnel roof must be protected from possible collisions of boulders or blocks of ice transported by the avalanche;
- if the tunnel is placed near the final part of the avalanche path, the tunnel may suffer overloading. The deposited snow can cause remarkable overloads. It is therefore opportune to dimension the roof in order to cope with such overloads and anchor the whole structure to the slope. The downstream part of the tunnel is solicited by the force [Menegus & Soranzo, 1986]:

$$P_{stat} = \frac{\gamma(h^2 - h_n^2)}{2(m-1)} \quad [\text{N}] \quad \text{force on the downstream part;}$$

h [m] overloaded tunnel height and height;

h_n [m] height overload;

m [-] coefficient:

$$\left\{ \begin{array}{ll} m = 2 & \text{for the ice;} \\ m = 4 - 5 & \text{for the hard snow;} \\ m = 50 & \text{for the fresh snow.} \end{array} \right.$$

In Fig. 4.85-Fig. 4.90 some example of avalanche tunnels are presented.

AVALANCHE TUNNELS



Fig. 4.85 – Val d'Isère, Savoie, France
[<http://cemadoc.cemagref.fr>].



Fig. 4.86 – Cohennoz, Savoie, France
[<http://cemadoc.cemagref.fr>].



Fig. 4.87 – Isafjordur, Bolungarvik, Iceland
[<http://www.orion.is/snow2008>].



Fig. 4.88 – Alpes-de-Haute-Provence, France
[<http://cemadoc.cemagref.fr>].



Fig. 4.89 – Pampeago, Val di Fiemme, Italy [Rossi, 2004].



Fig. 4.90 – Großer Gröber, Pfafflar, Austria [Höllner, 2007].

4.2.4. Criteria to choose protection structures

The previous structures are often linked between them to obtain the best combination, but their behaviour is not always clear with exceptional events. For this reason the best form of defence -which is also the less expensive- is to avoid the realization of infrastructures and settlements in the avalanche areas. When possible, combining various categories in one project of defence structures may be useful (Fig. 4.91).

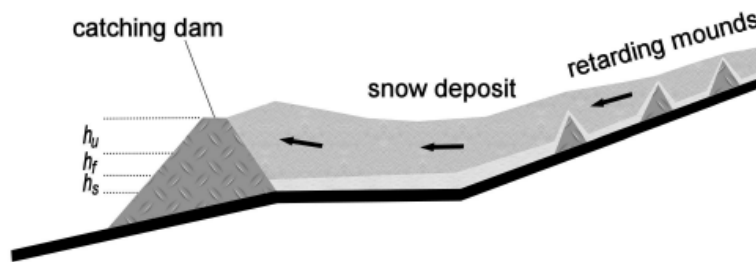


Fig. 4.91 – Scheme of a catching dam with retarding mounds [Margreth, 2004].

In the detachment zone, above the limit of the vegetation, stabilization structures are usually installed (snow bridges and snow nets), and structures that modify the deposit of the snow (snow wind fences). Instead, reforestation structures are realized in an area lower than the natural limit of vegetation, also foreseeing the necessity of terraces to protect plantations from the violent phenomenon of the flowing of the snowpack. Downstream, some slowing down mounds may be installed.

The preliminary phase of a project of defence from the avalanches consists in the definition of the general and particular snow conditions concerning the intervention zone.

In most cases long term observations for a determinate area that is to be defended are not available. When possible, to interpret local short term observations concerning the intervention zone, it is useful to utilize long term observations that may be collected in studies of areas in the vicinity.

In Fig. 4.92-Fig. 4.95 some example of combination of protection structures are presented.

COMBINATION OF AVALANCHE PROTECTION STRUCTURES



Fig. 4.92 – Taconnaz, France
[<http://cemadoc.cemagref.fr>].



Fig. 4.93 – Arzleralm, Innsbruck, Austria
[Höllner, 2007].



Fig. 4.94 – Gotthard Pass, Switzerland
[Ammann, 2008].



Fig. 4.95 – Neskaupstaður, Iceland
[Hákonardóttir et al., 2008].

Fundamental information to be found concerns the maximum intensity of the snow precipitations, the snow depth and density (maximums and minimums), the trends of the wind and the systems of snow deposit. If possible, it is useful to obtain information concerning the most probable points of detachment of the avalanches and their frequency.

It is possible that the zone of detachment of the avalanches be inaccessible during the winter period. A degree of extreme hazard actually occurs only for a few days or even only for a few hours and large periods during which monitoring of the same detachment zone is possible therefore exists.

The conditions of the ground concerning the detachment zone necessarily affect the costs of realization of the defence structures. On impervious slopes snow avalanches of poor cohesion can occur with high frequency, compromising the effectiveness of the structures. The detachment zones under the natural limit of the vegetation can be defended thanks to the possibility of easily replacing the structures, and reforestation.

Another aspect concerns problems related to transport and manpower. These -besides the problem of accessibility of the area- depend on the characteristics of the ground.

These problems are carefully evaluated also in function of the type of structure to be built: it is possible to use nets -for instance- only if the anchorages can be placed on a safe basement. If the ground is not stable it is necessary to turn to foundations equipped with linking beams. It is always necessary to make a relief of the area destined to the installation of the structures, in order to obtain useful information regarding the surface on which they will be placed, the exposure and the inclination of the slope, and the presence of compact rock and rivers.

After having decided if the use of defence structures in case of an avalanche is possible, the next decision to be taken concerns the type of structure that is to be utilized. When one wants to assure a high level of defence for frequent avalanches of big dimensions, choices fall on stabilization structures in the detachment zone or direct protection structures.

The deviation and slowing down structures or the use of explosives offer a sufficient defence in all those cases in which frequency of avalanches is more contained.



Fig. 4.96 – Active and passive defence structures at Davos, Canton of Grisons, Switzerland [McClung & Schaerer, 1996].

Stabilization structures in the detachment zone are the only ones which allow to protect the path and the stopping zone of the avalanches, also permitting reforestation.

Even if 80%-90% of the structures in areas defended from avalanches are constituted by snow bridges, snow racks are the best structures to block and to resist snow pressure. In the past structures were used for the defence from avalanches in the detachment zones capable of stabilizing the snow, such as walls, terraces and the embankments of earth, stone or masonry.

Nowadays, instead, the use of open structures is almost always preferred. However, if the slope to be protected is very steep, especially in detachment zones, massive structures can offer undoubtable advantages. They are furthermore useful, along with the open structures, in areas with deep snow storage where the open structures are not sufficiently robust to resist pressure.

The most commonly used materials are wood, steel, aluminium and concrete, which was mostly utilised in the past. Currently, tendency has turned to the use of steel. Wood remains the most suitable material for all stabilization structures, thanks to its flexibility (which allows it to resist under heavy loads without permanent deformations). The principal difficulty in the use of wood is its deterioration, which changes according to the climate of the zone. The steel used in the defence structures must own excellent malleability characteristics, to be able to resist the violent impact of the powder snow avalanches.

The structures made of cement are very heavy and require special equipment to be assembled. However, also these concrete structures do not need protection against corrosion and, thanks to their features, are not damaged by the pressure of the snow [Frutiger & Martinelli, 1983].

Chapter 5

EXPERIMENTAL ANALYSIS ON THE CHARACTERIZATION OF AVALANCHE DEPOSITS

The aim of this experimental analysis is to study, with a small-scale laboratory test, bi-disperses granular avalanches in an inclined chute with an important difference of diameter between the small and large particles.

This experimental analysis has been carried out at the *Laboratoire Avalanche of the ETNA, Unité de Recherche Erosion Torrentielle Neige et Avalanches – Cemagref – Groupement de Grenoble*.

5.1 Experimental set-up

The tests have been performed releasing, from a reservoir a mass of glass beads that flowed down an inclined channel and finally spread out on an inclined unconfined run-out zone (Fig. 5.1-Table 5.1). The support structure is an “inclined bi-plane”. As its name indicates, it consists of two planes of wood with slopes that could be varied independently (Fig. 5.3). A white glass paper sheet is stuck on the lower plane (Fig. 5.4). A reservoir provided with a gate -in which the granular material was arranged- is located at the top of the channel, (Fig. 5.2). The mass of glass beads is released.

The mass ratio between fine grains (150 μm – 250 μm) and large grains (1 mm) in the initial released mass was systematically changed to quantify its influence on:

- 1) the incoming flow depth and front velocity in the channel, measured by a Laser line technique;
- 2) the shape of the deposited mass, measured by an accurate Fringe analysis technique [Surrel, 1993].

feeding box	maximum volume	43 litres
upper plane	inclination	35°
	length	2,00 m
	width	0,60 m
flume	length	2,00 m
	width	0,30 m
	lateral height	0,07 m
lower plane	inclination	6°
	length	2,50 m
	width	1,20 m
glass paper white coloured sheet on the lower plane	length	2,30 m
	width	1,00 m

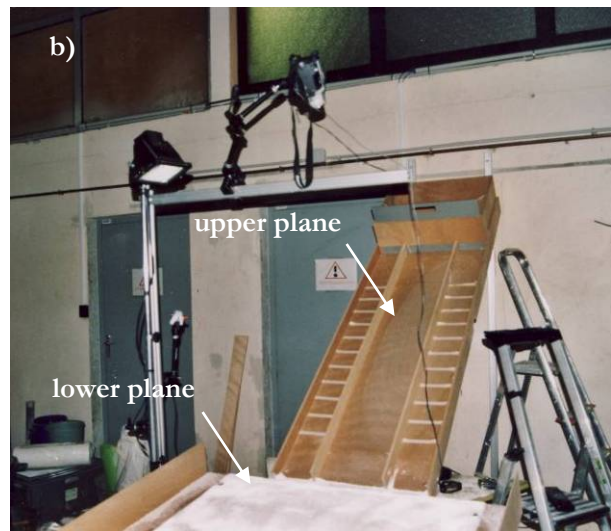
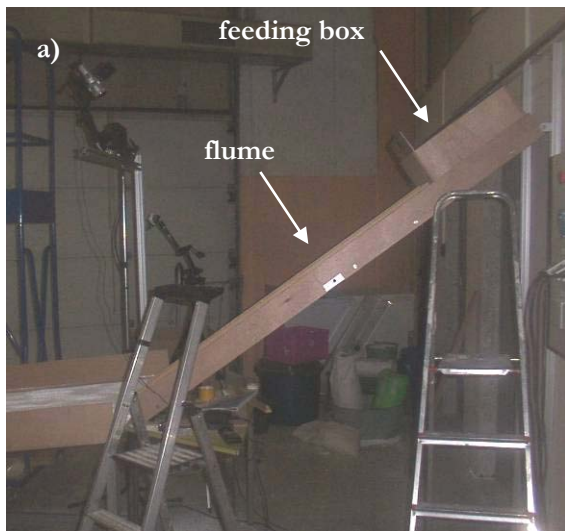


Fig. 5.1 – a) On the left, a lateral view of the experiment set-up; b) on the right, a view of the flume and its support structure.



Fig. 5.2 – The feeding box.



Fig. 5.3 – The flume.



Fig. 5.4 – Two views of the lower plane with the glass paper white coloured sheet.

Experimental set-up scheme. In Fig. 5.5-Fig. 5.6 a lateral and vertical view of the experimental set-up are presented.

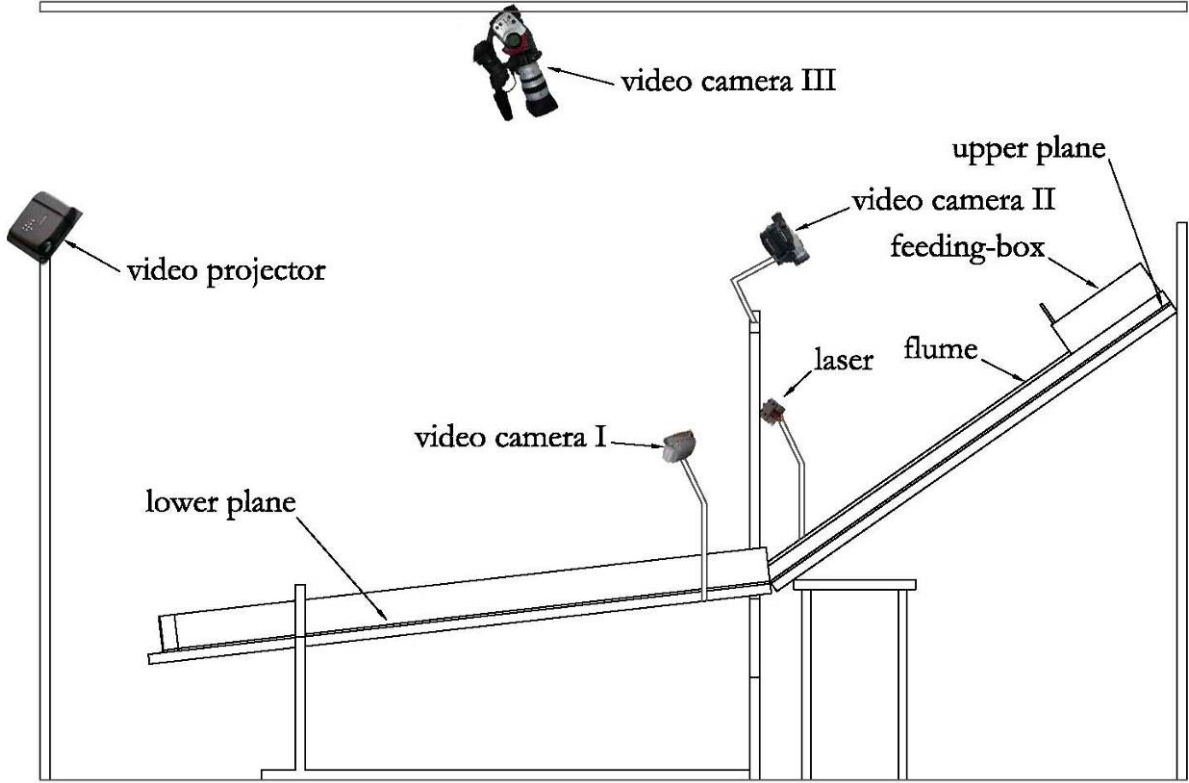


Fig. 5.5 – Lateral view of the experimental set-up.

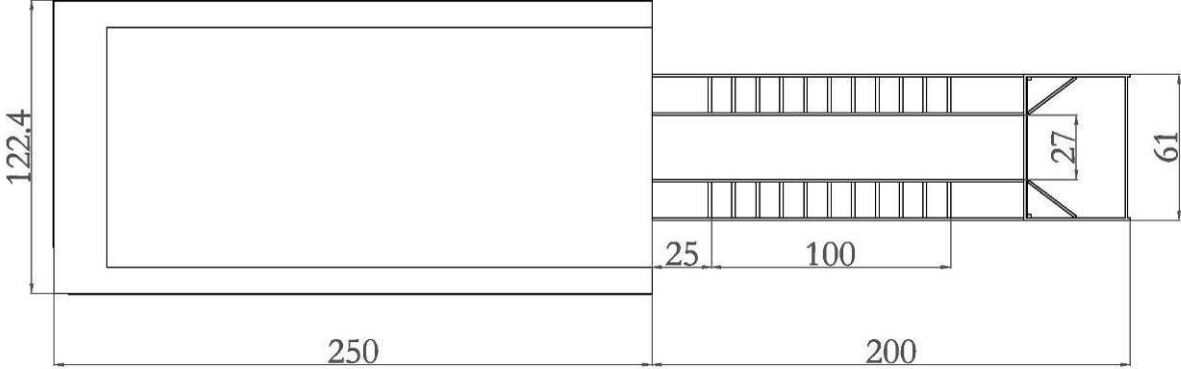


Fig. 5.6 – Vertical view of the experimental set-up (measures in cm).

5.2 Instrumentation

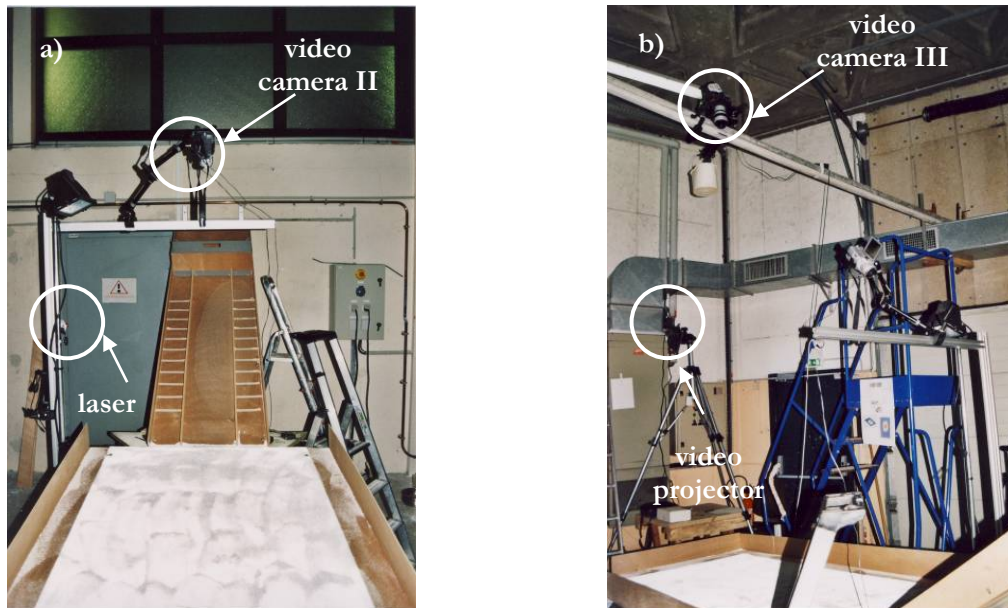


Fig. 5.7 – a) On the left, the instrumentation on the channel;
b) on the right, the instrumentation on the lower plane.

Preliminary experimental tests. In the preliminary tests the instrumentation was composed by:

- For the measuring of the flow depth at the measure section:

A video camera (video camera I) (Fig. 5.8), positioned laterally to the channel (Fig. 5.9), was used to film the channel area near the measure section (Fig. 5.10). The video camera was placed perpendicular to the measure section. It was used only during the preliminary tests, because then all the measures in the channel were realised with the Laser line technique.



Fig. 5.8 – The video camera I.
Model: Sony Handycam DCR-HC24;
exposition time: 1/250;
acquisition time: 0,04 s.



Fig. 5.9 – Two views of the video camera I.



Fig. 5.10 – The measuring section of the preliminary test. The measuring section is fixed at 91-93 cm from the feeding-box (section 0 cm).

- For the measuring of the front velocity in the channel:

A video camera (video camera II) (Fig. 5.12) was positioned above the upper plane (Fig. 5.13). It was used to film the channel area. The video camera was placed perpendicular to the channel. It was utilised both during the preliminary tests and the two tests series.

Experimental tests. In the experimental test the instrumentation was composed by (Fig. 5.7):

- For the description of the deposit shape in the feeding box:

A camera (Camera I) was used to take an image of the material in the feeding box (Fig. 5.11).

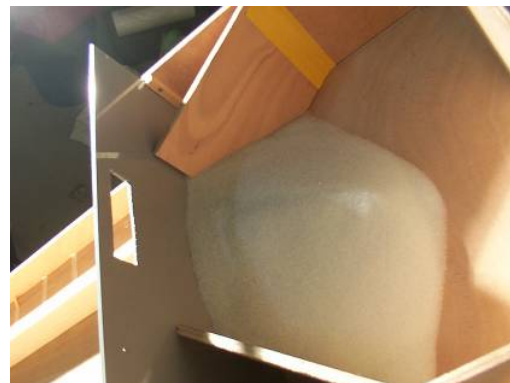


Fig. 5.11 – Two views of the feeding box with 10 kg of granular material.

- For the measuring of the flow depth and front velocity in the channel:

1) A video camera (video camera II) (Fig. 5.12) was positioned above the upper plane (Fig. 5.13). The video camera was placed perpendicular to the channel.



Fig. 5.12 – The video camera II.
 Model: Panasonic NV-MX500;
 exposition time: 1/250;
 acquisition time : 0,04 s.

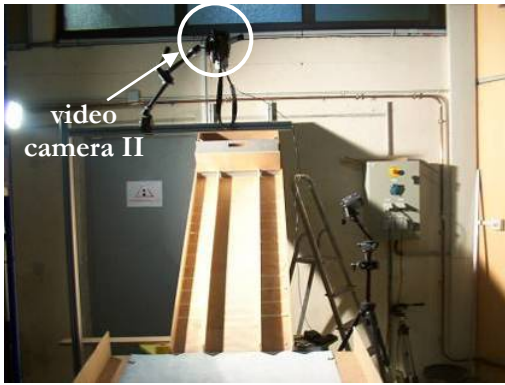
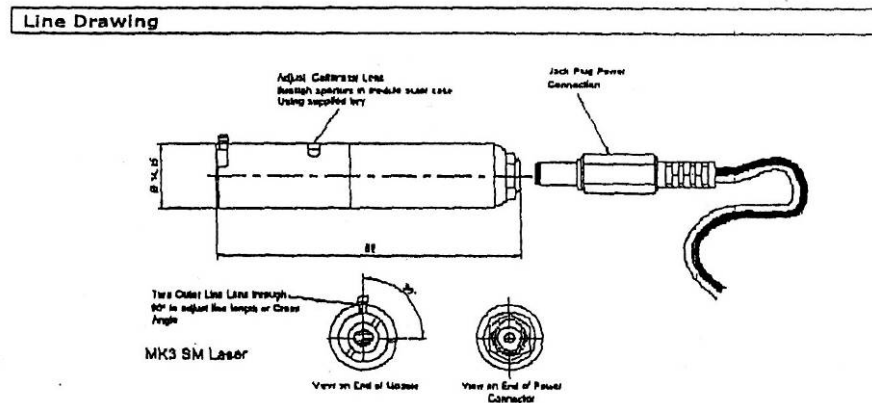


Fig. 5.13 – Two views of the video camera II.

2) A laser (Fig. 5.14-Fig. 5.15) was positioned beside the channel (Fig. 5.16). It was used to project a laser line along the centre of the channel, *reference line*, of the length of 80 cm and width of 4 mm.



Fig. 5.14 – The laserlyte alignment system.
 Model: V3VLL 5200-20;
 power: 5 mW;
 wavelength: 635 nm;
 projection: variable line.



Model	5200-00	5200-20	5200-21	5200-22
Description	V5D	V3VLL	V3LL+D	V3RXL
Power mW	1	5	5	5
Wavelength nm	650	635	635	635
Projection	Dot	Variable Line	Line with dot	Rotating cross

Fig. 5.15 – The technical sheet of the laserlyte alignment system.

The flow depth and the velocity that have been used in the description of the tests are the mean values of the flowing mass. The flow depth is measured at different measuring sections, while the velocity is the mean velocity of the flowing mass front at the same measuring sections (Fig. 5.32).

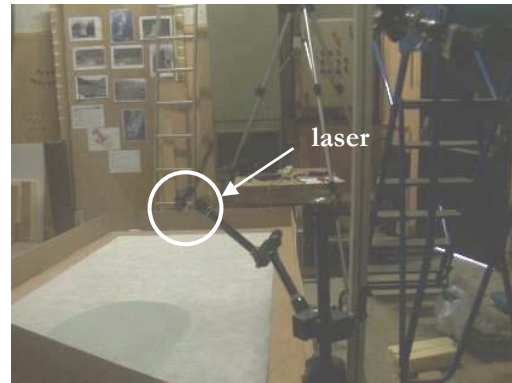
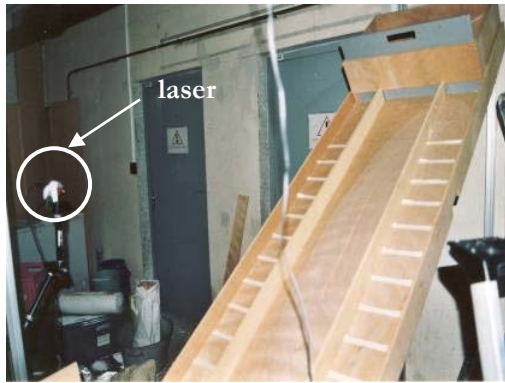


Fig. 5.16 – Two views of the laserlyte alignment system.

- For the measuring of the deposit stopping distance, width and depth:

1) A video projector (Fig. 5.17) was located in front of the lower plane (Fig. 5.18), in order to project a regular grid, constituted by white and black bands -alternatively- on the lower plane.



Fig. 5.17 – The video projector.
Model: Infocus LP70.



Fig. 5.18 – Two views of the video projector.

2) Four images of the fringes (Fig. 5.19) with the phase shift of $0, \pi/2, \pi, 3\pi/2$, which have to be projected with the video projector on the lower plane, were used.

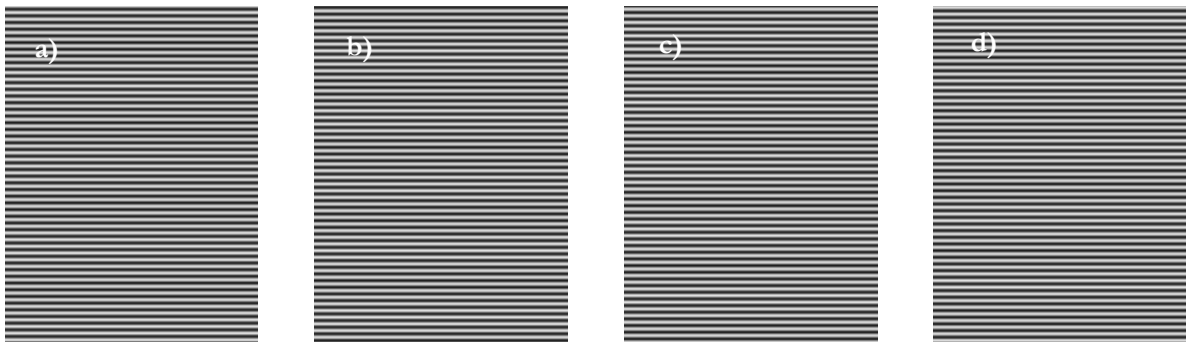


Fig. 5.19 – a), b), c), d) The images of the fringes with the phase shift of $0, \pi/2, \pi, 3\pi/2$.

- 3) A video camera (video camera III) (Fig. 5.20-Fig. 5.21) was positioned at the ceiling level. It was used to cover the total area of the lower plane. The video camera was placed perpendicular to the lower plane and, thus, to the regular grid. This made it possible to film the deformation of the grid at the passage of the mass. The video camera was placed so as to observe the largest area of the deposit including the lower *reference plane*. Maximum precision is obtained when the angle between the video projector and the video camera is of about 90°.



Fig. 5.20 – The video camera III.

Model: Canon XL1;
exposition time: 1/200;
acquisition time: 0,04 s.

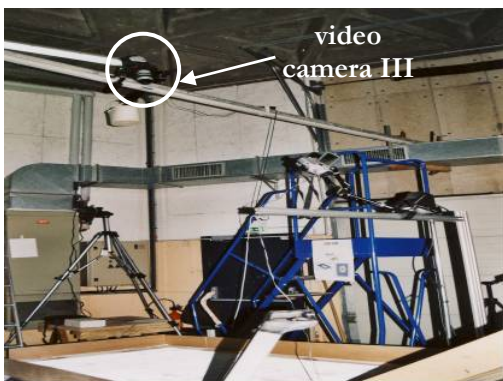


Fig. 5.21 – Two views of the video camera III.

The deposit depth that has been used in the description of the tests is the maximum value along the longitudinal direction of the deposit.

- For the measuring of the stopping distance and deposit width:

A metallic ruler is used for hand-made measurements of deposit width and deposit stopping distance.

- For the description of the deposit shape:

A camera (Camera I) (Fig. 5.22) was used to take two images of the deposit at the end of each test.

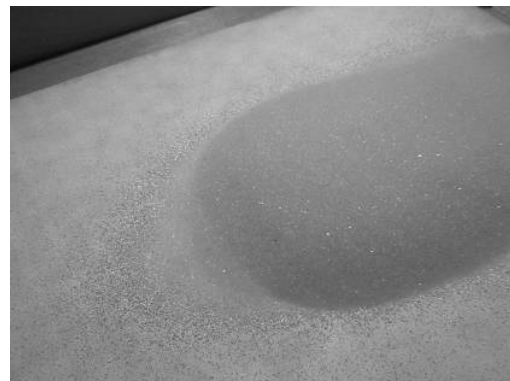



Fig. 5.22 –Deposit photo examples.

5.3 The material

Snow is simulated with a granular material - a mixture of glass beads of two different diameters (Fig. 5.23). The proportion between the masses of different diameter was varied, maintaining constant the total weight of the mixture. The shape of the beads is roughly spherical.

Table 5.2 – Physical and mechanical material characteristics.				
				
Fig. 5.23 – A mixture of glass beads.				
I – II series of tests	Glass beads I type		Glass beads II type	
grains diameter	1000 μm	1,00 mm	150 – 250 μm	1,50 – 2,50 mm
mean grains diameter	1000 μm	1,00 mm	200 μm	2,00 mm
density (glass)	2500 kg/m ³			
internal friction angle	28°			

The preliminary experimental tests were carried out with a mixture composed of 100% of the I type material (diameter of 1 mm). Later, in each experimental test, the mixture composition was changed, gradually increasing the percentage of the II type beads from 0% to 65% at a rate of 1% at a time (consequently the percentage of I type beads diminished). For values above 65% only the ratio of 0,8 and 1 were tested. The ratio between fine material mass and total mass is defined as follows:

$$M = \frac{m_{II}}{m_I + m_{II}} \times 100$$

m_I [kg] percentage of large beads;

m_{II} [kg] percentage of fine beads.

5.4 The calibration

Some tools were necessary to carry out all the reference images, for the use of the following two measurement techniques:

- Laser line technique:

Two boards of wood (Fig. 5.24) were used in the calibration along z to define the *line object*;



Fig. 5.24 – Two boards of wood.
 Length: 123,5 cm;
 width: 9,8 cm;
 thickness: respectively of 1 cm (one board) and
 2 cm (two boards together).

- Fringe analysis technique:

- 1) A white and black chess paper panel (Fig. 5.25) was used in the calibration in the plane (x, y) ;

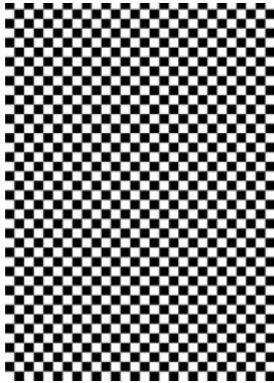


Fig. 5.25 – White and black chess paper panel.
 Format A0;
 Length: 118,9 cm;
 width: 84,1 cm;
 small squares: 3x3 cm.

- 2) Four white boards of wood (Fig. 5.26) were used in the calibration along z , to define the *image object*;



Fig. 5.26 – Four white boards of wood.
 Length: 200 cm;
 width: 6,7 cm;
 thickness: respectively of:
 0,9 cm (board n°1);
 1,9 cm (board n°2);
 3,0 cm (board n°2);
 4,0 cm (board n°4).

5.5 Preliminary tests

At the beginning of the experimental campaign 20 preliminary tests were performed in order to verify the repeatability of the tests and to write down the procedure protocol. The mixture (10 kg) was composed only by large glass beads (diameter 1 mm).

The physical parameters that have to be considered important for this test are:

- maximum flow depth at the measuring section in the channel (h);
- mean front velocity of the mixture in the channel (v);
- Froude Number (F_r);
- maximum deposit stopping distance (d);
- maximum deposit width (L).

The preliminary tests conducted by using a model with a geometrical scale of about 1/100 can be considered in the similarity of Froude.

5.5.1. Measurement techniques of the preliminary tests

The flow depth and the front velocity in the channel. The image processing of the video (video camera I) is made with the AviStep software, by finding the maximum height in each frame, to visualize the flow depth in function of the time (Fig. 5.27).



Fig. 5.27 – A sequence of frames obtained by the lateral video camera (video camera I) [Test 00 – 22/11/07].

The image processing of the video (video camera II) is made with the AviStep software, by finding the position of the avalanche front advance in each frame of the video, to visualize the avalanche front position in function of the time (Fig. 5.28).



Fig. 5.28 – A sequence of frames obtained by the frontal video camera (video camera II) [Test 00 – 22/11/07].

5.5.2. Preliminary results

Flow depth, front velocity and Froude Number in the channel. In the following figures it is possible to see the flow depth in function of the time at the measuring section (Fig. 5.29) and the front velocity along the channel (Fig. 5.30). The mean value of the Froude Number is equal to 7.

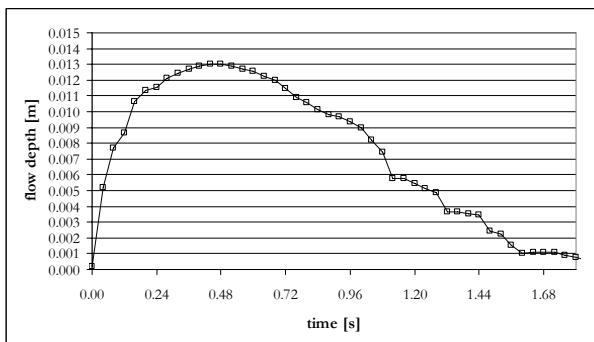


Fig. 5.29 – Flow depth in time at the measuring section (Fig. 5.10) [Test 00 – 22/11/07].

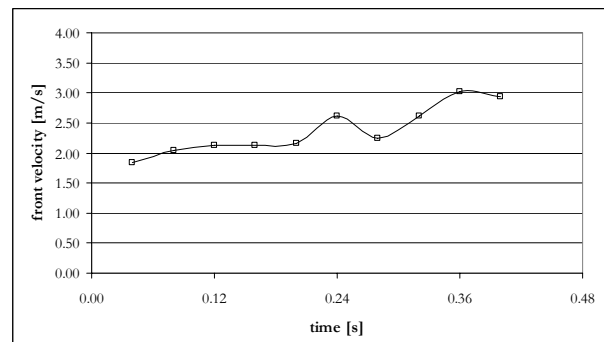


Fig. 5.30 – Front velocity in time along the channel [Test 00 – 22/11/07].

Deposit analysis: deposit stopping distance and width. With a ruler, it is possible to measure the deposit stopping distance and the deposit width (Fig. 5.31).



Fig. 5.31 – Two views of a preliminary test deposit [Test 00 – 22/11/07].

5.6 Measurement techniques of the tests

The mass ratio between fine grains (150 – 250 μm) and large grains (1 mm) in the initial released mass was systematically changed. The influence of this parameter was evaluated using the following techniques (Fig. 5.32):

- Laser line technique: flow depth and the front velocity in the channel are measured by projecting a laser line along the channel diagonally and observing the line shifting caused by the moving mass;
- Fringe analysis technique: the deposit shape is described by means of a Fringe analysis technique.

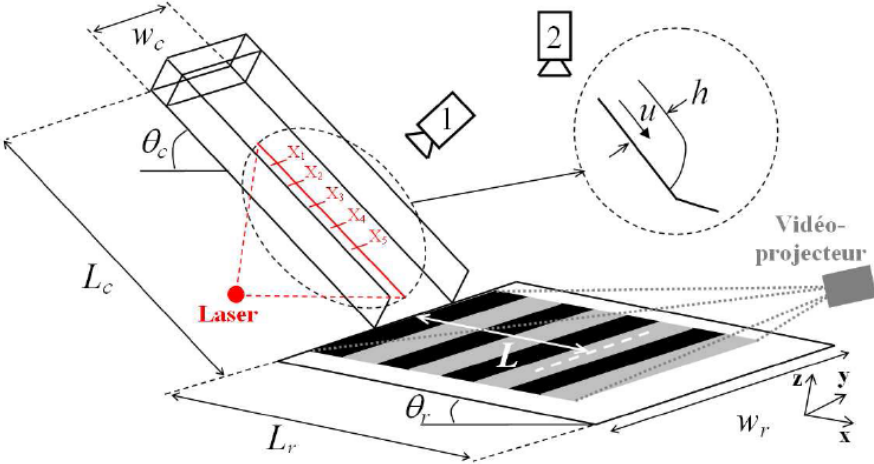


Fig. 5.32 – Scheme of the two measurement techniques: the Laser line technique on the channel and the Fringe analysis technique on the lower plane [Faug].

5.6.1. Laser line technique

The method is based on the analysis of the deformations of the projected laser line in the channel. The granular mass, flowing along the channel, produces a displacement of the projected line, *reference line*. The video camera II has to be perpendicular to the channel and to the *reference line*. It is then possible to visualize the displacement, frame by frame, from a test video and to quantify the height of the flow, which is proportional to the distance between the *reference line* and the *object line* (shifted line) in each frame.

In Fig. 5.33 a scheme of the laser line is presented; the displacement of the laser line depends on the height of the object.

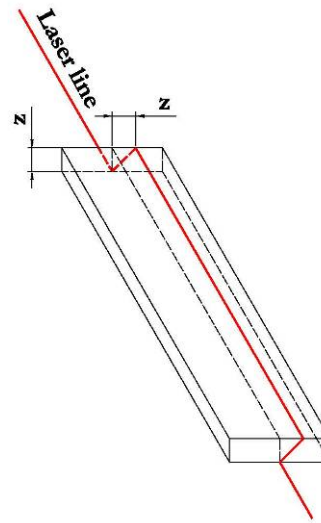


Fig. 5.33 – Scheme of the laser line.

Calibration. To make the calibration in the plane (x, y) and along z it is necessary to fix reference measurements. The reference is made with a board -1 cm thick- and two superimposed boards -2 cm thick-.

After having captured the corresponding images of the projected displacement of the laser line, the distance of the *reference distance* between the *reference line* and corresponding *object line* is established. The frames of the video are used to visualize the advancing of the avalanche front, by fixing the axis x on the *reference line*, and by calculating the position of the front in each frame. At the end it is possible to represent the position of the front in function of the time and to estimate the flow depth and the front velocity of the flowing mixture.

During the test it is necessary to carry out a certain number of images:

- image with the ruler positioned in the channel, without the laser line projected, at the beginning of the tests series (Fig. 5.34). This image is called *reference image* for the calibration in the plane (x, y) ;

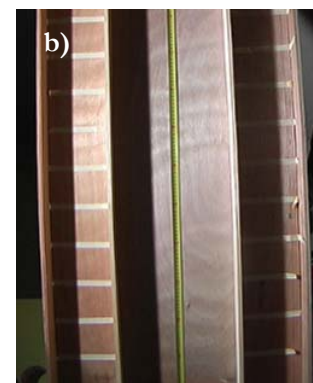


Fig. 5.34 – a) On the left, view of the channel with the ruler positioned in the centre of the channel; b) on the right, *Reference image – Calibration in the plane (x, y) , ruler image.*

- image of the channel, with the laser line projected, at the beginning of the tests series (Fig. 5.35). This image is called *reference image* for the calibration along z ;

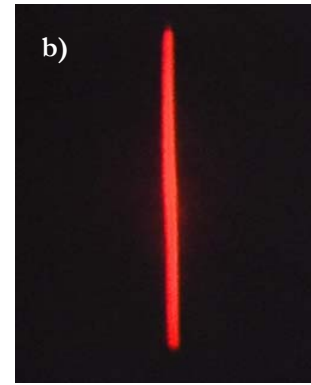
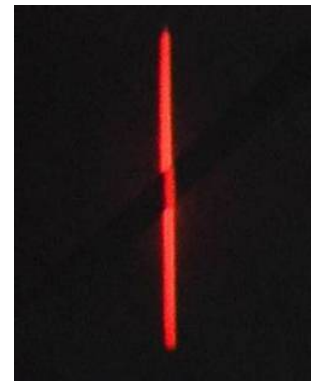


Fig. 5.35 – a) On the left, view of the channel with the laser line in the centre of the channel; b) on the right, *Reference image – Calibration along z*, channel plane image ($z = 0$ cm).

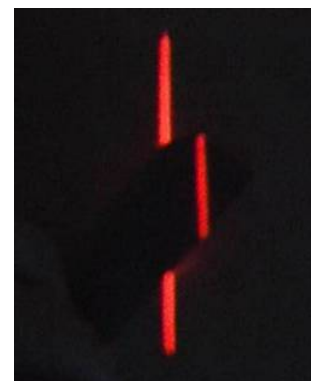
- image with a board positioned on the channel, with the laser line projected, at the beginning of the tests series (Fig. 5.36). This image is called *object image n°1* for the calibration along z ;

Fig. 5.36 – View of the laser line with the displacement due to one board taken with the video camera (video camera II), *Object image n°1 – Calibration along z*, board image ($z = 1$ cm).



- image with two boards superimposed positioned on the channel, with the laser line projected, at the beginning of the tests series (Fig. 5.37). This image is called *object image n°2* for the calibration along z .

Fig. 5.37 – View of the laser line with the displacement due to two superimposed boards, taken with the video camera (video camera II), *Object image n°2 – Calibration along z*, two boards image ($z = 2$ cm).



Test procedure of the Laser line technique. Video frames have to be extracted, for instance with Adobe Premiere. After the image processing with the ImageJ software filtering the red light of the laser and a Matlab™ script, it is possible to visualize the longitudinal profile of the flow depth, by finding the maximum height (maximum distance) in each frame of the video, in the measuring section.

By finding the position of the front advance in each frame of the video, it is possible to visualize the longitudinal profile of the front position. The front velocity can then be calculated. The procedure can be summarized as follows:

- 1) definition of the *reference line* – channel plane (Fig. 5.38);
- 2) definition of the *object line* – first object of calibration (one boards) (Fig. 5.39a);
- 3) definition of the *object line* – first + second object of calibration (two boards) (Fig. 5.39b);
- 4) definition of the *object lines* – granular material flow (Fig. 5.40);
- 5) calculation of the distance between *reference line* and *object line* (displacement of *reference line*);
- 6) determination of the flow depth and the front velocity.

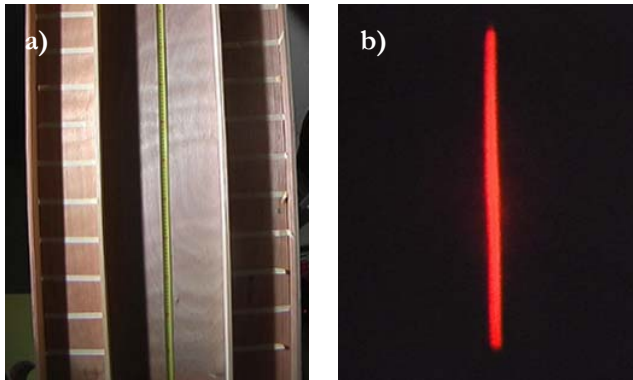


Fig. 5.38 – Reference Images: a) Calibration in the plane (x,y), ruler image; b) Calibration along z , channel plane image ($z = 0$ cm).

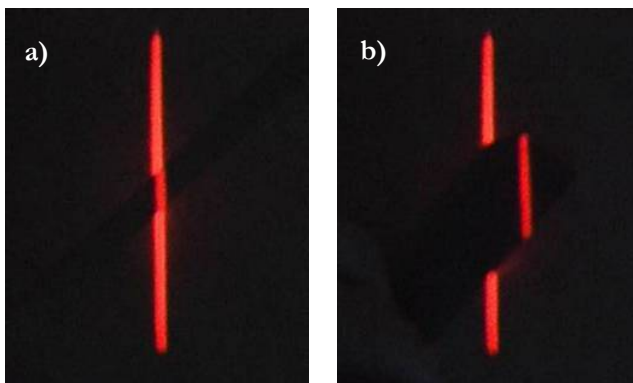


Fig. 5.39 – Object images: a) n°1 – Calibration along z , board image ($z = 1$ cm); b) n°2 – Calibration along z , two board image ($z = 2$ cm);

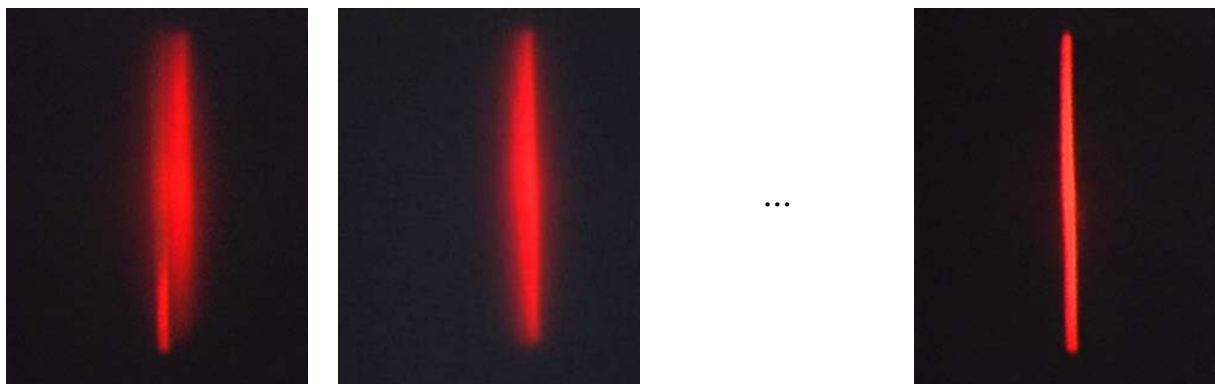


Fig. 5.40 – Test object images – A sequence of frames taken by the frontal video camera (video camera II).

5.6.2. Fringe analysis technique

The method is based on the analysis of the deformations of luminous projected fringes on an object (the granular mass in this analysis). At the passage of the granular mass the projected fringes are deformed [Sansoni et al., 1999]. The deformation makes it possible to deduce the height of the granular mass at any point. This height is proportional to the phase shift between the two signals: the *signal reference* (flat inclined plane) (equation 1) and the *signal object* (the granular mass) (equation 2).

The *signal* resulting from the *reference image* is represented by a sinusoidal signal. This reference signal is decomposed into an average term and a sinusoidal term (eq. 1):

$$I(x, y) = \bar{I}(x, y) + \bar{I}(x, y)\gamma(x, y)\cos(2\pi f_0 x + \varphi_0) \quad \text{reference signal (eq. 1);}$$

$$\left\{ \begin{array}{ll} \bar{I}(x, y) & \text{average term;} \\ \bar{I}(x, y)\gamma(x, y)\cos(2\pi f_0 x + \varphi_0) & \text{sinusoidal term;} \\ \gamma(x, y) & \text{contrast to the point } (x, y); \\ \varphi_0 & \text{phase by arbitrary origin;} \\ f_0 & \text{signal supporting frequency defined } 2i = I / f_0; \\ i & \text{distance between two fringes.} \end{array} \right.$$

The object image represented by defining $\overline{ab}(x, y)$, the local deviation of the fringes generated by the passage of the granular mass, is defines by:

$$I(x, y) = \bar{I}(x, y) + \bar{I}(x, y)\gamma(x, y)\cos(2\pi f_0 (x + \overline{ab}(x, y)) + \varphi_0)$$

The phase difference between the *reference signal* and the *object signal* is proportional to the displacement of the fringes and can be defined as follows:

$$\left\{ \begin{array}{ll} \varphi(x, y) = 2\pi f_0 \overline{ab}(x, y) + \varphi_0 & \text{local phase;} \\ I(x, y) = \bar{I}(x, y) + \bar{I}(x, y)\gamma(x, y)\cos(2\pi f_0 x + \varphi(x, y)) & \text{object signal;} \end{array} \right.$$

$$\left\{ \begin{array}{ll} \Delta\varphi(x, y) = 2\pi f_0 \overline{ab}(x, y) & \text{phase difference between the two signals;} \\ I(x, y) = \bar{I}(x, y) + \bar{I}(x, y)\gamma(x, y)\cos(2\pi f_0 x + \Delta\varphi(x, y) + \varphi_0) & \text{object signal (eq. 2);} \end{array} \right.$$

The difference with the reference plane phase is:

$$\Delta\varphi(x, y) = 2\pi f_0 \overline{ab}(x, y) \quad \text{(eq. 3).}$$

The main difficulty of the method is to determine the phase difference between the two *signals*, *reference* and *object* (eq. 3), in order to deduce the local deviation of the grid and the depth of the granular mass.

The fringes deformation allows the modelling of the 3-D surface. To obtain the 3-D surface the triangulation technique is used [Vincent, 2003].

A video projector P projects a fringe series towards the surface S of an object which forms the image I , observed by a video camera C (Fig. 5.41). The distances L_p (between the video projector P and the reference plane R), L_c (between the video camera C and the reference plane R) and V_p (between the video projector P and the video camera C), are estimated during the calibration phase.

An image I_R of the reference plane R on which the fringes are projected is acquired. The optical axes of the video projector and the video camera are supposed to be coplanar and the fringes parallel to each other.

One of the light planes of the video projector meets the surface S at the point M thus the image on I is m of coordinates (x, y) . This same plane intersects the reference plane R to the point B thus the image on I_R is b .

It is the displacement \overline{AB} of the fringe, where A is the retro projection of m on R , which leads to the distance Δz of the point M to the reference plane R .

$$P = [-V_p \quad 0 \quad L_c - L_p]^T \quad \text{video projector;}$$

$$C = [0 \quad 0 \quad 0]^T \quad \text{video camera;}$$

L_p distance between the video projector P and the reference plane R ;

L_c distance between the video camera C and the reference plane R ;

V_p distance between the video projector P and the video camera C ;

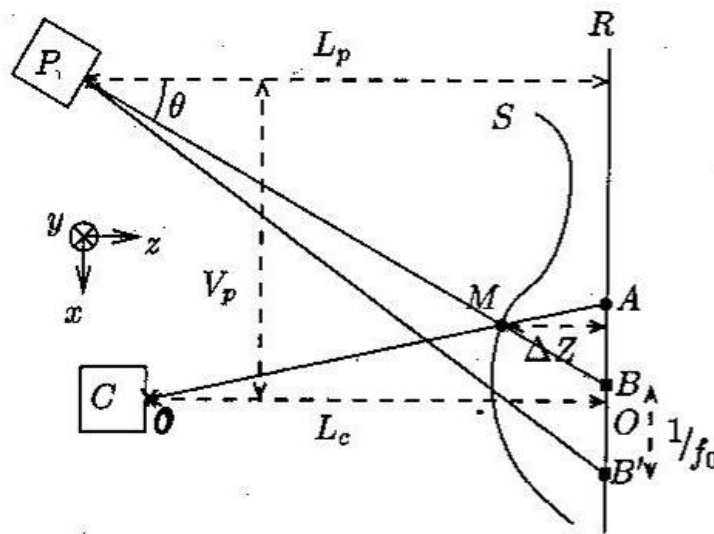


Fig. 5.41 – Fringe projection system and numerical 3D technique [Vincent, 2003].

$$\left\{ \begin{array}{l} R \\ I_R \end{array} \right. \quad \begin{array}{l} \text{reference plane;} \\ \text{image of the reference plane } R; \end{array}$$

$$\left\{ \begin{array}{l} S \\ I \end{array} \right. \quad \begin{array}{l} \text{object surface;} \\ \text{image of the object surface } S; \end{array}$$

$$\left\{ \begin{array}{l} B = [x_B \quad y_B \quad L_c]^T \\ b \end{array} \right. \quad \begin{array}{l} \text{surface point of the reference plane } R; \\ \text{image point of } B \text{ on the reference plane image } I_R; \end{array}$$

$$\left\{ \begin{array}{l} M = [x_M \quad y_M \quad L_C - \Delta z]^T \\ m \end{array} \right. \quad \begin{array}{l} \text{surface point of the object surface } S; \\ \text{image point of } M \text{ on the object surface image } I; \end{array}$$

$$\left\{ \begin{array}{l} A = [x_A \quad y_A \quad L_C]^T \\ a \end{array} \right. \quad \begin{array}{l} \text{retro projection point of } m \text{ on the reference plane } R; \\ \text{image point of } A \text{ on the reference plane image } I_R. \end{array}$$

The point M can be obtained by considering the intersection of the sight line \overline{OA} with the light plane (presumably perpendicular to the figure) defined by three points:

$$\left\{ \begin{array}{l} P = [-V_P \quad 0 \quad \Delta L]^T \\ B = [x_B \quad y_B \quad L_C]^T \\ P' = [-V_P \quad 1 \quad \Delta L]^T \end{array} \right.$$

$$\Delta L = L_C - L_P$$

Given three distinct not aligned points, P_1, P_2, P_3 the plane equation passing through P_1, P_2, P_3 is given by:

$$-xL_P + (x_B + V_P)z - V_P L_P - (x_B + V_P)\Delta L = 0 \quad \text{light plane equation.}$$

The sight line passing through A intersects the light plane in M so that $\overline{OM} = \alpha \overline{OA}$.

$$A = [x_A \quad y_A \quad L_C]^T$$

$$-x_A L_P + (x_B + V_P)L_C - V_P L_P - (x_B + V_P)\Delta L = 0 \quad \text{sight line for } A;$$

$$\alpha = \frac{V_P L_P + (x_B + V_P)\Delta L}{-x_A L_P + (x_B + V_P)L_C}$$

Considering the third component of M it results [Vincent, 2003]:

$$z_M = \alpha L_C$$

$$\Delta z = L_C - z_M = L_C - \alpha L_C = L_C(1 - \alpha) = L_C \left(1 - \frac{V_P L_P + (x_B + V_P)\Delta L}{-x_A L_P + (x_B + V_P)L_C} \right) =$$

$$\Delta z(x, y) = \frac{L_P \overline{AB}(x, y)}{V_P - \frac{L_P}{L_C} \overline{AB}(x, y) + \left(1 - \frac{L_P}{L_C} \right) \overline{OB}(x, y)}$$

The equation with $L_C = L_P$ becomes the equation [Takeda & Mutoh, 1983]:

$$\Delta z(x, y) = \frac{L_P \overline{AB}(x, y)}{V_P - \overline{AB}(x, y)} = \frac{L_C \overline{AB}(x, y)}{V_P - \overline{AB}(x, y)}$$

An ultimate simplification can be found if, moreover, $V_P \gg \overline{AB}$ [Surrel, 1998]:

$$\Delta z(x, y) = \frac{L_P \overline{AB}(x, y)}{V_P - \overline{AB}(x, y)} \approx -\frac{L_P \overline{AB}(x, y)}{V_P} \approx -\frac{\overline{AB}(x, y)}{\tan \theta_0} \quad \text{with } \tan \theta_0 = \frac{V_P}{L_P}.$$

With the equation 3 we defined the displacement object image \overline{ab} , then the displacement object \overline{AB} and finally the depth difference $\Delta z(x, y)$.

It is necessary to define the phase shift between the two signals. Two methods are available:

- Phase Shift method: for the static studies;
- Fourier Transform method: for the dynamic studies.

The Phase Shift method is based on the acquisition of a series of four images of the object, shifting the phase of $\pi/2$ each time. The technique using the Fourier Transform requires only one image. This second method can be used for objects in movement, to obtain dynamic results. On the contrary the Phase Shift method, being a more local approach, seems to be more interesting in order to solve these problems. But, since it requires four images of the object, captured when the four images of the fringes (with different phase shifts) are projected, it is possible to use it only in stationary mode.

In this thesis the Fringe analysis techniques has been applied with the Phase Shift method.

Calibration and images acquisition. To make the calibration in the plane (x, y) and along z it is necessary to fix reference measurements. The reference is made with four boards of wood with different thicknesses.

After having carried out the corresponding images of the projected deformation of the fringes, we established the measurement of the *phase difference* between the *reference images* and the corresponding *object images*. The frames of the video are used to visualize the distribution of the avalanche deposit. At the end it is possible to represent the evolution of the deposit in function of the time.

During the test it is necessary to carry out a certain number of images:

- image of the white and black chess paper panel positioned on the lower plane, at the beginning of the test series, without the projected fringes (Fig. 5.42). This image is called *reference image* for calibration in the plane (x, y) ;

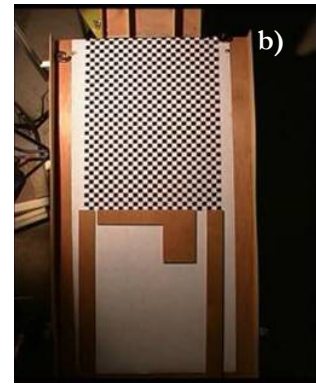
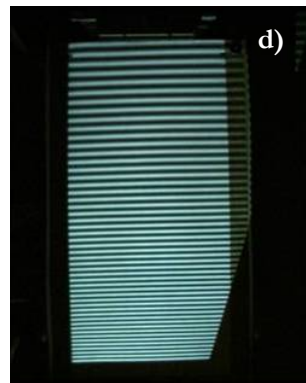
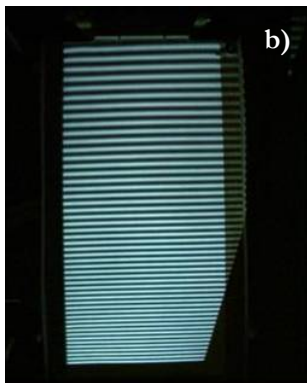


Fig. 5.42 – a) On the left, view of the white and black chess paper panel; b) on the right, *Reference image – Calibration in the plane (x,y)*, white and black chess paper panel image.

- four images of the lower plane, with the fringes projected, at the beginning of the test series (Fig. 5.43). These images are called *reference images* for calibration along z ;



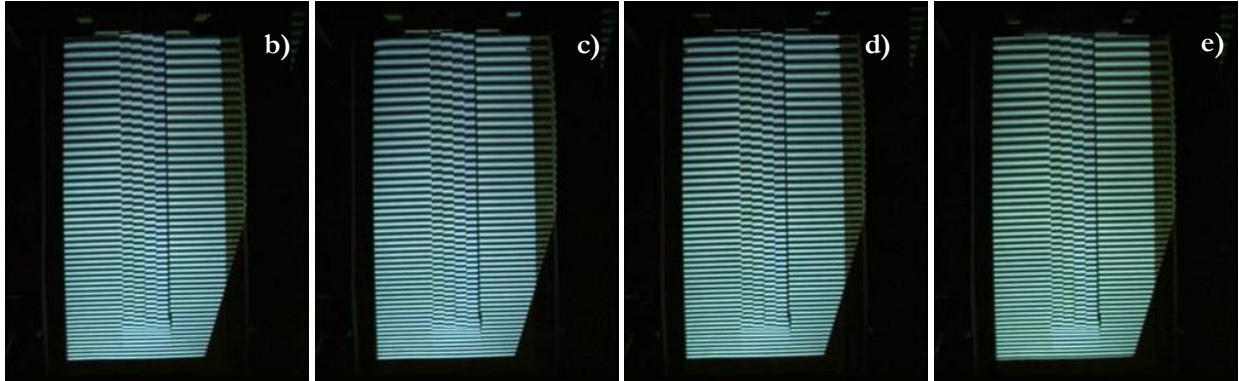
Fig. 5.43 – a) On the left, view of the lower plane with the fringes projected;
b), c), d), e) below, four images taken with the video camera (video camera III), *Reference images – Calibration along z* , lower plane images ($z = 0$) with the phase shift of $0, \pi/2, \pi, 3\pi/2$.



- four images of the boards positioned on the lower plane, with the projected fringes, at the beginning of the test series (Fig. 5.44). These images are called *object images* for calibration along z ;



Fig. 5.44 – a) On the left, view of the lower plane with the fringes projected and the boards of wood positioned in the centre of the plane; b), c), d), e) below, four images taken with the video camera (video camera III), *Object images – Calibration along z*, four images of the boards ($z = 0,9 ; 1,9 ; 3,0 ; 4,0$) with the phase shift of $0, \pi/2, \pi, 3\pi/2$.



The Phase Shift method can be applied to determine the 3D-representation of the deposit of granular mass. It implies the capturing of at least four images obtained by projecting images of the shifted fringes onto the deposit.

The *signal* resulting from the *reference image* and the *signal* of the *object image* can be modelled as in equation 1 and equation 2.

If considering that $\bar{I}(x, y)$ represents the luminous intensity in each pixel of an image of a fringes field, we can express the *object signal* in the following form:

$$I_i(x) = A + B \cos(\varphi(x) + \Delta\varphi_i) \quad (\text{eq. 4})$$

$$\left\{ \begin{array}{ll} A(x, y) = \bar{I}_i(x, y) & \text{mean value of the signal intensity;} \\ B(x, y) & \text{sinusoid amplitude;} \\ \varphi(x) = 2\pi f_0 x & \text{phase;} \\ \Delta\varphi_i = 0, \pi/2, \pi, 3\pi/2 & \text{phase shift.} \end{array} \right.$$

The intensity $I_i(x)$ (eq. 4) defines the image i to be projected. It depends on the phase $\varphi(x)$ and the $\Delta\varphi_i$ shift, which is imposed to it. The coefficients $A(x, y)$ and $B(x, y)$ correspond, respectively, to the sinusoidal amplitude and the mean value of the signal intensity. Knowledge of the four unknown factors requires at least four equations, obtained by adding four known phase shifts $\Delta\varphi_1, \Delta\varphi_2, \Delta\varphi_3, \Delta\varphi_4$ to the phase $\varphi(x)$.

The corresponding four intensities $I_i (i = 1,2,3,4)$ are then given by:

$$\left\{ \begin{array}{lll} I_1(x) = A + B \cos(\varphi(x)) & (i = 1) & \Delta\varphi_1 = 0; \\ I_2(x) = A + B \cos(\varphi(x) + \Delta\varphi_2) & (i = 2) & \Delta\varphi_2 = \pi/2; \\ I_3(x) = A + B \cos(\varphi(x) + \Delta\varphi_3) & (i = 3) & \Delta\varphi_3 = \pi; \\ I_4(x) = A + B \cos(\varphi(x) + \Delta\varphi_4) & (i = 4) & \Delta\varphi_4 = 3\pi/2. \end{array} \right.$$

The solution of the system leads to the following equation for calculation of the phase value:

$$\varphi(x) = \arctan \frac{(I_4(x) - I_2(x))}{(I_1(x) - I_3(x))} \quad (\text{eq. 5})$$

The four images ($\Delta\varphi_i = 0, \pi/2, \pi, 3\pi/2$) are comparable to a distribution of intensity $I_i(x)$ consisting of a sinusoidal signal. The displacement of the fringes formed on the object can be interpreted like a phase modulation of the fringes. This modulation can also be exploited to obtain the difference in phase φ and thus Δz .

Test procedure of the Phase Shift method. Video frames have to be extracted, for instance, with Adobe Premiere. After image processing with a Matlab™ script, it is possible to visualize the 3D-representation of the deposited mass:

- 1) calculation of the phase of the *reference signal* – lower plane (Fig. 5.46);
- 2) calculation of the phase of the *object signal* – objects of calibration (4 boards) (Fig. 5.47);
- 3) calculation of the phase of the *object signal* – granular material deposit (Fig. 5.48);
- 4) calculation of the phase difference between *reference* and *object signal* (deformation regular grid);
- 5) determination of the deposit depth, stopping distance and width.

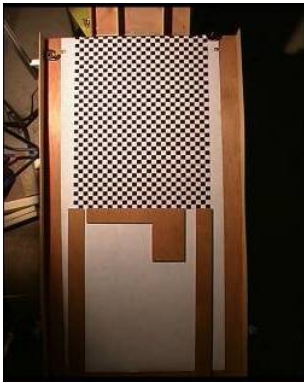


Fig. 5.45 – Reference image – Calibration in the plane (x,y), the white and black chess paper panel image.

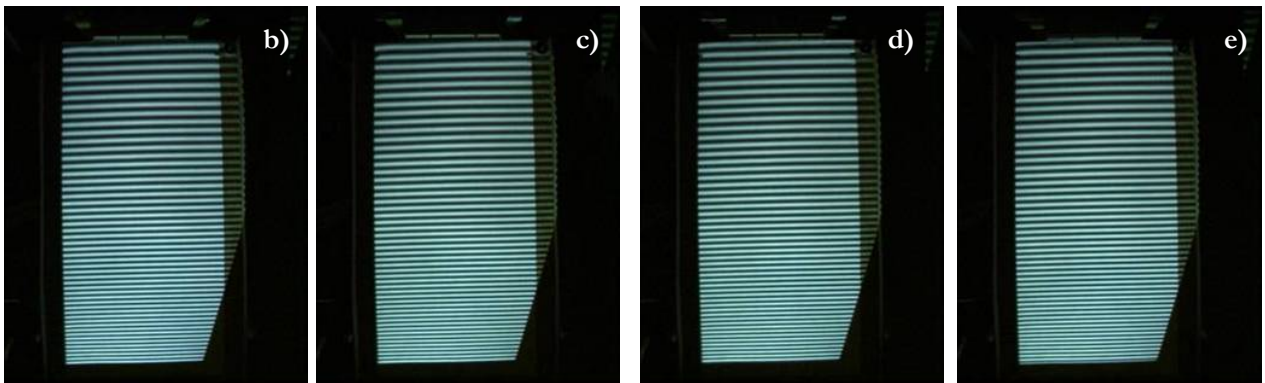


Fig. 5.46 – b), c) d) e) Reference images – Calibration along z, the lower plane images with the phase shift of $0, \pi/2, \pi, 3\pi/2$.

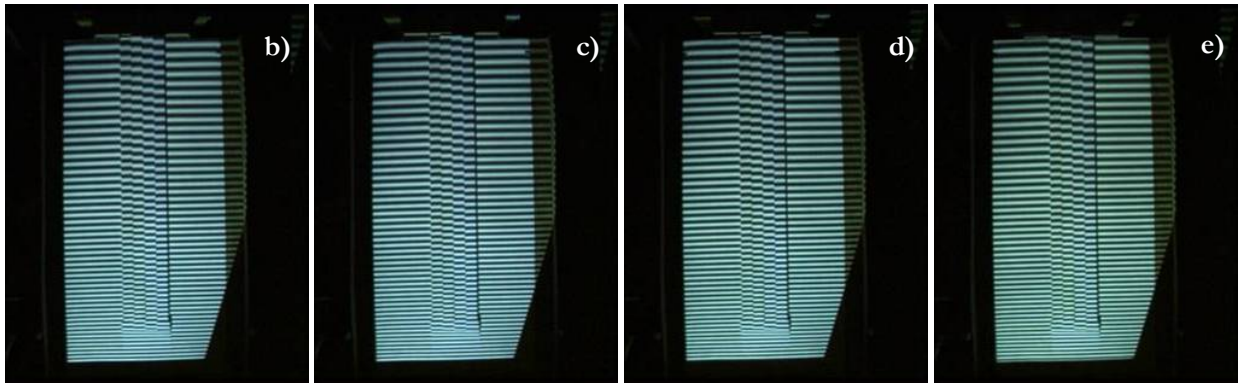


Fig. 5.47 – b), c) d) e) *Object images – Calibration along z*, images of the boards with the phase shift of $0, \pi/2, \pi, 3\pi/2$.

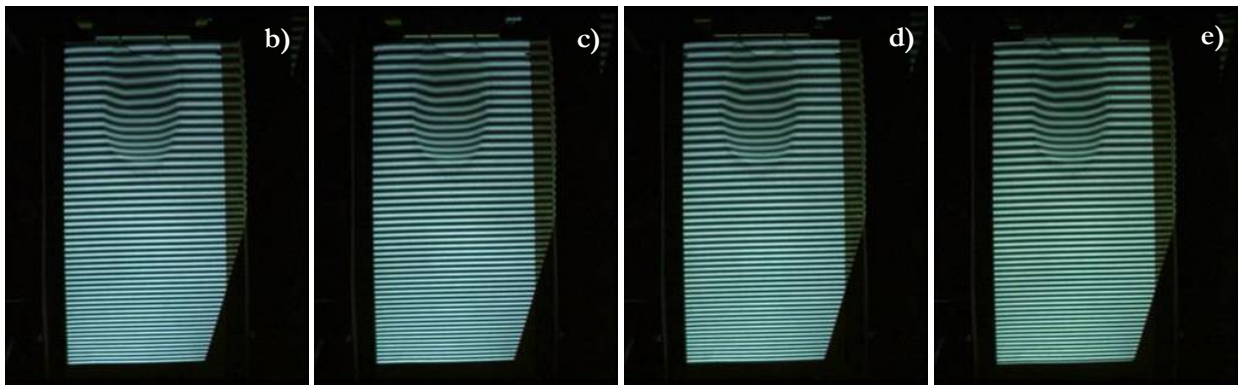


Fig. 5.48 – b), c) d) e) *Test object images*, images of the deposit with the phase shift of $0, \pi/2, \pi, 3\pi/2$.

5.7 Experimental tests

The physical parameters that have to be considered important for this study are:

- For the Laser line technique:

mean flow depth in the channel (h_c);

mean front velocity of the mixture flow in the channel (v_c);

Froude Number (F_r).

- For the Fringe analysis technique:

maximum deposit depth (h_d);

maximum deposit stopping distance (d_d);

maximum deposit width (L_d).

n°	date	Granular material composition		granular material weight	Measurements Techniques		
		glass beads I type	glass beads II type		Ruler	Laser line	Fringe Analysis Technique
							Phase Shift Method
Preliminary Tests							
01–02	08/11/07	100%	0%	10 kg	x	x	
03–05	16/11/07				x	x	
01–05	22/11/07				x	x	x
06–10	23/11/07				x	x	x
Tests – I series							
01–40	06/12/07	100–74,65%	0–25,35%	10 kg	x	x	x
41–50	07/12/07	74,00–78,15%	26,00–31,85%		x	x	x
51–101	12/12/07	67,50–35,00%	32,50–65,00%		x	x	x
Tests – II series							
102–104	12/12/07	0–20%	100–80%	10 kg	x	x	x
105–114	18/12/07	50–95%	50–5%		x	x	x

The experimental tests, conducted by using a model in reduced scale (approximately 1:100), are carried out in similarity of Froude.

5.8 Test results

- Laser line technique:

Flow depth and front velocity in the channel. The two parameters have an almost constant value until the value of the mass ratio equals 0,25, then the mean front velocity increases while the mean flow depth decreases. For a mass ratio larger than 0,35 the two parameters again present a constant behaviour (Fig. 5.49).

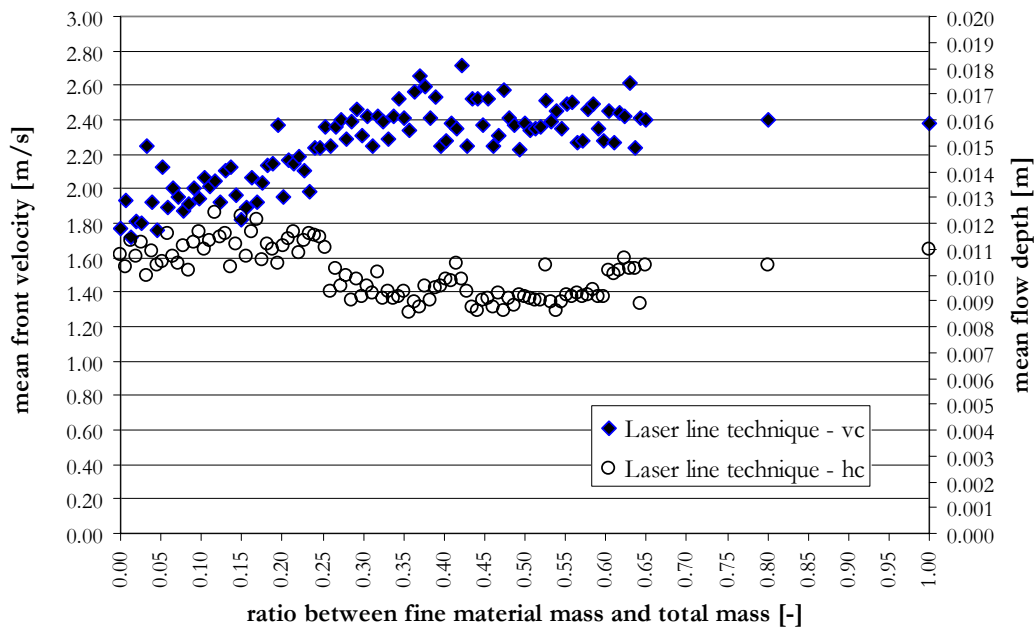


Fig. 5.49 – Effect of the mass ratio on the mean values of front velocity and of flow depth in the channel.

In the following table some values of mean front velocity and mean flow depth, for five specific tests, are presented:

mass ratio [%]	0,00	16,25	32,50	48,75	65,00
flow depth [m]	0,011	0,012	0,009	0,009	0,010
front velocity [m/s]	1,77	2,06	2,39	2,36	2,40

Froude Number. The mass ratio between the mass of the fine particles and the total mass of particles strongly influences the mean front velocity and the flow depth, and consequently the mean Froude Number in the channel. The Froude Number ranges between 6 and 10 (Table 5.5). The Froude Number presents an abrupt increment at the ratio value of roughly 0,20-0,30, then it decrease for a value of 0,60-0,70 (Fig. 5.50).

mass ratio [%]	0,00	16,25	32,50	48,75	65,00
Froude Number	6	7	9	10	8



Fig. 5.50 – Effect of the mass ratio on the values of Froude Number.

- Fringe analysis technique:

Deposit analysis: deposit depth, stopping distance and width. In the case of a mixture composed only by large glass beads (diameter 1 mm), the deposit has a rather uniform shape (Fig. 5.56).

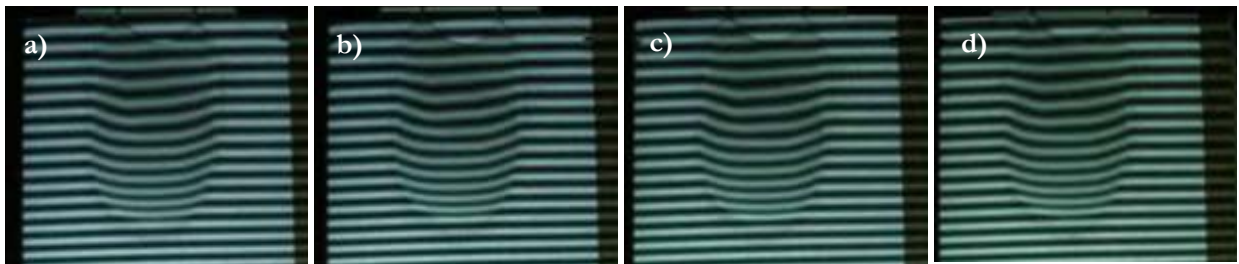


Fig. 5.51 – a), b), c), d) Images of deposit with the phase shift of $0, \pi/2, \pi, 3\pi/2$.

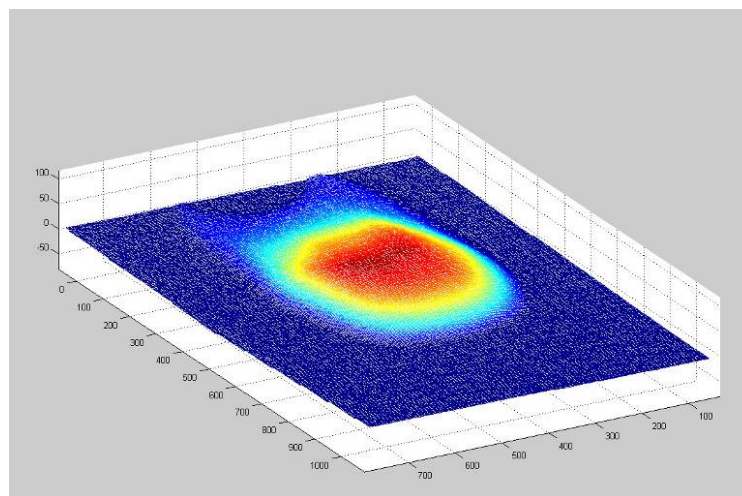


Fig. 5.52 – Example of a deposit: the colours represent the depth of the granular mass ranging from high values (red) to low values (blue) (measures in mm).

Then, by increasing the percentage of the glass beads of the II type (diameter 200 μm), there occurs a phenomenon of segregation between the glass beads of the II type and the glass beads of the I type. The large grains tend to accumulated at the top of the deposit, whereas fine grains at the bottom of the deposit.

Considering the maximum and minimal distances for different deposits, it is possible to observe two modes. In fact, initially the stopping distances increase due to a lubrication phenomenon caused by the presence of less glass beads of II type. However, when the mass ratio exceeds a certain critical point (0,25) the distances diminish until they reach the value obtained with the first test. This is due to cohesion caused by the presence, in greater quantity, of the glass beads of the II type.

It can be noticed that the deposit width remains almost constant. Its sensitivity with concern to the percentage of glass beads of II type seems to be very low (Fig. 5.53).

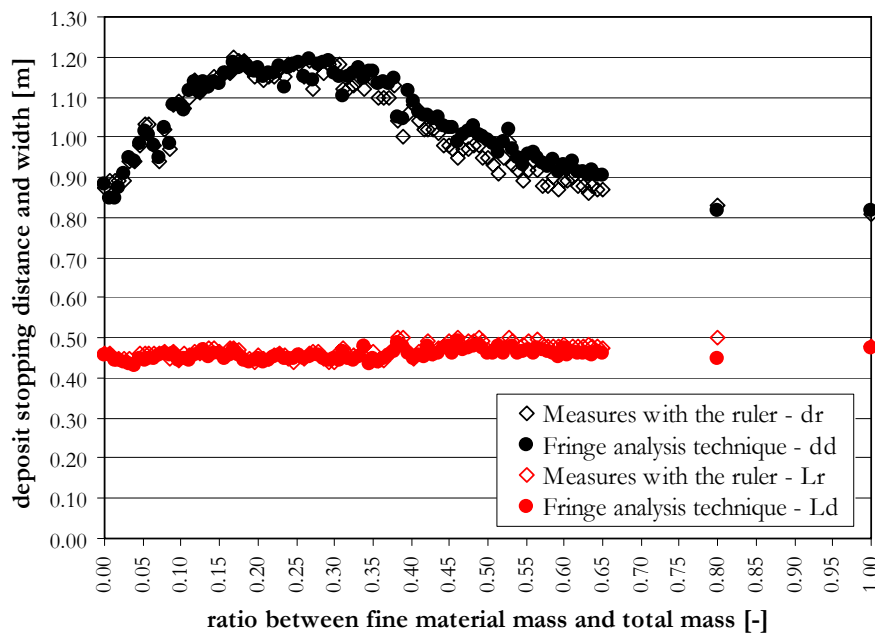


Fig. 5.53 – Effect of the mass ratio on the values of deposit stopping distance and width.

This method makes it possible to determine the 3D-shape of the deposit. The value of $h = 0$ gives the boundary of the deposit and, for instance, permits the determination of the maximum run-out distance, which is strongly influenced by the mass ratio.

Stopping distance and deposit width are also measured by a ruler, in order to make a comparison with the measurements obtained by the image processing: stopping distance is indicated with d_r and the deposit width with L_r (Fig. 5.53).

The Phase Shift method allows to measure the deposit depth (Fig. 5.55), and to define a longitudinal profile of the deposit for each test (Fig. 5.54).

The maximum deposit depth behaves in an opposite manner to that of the stopping distance. In fact, if the mixture is uniform the maximum deposit depth is the same. When the mass ratio is increased, the parameter of the deposit depth reaches a minimum value (mass ratio = 0,20-0,30) and then it increases (Fig. 5.55). Table 5.6 presents some values of maximum deposit depth, deposit stopping distance and width, for five specific tests:

Table 5.6 – Maximum values of deposit depth, stopping distance and width for a mass ratio between 0,00% to 65,00%.					
mass ratio [%]	0,00	16,25	32,50	48,75	65,00
deposit depth [m]	0,039	0,028	0,027	0,035	0,035
deposit stopping distance [m]	0,88	1,16	1,16	1,01	0,91
deposit width [m]	0,46	0,48	0,46	0,50	0,48

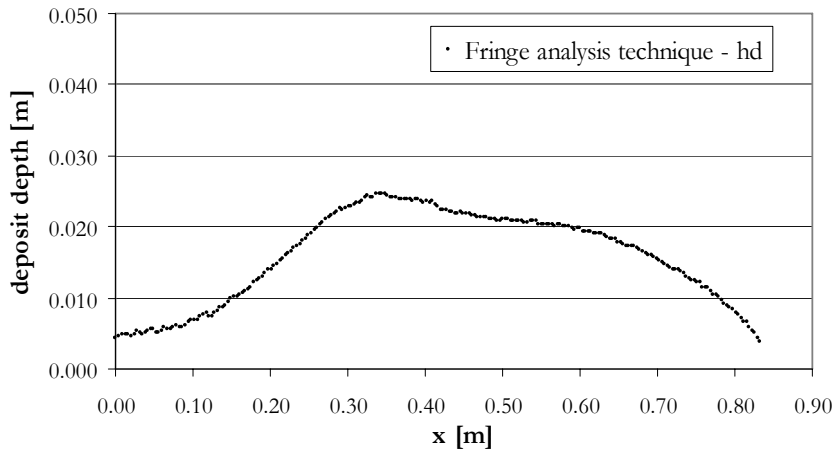


Fig. 5.54 – Example of the longitudinal profile of the deposit (mass ratio = 0,00%) [Test 08 – 23/11/07].

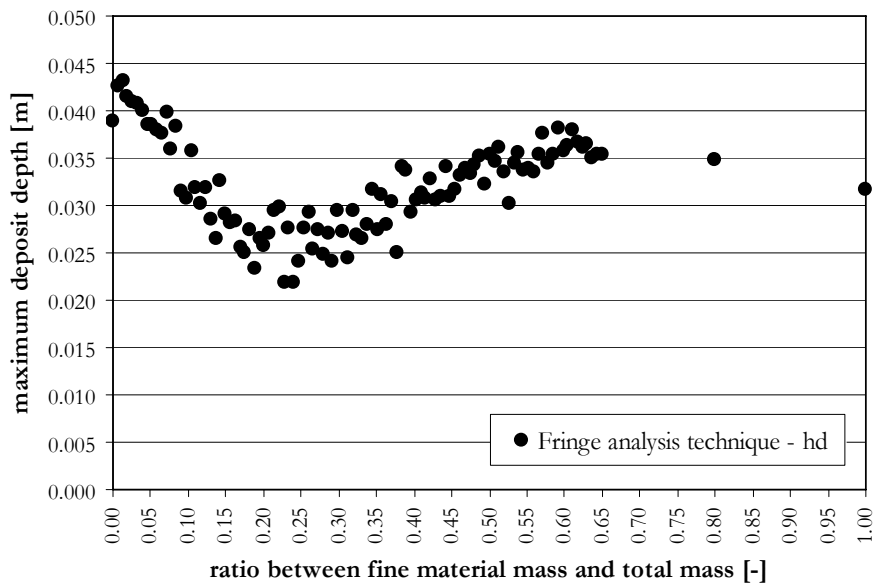


Fig. 5.55 – Effect of the mass ratio on maximum values of the deposit depth.

The mean relative error for the stopping distance is equal to 2%. The relative error is calculated as:

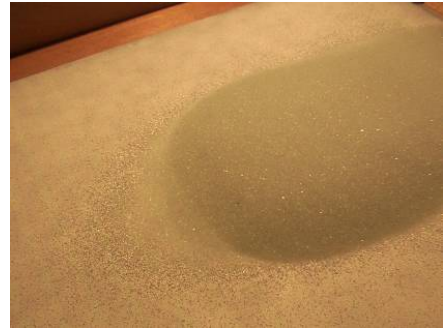
$$\varepsilon = \frac{d_d - d_r}{d_r} \times 100$$

d_d [m] maximum stopping distance (Phase Shift method);

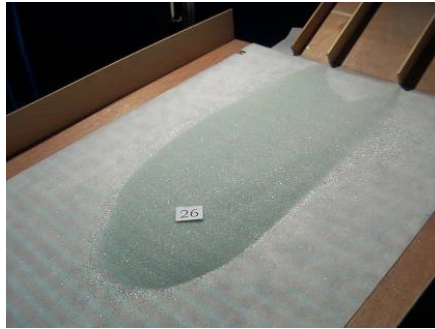
d_r [m] maximum stopping distance (ruler).

In Fig. 5.58 the deposit shapes for five specific tests are presented.

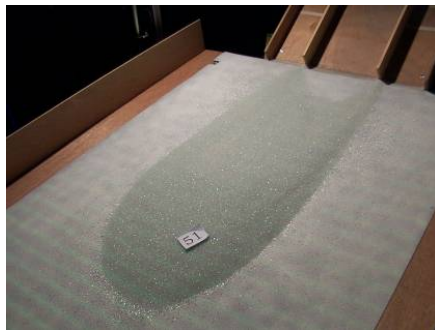
mass ratio 0,00%
[Test 01 – 06/12/07]



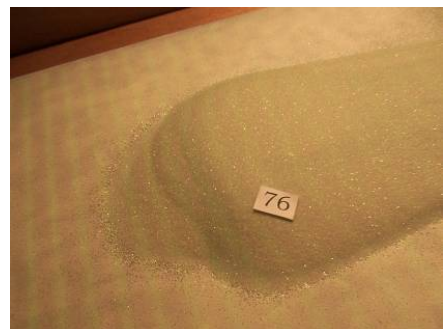
mass ratio 16,25%
[Test 26 – 06/12/07]



mass ratio 32,50%
[Test 51 – 12/12/07]



mass ratio 48,75%
[Test 76 – 12/12/07]



mass ratio 65,00%
[Test 101 – 12/12/07]



Fig. 5.56 – Deposit shapes with variation of mass ratio.

5.9 Conclusions

This study shows that the main characteristics of the deposit originated by a bi-disperse granular avalanche are strongly influenced by the ratio between the fine particles and the large particles. The deposit is either smooth or characterized by waves, depending on the initial mass ratio (Fig. 5.56).

It was observed that the maximum stopping distance was obtained with a poorly sorted material composition.

Similar results, attributed to segregation processes, were also shown in recent literature concerning laboratory tests made by Phillips et al. (2006) and numerical simulations made by Linares-Guerrero et al. (2007).

The dynamic properties of the flow along the channel were measured. The study proves that the initial mass ratio strongly influenced the flow depth and front velocities just after the release. The resulting Froude number is largely influenced by the mass ratio.

This study offers interesting research perspectives in order to develop avalanche models that take into account the effects of possible segregation inside the flowing snow (particularly due to properties of cohesion leading to poly-disperse features) [Rognon, 2006].

Chapter 6

EXPERIMENTAL ANALYSIS OF RETARDING STRUCTURES IN THE DEFENCE AGAINST DENSE SNOW AVALANCHES

The aim of this experimental analysis is that of investigating the behaviour of some types of passive defence structures used in the practice of environmental engineering to slow down granular dense snow avalanches. The research considers retarding mounds and tooth-shaped structures, taken as single elements and in a system of three elements arranged in two lines [Scotton & Moro].

This experimental analysis has been carried out at the *Laboratorio di Idraulica e Difesa del Suolo – DICA – Università di Trento*.

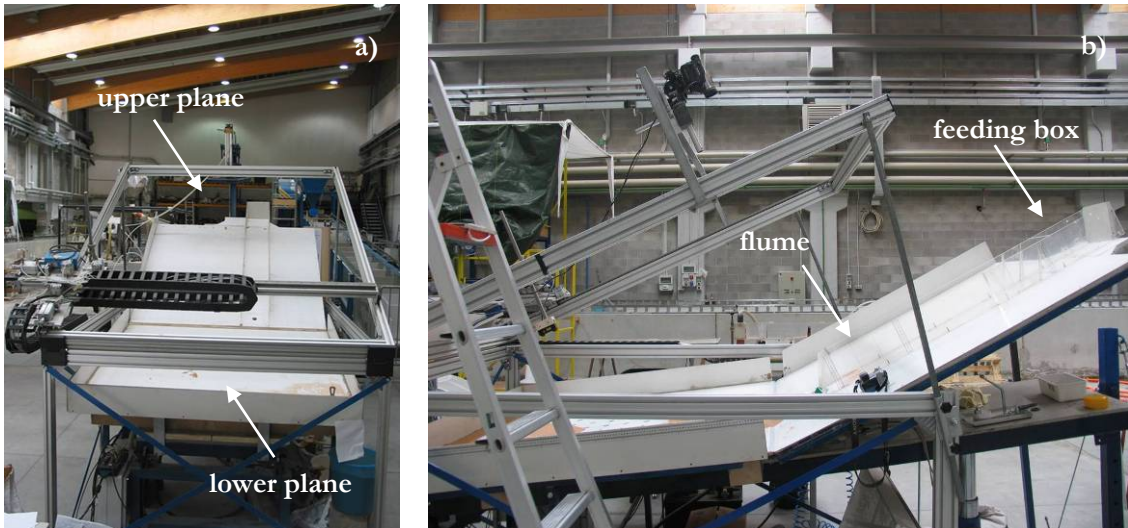
6.1 Experimental set-up

The experimental apparatus consists of two inclined planes in Forex, with an adjustable slope, connected by a narrow flexible strip (Fig. 6.1-Table 6.1). A rectangular inclined chute, 20 cm in width, with transparent 15 cm walls -in Perspex- is mounted on the upstream plane. The flume ends 20 cm upstream the change of slope. Surface continuity between the upper and the lower plane is obtained by using a thin and smooth adhesive tape (Fig. 6.3).

The granular flow is simulated by releasing a given amount of granular material down the rectangular chute from a feeding box (Fig. 6.2). The granular material is zeolite, a synthetic resin, with roughly spherical grains with a mean diameter of 1 mm. The motion spreads out of the chute and then stops on the unconfined downstream surface with a slope fixed at 7°. Some conical or wedge-shaped elements, located on the upper plane downstream the flume (just above the change of slope), slow down the motion (Fig. 6.4).

Different experiments were carried out varying the upper plane slope (24°, 27° and 30°), the mass of zeolite (3 and 7 kg) and using 1 or 3 slowing down elements. In the case of three elements, these were distributed at the vertices of an isosceles triangle, symmetrical with respect to the axis of the chute. The angle θ at the upper vertex was modulated to verify the efficiency of the apparatus with different geometrical arrangements.

feeding box	maximum volume	9 litres
upper plane	inclination	24°
		27°
		30°
flume	Length	1,50 m
	Width	1,50 m
	lateral height	0,15 m
lower plane	inclination	7°
	Length	1,50 m
	Width	1,50 m



**Fig. 6.1 – a) On the left, a view of the flume and its support structure;
b) on the right, a lateral view of the experiment set-up.**



Fig. 6.2 – The feeding box.

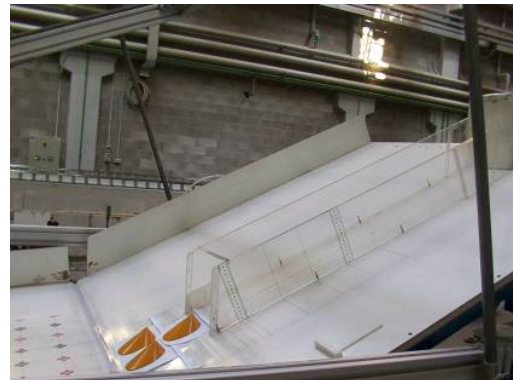


Fig. 6.3 – The flume.



Fig. 6.4 – Two views of the lower plane.

Experimental set-up scheme. In Fig. 6.5-Fig. 6.6 a lateral and vertical view of the experimental set-up are presented.

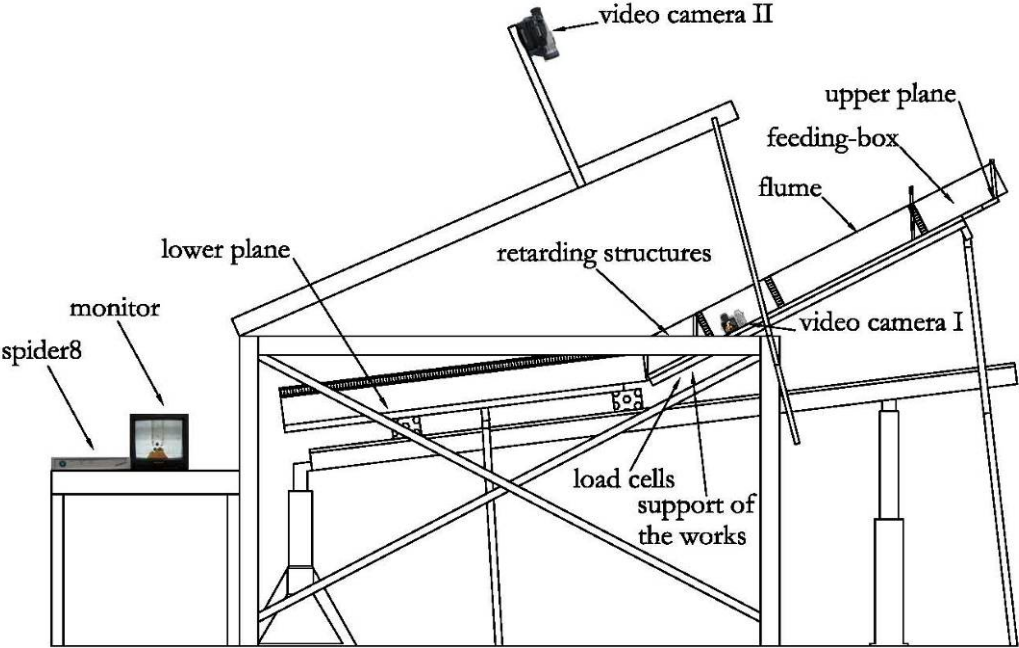


Fig. 6.5 – Lateral view of the experimental set-up.

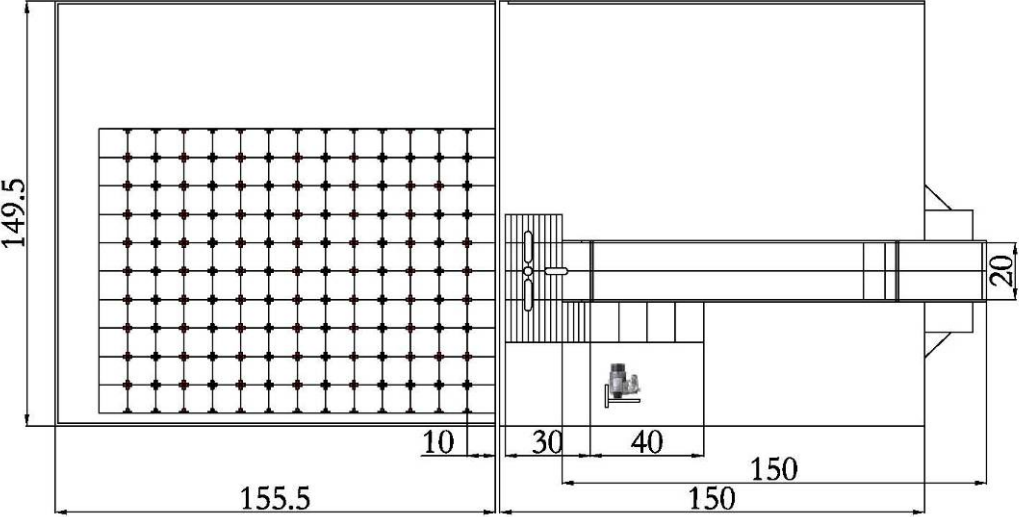


Fig. 6.6 – Vertical view of the experimental set-up (measures in cm).

6.2 Instrumentation

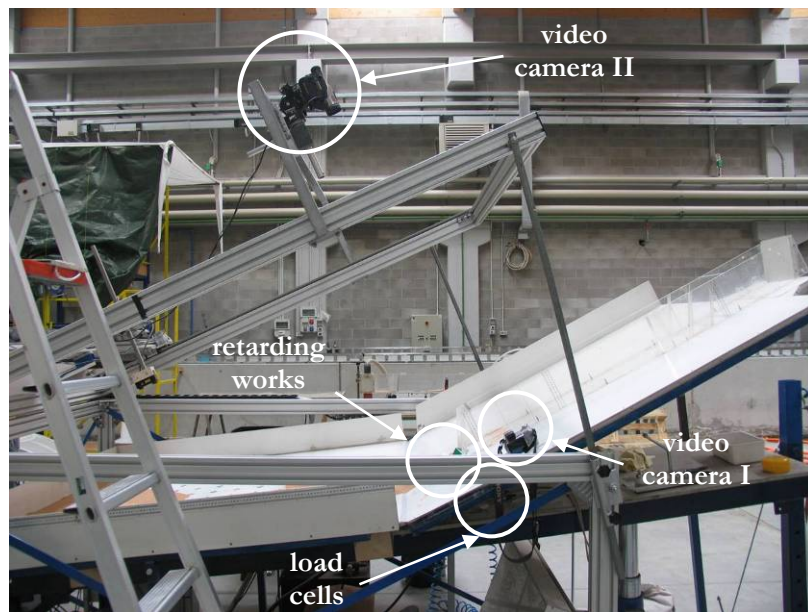


Fig. 6.7 – The instrumentation in the channel and on the lower plane.

The instrumentation was composed by (Fig. 6.7):

- For the description of the deposit shape in the feeding box:

A video camera (video camera I) (Fig. 6.8) was used to take an image of the material in the feeding box (Fig. 6.9).



Fig. 6.8 – The video camera I.
Model: Sony Cyber-shot DSCH1 5.1 MP;
zoom: 12x “Steady Shot” Zoom;
acquisition time: $1/25 \text{ s} = 0,04 \text{ s}$.



Fig. 6.9 – a) On the left, the feeding box with 3 kg of granular material;
b) on the right, the feeding box with 7 kg of granular material.

- For the measuring of the impact force:

- 1) Two load cells of different type (Fig. 6.10-Fig. 6.12) were used to perform the laboratory experiments. They were used to measure the impact force against the retarding frontal structure and against one of the rear works.



Fig. 6.10 – The load cell I – impact force on the rear structure (channel CH3 of the Spider8).

Model: FUTEK MODEL L1510
protected load cell;
capacity: 2 lb – 8,9 N;
sensitivity: 0,0004 lb – 0,181 g;
response time: 0,005 s.

Fig. 6.11 – The load cell II – impact force on the front structure (channel CH0 of the Spider8).

Model: FUTEK MODEL L1501
non-protected load cell;
capacity: 1 lb – 4,5 N;
sensitivity: 0,002 lb – 0,906 g;
response time: 0,005 s.

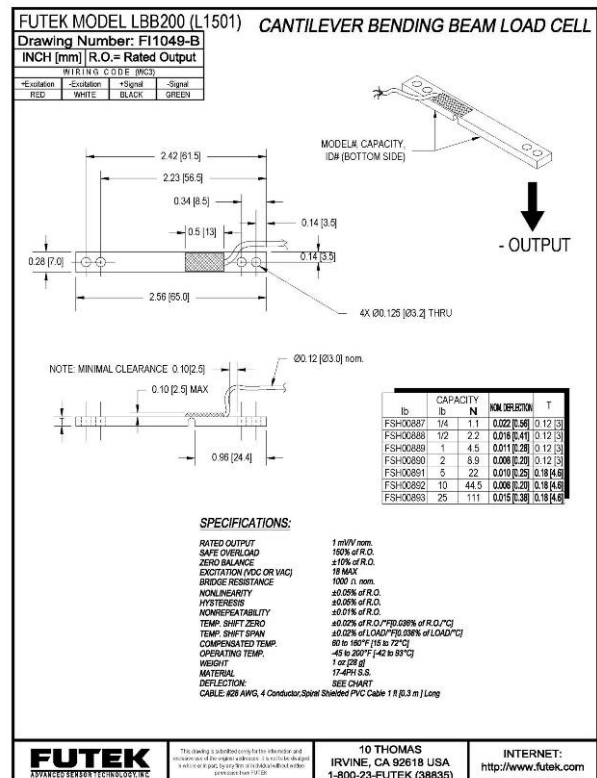
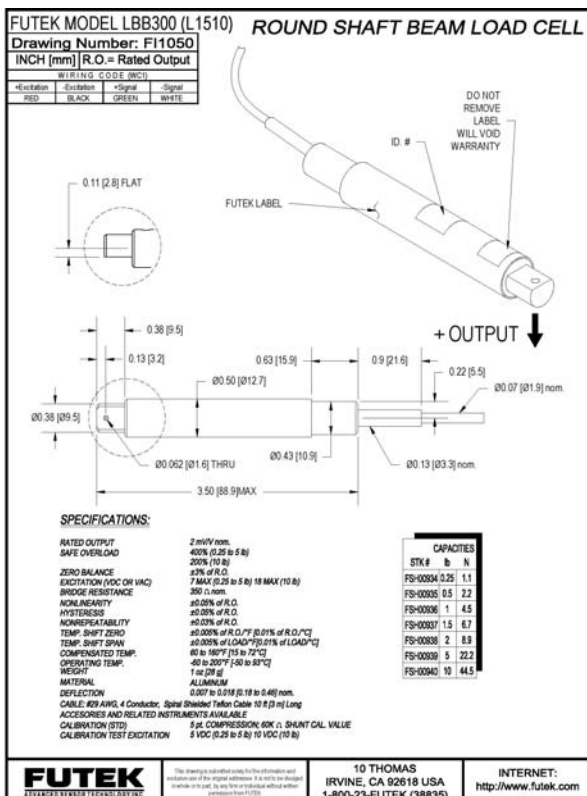


Fig. 6.12 – The technical sheets of the load cells.



Fig. 6.13 – a) On the left, the protected load cell installed on the support under the upper plane that measured the impact force against the rear structure; b) on the right, the non-protected load cell that measured the impact force against the front structure.

2) The acquisition system -Spider8- is an electronic measuring system -run by PC- for the electric measuring of mechanical variables such as strain, force, pressure, path, acceleration and temperatures (Fig. 6.14-Fig. 6.15). The entire signal conditioning -excitation for passive transducers and amplification, digitalization, computer interface and connection technology for a maximum of 8 channels- is combined in one housing. Spider8 is connected to the computer via the printer port or via an RS232 interface (Fig. 6.16).



Fig. 6.14 – The acquisition data system.
Model: Spider 8 – HBM;
4 carrier-frequency channels:
CH1, CH2 not utilised in the experiments;
CH0, CH3 utilised by the acquisition data system.

Specifications					
Series	Spider8 / SR85	Spider8-30 / SR30	Spider8-01 / SR01		
Accuracy class	0.1				
Digital resolution in the case of final value of the measuring range	Digit	± 25000			
Measured value buffer	Meas	< 20000			
Transfer rate:	serial	Baud	600, 1200, 2400, 4800, 9600, 19200, 38400, 57600		
	parallel ¹⁾	Nibble mode	Meas/s	> 6200	
		8Bit mode	Meas/s	> 19000	
	USB	Byte mode (two-way)	Meas/s	> 24000	
		EPP mode	Meas/s	> 76000	
	view data sheet USB	-			
Sampling rate (21 levels per channel)	1/s	1...9600			
Digital filter	asapodic	Hz	0.1		
	Average value	Hz	Sampling rate/8 to sampling rate/4		
	Butterworth (4th order)	Hz	0.1...1200	0.1...200	0.1...1200
	Bessel (4th order)	Hz	0.1...1200	0.1...200	0.1...1200
Number of amplifiers		4/1	4/1	4/1	
Transducers that can be connected		Strain gauge and inc. full bridge/half bridge	SIG full bridge / half bridge/ quarter bridge		
			DC voltage sources		
			DC power sources Resistors Thermocouples		
Channel 0 ²⁾ and 1 ³⁾ in addition		Pulse/frequency	2-phase sensor		
Transducer current supply	mA	-			
Transducer excitation voltage	V _{max}	2.5			
Carrier frequency (one / symmetric)	Hz	4800	600	-	
Transducer resistance	Ω	110...1160	-		
Compensation resistors	Ω	-	120, 500, 700	-	
Shunt calibration signal	mV/V	-	1	-	
Transducer cable length up to	m	50	200	50	
Dimensions (W x H x D) housing	mm	330 x 76 x 270			
Measuring ranges	Strain gauge / ind. transducer	mV/V	± 8; ± 12; ± 120; ± 500		
	Voltage	V	± 10	± 0.1; ± 1; ± 10	
	max. differential input voltage	V	± 10	± 15	
	max. permissible common-mode voltage (differential voltage input-ground)	V	± 10	50	
	input resistance	MΩ	0.25	1	
	Current	mA	-	± 20; ± 200	
	Resistance	Ω	-	400; 4000	
	Frequency ²⁾	kHz	0.1; 1; 10; 100; 1000	-	-
	Period length ²⁾	s	0.01; 0.1; 1; 10; 100	-	-
	Counter ³⁾	s	25,000; 2,500,000%	-	-

¹⁾ Depends on the computing power and hardware of the PC.
²⁾ Only for the Spider8 basis device (channels 0 and 1).
³⁾ Transmission format: counter/100

Series	Spider8 / SR85	Spider8-30 / SR30	Spider8-01/SR01
Linearity variation in relation to nominal value	%		
Influence of temperature per 10K in nominal temperature range in relation to zero point (in relation to nominal value)	%		
sensitivity (in relation to nominal value)	0.1	0.1	0.2
Nominal temperature range	°C		
Operating temperature range	°C		
Storage temperature range	°C		
Supply voltage	V		
Power consumption	W	4 / 0.25	8.2 / 0.8
Dimensions (W x H x D) Housing	mm		
Weight	kg		
Connections			
Transducer	DB-15 socket	DB-15 socket	SUBCON 5-pin socket
Digital I/O		DB-25 socket	
RS-232 computer interface		DB-9 socket	
Printer port		DB-25 socket	
PC interface		DB-25 socket	

Fig. 6.15 – The technical sheets of the acquisition data system.

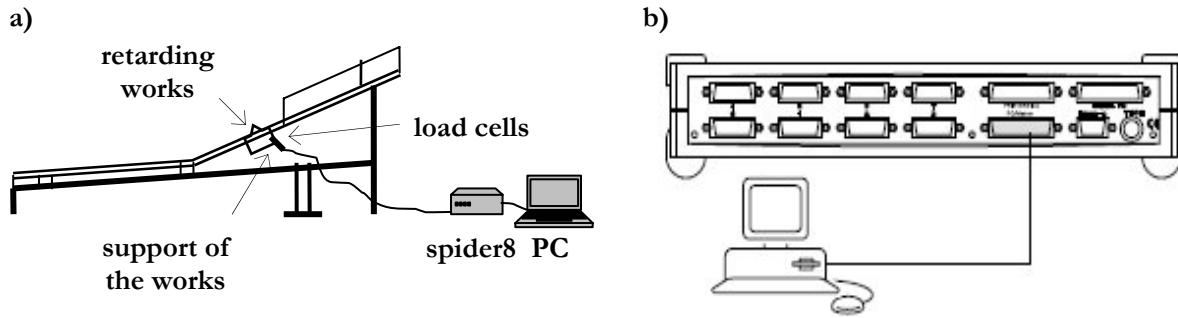


Fig. 6.16 – a) On the left, a scheme of the acquisition system; b) on the right, posterior view of the Spider8 connected with the PC.

All the required settings were made using PC commands - there were no potentiometers, switches, solder bridges or jumpers.

The device type contains 4 complete digital amplifiers in 4.8 kHz carrier-frequency technology for S/G or inductive transducers with channel numbers 0 to 3, and channels 4 to 7 are closed off with blank plates (CH0, CH1, CH2, CH3).

A channel for all of the 4 available load cells was used, and during the carrying out of the different tests, these were left always connected to maintain the configuration constant.

To configure the system, a specific software was used -Catman professional 4.5 – HBM- that automatically recognizes the amplifiers, configures the channels, makes defining the operational parameters possible (type of connected apparatus, frequency of sampling, filter, etc.). It acquires and saves the measuring data.

- For the measuring of the flow depth at the measuring section:

A video camera (video camera I) (Fig. 6.17) was located laterally to the final part of the channel in order to shoot the maximum flowing depth of the mixture at a section very near to the works - roughly 10 cm before the retarding works (Fig. 6.18).



Fig. 6.17 – The video camera I.
 Model: Sony Cyber-shot DSCH1 5.1 MP;
 zoom: 12x “Steady Shot” Zoom;
 acquisition time: $1/25 \text{ s} = 0,04 \text{ s}$.



Fig. 6.18 – The measuring section of the tests.
 The measuring section is fixed at 108 cm from the feeding box (section 0 cm).

- For the measuring of the front velocity in the channel:

A video camera (video camera II) (Fig.6.19-Fig. 6.20) was located above the upper plane. It was used to cover the area between the end of the channel and the slowing down elements. The velocity in the description of the tests is the mean velocity of the flowing mass front in the last 20 cm before the impact against the retarding structures.



Fig. 6.19 – The video camera II
Model: Panasonic Digital 3CCD NV-MX300EG;
Acquisition time: 0,04 s.



Fig. 6.20 – The monitor.
Model: Panasonic BTS1050.

- For the measuring of the stopping distance, deposit width and shape:

A photo camera (Fig. 6.21) was located above the lower plane. It was used to take the image of the deposit at the end of each test (Fig. 6.22).



Fig. 6.21 – The photo camera.
Model: Canon PowerShot Pro1 8.0 MP;
zoom: 7x Optical Zoom;
acquisition time : 0,04 s.

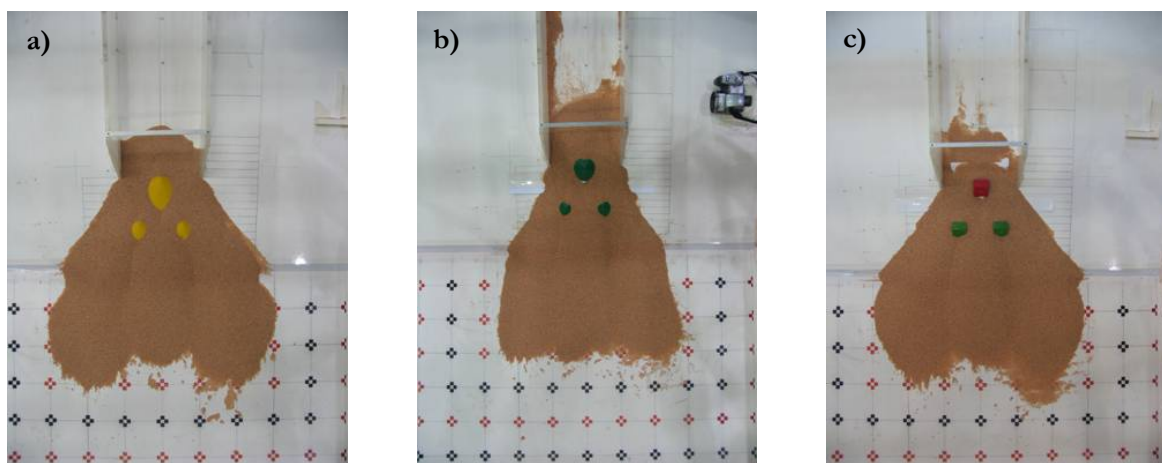


Fig. 6.22 – examples of deposits with different types of retarding structures:
a) elliptical cone-shaped structures; b) tooth-shaped structures;
c) circular cone-shaped structures.

6.3 The retarding structures

Various types of slowing down elements were used to simulate structures which are in use (Fig. 6.23).

A first series of tests were conducted using wooden cones with a height of 3,0 cm and a base diameter of 3,0 cm, and vertical elements -walls or tooth-shaped structures -also made of wood-with a height of 3,0 cm and a width of 4,5 cm.

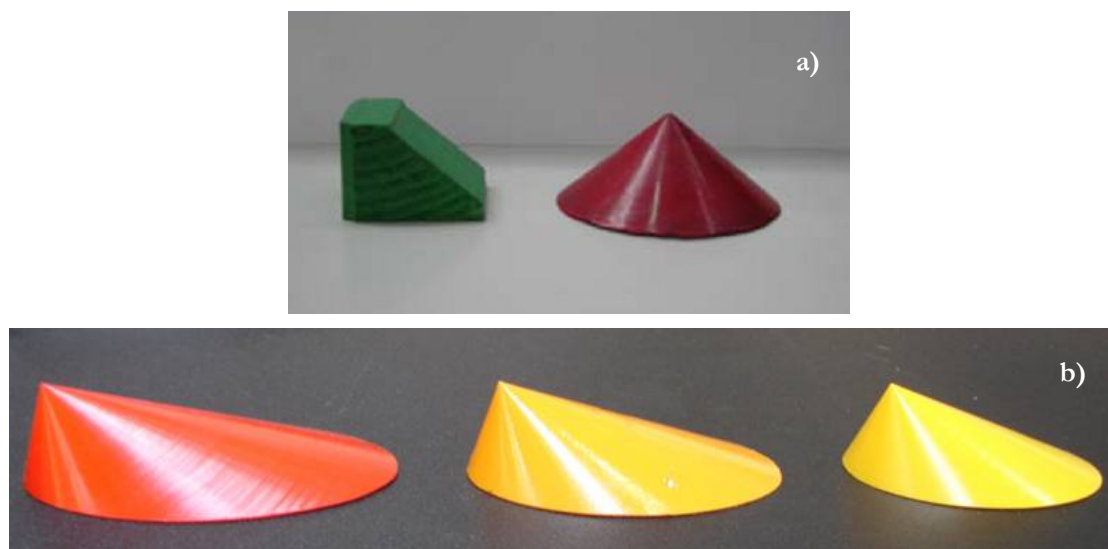


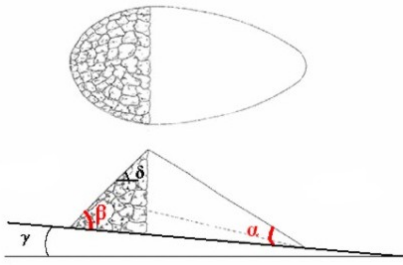
Fig. 6.23 – The retarding structures used in the experiments:
a) above, the tooth-shaped structure and the circular cone-shaped structures;
b) below, three elliptical cone-shaped structures used, respectively,
at inclinations of 30°, 27° and 24°.

In a following series of tests three cone-shaped elements were also tested. They were realized taking into account that real structures present an angle on the upstream face of about 40°. Their height was 3,0 cm and their inclination depended on the slope of the upstream plane (Table 6.2). The weight of the elements ranged from 20 g to 30 g, in order to reduce inertial effects as much as possible. For this purpose the nylon elements (cone shaped elements) were lightened by removing the inner volume.

type of works	upper plane tilting	height	length/ diameter	width/ diameter	lateral inclination
		H	L	B	θ
elliptical base cones	30°	3,0 cm	12,0 cm	8,3 cm	36°
	27°		10,2 cm	7,8 cm	38°
	24°		9,0 cm	7,5 cm	39°
circular base cones	-		7,3 cm	7,3 cm	39°
teeth	-		4,5 cm	3,8 cm	90°

The inclination of a real mound depends on the slope where they are realized and the internal friction angle of the used material. During the experiments three different inclinations of the upper plane were considered: 24°, 27° and 30°.

a)



b)

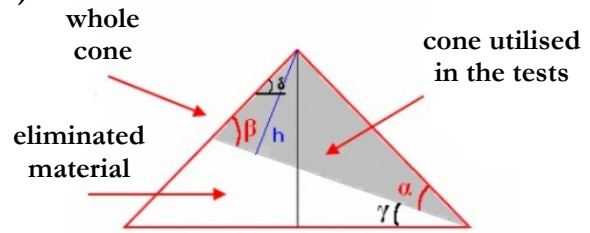


Fig. 6.24 – a) On the left, a vertical and lateral view of a mound, carried out in many valleys of the *Trentino Alto Adige* region (Italy); b) on the right, scheme of the nylon isosceles cone. The grey coloured part represents the mound model that was used for the experiments.

To determine the final dimensions of the elliptical base cones, a height of 30 cm was fixed. The dimensions of the three cones are reported in Fig. 6.24 and Fig. 6.25.

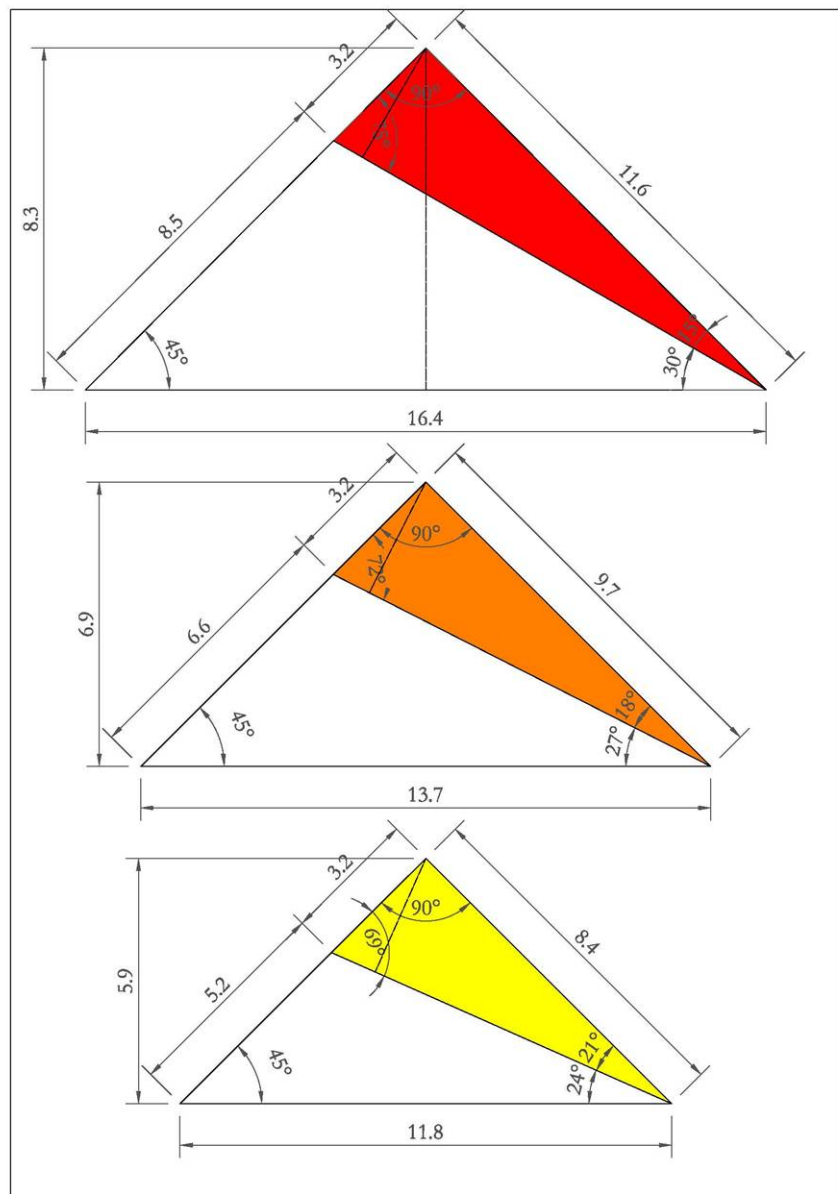


Fig. 6.25 – Elliptical base cones (measures in cm).

The schemes of the retarding structures. In Fig. 6.26-Fig. 6.30 different views of all retarding structures are presented.

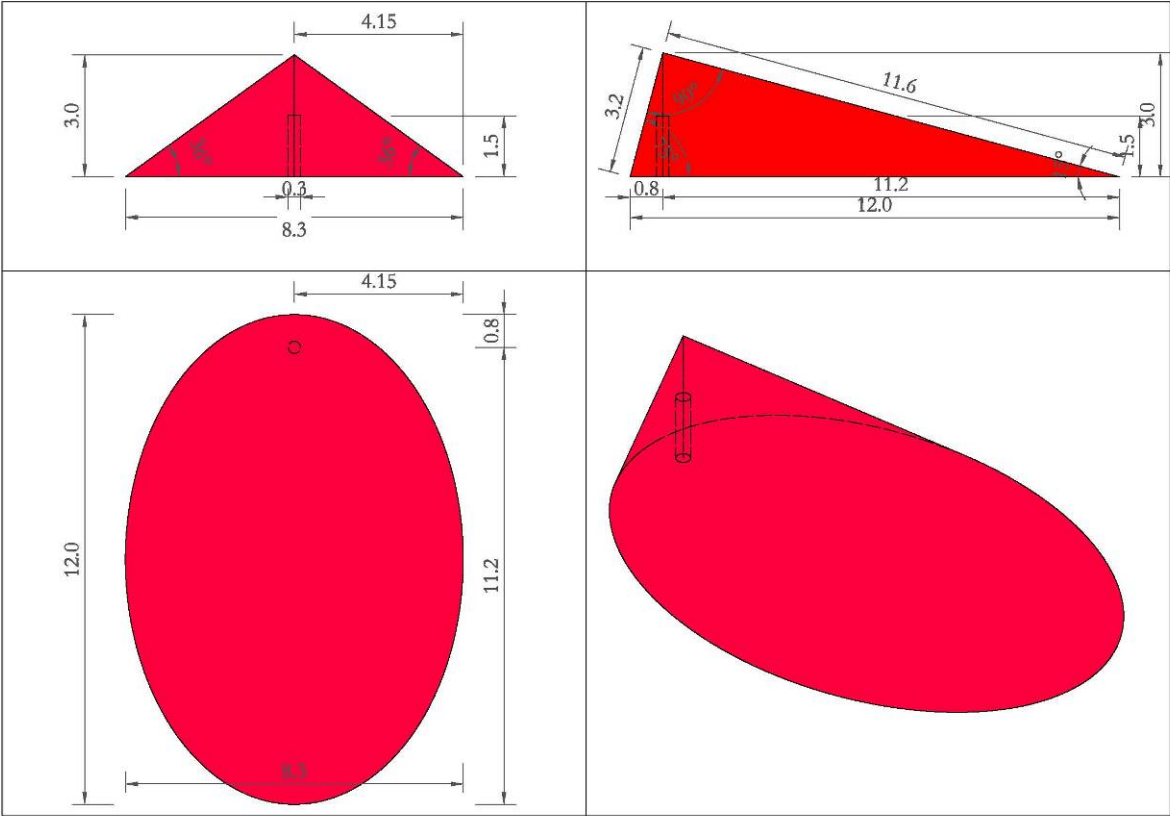


Fig. 6.26 – Elliptical base cones – 30° (measures in cm).

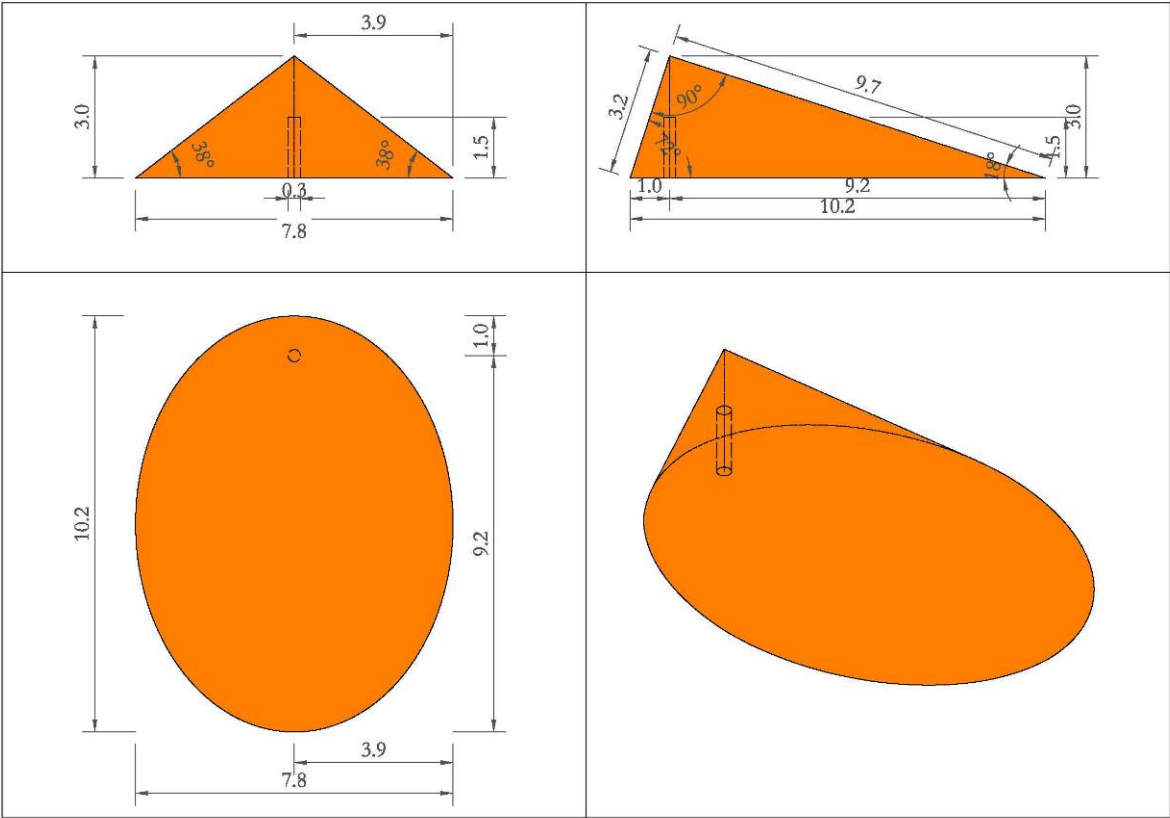


Fig. 6.27 – Elliptical base cones – 27° (measures in cm).

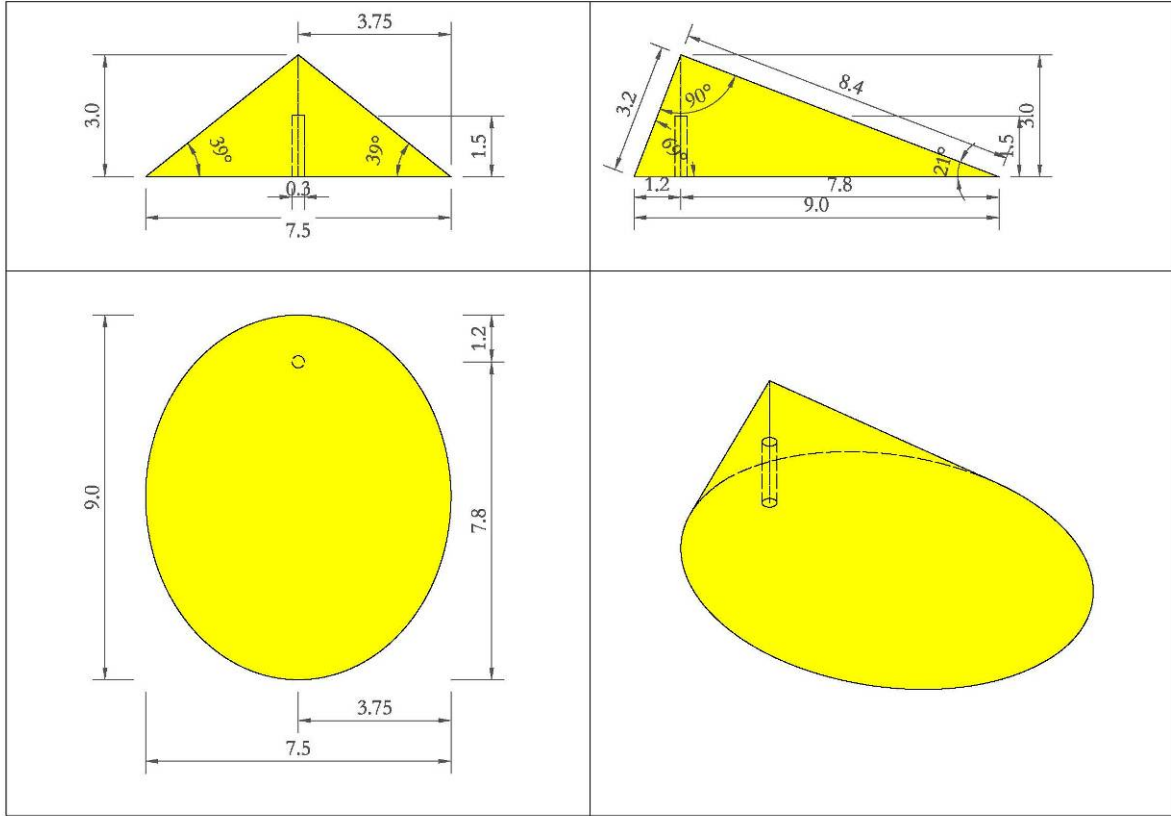


Fig. 6.28 – Elliptical base cones – 24° (measures in cm).

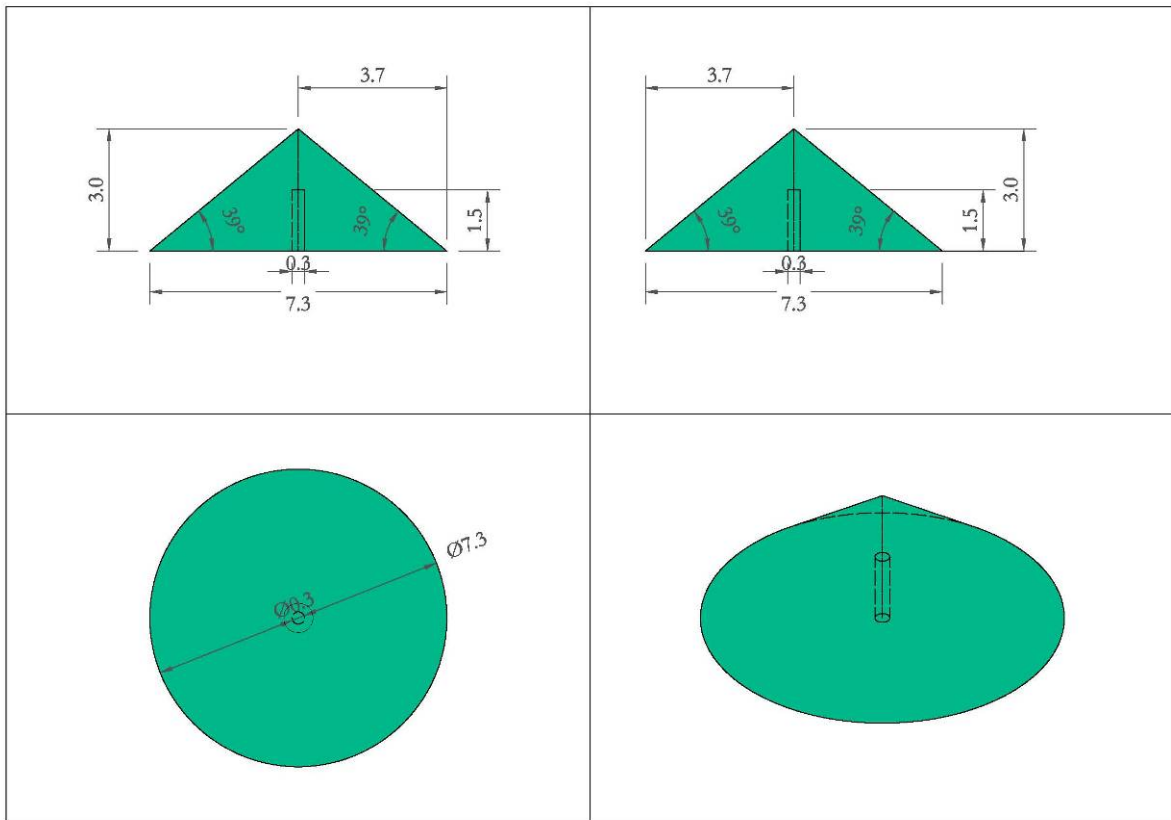


Fig. 6.29 – Circular base cones (measures in cm).

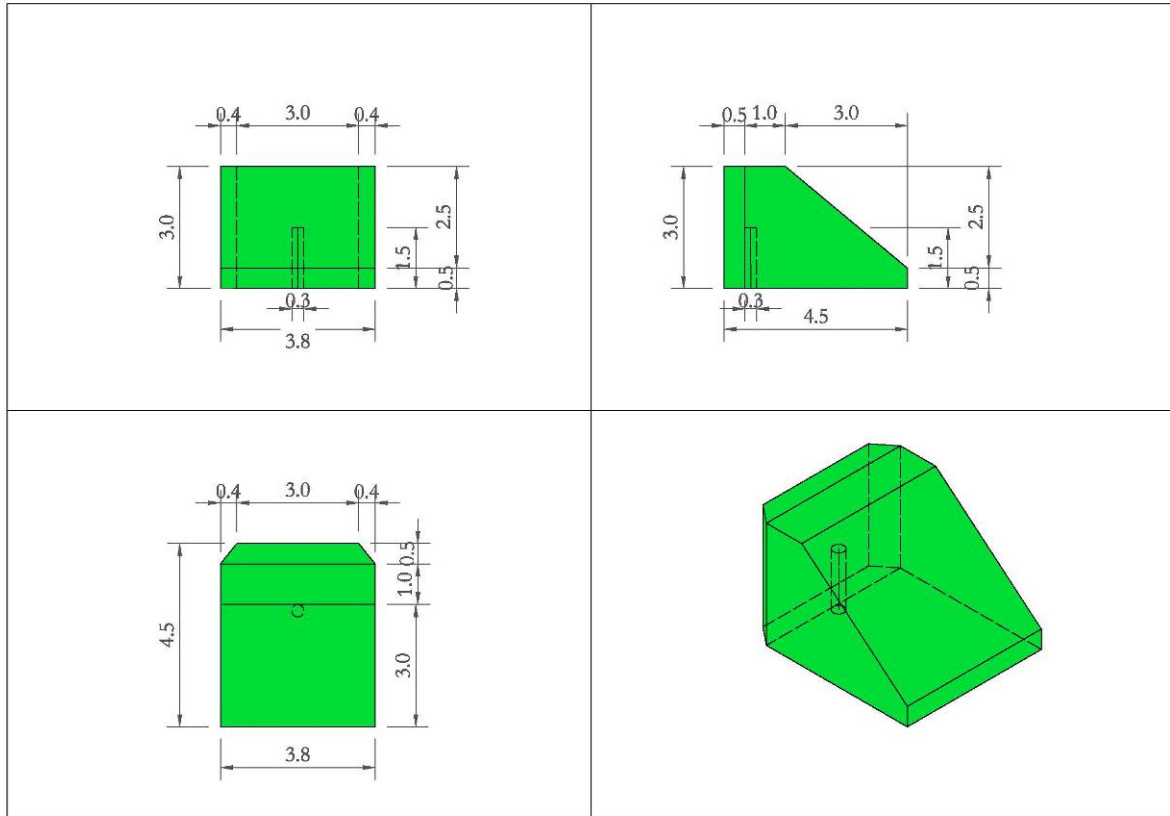


Fig. 6.30 – Tooth-shaped structures (measures in cm).

6.4 The support of the retarding elements

The single slowing down element (cone or tooth-shaped) is mounted on a T-shaped support - a linear low-friction sliding mechanism. The force exerted on the element is transmitted to the load cell mounted on the T-shaped support. No moment of the force results transmitted. All the slowing down elements (a maximum number of three) are mounted onto a support plate which is placed below the upper plane. The mechanical system is composed by:

- 1) the T-shaped support used to transfer the force acting on the retarding element (Fig. 6.31-Fig. 6.32). It is composed of a linear guide (model SN22-40-130-200) on which the retarding structure is positioned and with this system the impact force received by the retarding mound is transmitted to the load cell and recorded by the acquisition system (Fig. 6.33-Fig. 6.34);

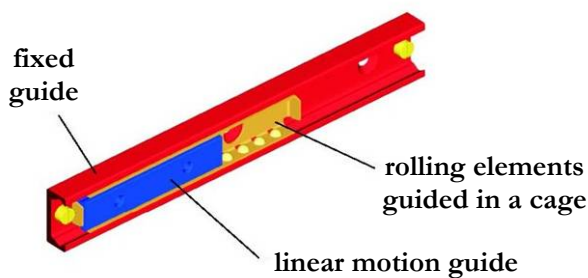


Fig. 6.31 – The linear guide.

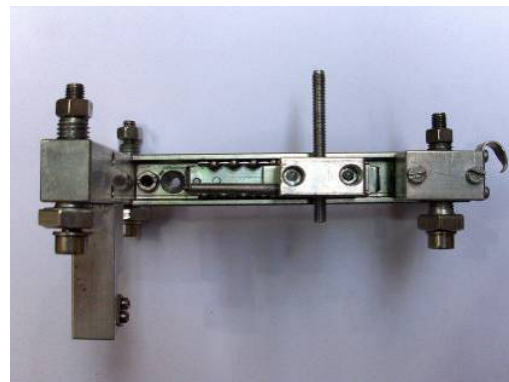


Fig. 6.32 – The T-shaped support.

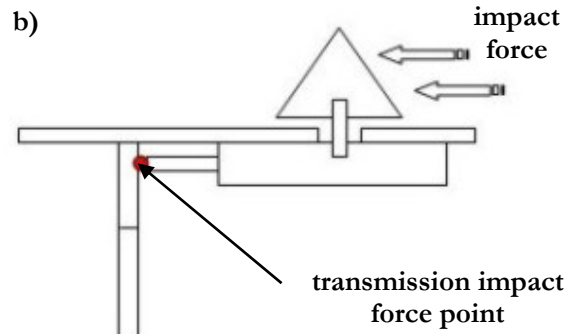
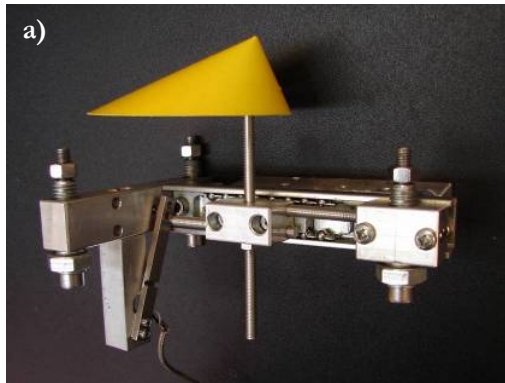


Fig. 6.33 – a) On the left, one of the T-shaped supports with a sample of a retarding structure; b) on the right, scheme of the transmission of impact force to the load cell.

DATI TECNICI

L'opportuno accoppiamento tra le diverse lunghezze di cursori e guida (vedi Regole "chiave"), rende possibile l'ottenimento di una gamma più che completa di corse realizzabili (per i codici di ordinazione, vedi pag. D6, per le configurazioni standard vedi pag. D10 - D11).

K/2 Corsore mobile "S" Corsa "H" (L-S-K) K/2

REGOLE "CHIAVE":

- Per garantire l'accesso a tutti i fori di fissaggio, è necessario verificare la seguente relazione: $S \leq L/2 - K$ (tutti i valori di S, L e K sono indicati nelle tabelle successive).
- Ricordare che: $H = L - S - K$, che equivale a dire: $L = S + H + K$ (la lunghezza della guida L è quindi da intendersi sempre come la somma della lunghezza del cursore S, più il valore della corsa H e quello della costante K).
- Per ottenere sempre la massima qualità di scorrimento è necessario che sia verificata anche la seguente relazione:
H \leq 7S. Per cui, la corsa H non deve mai essere superiore al 70% della lunghezza del cursore S.

• SERIE "SN22"

Esempio di Corsore d'Ordinazione:
- Corsore mobile S 210 mm
- Corsa (spazza) H 610 mm
Il codice completo sarà: **SN22-210-610-450** (vedi pag. D6 per la "costruzione" del codice).

Corsore mobile			Capacità di carico						Pesa (cursori mobile)
S [mm]	a [mm]	N. fori	C _{cur} [N]	M ₁ [Nmm]	M ₂ [Nmm]	M ₃ [Nmm]	M ₄ [Nmm]		
40	10	20	2	1320	924	8	6	9	
60	10	20	3	1980	1386	12	14	20	
80	10	20	4	2640	1848	16	25	35	
100	10	20	5	3300	2310	20	35	50	
130	25	80	2	4200	2913	28	65	63	
210	25	80	3	6300	4369	42	110	243	
290	25	80	4	8400	5826	56	165	426	

Guida fissa				Capacità di carico				Pesa (guide fissa)
L [mm]	m [mm]	n [mm]	N. fori	C _{cur} [N]	M ₁ [Nmm]	M ₂ [Nmm]	M ₃ [Nmm]	
130	25	80	2	690	25	80	9	30
210	25	80	3	770	25	80	10	30
290	25	80	4	850	25	80	11	30
370	25	80	5	930	25	80	12	30
450	25	80	6	1010	25	80	13	30
530	25	80	7	1110	25	80	15	30
610	25	80	8	1170	25	80	15	30

• SERIE "SN28"

Corsore mobile			Capacità di carico						Pesa (cursori mobile)
S [mm]	a [mm]	N. fori	C _{cur} [N]	M ₁ [Nmm]	M ₂ [Nmm]	M ₃ [Nmm]	M ₄ [Nmm]		
60	10	20	3	2460	2436	28	24	35	
80	10	20	4	3280	3248	38	43	62	
130	25	80	2	7540	5278	61	114	183	
210	25	80	3	12180	8626	98	208	428	
290	25	80	4	16820	11974	136	369	813	
370	25	80	5	21460	15322	174	528	1323	
450	25	80	6	26100	18670	211	730	1958	

Guida fissa				Capacità di carico				Pesa (guide fissa)
L [mm]	m [mm]	n [mm]	N. fori	C _{cur} [N]	M ₁ [Nmm]	M ₂ [Nmm]	M ₃ [Nmm]	
130	25	80	2	770	25	80	10	40
210	25	80	3	850	25	80	11	40
290	25	80	4	930	25	80	12	40
370	25	80	5	1010	25	80	13	40
450	25	80	6	1110	25	80	15	40
530	25	80	7	1170	25	80	17	40
610	25	80	8	1190	25	80	19	40
690	25	80	9	1250	25	80	21	40

PRESTAZIONI GENERALI

• SERIE "SN22"

Capacità di carico			Capacità di carico		
Lunghezza Corsore [mm]	C _{cur} [N]	M ₁ [Nmm]	M ₂ [Nmm]	M ₃ [Nmm]	M ₄ [Nmm]
40	1320	924	8	6	9
60	1980	1386	12	14	20
80	2640	1848	16	25	35
100	3300	2310	20	35	50

Lunghezza Guida [mm]: 130, 210, 290, 370, 450, 530, 610, 690, 770, 850, 930, 1010, 1170

• SERIE "SN28"

Capacità di carico			Capacità di carico		
Lunghezza Corsore [mm]	C _{cur} [N]	M ₁ [Nmm]	M ₂ [Nmm]	M ₃ [Nmm]	M ₄ [Nmm]
60	2460	2436	28	24	35
80	3280	3248	38	43	62
130	7540	5278	61	114	183
210	12180	8626	98	208	428
290	16820	11974	136	369	813
370	21460	15322	174	528	1323
450	26100	18670	211	730	1958

Lunghezza Guida [mm]: 130, 210, 290, 370, 450, 530, 610, 690, 770, 850, 930, 1010, 1170, 1330, 1490, 1650

• SERIE "SN35"

Capacità di carico			Capacità di carico		
Lunghezza Corsore [mm]	C _{cur} [N]	M ₁ [Nmm]	M ₂ [Nmm]	M ₃ [Nmm]	M ₄ [Nmm]
130	3750	8826	95	148	211
210	15750	11025	153	368	581
290	21750	15225	211	739	1051
370	27750	19425	269	1108	1711

Lunghezza Guida [mm]: 290, 370, 450, 530, 610, 690, 770, 850, 930, 1010, 1170, 1330, 1490, 1650, 1810

• SERIE "SN43"

Capacità di carico			Capacità di carico		
Lunghezza Corsore [mm]	C _{cur} [N]	M ₁ [Nmm]	M ₂ [Nmm]	M ₃ [Nmm]	M ₄ [Nmm]
130	13910	3737	172	211	301
210	22470	15729	278	351	788
290	31030	21721	383	1050	1500
370	39590	27713	489	1709	2441

Lunghezza Guida [mm]: 290, 370, 450, 530, 610, 690, 770, 850, 930, 1010, 1170, 1330, 1490, 1650, 1810, 1970

• SERIE "SN63"

Capacità di carico			Capacità di carico		
Lunghezza Corsore [mm]	C _{cur} [N]	M ₁ [Nmm]	M ₂ [Nmm]	M ₃ [Nmm]	M ₄ [Nmm]
130	28200	18200	443	394	563
210	42300	28400	716	1029	1470
290	56400	42600	989	1802	2803
370	70500	56800	1261	3104	4563

Lunghezza Guida [mm]: 610, 690, 770, 850, 930, 1010, 1170, 1330, 1490, 1650, 1810, 1970

Per i codici di ordinazione, vedi pag. D6.
Per ulteriori dati tecnici, vedi pag. D8 - D11.

Fig. 6.34 – The technical sheets of the linear guide.

2) the support plate for the three T-shaped supports mounted below the upper plane (Fig. 6.35 and Fig. 6.36).

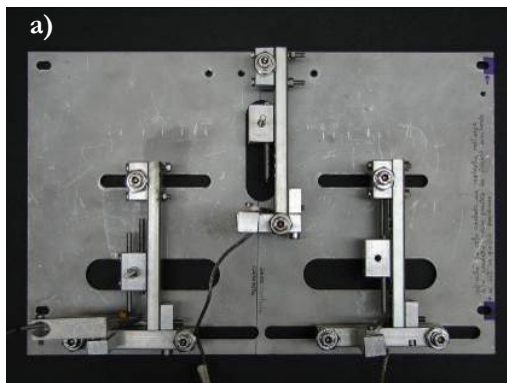


Fig. 6.35 – a) On the left, a view from below of the support plate of the three T-shaped supports; b) on the right, a view from above.



Fig. 6.36 – Two views of the support plate with the three T-shaped supports below the upper plane.

The mixture spreading depends on the type of structure (circular base cones, elliptical base cones and tooth-shaped) and on the arrangement of the retarding elements. The front structure is always located at the final section of the channel, on its axis. The rear line of structures is located at a longitudinal distance from the upstream element at a distance of about twice the height of these structures (70 mm). The rear elements can be placed in various points along the cross-sectional guide. The angle θ , between the original flow direction (the direction defined by the axis of the channel) and the line passing through the front and the rear element can be fixed in the range of 25° - 50° (Fig.6.37-Fig. 6.38).

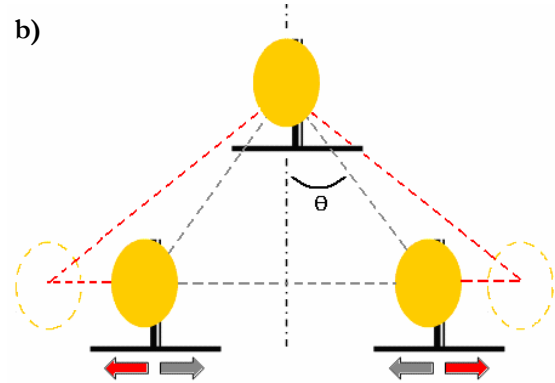
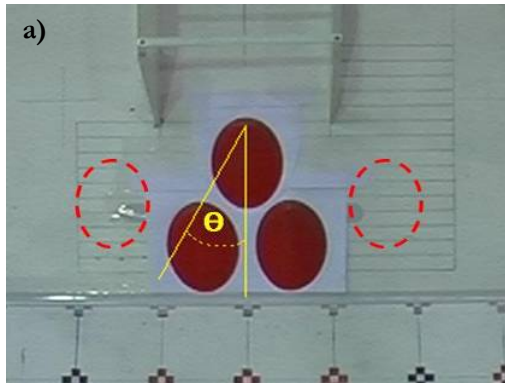


Fig. 6.37 – a) On the left, a view from above of the retarding system; b) on the right, scheme of the retarding structures: the rear structures form an angle of θ° with the longitudinal flow direction.

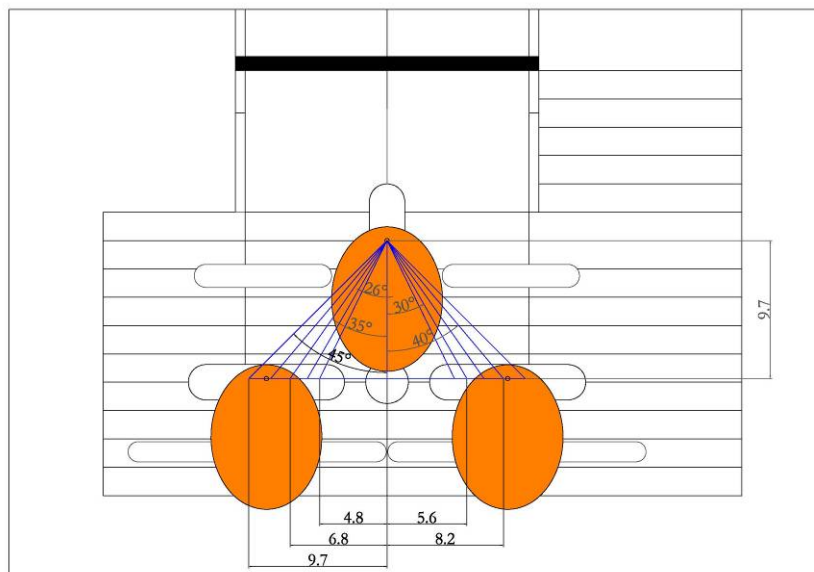


Fig. 6.38 – A view from above of the upper plane with the retarding structures (measures in cm).

Schemes of the T-shaped supports for the retarding elements. Schemes of the T-shaped support and the support plate are presented in Fig. 6.39 and Fig. 6.40.

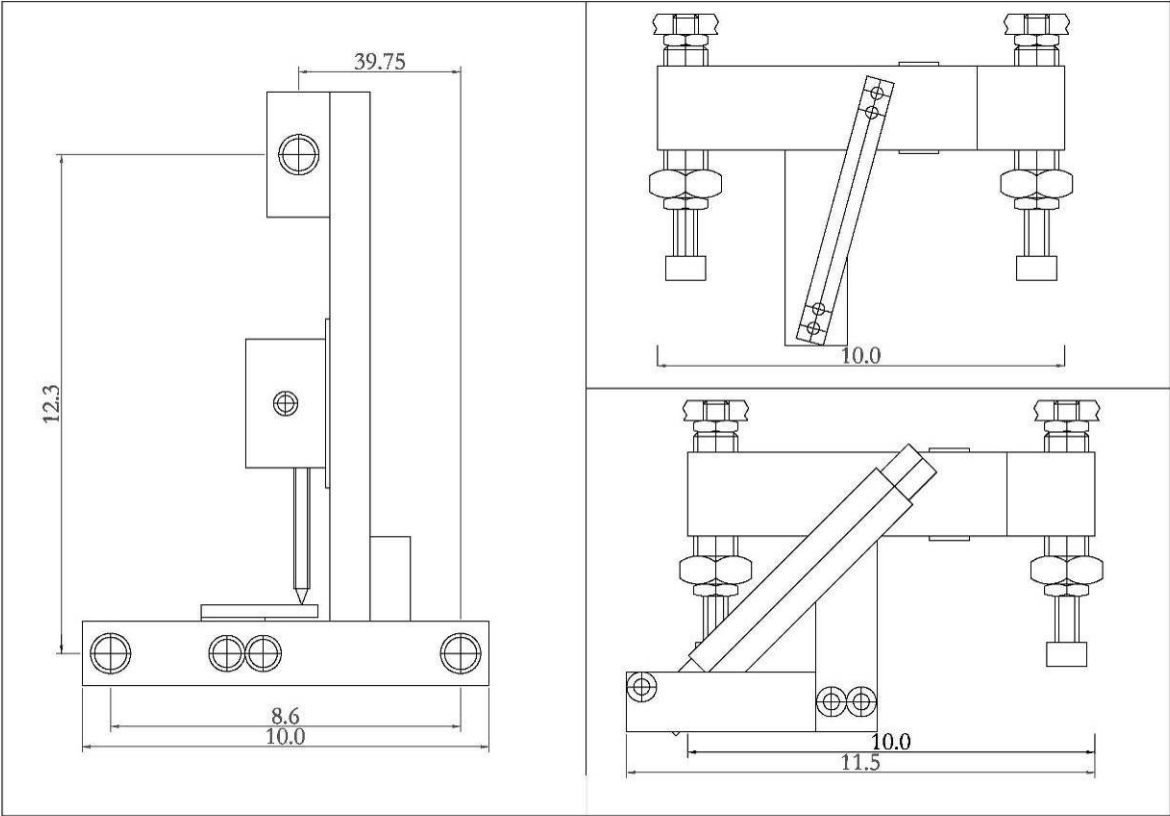


Fig. 6.39 – The T-shaped support used to transfer the force acting on the retarding elements (measures in cm).

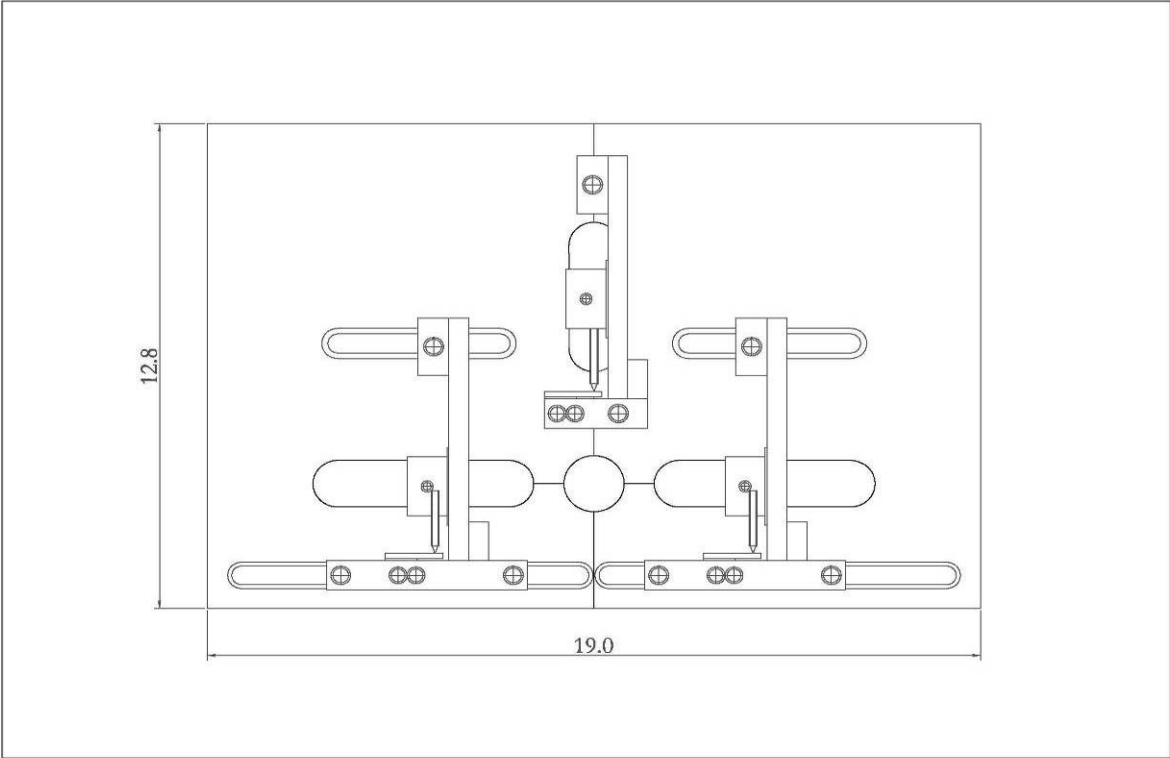


Fig. 6.40 – A view from above of the upper plane with the support (measures in cm).

6.5 The material

During the experiments a dry granular mass, constituted by grains of synthetic zeolite, was used to simulate dense snow avalanches (Fig. 6.41-Table 6.3). This choice follows field experience made by the authors -over the years- mainly in the *Trentino Alto Adige* region (Italy). Also according to this experience it can be inferred that a large number of avalanches events are of the type called dense snow avalanches and that they present deposits that look like a granular mass.

The shape of the grains is roughly spherical (the shape factor is practically equal to 1) - their diameters range from 0,1 mm to 2 mm, with a mean diameter of about 1 mm. The internal friction angle is 28° [D'Accordi, 1999]. The bottom static friction angle, obtained by a shear box, is equal to 18° with a standard deviations equal to 0,8° [De Toni et al., 2004].

Table 6.3 – Physical and mechanical material characteristics.



Fig. 6.41 – The synthetic zeolite.

I – II – III series of tests	Grains of zeolite	
grains diameter	10 – 200 μm	0,10 – 2,00 mm
mean grains diameter	100 μm	1,00 mm
density (zeolite)	1080 kg/m ³	
internal friction angle	28°	
bottom static friction angle	18°	
bottom cinematic friction angle	15°-16°	

6.6 Calibration

Two types of calibration apparatus were used: the first for the calibration of the load cells (Fig. 6.42a); the second for the calibration -on site- of the force measuring system (Fig. 6.42b). Particular attention was necessary to avoid that some grains of the mixture get stuck between the base of the retarding elements and the support plane, and in the mechanical sliding system underneath the plane (to avoid serious problems in the measurement of impact force). This was particularly important because of the minute dimensions of the smallest particles in the granulometric distribution curve of the granular material. Calibration of the force measurement system was executed before each test, also to avoid this problem.

For the second calibration a procedure based on the UNI EN ISO 376:2004 was followed.

Extract UNI EN ISO 376:2004 “*Metallic materials – Calibration of force-proving instruments used for the verification of uniaxial testing machines.*”

“*Preloading: before the calibration forces are applied -in a given mode (tension or compression)- maximum force is to be exerted to the instrument three times. The duration of the application of each preload will range between 1 min and 1,5 min.*”

Procedure: calibration is carried out by applying two series of calibration forces to the force-proving instrument, only with increasing values and without disturbing the device. At least two further series of increasing and decreasing values are then applied (in this experimental analysis: 10 g, 20 g, 50 g, 100 g and 200 g). To determinate the interpolation curve, the number of forces should not be less than eight, and these forces should be distributed as uniformly as possible over the calibration range.”

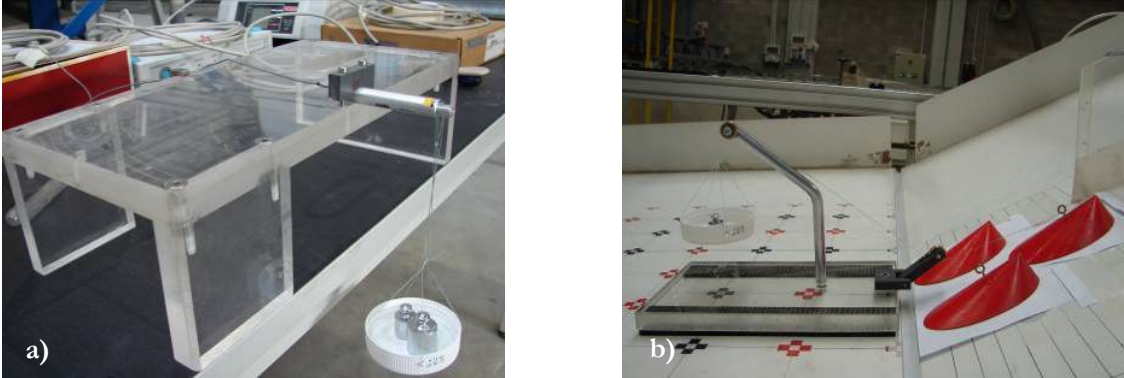


Fig. 6.42 – a) On the left, the experimental set-up used to perform the calibration of the load cells; b) on the right, the on site calibration of the force measurement system.

At the beginning of the experimental campaign some tests were performed, using the Fast Fourier Transform (FFT), in order to define an adequate acquisition frequency for the phenomenon. A frequency of 50 Hz was judged to be sufficient.

In Fig. 6.43 and Fig. 6.44 two examples of calibration of the load cells are presented: F is the impact force (N) and V the voltage (mV/V).

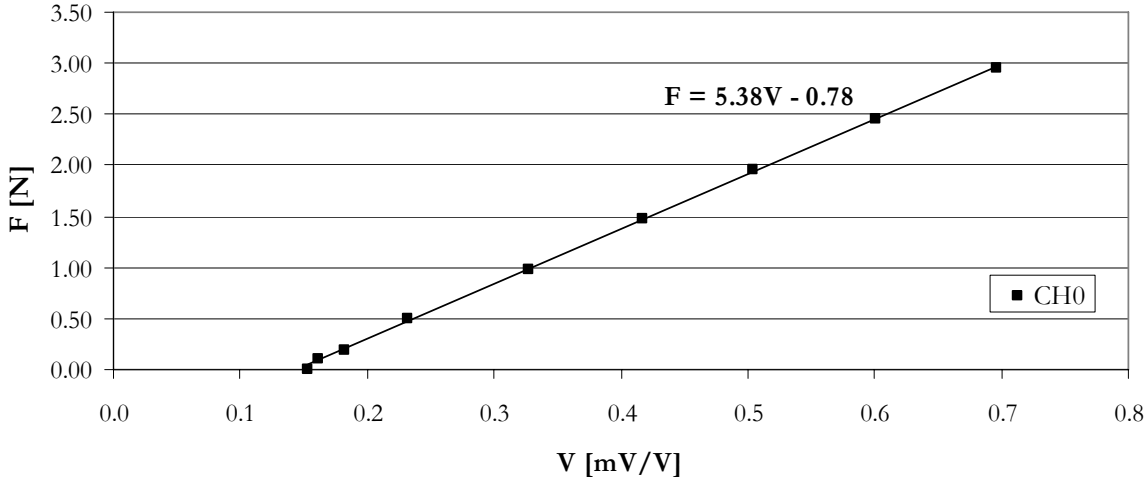


Fig. 6.43 – Example of calibration of the load cell on the front element (CH0) [Test 03_EC_26_3_24].

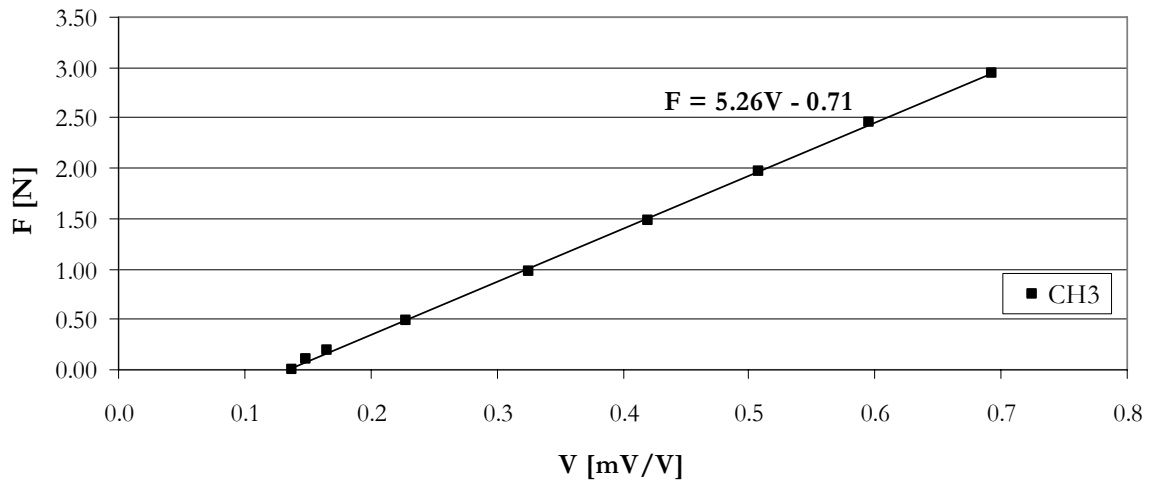


Fig. 6.44 – Example of calibration of the load cell on the rear elements (CH3) [Test 03_EC_26_3_24].

6.7 Measuring techniques

Calibration. Calibration of the force measurement system was executed before each test.

The flow depth and the front velocity in the channel. The image processing of the video made with video camera I, permits determining the maximum depth in each frame, to estimate the depth of the flowing mixture near the retarding structures (Fig. 6.45). Flow depth is here defined as the maximum depth of the front.



Fig 6.45 – A sequence of frames obtained by the lateral video camera (video camera I).

The image processing of the video made with video camera II allows finding the position of the avalanche front -in each frame- to estimate the front velocity of the flowing mixture near the retarding structures (Fig. 6.46). The velocity calculated in the tests is the mean front velocity in the last 20 centimetres before impact against the retarding structures.

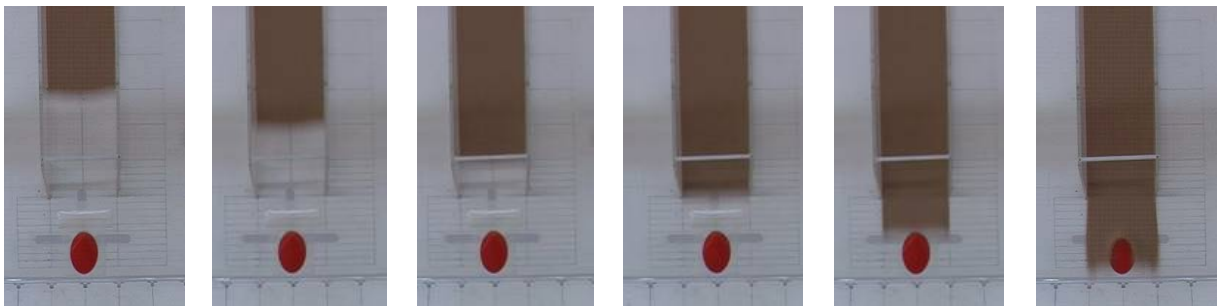


Fig 6.46 – A sequence of frames obtained by the frontal video camera (video camera II).

The dimensionless impact force – front and rear elements. Dimensionless impact force is obtained in the following way:

$$F_{d_less} = \frac{F}{\rho v^2 A}$$

F [N]	impact force;
ρ [kg/m ³]	granular material density (zeolite: $\rho = 1080$ kg/m ³);
v [m/s]	mean front velocity of the mixture flow near to the works;
A [m ²]	impact area (Fig. 6.47);
H [m]	element height ($H = 0,030$ m);
B [m]	maximum width of the element;
h [m]	maximum flow depth near the structures;
α [rad]	lateral inclination of the cones element.

Front velocity and impact area are similarly used for the front and rear elements.

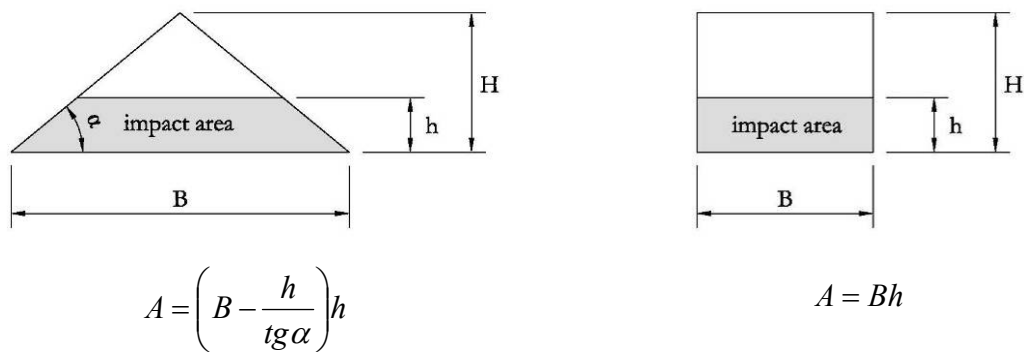


Fig. 6.47 – Definition of impact area for the cone-shaped (on the left) and for the tooth-shaped structures (on the right) in the calculus of the dimensionless impact force.

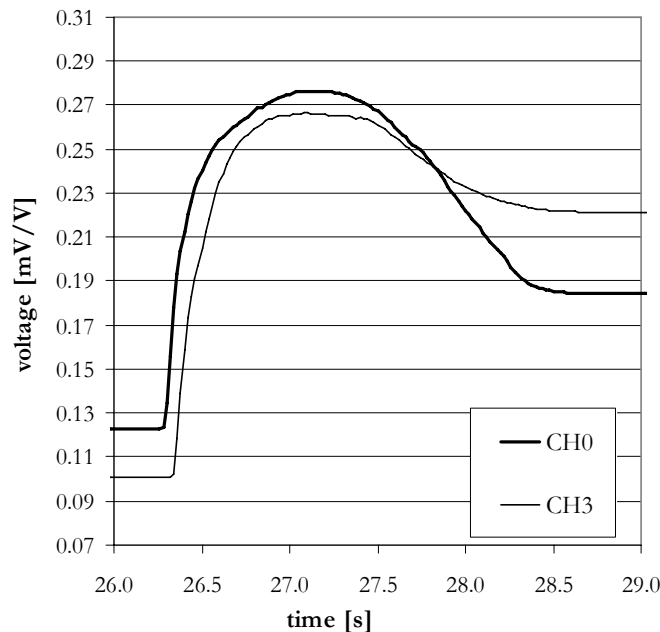


Fig. 6.48 – Example of the acquired impact forces raw data (in terms of voltage) against front element (CH0) and rear elements (CH3) [Test 03_EC_26_3_24].

The measuring of mixture spreading. Two physical parameters are defined in order to characterize the mixture spreading: longitudinal efficiency and cross-sectional efficiency.

The cross-sectional efficiency is defined as follows (Fig. 6.49):

$$\varepsilon_T = \frac{L - L_{NW}}{L_{NW}}$$

L	[m]	deposit width;
L_{NW}	[m]	maximum width of the mixture in the case of absence of slowing down elements.

The longitudinal efficiency is defined as follows:

$$\varepsilon_L = \frac{d_{NW} - d}{d_{NW}}$$

d	[m]	deposit distance;
d_{NW}	[m]	maximum distance of the mixture in the case of absence of slowing down elements.

Mixture spreading depends on the type of structures (circular base cones, elliptical base cones and tooth-shaped structures) and on the geometric arrangement of the elements.

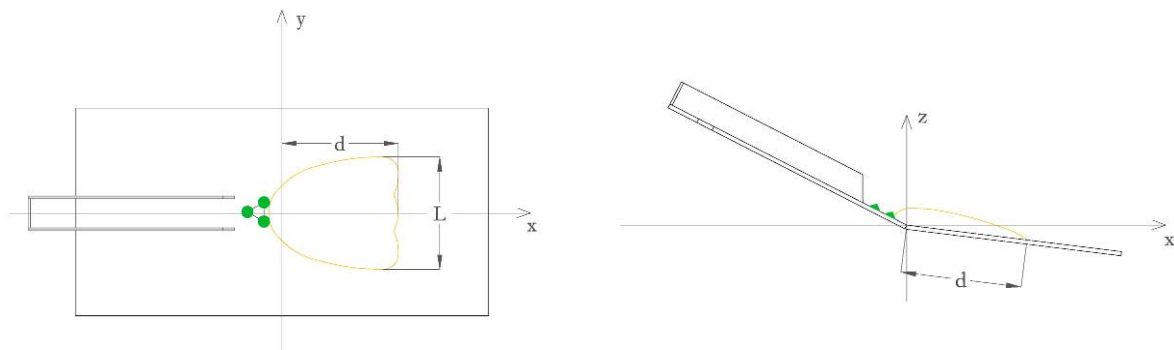


Fig. 6.49 – Scheme showing the physical parameters used to define the longitudinal and the cross-sectional efficiency of the retarding elements.

The evaluation of final longitudinal and cross-sectional mixture spreading was obtained through image processing.

6.8 Experimental tests

The physical parameters that have to be considered important for this analysis are:

- flow depth in the channel, the maximum value at the final section of the channel (h);
- front velocity of the mixture near the structures (v);
- Froude Number (F_r);
- impact force (F) and dimensionless impact force (F_{d_less}) – front element (CH0) and rear elements (CH3);
- deposit stopping distance (d) and maximum longitudinal distance reached by the deposit (d_{max}) without the use of any slowing down element;
- deposit width (L) and maximum width reached by the deposit (L_{max}) without the use of any slowing down element;
- cross-sectional efficiency (ε_T);
- longitudinal efficiency (ε_L).

Table 6.4 – List of the tests.						
n°	date	upper plane tilting	lower plane tilting	type of structure	rear structure opening angle	granular material weight
		φ	β		θ	P
Tests – I series						
01–02	-	24°	7°	-	-	3 kg 7 kg
03–12	07/12/06 13/12/06			elliptical cone-shaped structures	26° 30°	
13–22	15/12/06 29/12/06			circular cone-shaped structures	35° 40°	
23–32	03/01/07 10/01/07			tooth-shaped structures	45°	
Tests – II series						
33–34	-	27°	7°	-	-	3 kg 7 kg
35–44	25/01/07 28/02/07			elliptical cone-shaped structures	26° 30°	
45–54	13/03/07 14/03/07			circular cone-shaped structures	35° 40°	
55–64	12/03/07 13/03/07			tooth-shaped structures	45°	
Tests – III series						
65–66	-	30°	7°	-	-	3 kg 7 kg
67–76	29/09/06 03/10/06			elliptical cone-shaped structures	26° 30°	
77–86	14/10/06 19/10/06			circular cone-shaped structures	35° 40°	
87–96	14/10/06 19/10/06			tooth-shaped structures	45°	

Besides this, some shapes of the retarding structures (circular base cone, elliptical base cone, tooth-shaped structures) were considered. The geometrical distribution of the retarding elements, the density of the granular material and the cross sectional dimension of the confined flow were not investigated.

Fig. 6.50 presents an example of data sheet, realized for each test.

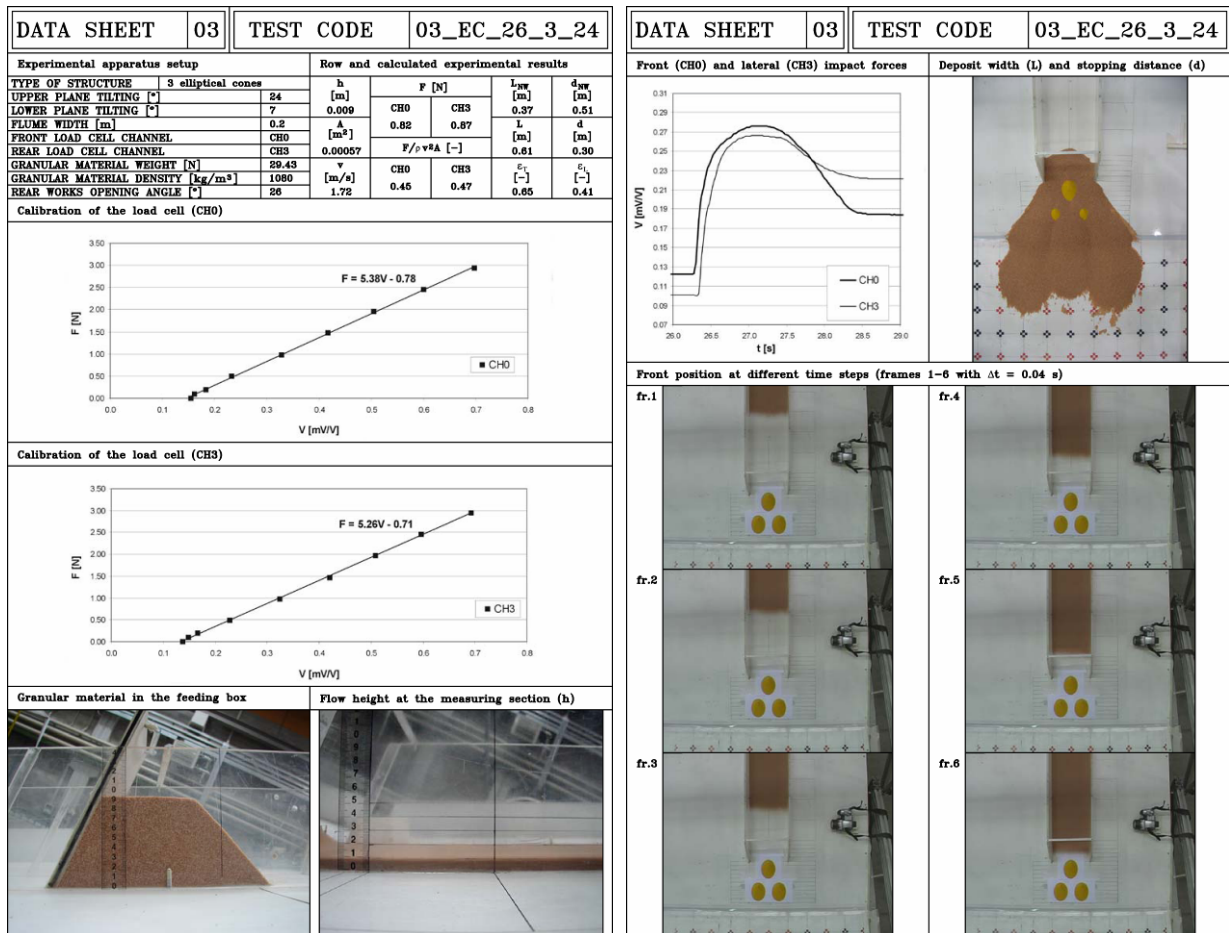


Fig. 6.50 – Example of data sheet realized for each experimental test [Test 03_EC_26_3_24].

6.9 Test results

The volume of the mixture and its shape at the beginning of the motion, the rheology of the mixture, the slope of the flume and its bottom and side wall roughness contribute to define all the properties of the mixture distribution before impact occurs. In particular, it was not possible to define the bulk density of the mixture. For this reason in the experimental calculations the density of the material (synthetic zeolite) was used. Some particular shapes of retarding elements were investigated, in order to geometrically simulate the type of structures which are effectively in use. The distribution of the retarding elements also tends to simulate the disposal adopted in real designs, even if limited only to two lines of elements.

The ratio between the width of the flowing mass and the width of the retarding elements is always the same and not far from the unit.

Flow depth and front velocity in the channel. In the experiments the measured values of the mixture depth ranged from 0,008 m to 0,021 m (3 kg and 7 kg) (Table 6.5).

type of work	24°		27°		30°	
	3 kg	7 kg	3 kg	7 kg	3 kg	7 kg
	h [m]					
elliptical cone-shaped structures	0,010	0,018	0,010	0,019	0,010	0,021
circular cone-shaped structures	0,008	0,018	0,010	0,019	0,010	0,021
tooth-shaped structures	0,008	0,017	0,010	0,019	0,010	0,019

The values related to front velocity ranged from 1,5 m/s to 2,6 m/s. The front velocity is more sensible to the variability of the weight of the granular material (Table 6.6).

type of work	24°		27°		30°	
	3 kg	7 kg	3 kg	7 kg	3 kg	7 kg
	v [m/s]					
elliptical cone-shaped structures	1,81	1,94	2,14	2,34	2,40	2,64
circular cone-shaped structures	1,77	1,82	1,96	2,11	2,45	2,55
tooth-shaped structures	1,74	1,83	2,11	2,20	2,55	2,59

The Figure 6.51 presents an example of the flow depth -in function of time- at the measuring section in the channel; while in the Fig. 6.52 an example of the front velocity profile -this also in function of time- along the channel and after the impact against the retarding structures is presented.

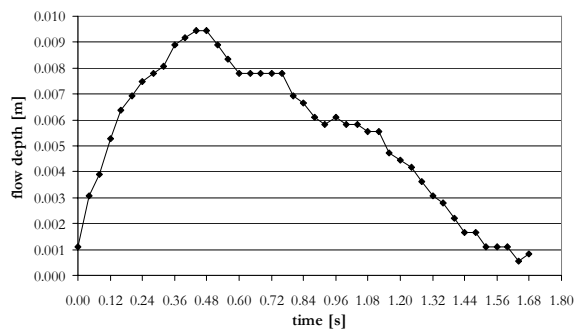


Fig 6.51 – Example of the flow depth in time at the measuring section in the channel [Test 03_EC_26_3_24].

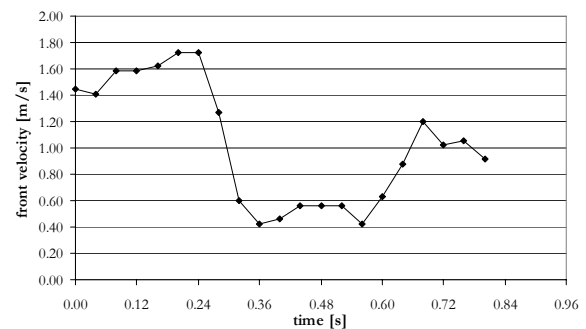


Fig 6.52 – Example of the front velocity in time along the channel and after the impact against the structures [Test 03_EC_26_3_24].

Froude Number. The Froude Number ranged from 4 to 8. Fig. 6.53 shows a good capability of the experimental apparatus to produce repeatable events, under the same boundary conditions (same upper plane slope, same amount of granular material and same arrangement inside the feeding box), before impact against the retarding elements. Besides, it also shows that the Froude numbers increase on increasing the channel slope -with a constant granular mass volume- while they tend to decrease on increasing the granular mass volume, maintaining the same sloping inclination. The Froude numbers are generally quite high.

In Fig. 6.53 Froude numbers of the events generated in the laboratory with various experimental conditions are represented: N is the sample number of events with those conditions; σ is the standard deviation.

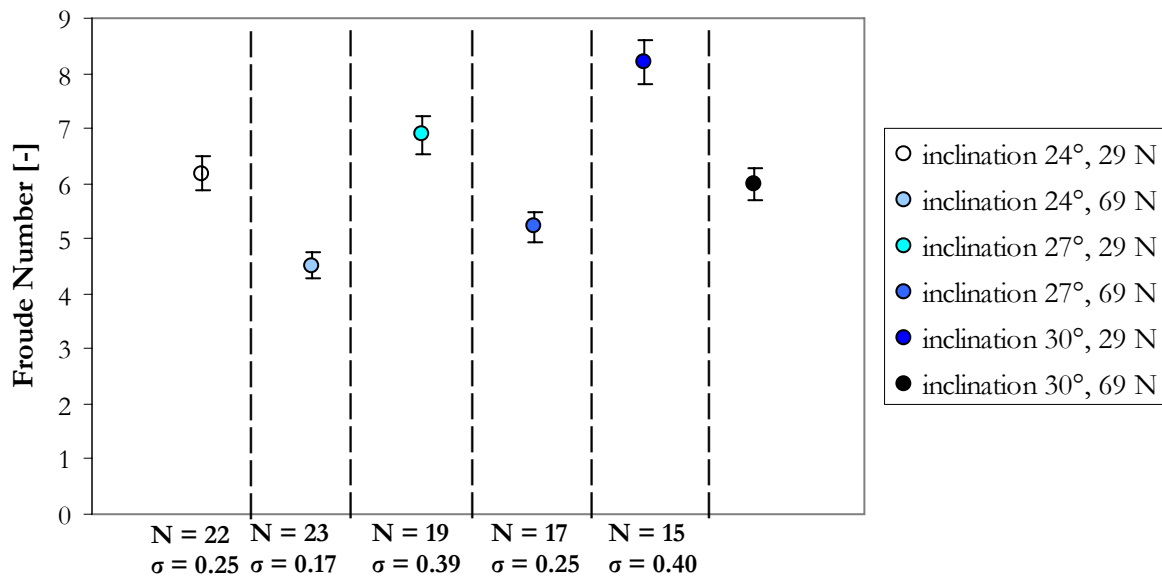


Fig. 6.53 – The Froude numbers of the events generated in the laboratory with various experimental conditions.

Fig. 6.54 and Fig. 6.55 present some frames showing the typical impact of a mixture against a system of three tooth-shaped structures. The presence of the obstacles tends to deviate the mixture normally to the bottom. This is true both for the front element and for the rear elements. There is no influence of the impact upstream.

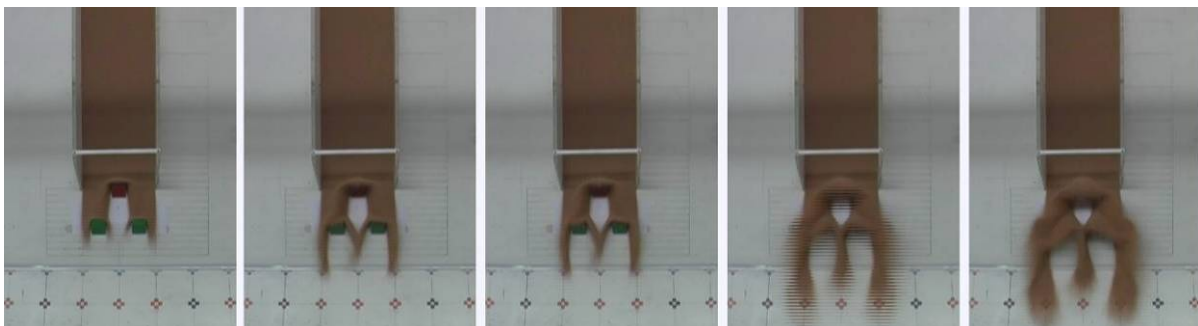


Fig. 6.54 – A sequence of frames taken by the front video-camera (time interval 0,04 s) during the impact of a granular flow against a system of three tooth-shaped structures. The opening angle is equal to 26°.

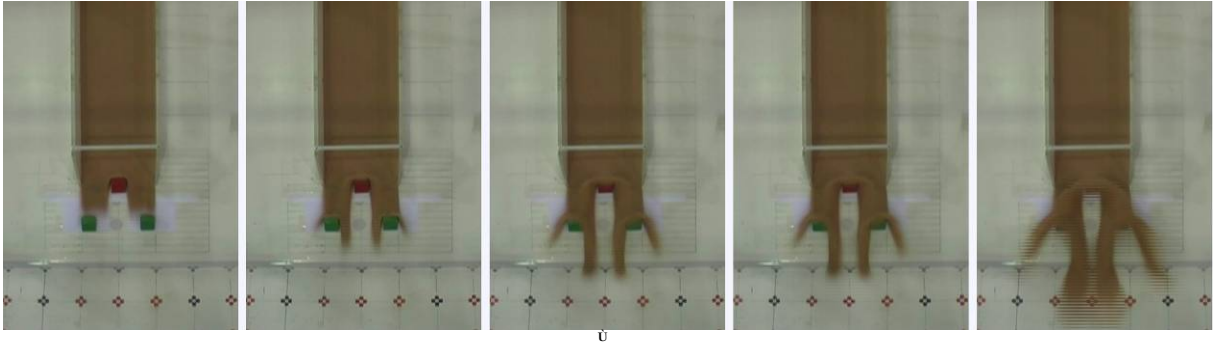


Fig. 6.55 – A sequence of frames taken by the front video-camera (time interval 0,04 s) during the impact of a granular flow against a system of three tooth-shaped structures. The opening angle is equal to 35°.

The observed dynamic impact was always of the “vertical jet” type (Fig. 6.56).

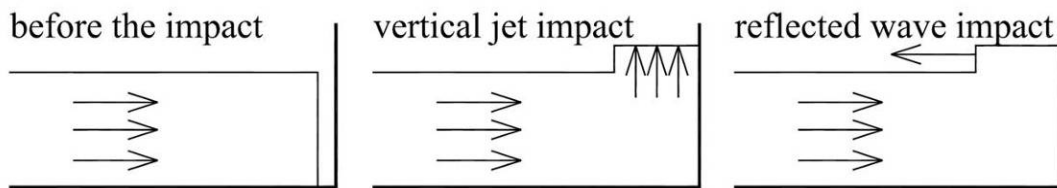


Fig. 6.56 – Scheme of types of impact of a three-phase mixture [Armanini & Scotton, 1993].

Dimensionless impact force – front element. Dimensionless impact force is represented for circular base cones, elliptical base cones and tooth-shaped structures. The behaviour of the two types of cones does not differ significantly (Fig. 6.57-Fig. 6.59).

The values of force against the front element ranged from 0,64 N to 2,84 N.

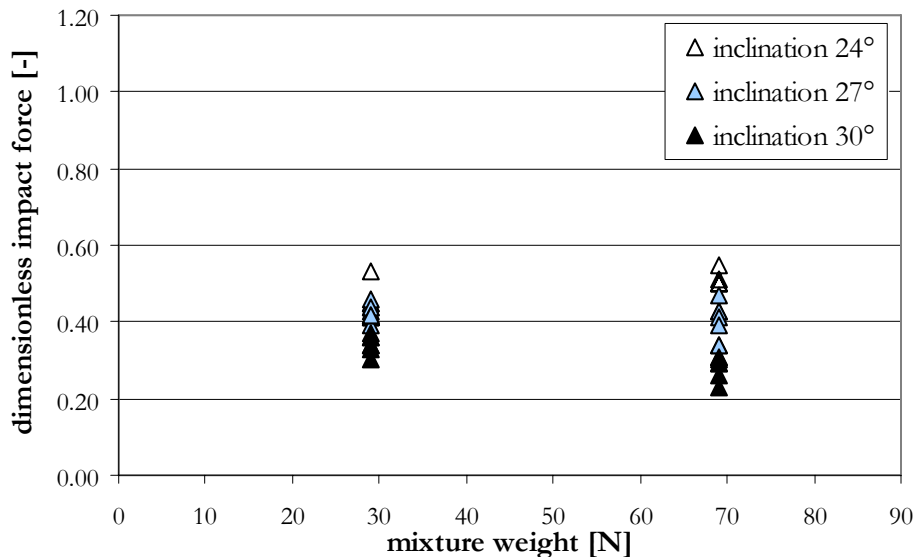


Fig. 6.57 – Dimensionless impact force against retarding elements having the shape of elliptical base cones at various inclination angles and with various mixture weights.

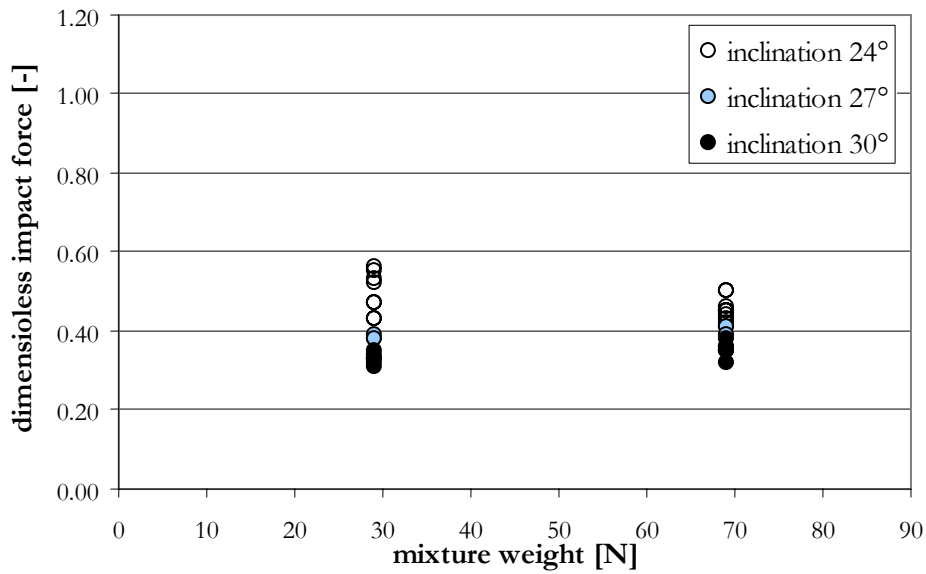


Fig. 6.58 – Dimensionless impact force against retarding elements having the shape of circular base cones at various inclination angles and with various mixture weights.

About 20 tests were performed in order to examine repeatability. The mean variability of dimensionless force was of about 12 %, with a standard deviation of about 10 %.

The mean value of dimensionless impact force is 0,41 for circular base cones, while it is 0,40 for elliptical base cones. A certain variability, observable around the mean value, should owe mostly to the variability of the bulk density, the parameter that should be used to construct the dimensionless force.

In case of tooth-shaped structures the mean value of the dimensionless force is much greater than that registered above and equals 0,74. In this case -besides the dispersion around the mean value- a different mean value in the tests performed with a weight of material of 3 kg and the tests performed with a weight of 7 kg. is observable.

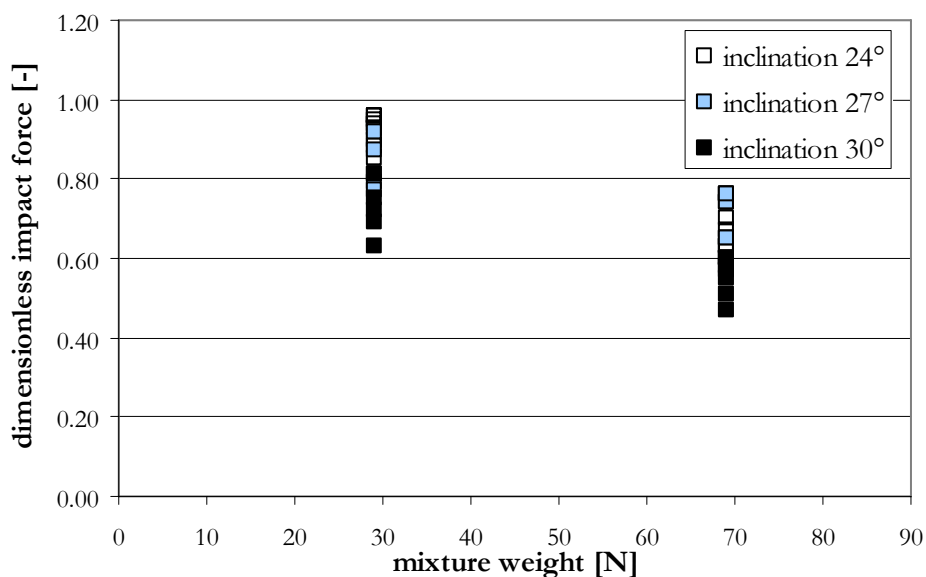


Fig. 6.59 – Dimensionless impact force against retarding elements having a tooth-shaped structure, at various inclinations and with various mixture weights.

Another important dimensionless parameter should be responsible for this behaviour: the relative height, defined as the ratio between the depth of the flowing mixture and the height of the retarding elements h/H . The dimensionless impact force is greater when the relative height is lower.

Multiple regression analysis. The experimental data is treated by means of a multiple regression analysis, following a dimensional analysis of the phenomenon. A sufficiently good model was obtained, representing the dimensionless force in function of the Froude Number and with the ratio between the depth of the mixture and the height of the structure h/H .

For the front elliptical cone the model obtained is the following:

$$F_{d_less} \text{ calculated} = 1,19 - 0,09 \cdot Fr - 0,54 \cdot \frac{h}{H}$$

that can be used in the following experimental range: $4 < Fr < 8$ and $0,3 < h/H < 0,7$.

The model is able to describe 78% (R^2) of the information contained in the sample. The standard error of the estimation is 0,038, while the mean absolute error is 0,031. The comparison between measured and calculated values of the non-dimensional force for the front elliptical cone is illustrated in the Fig. 6.60.

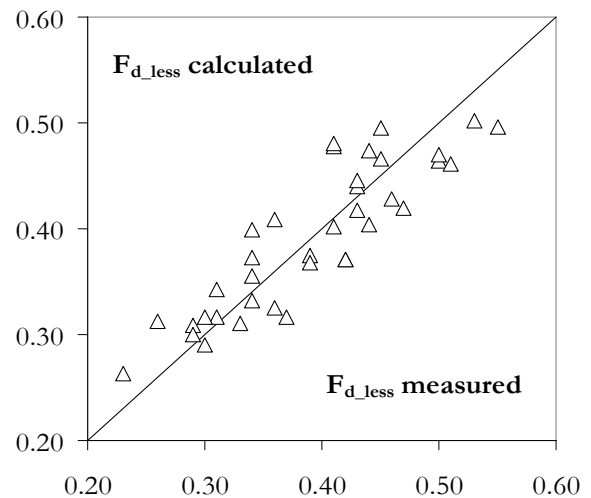


Fig. 6.60 – The dimensionless force measured and calculated following the model for the front elliptical cone.

For the front circular cone the obtained model is the following:

$$F_{d_less} \text{ calculated} = 0,94 - 0,06 \cdot Fr - 0,39 \cdot \frac{h}{H}$$

that can be used in the following experimental range: $4 < Fr < 8,5$ and $0,3 < h/H < 0,7$.

The model is able to describe the 80% of the information contained in the sample. The standard error of the estimation is 0,032, while the mean absolute error is 0,024. A comparison between measured and calculated values of the non-dimensional force for the front circular cone is showed in the Fig. 6.61 on the right.

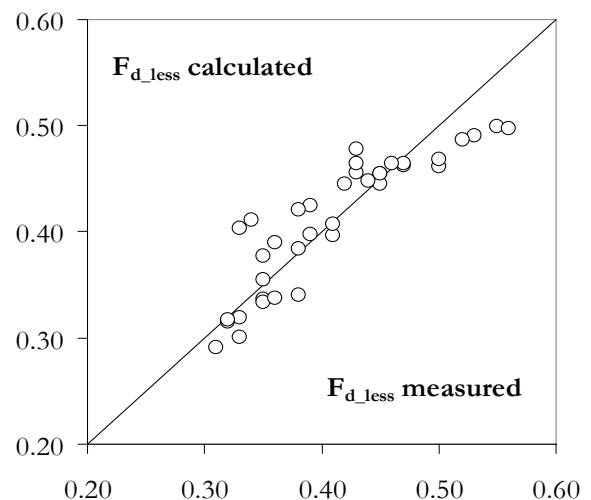


Fig. 6.61 – The non-dimensional force measured and calculated following the model for the front circular cone.

For the front tooth-shaped structure a good interpretation of the experimental data is obtained with the following model:

$$F_{d_less} \text{ calculated} = 1,37 - 0,005 \cdot Fr^2 - 0,99 \cdot \frac{h}{H}$$

that can be used in the following experimental range: $4 < Fr < 8,5$ and $0,27 < h/H < 0,7$.

The model is able to describe 79% of the information contained in the sample. The standard error of the estimation is 0,068, while the mean absolute error is 0,053. The comparison between measured and calculated values of the non-dimensional force for the front tooth-shaped structure is illustrated in Fig. 6.62.

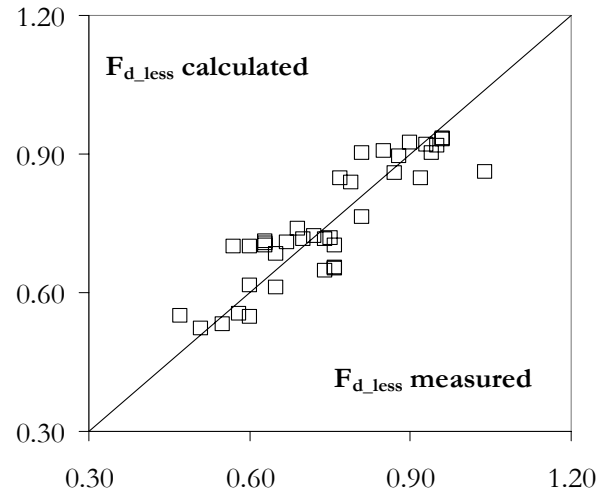


Fig. 6.62 – The non-dimensional force measured and calculated following the model for the front tooth-shaped structure.

A significant difference between the models for the two kinds of cones is not observable. On the contrary, quite a different model arises for the tooth-shaped structure, both in terms of values of the non-dimensional force and in terms of the shape of the model that better fits the data assuming a quadratic dependence from the Froude Number.

Dimensionless impact force – rear elements. Dimensionless impact force is illustrated for the three types of considered retarding elements located in the rear line, when the opening angle changes from 26° to 45° (Fig. 6.63-Fig. 6.65).

The values of force against the rear elements ranges from 0,16 N to 2,26 N.

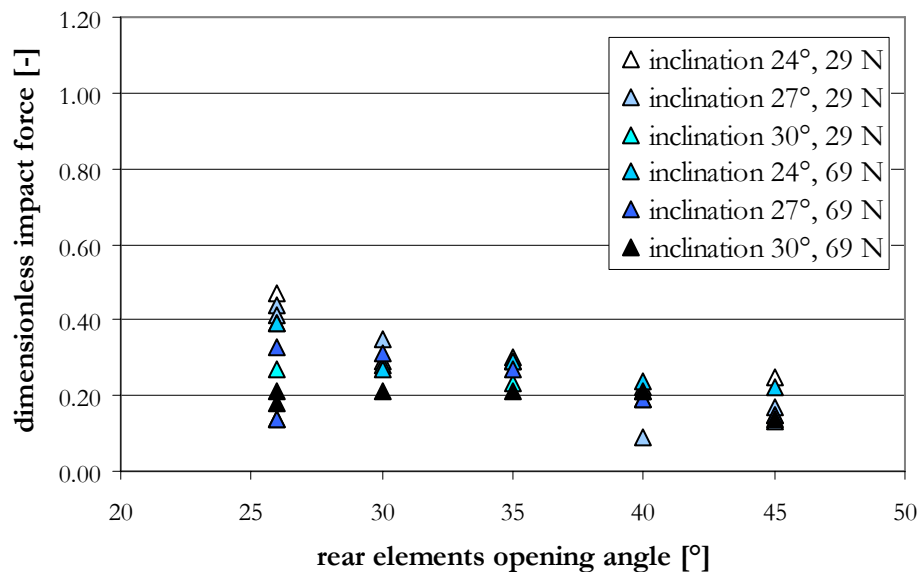


Fig. 6.63 – Dimensionless impact force against rear retarding elements which have the shape of elliptical base cones positioned with various inclination angles, mixture weight and opening angles.

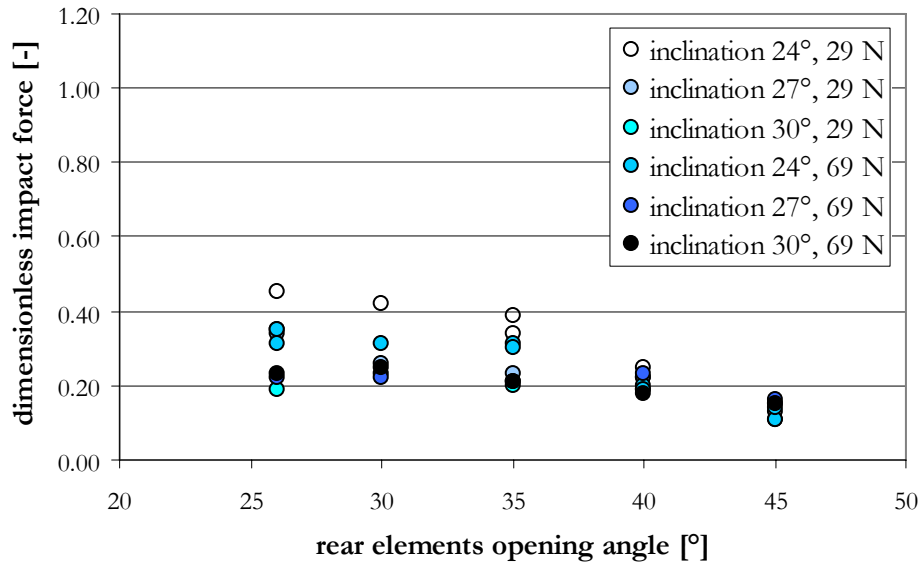


Fig. 6.64 – Dimensionless impact force against rear retarding elements which have the shape of circular base cones positioned with various inclination angles, mixture weight and opening angles.

With the rear structures, in case of cones, the maximum impact force is produced with an opening angle which is less than 26°. On the other hand, in the case of tooth-shaped structures, the maximum impact force is observed at opening angles near to 30°.

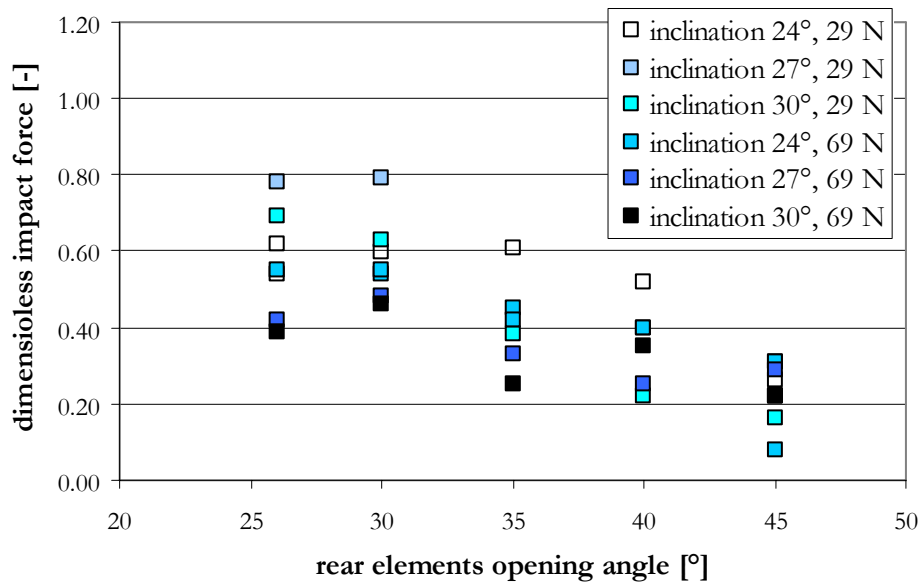


Fig. 6.65 – Dimensionless impact force against rear retarding elements which have the shape of tooth-shaped structures with various inclination angles, mixture weight and opening angles.

In Fig. 6.66 the mean value of the non-dimensional measured impact force is illustrated. In case of cones, the maximum impact force is actually produced at the minimum opening angle, while, in the case of tooth-shaped structures, the maximum value is observed at an opening angle between 26° and 30°.

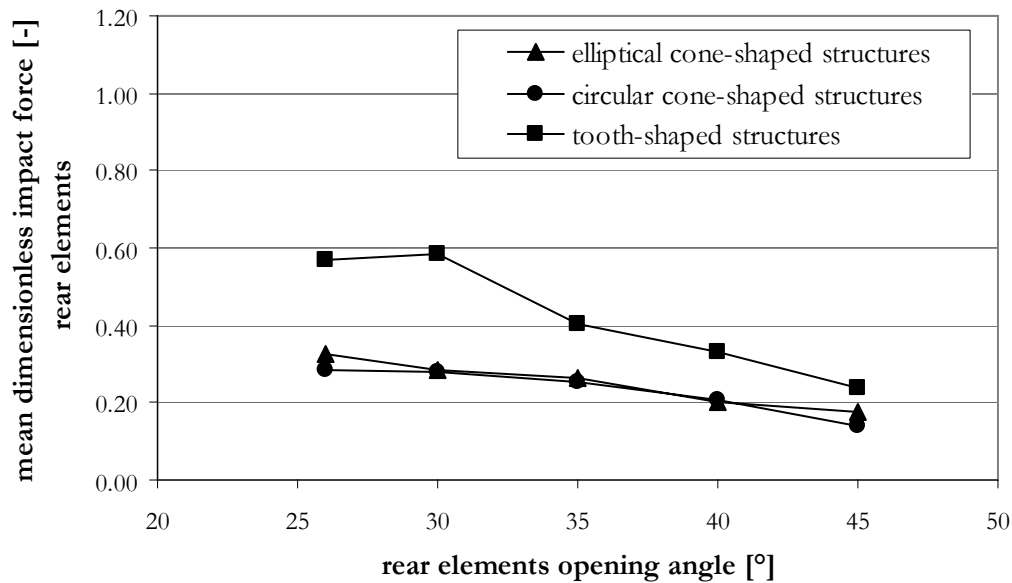


Fig. 6.66 – Behaviour of the mean value of dimensionless impact force for the rear retarding elements when the opening angle varies from 26° to 45°.

In Fig. 6.67 a sequence of frames illustrates the effect of the opening angle at the moment of the impact of a granular mixture against a system of three elliptical cones. Also in this case the impact is of the “vertical jet” type, modified by the shape of the retarding element.

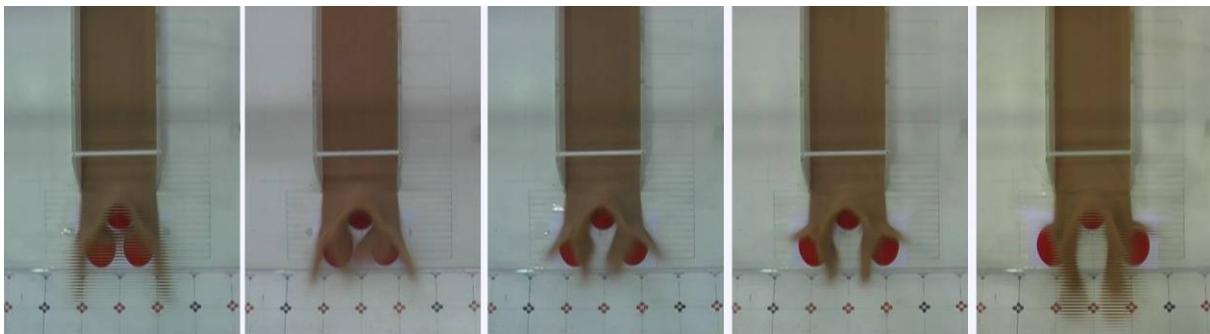


Fig. 6.67 – A sequence of frames taken by the front video camera during five different events at the moment of impact against a system of three elliptical cones. The opening angles are -from left to right- 26°, 30°, 35°, 40° 45°.

Multiple regression analysis. Also for the rear elements the experimental data was analysed with the help of the multiple regression analysis. In this case, the best results are obtained considering -along with the previous variables- also the opening angle θ expressed in radian. The Froude number and the ratio h/H used in the following calculations are those measured in front of the front element.

For the rear elliptical cone the model is as follows:

$$F_{d_less \text{ calculated}} = 1,05 - 0,05 \cdot Fr - 0,46 \cdot \frac{h}{H} - 0,42 \cdot \theta$$

that can be used in the following experimental range: $4 < Fr < 8$, $0,3 < h/H < 0,7$, $0,44 < \theta < 0,87$.

The model is able to describe 68% (R^2) of the information contained in the sample. The standard error of the estimation is 0,055 , while the mean absolute error is 0,038.

For the rear circular cone the following model is proposed:

$$F_{d_less} \text{ calculated} = 1,74 - 0,04 \cdot Fr - 0,72 \cdot \frac{h}{H} - 1,13 \cdot \theta$$

that can be used in the following experimental range: $4 < Fr < 8,5$, $0,3 < h/H < 0,7$, $0,44 < \theta < 0,87$.

The model is able to describe 70% of the information contained in the sample. The standard error of the estimation is 0,12 , while the mean absolute error is 0,088.

For the rear tooth-shaped structure a good interpretation of the experimental data was obtained with the following model:

$$F_{d_less} \text{ calculated} = 1,61 - 0,004 \cdot Fr^2 - 0,72 \cdot \frac{h}{H} - 1,13 \cdot \theta$$

that can be used in the following experimental range: $4 < Fr < 8,5$, $0,27 < h/H < 0,7$, $0,44 < \theta < 0,87$.

The model is able to describe 70% of the information contained in the sample. The standard error of the estimation is 0,12 , while the mean absolute error is 0,088.

For the rear elements the capability of the models to describe the phenomena is lower than for the front elements. Other parameters, such as the ratio between the width of the flow and the total width of the structure system, are not explicitly taken into consideration.

The maximum non-dimensional force occurs when the opening angle is at the minimum value in the experimental range.

Deposit analysis: deposit stopping distance and width. The deposit stopping distance and width of the systems are plotted when the opening angle of rear works varies from 26° to 45° (Fig. 6.68). The image processing permits to observe the variability of the deposit shape.

Table 6.7 – Maximum values of the deposit stopping distance.						
type of work	24°		27°		30°	
	3 kg	7 kg	3 kg	7 kg	3 kg	7 kg
	d [m]					
elliptical cone-shaped structures	0,43	0,54	0,62	0,78	0,71	0,94
circular cone-shaped structures	0,48	0,63	0,60	0,79	0,80	0,96
tooth-shaped structures	0,46	0,58	0,66	0,80	0,90	1,00

In Tables 6.7 and 6.8 the maximum values of the deposit stopping distance and width are presented.

Table 6.8 – Maximum values of the deposit width.						
type of work	24°		27°		30°	
	3 kg	7 kg	3 kg	7 kg	3 kg	7 kg
	L [m]					
elliptical cone-shaped structures	0,61	0,72	0,74	0,87	0,83	0,97
circular cone-shaped structures	0,61	0,67	0,65	0,77	0,75	0,90
tooth-shaped structures	0,58	0,75	0,67	0,83	0,80	0,97

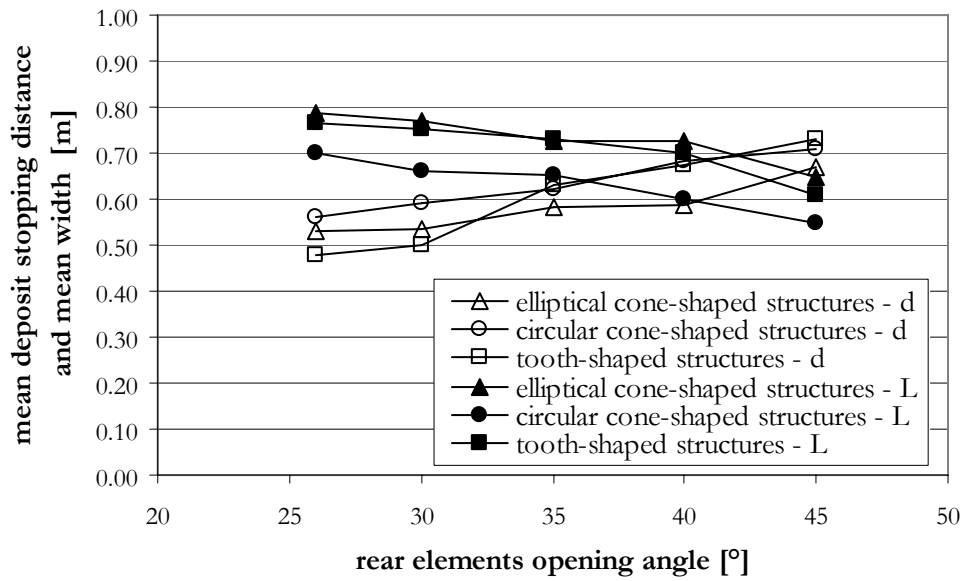


Fig. 6.68 – Behaviour of the mean value of deposit stopping distance and width when the opening angle varies from 26° to 45°.

It is interesting to observe the change of the deposit shape when variation of the type of structures and their configuration occurs: it is possible to register the different deposit stopping distances and widths (Fig. 6.69-6.77).

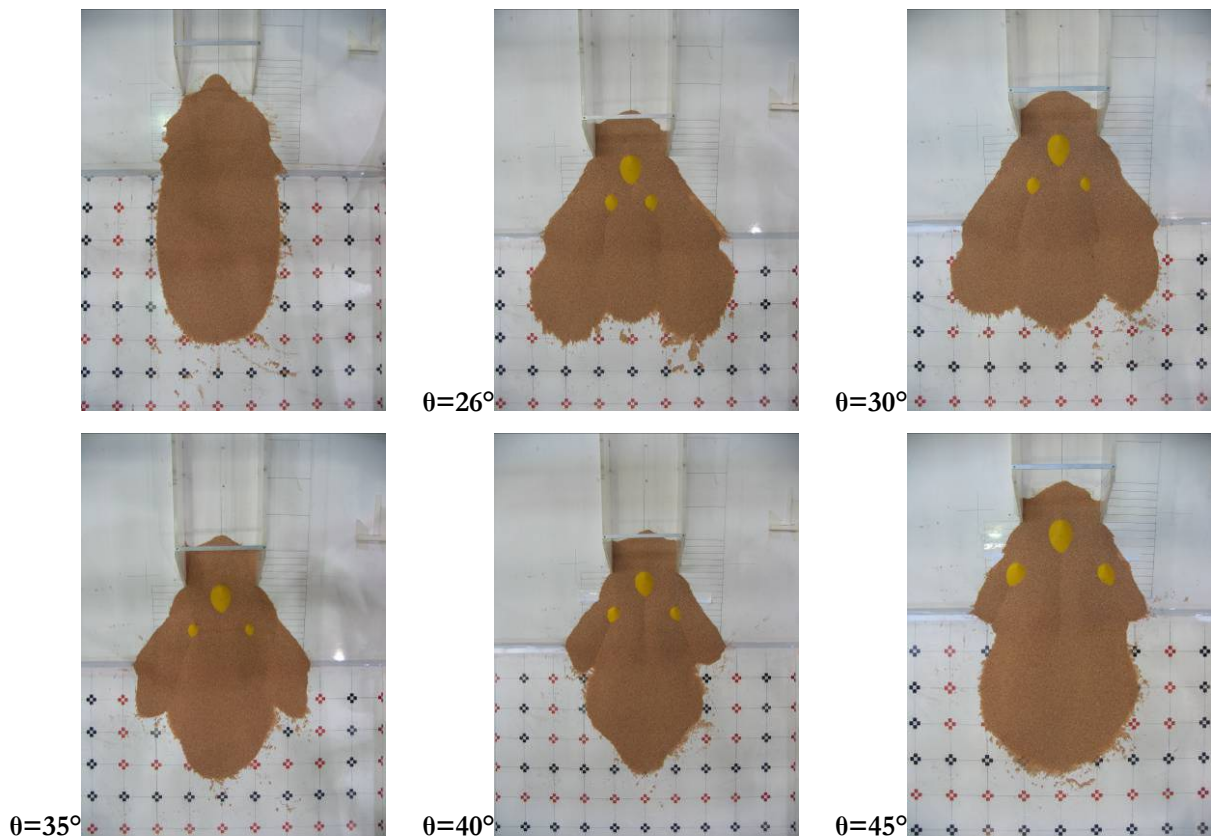


Fig. 6.69 – Deposit shapes: upper plane tilting 24°, elliptical base cones, granular material weight of 3 kg and the opening angle of rear structures from 26° to 45°.

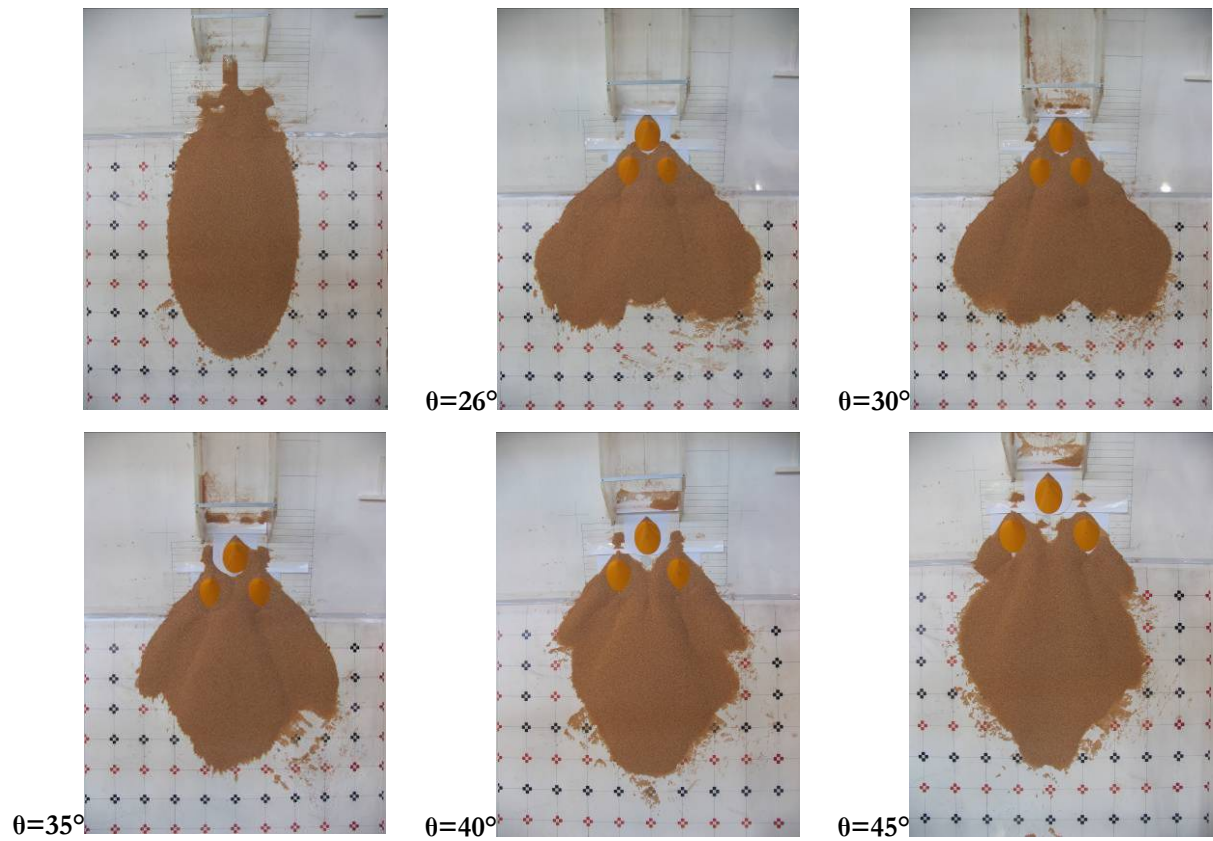


Fig. 6.70 – Deposit shapes: upper plane tilting 27°, elliptical base cones, granular material weight of 3 kg and the opening angle of rear structures from 26° to 45°.

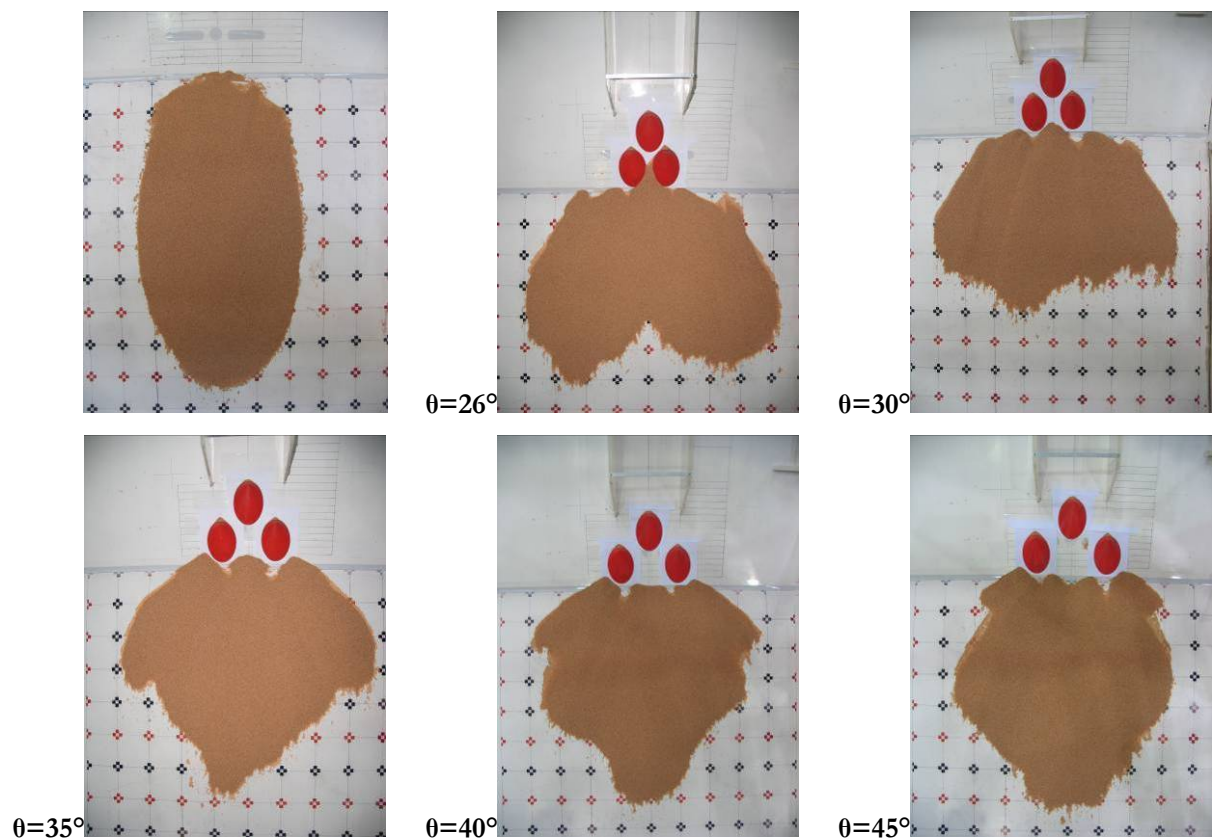


Fig. 6.71 – Deposit shapes: upper plane tilting of 30°, elliptical base cones, granular material weight of 3 kg and the opening angle of rear structures from 26° to 45°.

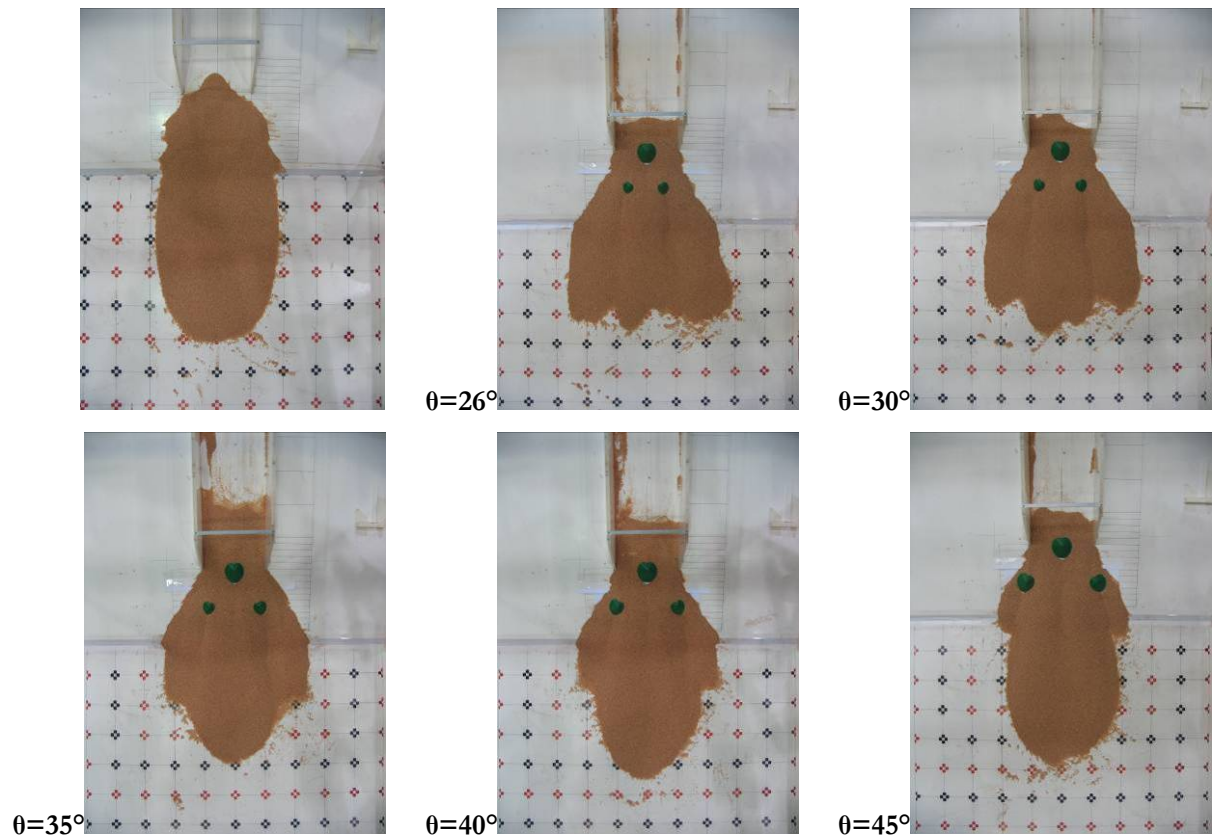


Fig. 6.72 – Deposit shapes: upper plane tilting of 24° , circular base cones, granular material weight of 3 kg and the opening angle of rear structures from 26° to 45° .

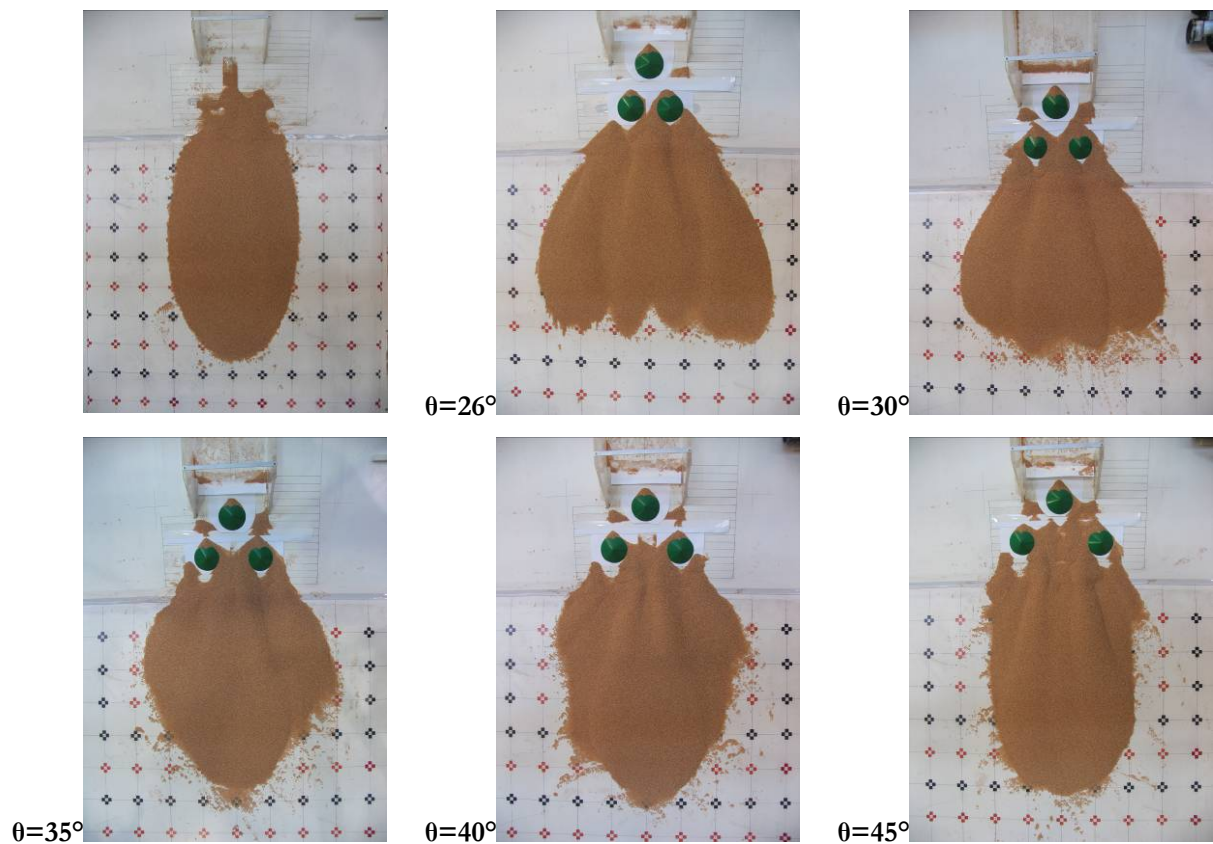


Fig. 6.73 – Deposit shapes: upper plane tilting of 27° , circular base cones, granular material weight of 3 kg and the opening angle of rear works from 26° to 45° .

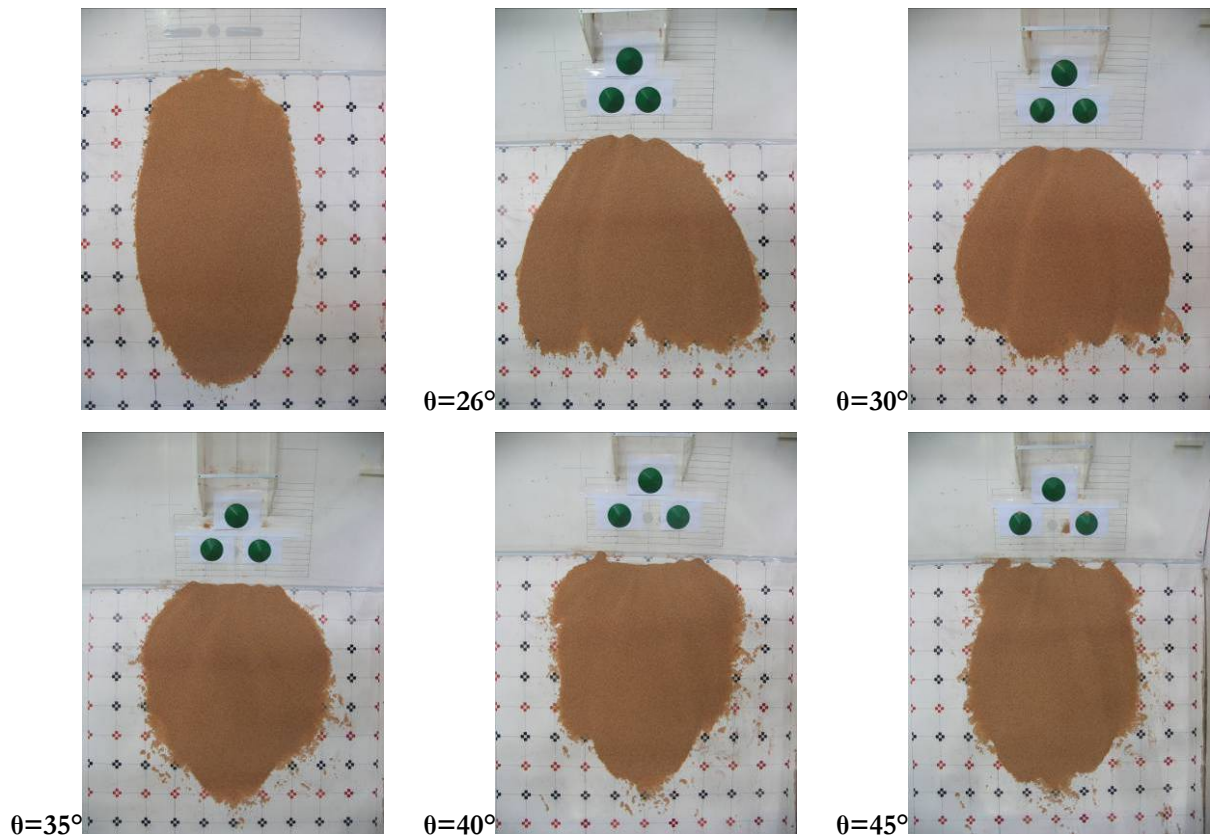


Fig. 6.74 – Deposit shapes: upper plane tilting of 30° , circular base cones, granular material weight of 3 kg and the opening angle of rear structures from 26° to 45° .

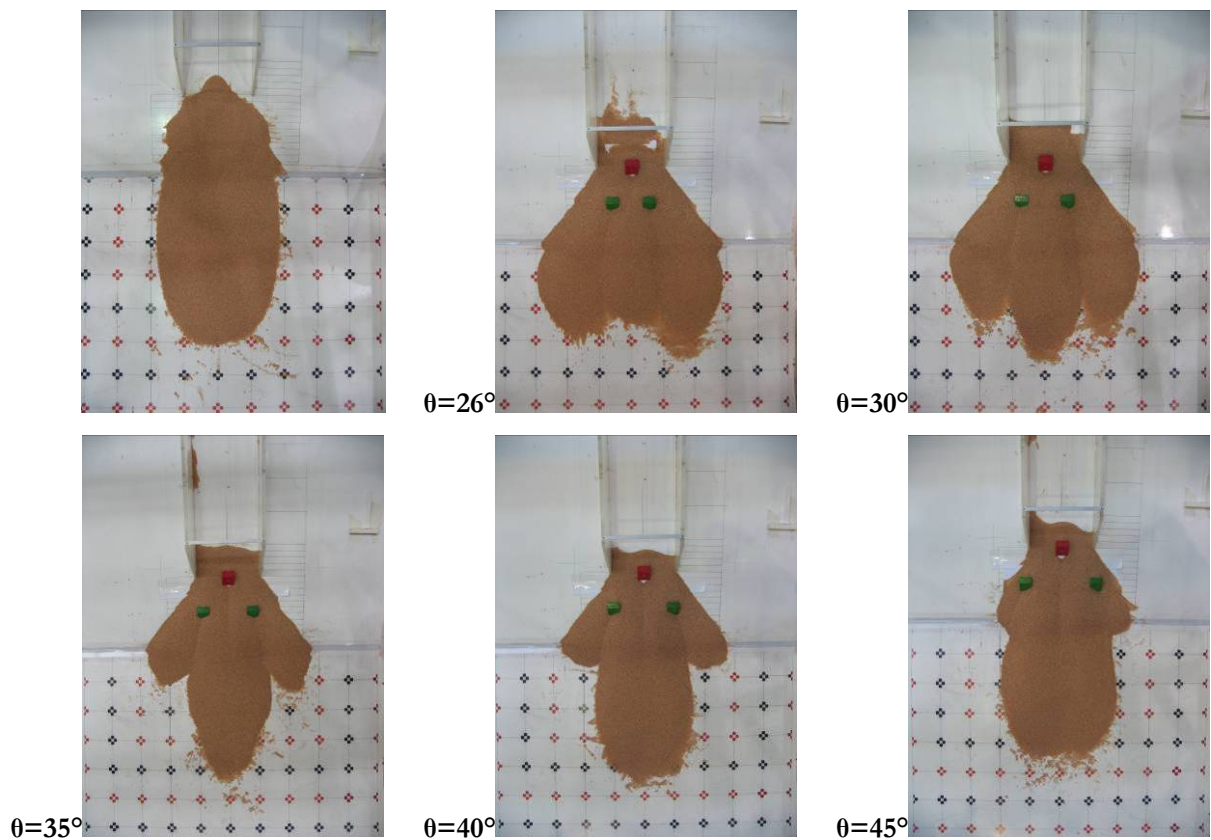


Fig. 6.75 – Deposit shapes: upper plane tilting of 24° , tooth-shaped structures, granular material weight of 3 kg and the opening angle of rear structures from 26° to 45° .

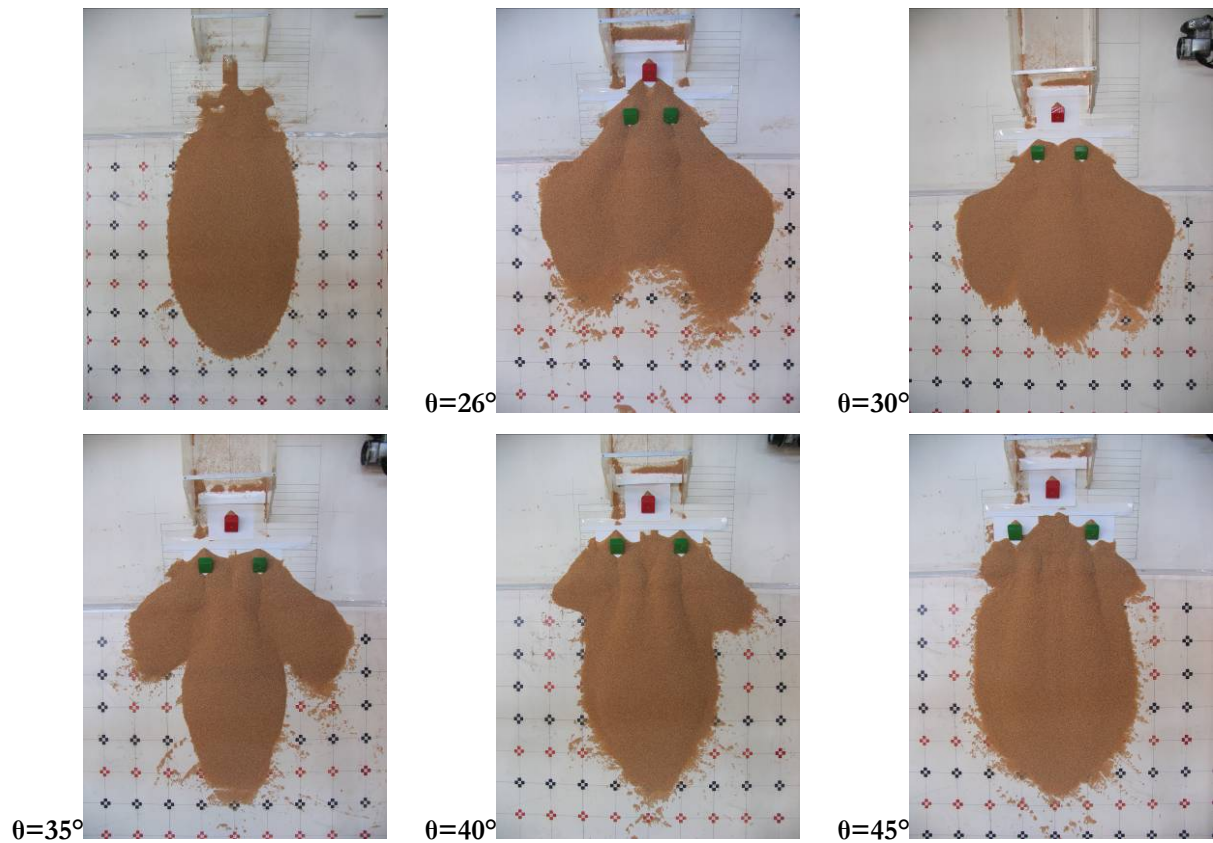


Fig. 6.76 – Deposit shapes: upper plane tilting of 27°, tooth-shaped structures, granular material weight of 3 kg and the opening angle of rear structures from 26° to 45°.

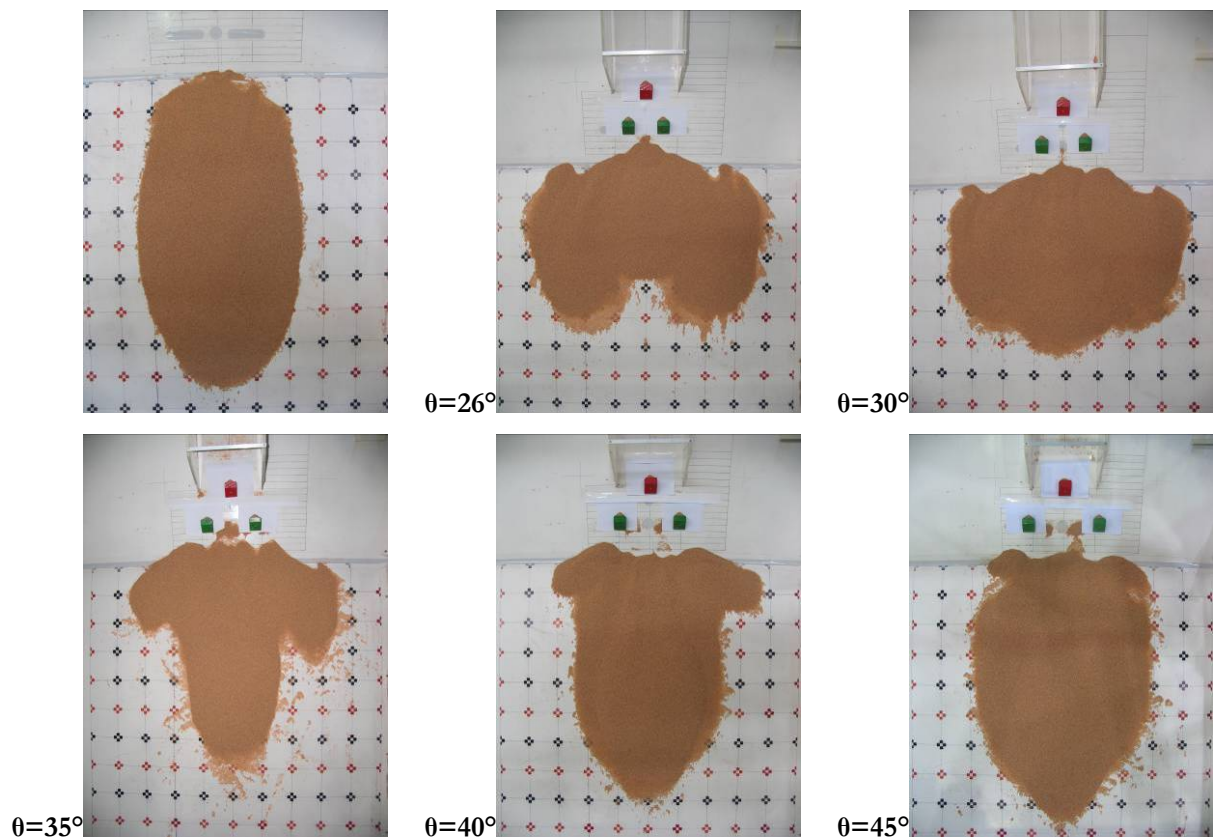


Fig. 6.77 – Deposit shapes: upper plane tilting of 30°, tooth-shaped structures, granular material weight of 3 kg and the opening angle of rear structures from 26° to 45°.

Cross-sectional and longitudinal efficiency. The efficiencies of the systems are plotted when the opening angle of rear works varies from 26° to 45° (Fig. 6.78-Fig. 6.79).

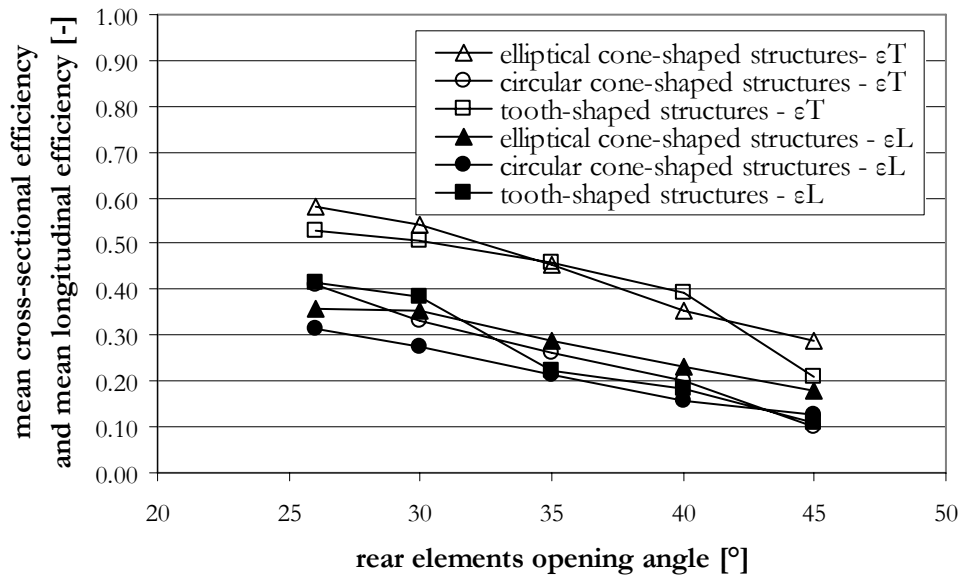


Fig. 6.78 – Behaviour of the mean value of cross-sectional and longitudinal efficiency when the opening angle varies from 26° to 45° .

All the retarding systems tend to reduce their longitudinal and cross-sectional efficiency when the opening angle is larger than 26° . Around 26° - 30° the efficiency of tooth-shaped structures and elliptical base cones appears to be greater than that of circular base cones. However, when using cones a more regular behaviour of the efficiency loss is noticeable as the opening angle increases. The maximum longitudinal and cross-sectional efficiency tends to occur when the maximum dimensionless force occurs.

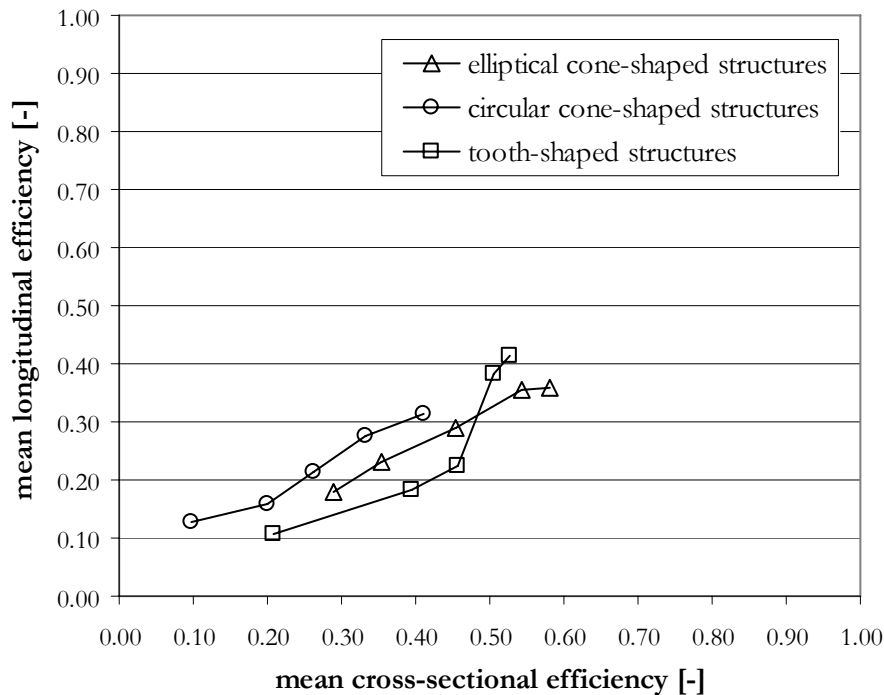


Fig. 6.79 – Relationship between mean values of longitudinal and cross-sectional efficiency for the various type of retarding structure systems.

6.10 Conclusions

The experimental analysis provides important information on how these types of structures behave, confirming and improving the knowledge acquired with previous experimental campaigns [Bezzi, 2004; Pederzoli, 2006].

In the case of only one element with a conical shape, the dimensionless impact force has values varying in a fixed range (independently from the type of experiment), while in the case of one tooth-shaped element, the dimensionless impact force depends on the ratio between the flowing depth and the height of the element. When three elements interfere with the motion, the maximum non-dimensional impact force against the rear elements is registered when the angle θ is 30° . Accordingly, maximum efficiencies are obtained with θ included between 26° and 30° .

The tooth-shaped elements proved themselves to be more effective than cone-shaped elements, offering a greater resistance to the motion.

Chapter 7

NUMERICAL-MATHEMATICAL ANALYSIS OF A STUDY SITE: THE *VAL DEI SPINI* AVALANCHE

This study describes a procedure for the determination of the snow avalanches hazard map. The procedure has been developed after the observation over some years of the behaviour of some avalanches sites located in the province of Trento, in the north-eastern part of Italy and is applied to one case study: the site of the *Val dei Spini* (*Val di Pejo*, *Trentino Alto Adige* Region, Italy). The dynamics of granular avalanches was simulated by means of a 1-D model [Scotton et al., 2006].

SnowScotton, by Paolo Scotton – *Dipartimento di Ingegneria Civile e Ambientale, Università di Trento, Italy*, is a one-dimensional numerical model with variable width based on the rheology of Savage & Hutter (1989).

The snow mass of the avalanche is defined statistically estimating the seasonal precipitation of fresh snow and snow density, and the surface of the accumulation catchments.

In SnowScotton model, the snow mass of the avalanche is distributed in the channels in the upper part of the basin; the snow density and the depth are defined using schemes that follow the observed natural behaviour. The physical parameters of the numerical and mathematical model, and in particular the Coulombian bottom friction coefficient, are calibrated on the basis of the knowledge of extreme events associated to defined return period almost in an arbitrary way, given the law historical sample site. The physical parameters vary along the flowing and the stopping zones depending on the volume of the avalanche and, consequently, on the return period.

It is hypothesized that, in the stopping area, the avalanche can travel different trajectories, defined on the basis of the local topography and on the assumption that the most likely trajectory, the one defined by the maximum slope, can be modified by unpredictable causes of deviation (for instance the deposit of a previous avalanche).

The hazard zone is divided into three areas: the **red area**, associated to a return period of **30 years**, the **blue area**, associated to a return period of **100 years**, and the **yellow area**, associated to a return period of **300 years**. The different areas are defined by the conjunction of the points representing the stopping distances along the different trajectories for the same return period [Scotton et al., 2006].

A 2-D model has been selected with the aim to define the hazard map already realized with the first model. The necessary physical parameters have been calibrated by means of both two events.

FLO-2D™, **two dimensional flood routing model** by Jim O'Brien, Craig R. Jorgensen, Reinaldo Garcia and HydroSoft, C.A. – *FLO-2D Software, Inc., Nutrioso, USA*, is a dynamic flood routing model that simulates channel flow, unconfined overland flow and street flow. The model uses the full dynamic wave momentum equation and a central finite difference routing scheme with eight potential flow directions to predict the progression of a flood hydrograph over a system of square grid elements.

7.1 The study site: the *Val dei Spini* avalanche

7.1.1 Geographical setting

The avalanche site of *Val dei Spini* is located in the north-western part of the *Trentino Alto Adige* Region, in Italy, near the border with the *Lombardia* Region, south of the group of *Ortles-Cevedale*.

The *Val dei Spini*, oriented NE-SW, is a lateral valley of the *Val di Pejo*, oriented NW-SE (Fig. 7.1). *Val di Pejo* merges to the *Val Vermiglio*, creating the *Val di Sole*, with a west-east orientation.

The basin of *Val dei Spini* (Fig. 7.2-7.3) is characterized by an intense avalanche activity with an event periodicity almost annual.

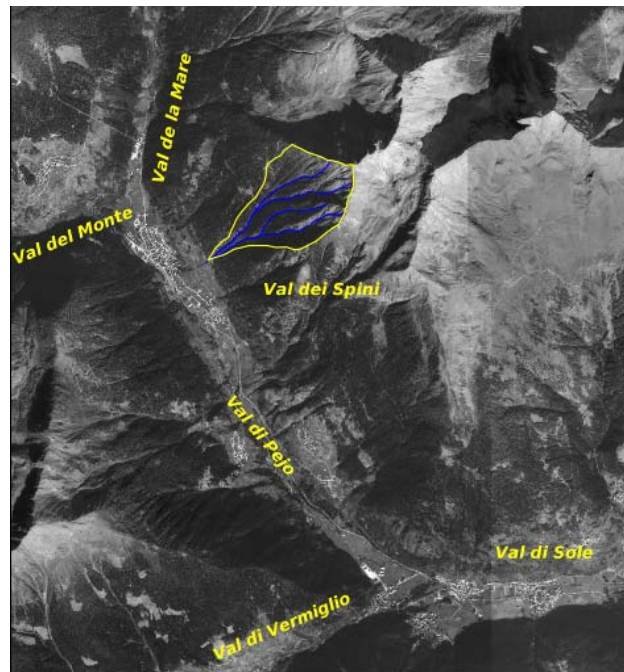


Fig. 7.1 – Geographical setting of the *Val dei Spini* [Scotton et al., 2002].



Fig. 7.2 – IGM map extract: the *Val dei Spini* catchments (scale 1:25.000)
[<http://www.pcn.minambiente.it>]

The morphology is funnel-shaped above the tree line (about 2300 m a.s.l.), with mean slopes of about 35°-40°.

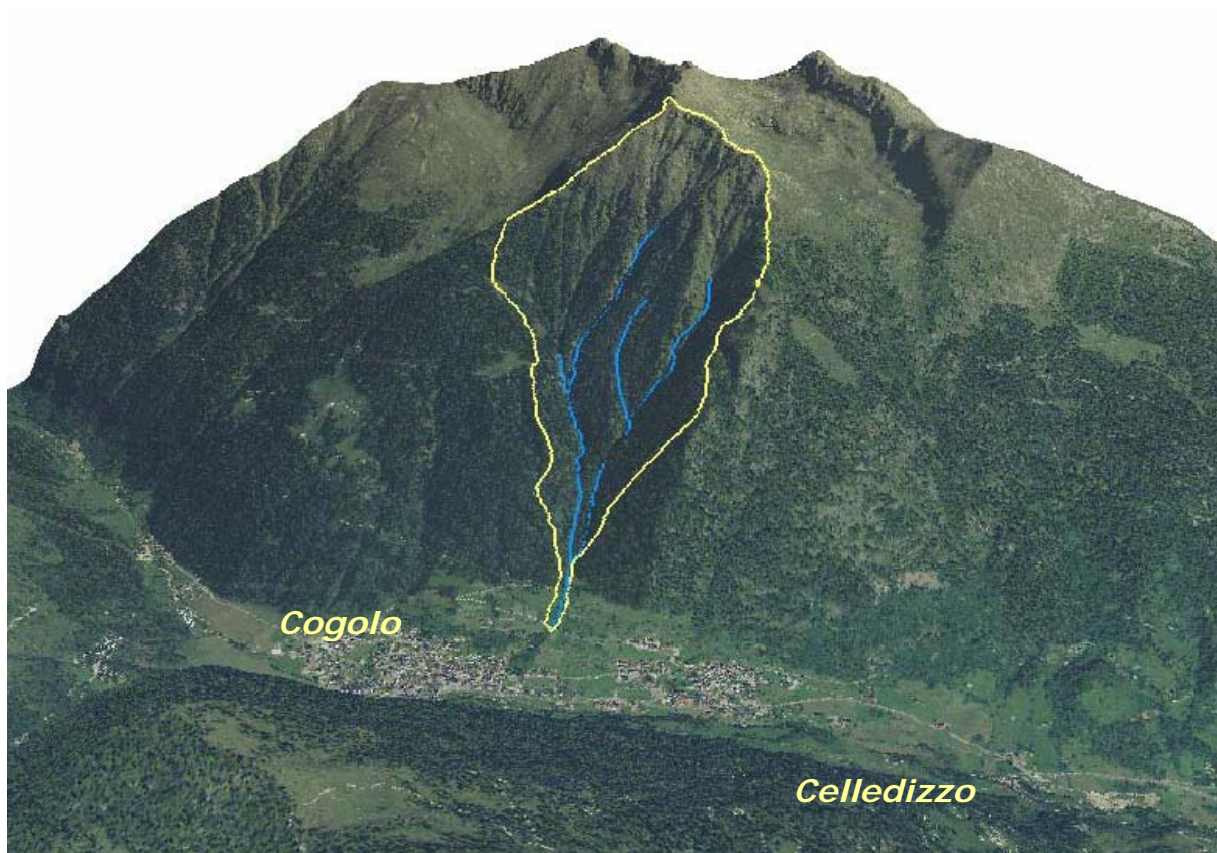


Fig. 7.3 – Scenic-view of the study site with the *Val dei Spini* catchments [DTM and Ortho photo, Provincia Autonoma di Trento].

7.1.2 Geological setting

The table 42 IV “PEIO” (Fig. 7.4) at the scale of 1:25.000 corresponds to the quadrant NO of the Sheet n°42, *Malè*, of the Italy Geologic Map at the scale of 1:50.000 and it is located in the western *Trentino Alto Adige* Region. It takes its name from the village of *Pejo* situated at the *Ortles-Cevedale Group* between the *Val del Monte*, the *Val de la Mare* and the *Val di Pejo*, at the western extremity of the table (Fig. 7.1).

The detachment area and the flowing channels are characterized by metamorphic rocks that appear in many sections.

The alluvial fan is formed by coarse material, formed by big boulders in sandy-gravelly matrix resulting from the physical and chemical weathering rocks of the catchments area and transported downstream by streams and avalanches [Scotton et al., 2002].

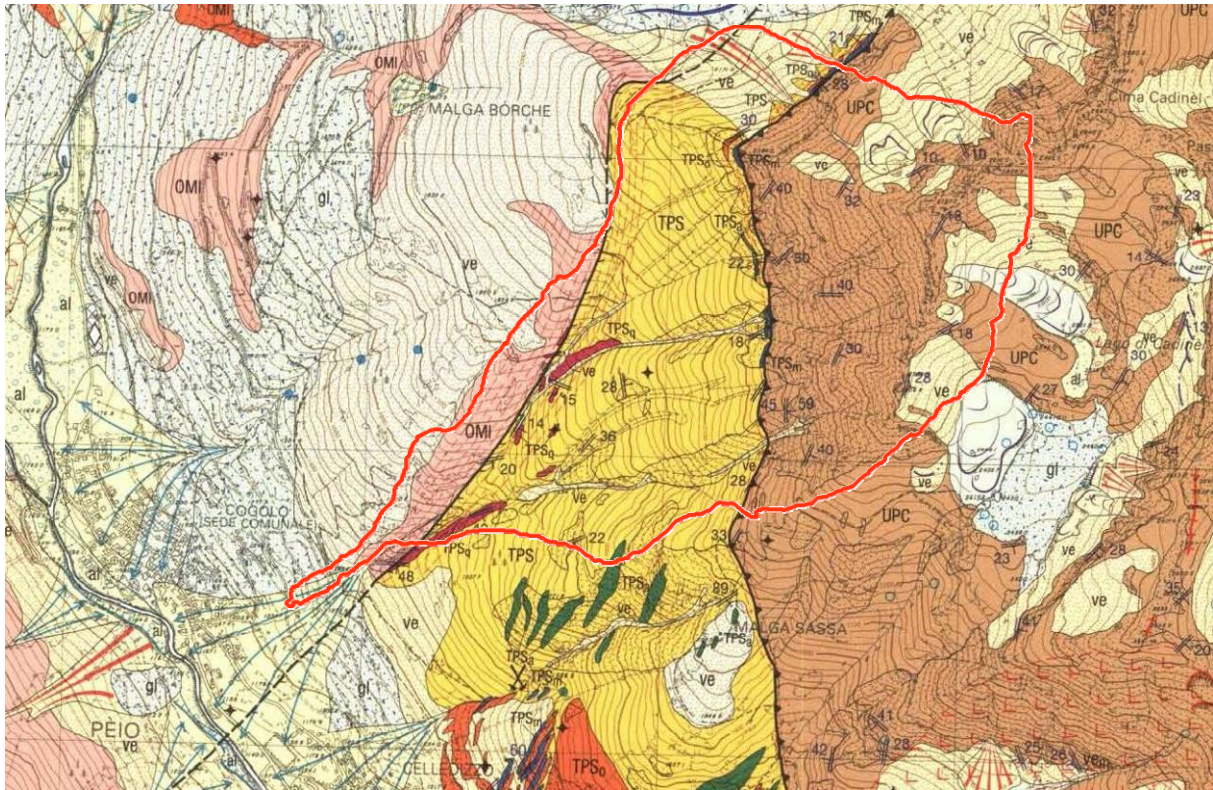


Fig. 7.4 – The geological map of the Val dei Spini catchments (scale 1:25,000) [Martin et al., 2001].

7.1.3 Geomorphological setting

The basin of *Val dei Spini* develops from a height of 1310 m a.s.l., where the fan is located, to a maximum height of 2775 m a.s.l. In few points inside the basin, the sides slopes get down under 30° and in the storage basin it keeps on average about 45° . Only on the fan the inclination gets down under 20° .

Four main storage basins can be distinguished in the *Val dei Spini* (Fig. 7.5). The avalanches start at elevation 2200 and 2300 m a.s.l. prevailing on south-west and west slopes. The mean exposure is west-south-west.

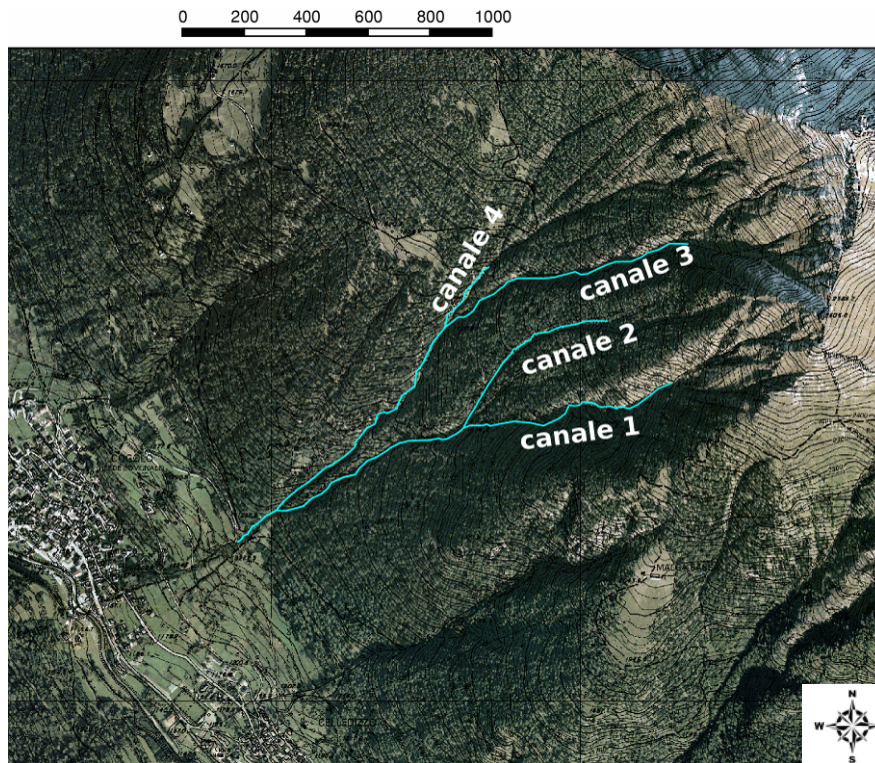


Fig. 7.5 – The four main channels of the *Val dei Spini* [Scotton et al., 2006].

The channel 1 gets down from the burned forest, on the left side of the basin of *Val dei Spini*. The channel 2 is a tributary of the channel 1, with a reduced feeding basin. The channel 3 is the central channel. The channel 4 gets down under the separation ridge with the *Val di Levi*.

The longitudinal profiles are initially almost identical, with growing inclinations from 15° on the fan to $20\text{-}25^\circ$ at the height of 1600 m a.s.l. Upstream channels 1 and 2 inclinations grow quickly to a mean value of 30° and maximum values of 40° . The channel 3 and the channel 4 begin to have on average inclination higher than 30° only over 1800 m a.s.l. [Scotton et al., 2006].

In Fig. 7.6-Fig. 7.7 the slope and the exposure map are presented.

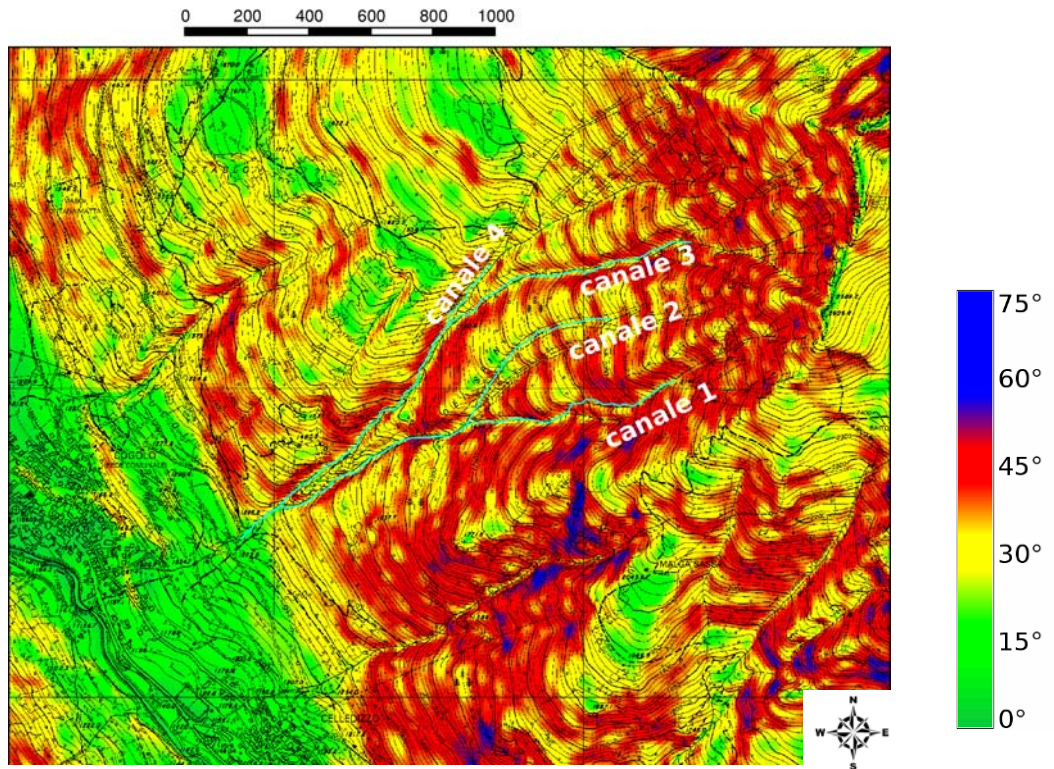


Fig. 7.6 – The slope map of the *Val dei Spini* [Scotton et al., 2006].

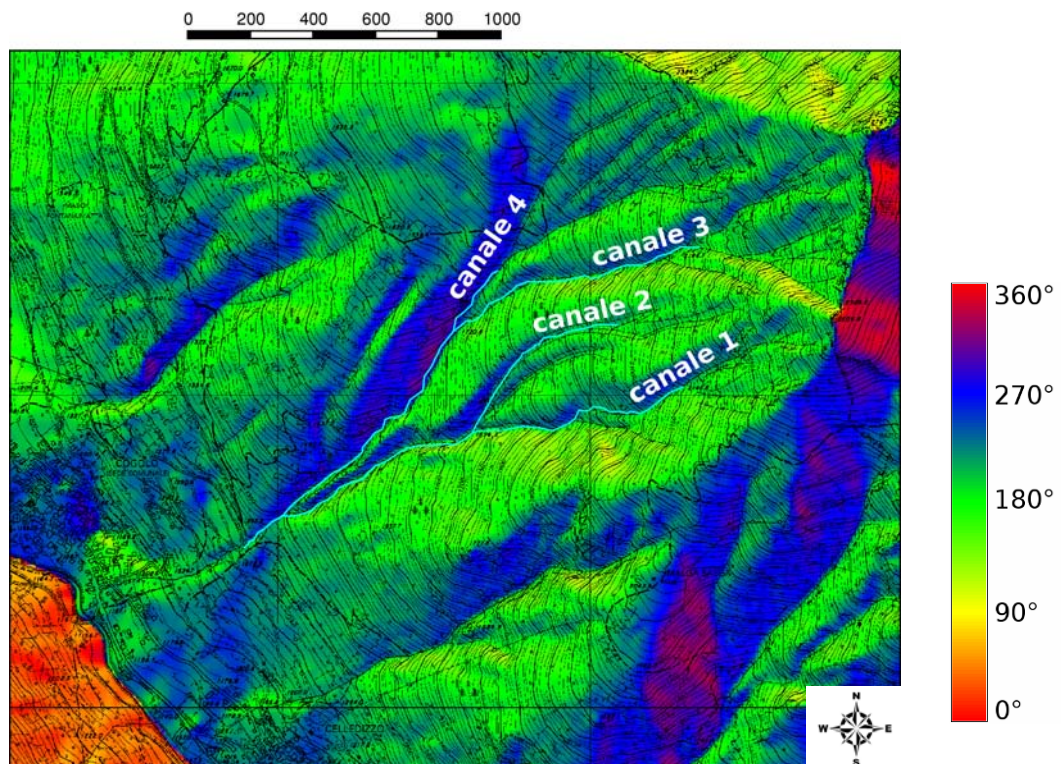


Fig. 7.7 – The exposure map of the *Val dei Spini* [Scotton et al., 2006].

7.1.4 Forestal setting

The covering is almost exclusively formed by high forest. At the lower heights (Fig. 7.8a) there are the red fir (*Picea abies*) and the larch (*Larix decidua*). In wide zones the larch (*Larix decidua*) is the dominant specie, depending on the exposure. At higher elevations (Fig.7.8b/c), the larch becomes the exclusive species, because the low temperatures and the snow movements create an hostile environment for the red fir development. At elevation higher than 2200 – 2400 m a.s.l. the vegetation disappears (Fig. 7.8d).

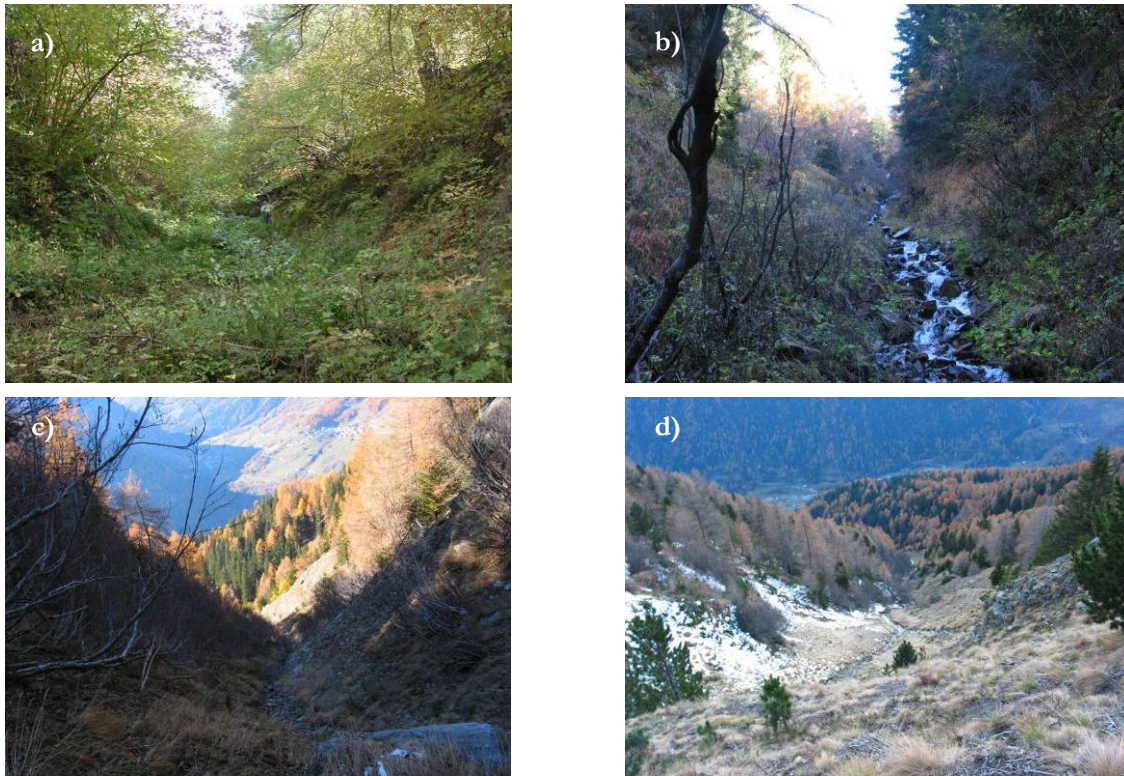


Fig. 7.8 – Vegetation in the Val dei Spini: a) in the accumulation zone; b)c) in the flowing zone; d) in the detachments zone [Scotton et al., 2006].

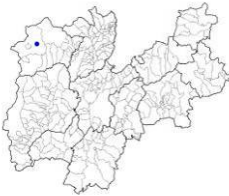

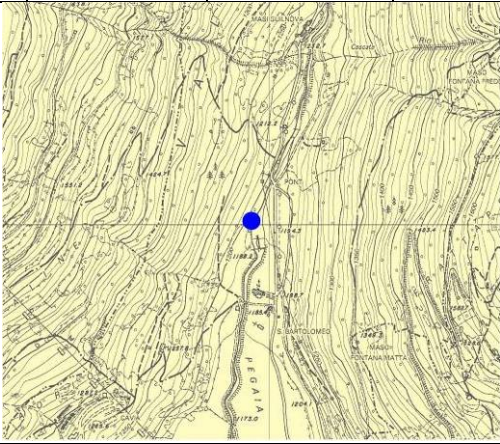


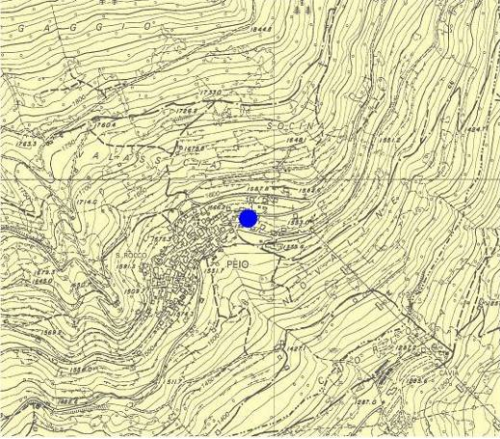


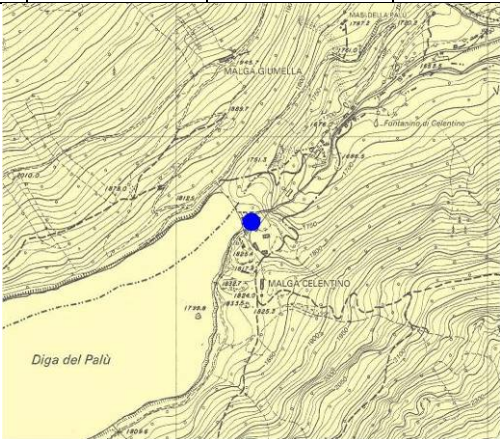
Along the avalanche tracks, white alder (*Alnus incana*), green alder (*Alnus viridis*) and birch (*Betulla pendula*) are growing; elsewhere the broad-leaves are present; sporadically. The green alder (*Alnus viridis*) is especially located along the steep sides and the canyons interested by avalanche phenomena, while borders are generally colonized by the larch (*Larix decidua*).

The soils have a siliceous composition, so it is absent the mountain pine (*Pinus mugo*) which prefers calcareous soils.

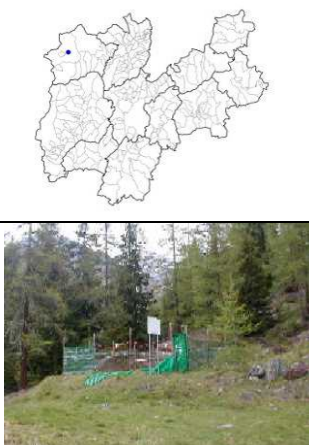
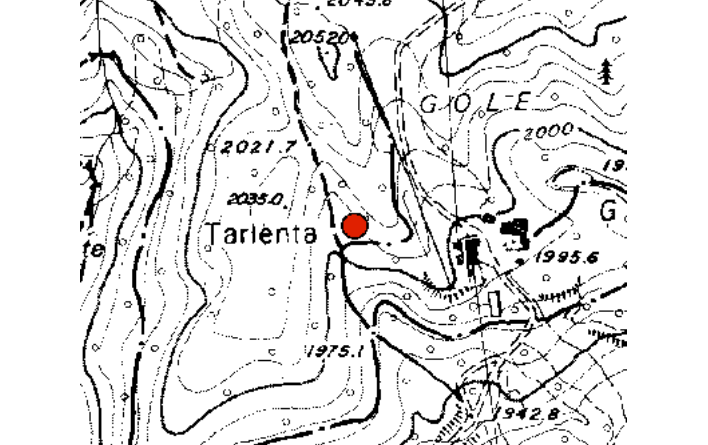
7.1.5 Climatic setting

The valley presents the typical climate of the south sides versant of the Central Alps and it is moderately subjected to the effects of the influence of the *Padano* climate. The local thermal and pluviometric trend is considerably complicated by the altitude and the slopes exposure.

The precipitations have been determined on the basis of the available data of the meteorological measurements stations of *Cogolo Pont* (1185 m a.s.l.), *Pejo* (1565 m a.s.l.), *Pian Palù* (1795 m a.s.l.) (Table 7.1).

Table. 7.1 – Climatic meteorological measurement stations [http://www.meteotrentino.it/].					
Station	Height	Coord. EAST	Coord. NORTH	Rain data	Temperature data
	[m a.s.l.]	Gauss-Boaga			
Cogolo Pont	1185	1629885	5135701	1929-2008	1973-2008
					
Pejo	1565	1628924	5135878	1921-2007	1925-2007
					
Pian Palù	1795	1624241	5132728	1978-2008	1973-2008
					

The snowpack depth used to estimate the volumes for the simulated avalanches, the wind and the temperature data have been determined on the basis of the available data of the snow-meteorological measurements station of *Pejo-Tarlenta* (height 2010 m a.s.l.) (Table 7.2).

Table 7.2 – Snow-meteorological measurements station [http://www.meteotrentino.it].				
Station	Height	Coord. EAST	Coord. NORTH	Snow data
	[m a.s.l.]	Gauss-Boaga		
Pejo-Tarlenta	2010	1627598	5136569	1981-2008
				

Precipitations. Precipitations are well distributed in the year with spring and autumnal maximums. Snow precipitations interest the months from November to March. In January and February there are low snow precipitations (Fig. 7.9).

The pluviometric regime is summer solstitial with a maximum of precipitation at the peak of the vegetative season. At *Fucine*, at the entrance of the *Val di Pejo*, the pluviometric regime is already more affected by Mediterranean regime [Scotton et al., 2006].

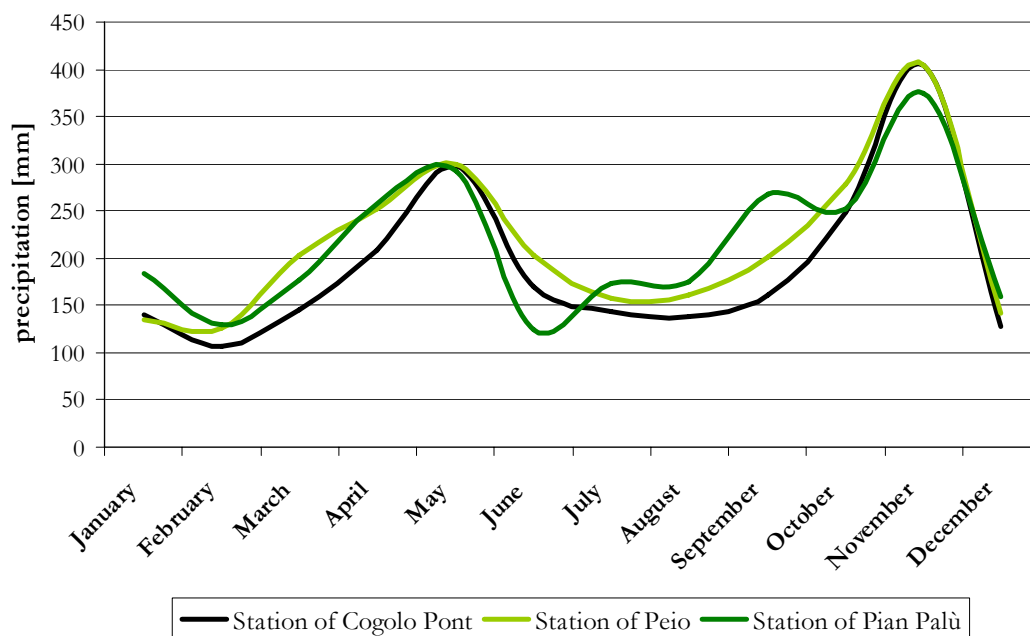


Fig. 7.9 – Monthly total precipitations values in three meteorological stations: Station of *Cogolo Pont* (1185 m a.s.l.), *Pejo* (1565 m a.s.l.), *Pian Palù* (1795 m a.s.l.). The data cover the period from 1978 to 2008.

Temperature. From the temperature data analysis register at the station of *Pejo-Tarlenta*, it is possible to observe as the annual average temperature is equal to -4°C (Fig. 7.10). The coldest month is January, while the hottest month is August. Both the thermal excursions of the monthly averages and the thermal excursions between day and night are remarkable. The frosts in May/June and September/October are frequent [Scotton et al., 2002].

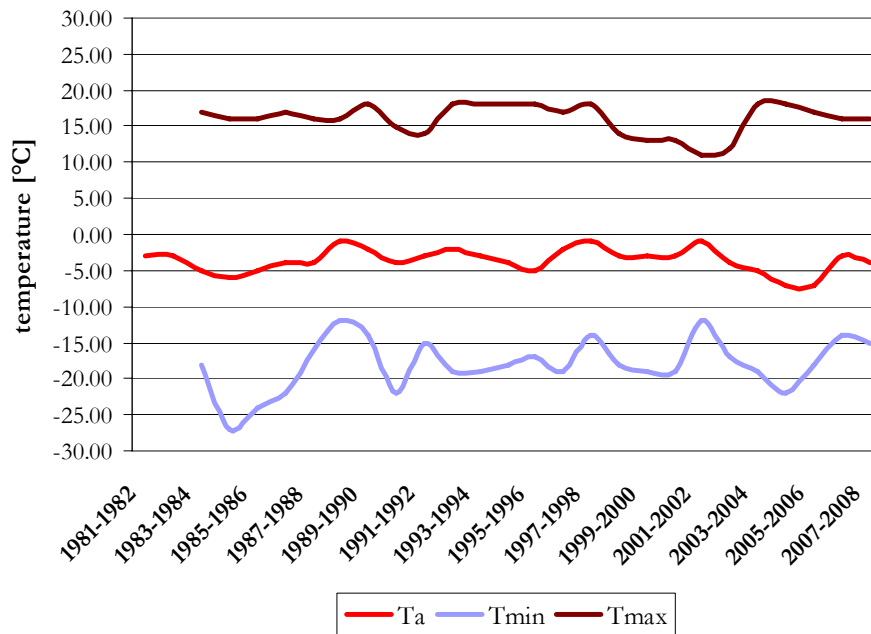
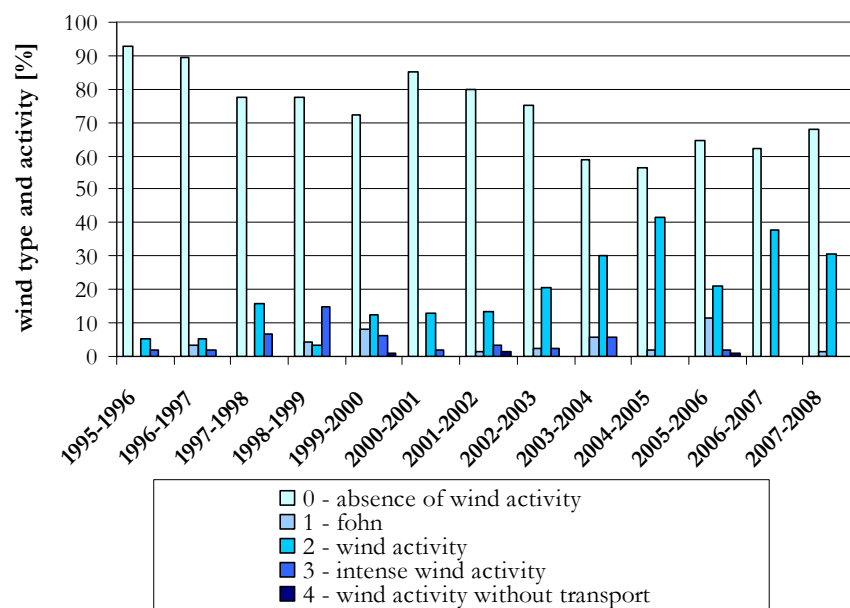


Fig. 7.10 – Mean air temperature values (T_a) and maximum/minimum air temperature values (T_{\min} , T_{\max}) at the meteorological station of *Pejo-Tarlenta* (2010 m a.s.l.). The data cover the period from 1978 to 2008.

Wind. The prevailing winds come from west and south-west in spring and autumn, while in summer there are south-east winds. Winds coming from other directions are very rare [Scotton et al., 2002]. (Fig. 7.11).

a)



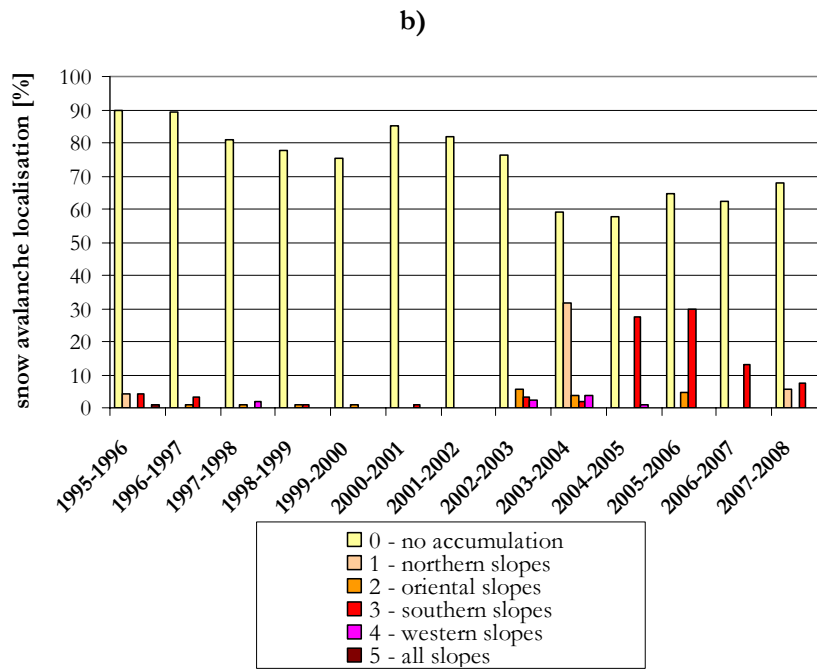


Fig. 7.11 – a) Above, wind type and activity (VQ1); b) above, localisation snow avalanche (VQ2) at the meteorological station of *Pejo-Tarlena* (2010 m a.s.l.). The data cover the period from 1978 to 2008.

Snow depth. The data cover the period from 1981 to 2008 (Fig. 7.12-Fig. 7.14).

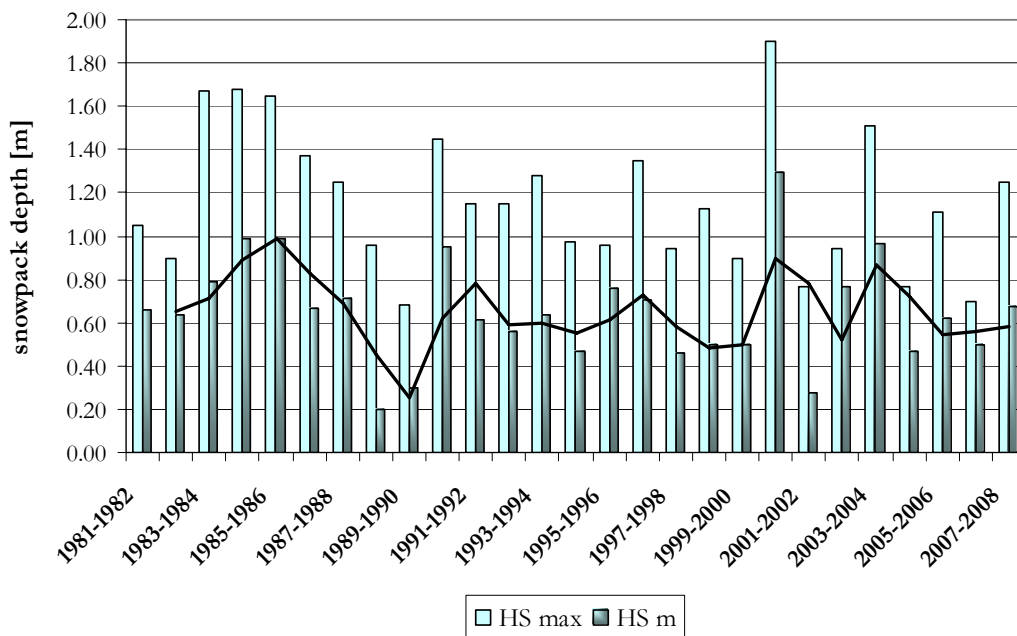


Fig. 7.12 – Maximum and mean snowpack depth values (HS) at the meteorological station of *Pejo-Tarlena* (2010 m a.s.l.).

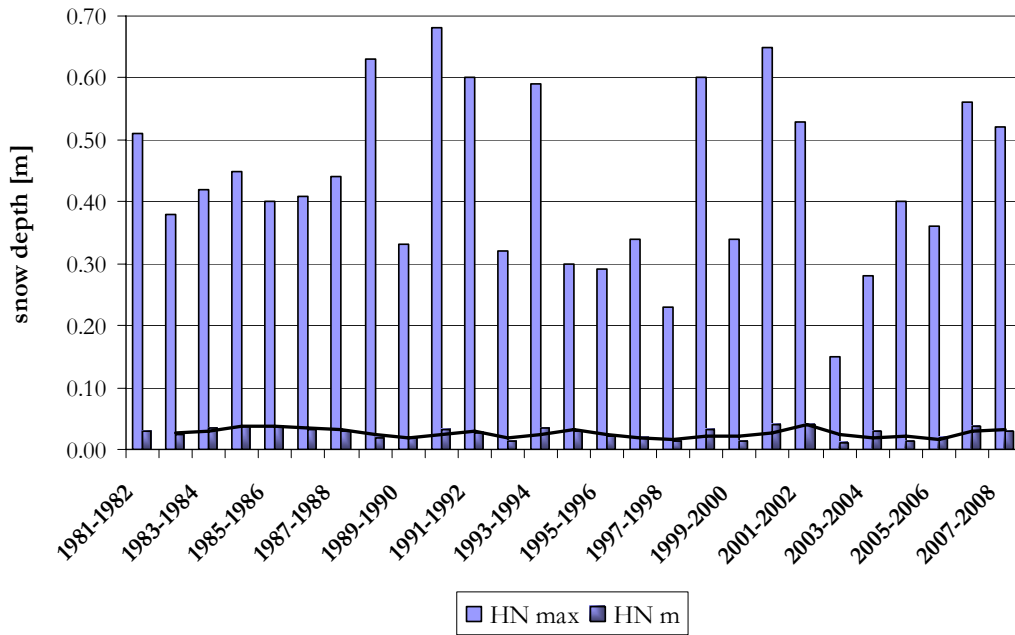


Fig. 7.13 – Maximum and mean fresh snow depth values (HN) at the meteorological station of *Pejo-Tarlenta* (2010 m a.s.l.).

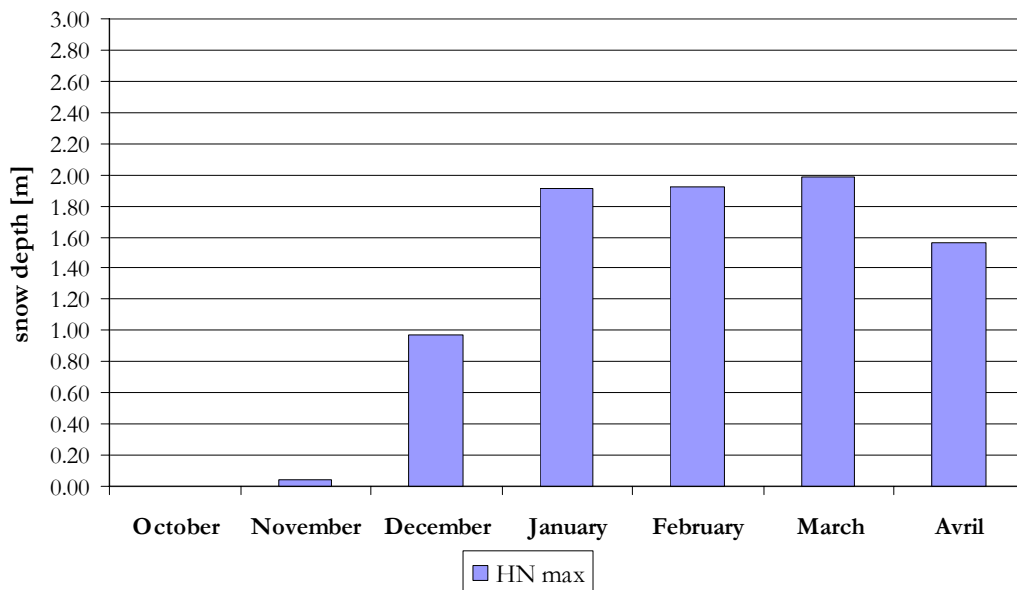


Fig. 7.14 – Monthly maximum fresh snow depth values (HN) at the meteorological station of *Pejo-Tarlenta* (2010 m a.s.l.).

7.1.6 Statistical analysis of snow-meteorological data

It has been adapted the Gumbel and Lognormal distribution with two different estimate methods of the parameters, to calculated the annual maximums on three consecutive days (Table 7.3-Table 7.4).

Table 7.3 – Snow maximal depths values at the meteorological station of *Pejo-Tarlenta*. The data cover the period from 1981 to 2008.

Station	Year	Snowpack depth HS max	Fresh snow depth HN max	Fresh snow depth on three consecutive days DH3gg max	Accumulated frequency
		[m]	[m]	[m]	
<i>Pejo-Tarlenta</i>	2002 – 2003	0,94	0,15	0,24	0,04
	1995 – 1996	0,96	0,29	0,31	0,07
	1997 – 1998	0,94	0,23	0,36	0,11
	1989 – 1990	0,68	0,33	0,39	0,14
	1994 – 1995	0,97	0,30	0,44	0,18
	1992 – 1993	1,15	0,32	0,45	0,21
	2003 – 2004	1,51	0,28	0,45	0,25
	1982 – 1983	0,90	0,38	0,50	0,29
	1981 – 1982	1,05	0,51	0,53	0,32
	1985 – 1986	1,65	0,40	0,57	0,36
	2001 – 2002	0,77	0,53	0,58	0,39
	2004 – 2005	0,77	0,40	0,58	0,43
	2005 – 2006	1,11	0,36	0,61	0,46
	1987 – 1988	1,25	0,44	0,63	0,50
	1999 – 2000	0,90	0,34	0,66	0,54
	1996 – 1997	1,35	0,34	0,67	0,57
	1986 – 1987	1,37	0,41	0,68	0,61
	2006 – 2007	0,70	0,56	0,70	0,64
	1983 – 1984	1,67	0,42	0,73	0,68
	1998 – 1999	1,13	0,60	0,73	0,71
	2000 – 2001	1,90	0,65	0,75	0,75
	2007 – 2008	1,25	0,52	0,77	0,79
	1984 – 1985	1,68	0,45	0,81	0,82
1990 – 1991	1,45	0,68	0,82	0,86	
1991 – 1992	1,15	0,60	0,85	0,89	
1993 – 1994	1,28	0,59	0,92	0,93	
1988 – 1989	0,96	0,63	1,19	0,96	

Table 7.4 – Maximal values of snow depth on three consecutive depth realised with the statistical distributions of Gumbel and Lognormal for the $T_r = 30, 50, 100, 300$ years.

Distribution	Parameters estimation method	$T_r = 30$ years	$T_r = 50$ years	$T_r = 100$ years	$T_r = 300$ years
		[m]	[m]	[m]	[m]
Gumbel	Method of moments	1,08	1,16	1,27	1,45
	Maximum likelihood estimation	1,15	1,24	1,37	1,57
Lognormal	Method of moments	1,07	1,15	1,25	1,42
	Maximum likelihood estimation	1,12	1,21	1,33	1,52

7.1.7 Avalanche protection structures

In the 2003 the *Provincia Autonoma di Trento* has decided to realise some active defence structures, snow nets, at the height of 2400 – 2700 m a.s.l., to defence the villages of *Cogolo* and *Celledizzo* (Fig. 7.15-Fig. 7.17).

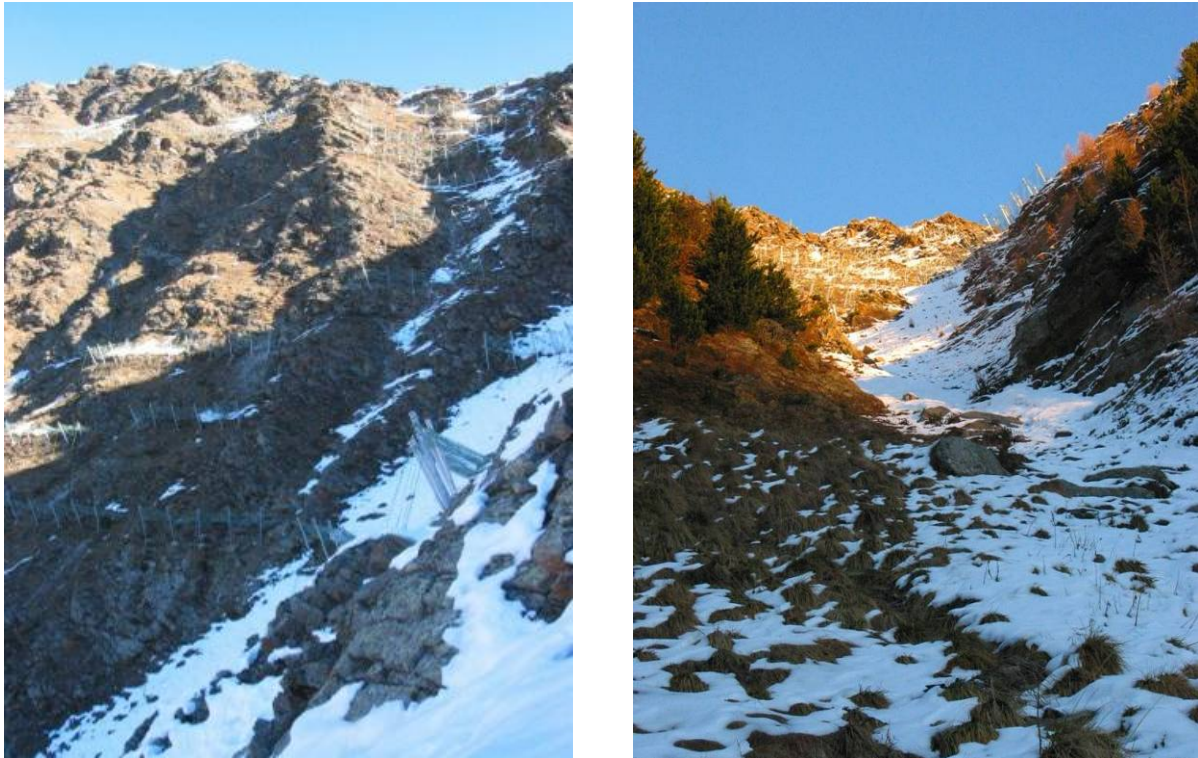


Fig. 7.15 – Two views of the snow nets in the *Val dei Spini* [Scotton et al., 2006].

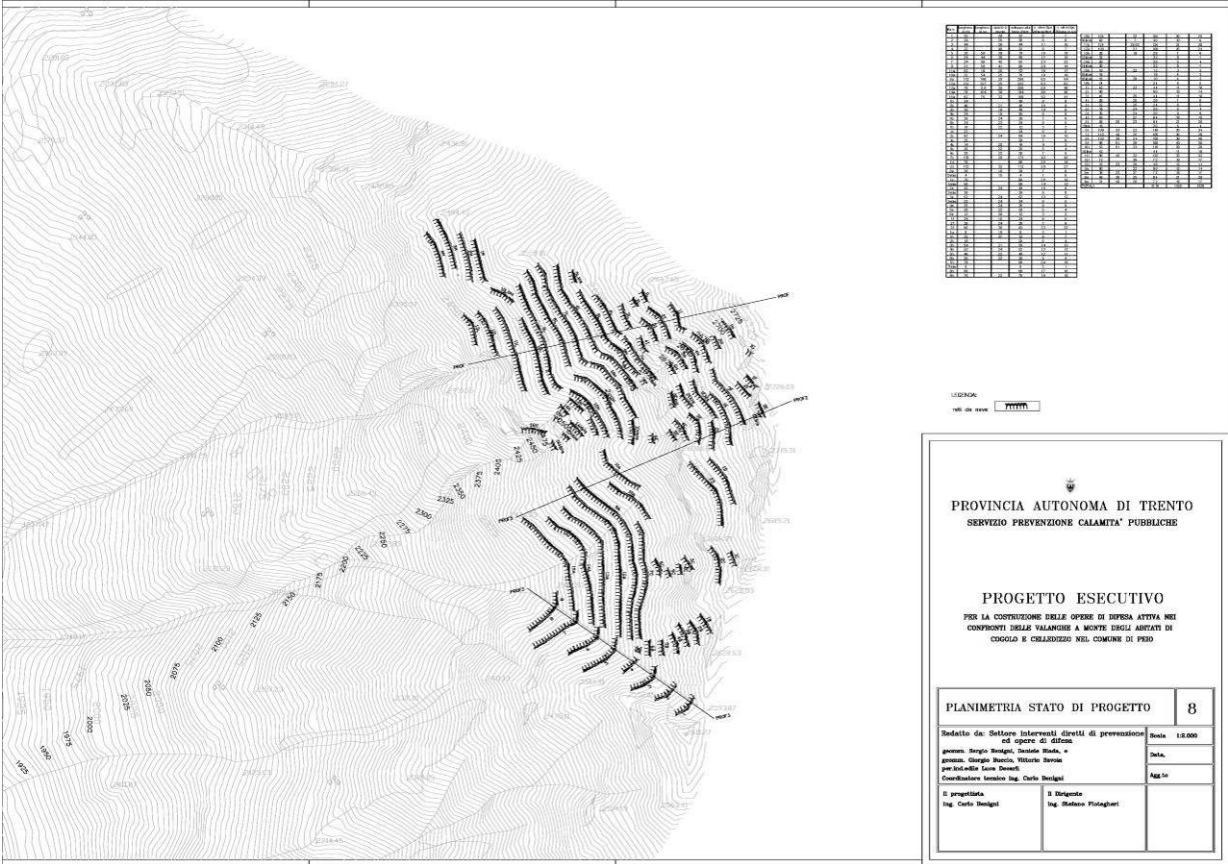


Fig. 7.16 – Project for the realisation of active defence structure [Provincia Autonoma di Trento, 2003]



Fig. 7.17 – The project area [Provincia Autonoma di Trento, 2003].

7.1.8 Historical analysis of the avalanche events

In the CLPV (*Carta di Localizzazione Probabile delle Valanghe*) (Fig. 7.18), the map of avalanche probable localisation, the *Val dei Spini* avalanche is defined like as avalanche with an almost annual occurrence.

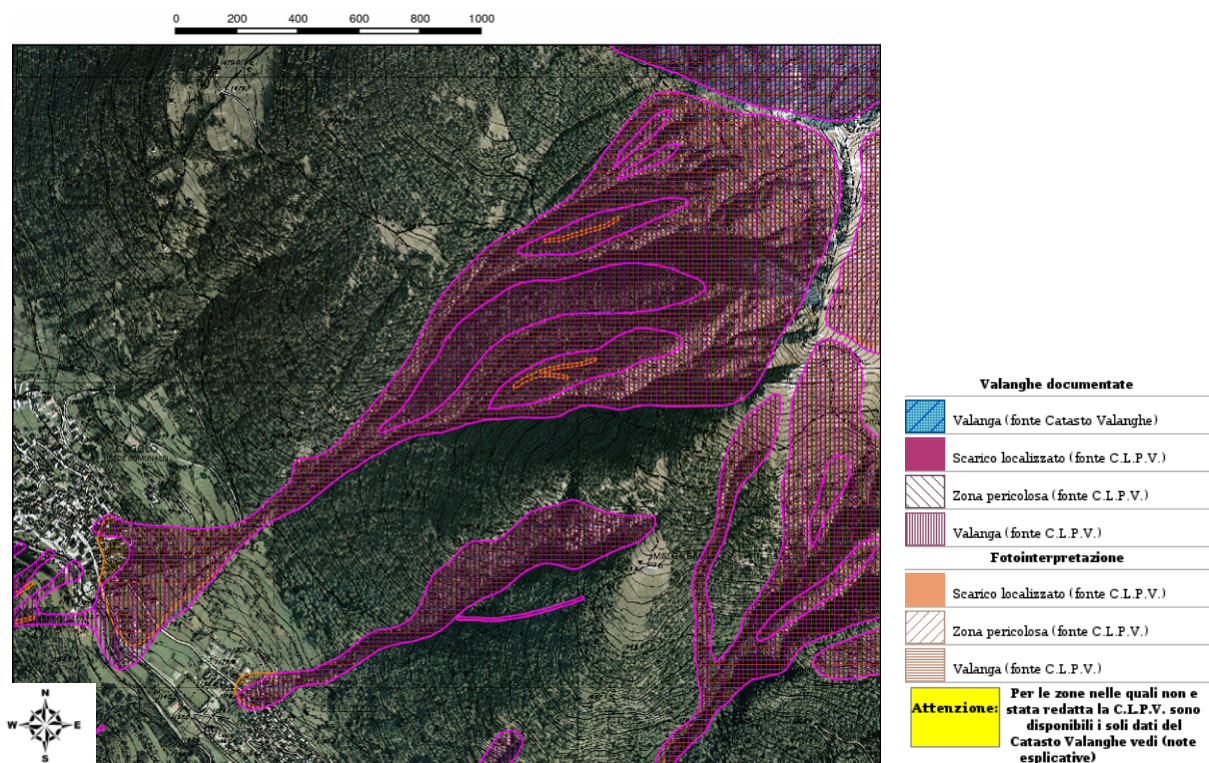


Fig. 7.18 – CLPV, map of avalanche probable localisation of the *Val dei Spini* [Provincia Autonoma di Trento].

Normally avalanches of wet snow occurred at the end of the winter season and in spring. It has been surveyed only a single case, verified on December 22nd 1979, characterized by dry snow with weak cohesion. The more probable detachment mechanism is the following: during the winter, after a snow precipitation there are frequent discharges from the steep sides that fill the canyon head zone; the snow accumulates here; spring temperature raisings or overloads due to fresh snowfalls, triggers the movement of the avalanches. Also small dimension avalanches, with volumes of few thousands cubic metres, easily reach the fan at the height of 1250 m a.s.l. in the spring period, if some events occurred during the previous months, have brought progressively the front of the avalanche deposits to low height, reducing in this way the channel roughness. The most important avalanche events are presented in Table 7.5.

Table 7.5 – Historical avalanche events.

Date		Avalanche characteristics		Detachment zone			Flowing zone	Runout zone				
Year	Date	Snow	Causes	Height	Exposure	Description	Description	Height	Length	Width	Volume	Description
1901	-	Avalanche of wet snow.	Raising of temperature.	-	-	-	-	-	-	-	-	The avalanche, probably formed by the contemporary detachment of the two main basins, with a thickness of 7-8 m, has get down up to the torrent <i>Noce</i> , obstructing it and forming a dam which upstream caused the formation of a lake. In that event the avalanche almost reached a farm on the right bank of the <i>Noce</i> .
1908	-	-	-	-	-	-	-	-	-	-	-	The avalanche has reached the road bridge little upstream the provincial road; in that event, an avalanche branch took himself in direction of <i>Cogolo</i> and stopped at 7-8 m from a farm, about 50 m upstream the old municipality.
1932	-	Avalanche of wet snow.		-	-	-	-	-	-	-	-	The avalanche has reached the fields upstream the old municipality of <i>Cogolo</i> .
1972	March 13 th	Avalanche of wet snow.	Raising of temperature.	2300 m a.s.l.	W	At the top of the channel 4.	Canalized.	1250 m a.s.l.	1900 m	-	67500 m ³	The avalanche has produced light agricultural cultivation damages.

Date		Avalanche characteristics		Detachment zone			Flowing zone	Runout zone				
Year	Date	Snow	Causes	Height	Exposure	Description	Description	Height	Length	Width	Volume	Description
1977	-	-	-	-	-	-	-	-	-	-	-	Avalanche has stopped at about 10 m from the new settlements house, going beyond the road of <i>Borche</i> , destroying the little bridge.
1979	December 22 nd	Avalanche of dry snow and weak cohesion with solid transport.	Slope inclination and snow depth.	2200 m a.s.l.	SW	In the channel.	Canalized.	1250 m a.s.l.	150 m	70 m	30000 m ³	The avalanche has stopped near some infrastructures and it has caused damages to the bridge on the road to <i>Malga Borche</i> .
1986	May 1 st	Slab avalanche of wet snow.	Slope inclination.	2250 m a.s.l.	SW	At the top of the valley.	Canalized.	1250 m a.s.l.	150 m	50 m	3000 m ³	-
1987	April 4 th	Avalanche Surface of wet snow.	Slope inclination.	2200 m a.s.l.	SW	In different points.	Canalized.	Valley bottom	100 m	20 m	4000 m ³	The avalanche hasn't produced any damages.
1991	March 9 th	Avalanche Surface of wet snow and of weak cohesion.	Slope inclination.	2300 m a.s.l.	-	In the channel.	-	1300 m a.s.l.	-	-	-	-
1998	February 27 th	-	-	1700 m a.s.l.	-	-	-	1320 m a.s.l.	-	-	1000 m ³	-

7.1.9 Surveys on the avalanche site and topographical measurements

The field activity has been oriented to the survey of the avalanche parameters necessary for integrating the already available data. Its importance appears clear if one considers that avalanche phenomena characters are extremely dependent from the local site properties and that the number of events observed in the past is limited. Of special importance is the comprehension of the local detachment mechanisms, the snow mass volume evaluation and assessment of the dynamic parameters.

For a complete presentation of the avalanche site, some results of a previous study, realised in 2002 on the *Val dei Spini* avalanche, are presented.

The activity field has been developed from the beginning of winter 1997/98 to summer 1999, including two winter seasons [Scotton et al., 2002].

During the first winter season the basin has been equipped with 5 snow boles in order to evaluate the depth of the snow precipitation and the wind transport. The snow boles have been distributed in the basin, above the vegetation line, at elevation included between 2350 and 2400 m a.s.l. In the final part of the flowing zone, little upstream the outlet on the fan, two sections have been equipped inside the two main channels in order to obtain information about avalanches flowing depth and velocity. The instrumentation allowed determination of the average flow velocity of avalanches (cross length of about 200 m) and the maximum flow depth.

The preparation of the basin at the winter 1998-1999 has been made (of all sections of velocity and maximum flow depth measure) restoring the existing instrumentation and distributing about 80 wood tracers in the high basin part in order to obtain information regarding the sides activity.

In the 2 years of observation various snow deposits have been surveyed, located in the high part of the site (over 1700 m a.s.l.).

Another one has been surveyed near to the exit on the fan, as a consequence of the small avalanche of the February 27th 1998. The deposit near to the aqueduct had a slope of 34% (19°), about 80 m of length, about 8 m of width and depth of 3 m, and it was almost formed by spherical form elements of diameter included between 5 and 10 cm. In the deposit there were rocky boulders (about 1,5 m), and it showed the high erosive capacity of the small granular avalanche. The flow velocity of the front in the control segment was about 3 m/s and his depth about 2 m. Deposits dimensional features have been observed by stratigraphic profiles (Table 7.6).

Volume	Length	Bed slope		Depth	Layer density
[m³]	[m]	[%]	[°]	[m]	[kg/m³]
1000 – 20.000	100 – 800	53 – 67	28 – 34	2 – 3,5	370 – 470

The only surveyed avalanche event near to the fan, happened in spring time and in correspondence with a thermal raise, confirming observations already made in the past. The particle form of the deposits witnesses the presence of a significant percent of water inside the snow mass at the measure of detachment. The high density of the moving mass gave high erosive capacity. The low flow velocity in the control zone is justified by the low relative roughness and the small avalanche volume [Scotton et al., 2002].

7.2 Numerical-mathematical analysis

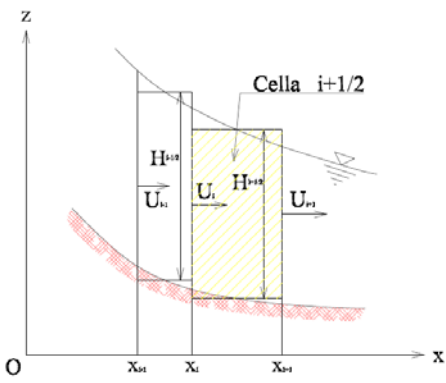
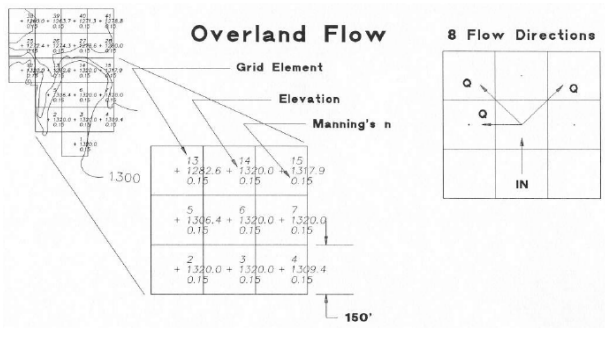
7.2.1 Models description

SnowScotton. It is a one-dimensional model at variable width based on the rheology of Savage & Hutter (1989) modified to take into account the lateral frictions. The model requires as input data the channel geometry and the data of the initial pile, let alone values of the bottom friction angle and lateral friction angle, that can change along the slope, and inner friction angle.

FLO-2D™. FLO-2D™ is a two-dimensional hydraulic model based on volume conservation for routing debris floods and flows on alluvial fans. This is performed by modelling the progress of a flow hydrograph through the topographic domain both as channel flow and overland flow.

In Table 7.3 the two models are presented.

Table 7.7 – Comparison between the two numerical-mathematical models.

SnowScotton	FLO-2D
by Stefano De Toni, Paolo Scotton, Enrico Bertolazzi Dipartimento di Ingegneria Civile e Ambientale, Università di Trento, Italy, 2004	by Jim O'Brien, Craig R. Jorgensen, Reinaldo Garcia and HydroSoft, C.A. FLO-2D Software, Inc., Nutrioso, USA, 1985
One-dimensional model	Two-dimensional model
Geometry:	
 <p style="text-align: center;">Fig. 7.19 – Model grid [De Toni et al., 2005].</p>	 <p style="text-align: center;">Fig. 7.20 – Discharge flux across grid boundaries [FLO-2D, 2006].</p>
MODEL THEORY	
Governing equations:	
<ul style="list-style-type: none"> THE CONTINUITY EQUATION: $\frac{\partial u_x}{\partial x} + \frac{\partial u_z}{\partial z} = 0$ <p>u_x, u_z velocity components;</p> THE ONE-DIMENSIONAL EQUATIONS OF MOTION (MOMENTUM EQUATIONS): $\begin{cases} \frac{\partial u_x}{\partial t} + u_x \frac{\partial u_x}{\partial x} + u_z \frac{\partial u_x}{\partial z} = \frac{1}{\rho} \left(\frac{\partial p_{xx}}{\partial x} + \frac{\partial p_{zx}}{\partial z} \right) \\ \frac{\partial u_z}{\partial t} + u_x \frac{\partial u_z}{\partial x} + u_z \frac{\partial u_z}{\partial z} = \frac{1}{\rho} \left(\frac{\partial p_{xz}}{\partial x} + \frac{\partial p_{zz}}{\partial z} \right) - g \end{cases}$ 	<ul style="list-style-type: none"> THE CONTINUITY EQUATION: $\frac{\partial h}{\partial t} + \frac{\partial (hV_x)}{\partial x} + \frac{\partial (hV_y)}{\partial y} = i$ <p>h flow depth; V_x, V_y depth-average velocity components; i rain intensity;</p> THE TWO-DIMENSIONAL EQUATIONS OF MOTION (MOMENTUM EQUATION): $\begin{cases} S_{fx} = S_{ox} - \frac{\partial h}{\partial x} - \frac{V_x}{g} \frac{\partial V_x}{\partial x} - \frac{V_y}{g} \frac{\partial V_x}{\partial y} - \frac{1}{g} \frac{\partial V_x}{\partial t} \\ S_{fy} = S_{oy} - \frac{\partial h}{\partial y} - \frac{V_y}{g} \frac{\partial V_y}{\partial y} - \frac{V_x}{g} \frac{\partial V_y}{\partial x} - \frac{1}{g} \frac{\partial V_y}{\partial t} \end{cases}$

u_x, u_z velocity components; $P_{xx}, P_{xz}, P_{zx}, P_{zz}$ strain components; ρ granular material density; g gravitational acceleration.	S_{fx}, S_{fy} friction slope components; S_{ox}, S_{oy} bed slopes components; $\frac{\partial h}{\partial x}, \frac{\partial h}{\partial y}$ pressure gradient components; $\frac{V_x}{g} \frac{\partial V_x}{\partial x}, \frac{V_y}{g} \frac{\partial V_y}{\partial y}$ convective acceleration components; $\frac{1}{g} \frac{\partial V_x}{\partial t}, \frac{1}{g} \frac{\partial V_y}{\partial t}$ local acceleration components.
--	---

Flow data:

- INITIAL MASS POSITION:

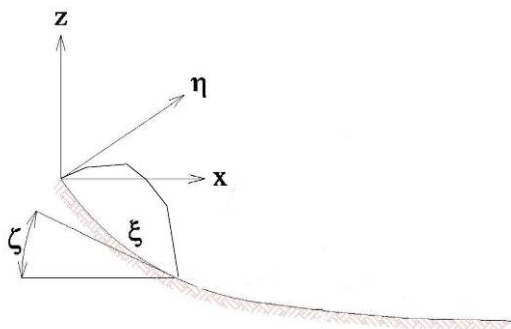


Fig. 7.21 – Initial mass position example.

- INFLOW HYDROGRAPH:

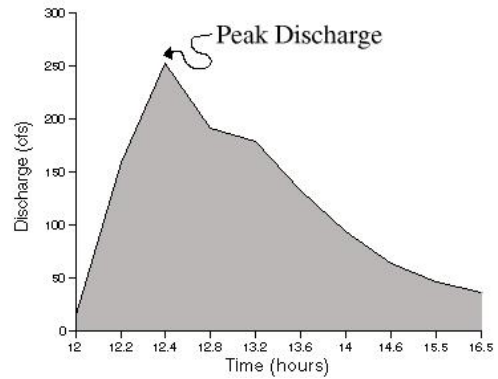


Fig. 7.22 – Inflow hydrograph example
[\[http://water.me.vccs.edu\]](http://water.me.vccs.edu).

Rheology:

- STRESS TENSOR:

$$\tilde{P} = \begin{pmatrix} P_{\xi\xi} & P_{\xi\eta} \\ P_{\xi\eta} & P_{\eta\eta} \end{pmatrix}$$

$$\begin{cases} P_{\xi\xi} = -k_{a/p} P_{\eta\eta} \\ P_{\xi\eta} = -\text{sgn}(u_\xi) \tan \delta \\ P_{\eta\eta} = -\rho (\chi(u_\xi)^2 + g \cos \zeta) (h - \eta) \end{cases}$$

$$\left. \begin{matrix} k_p \\ k_a \end{matrix} \right\} = \frac{2}{\cos^2 \phi} \left[1 \pm \sqrt{1 - \frac{\cos^2 \phi}{\cos^2 \delta}} \right] - 1$$

- \tilde{P} stress tensor;
- $P_{\xi\xi}, P_{\xi\eta}, P_{\eta\eta}$ stress components;
- $k_{a/p}$ coefficient force;
- ϕ internal friction angle;
- $\text{sgn}(u_\xi)$ mark function;
- u_ξ velocity component;
- δ bed friction angle;
- ρ granular material density;

- SHEAR STRESS:

$$\begin{aligned} \tau &= \tau_c + \tau_{mc} + \tau_v + \tau_t + \tau_d = \\ &= \tau_y + \eta \left(\frac{dv}{dy} \right) + C \left(\frac{dv}{dy} \right)^2 \\ &\quad \underbrace{\hspace{10em}}_{\text{flow (viscous flow regime)}} \\ &\quad \underbrace{\hspace{10em}}_{\text{mud flood (inertial flow regime)}} \end{aligned}$$

- τ_c cohesive yield stress;
- $\tau_{mc} = p_s \tan \phi$ Mohr-Coulomb shear;
- $\tau_v = \eta \left(\frac{dv}{dy} \right)$ viscous shear stress;
- τ_t turbulent shear stress;
- τ_d dispersive shear stress;
- $\tau_y = \tau_c + \tau_{mc}$ yield stress;
- $\tau_{td} = \tau_t + \tau_d = C \left(\frac{dv}{dy} \right)^2$ turbulent-dispersive shear stress.

χ	curvature at the bottom;
g	gravity acceleration;
ζ	bed slope;
h	snowpack depth;
η	curvilinear coordinate.

$C = \rho_m l^2 + f(\rho_m, C_v) d_s^2$
 $C_v = \frac{V_s}{V_w + V_s}$
 τ total shear stress;
 p_s intergranular pressure;
 ϕ angle of repose of the material;
 C inertial shear stress coefficient;
 ρ_m mass density of the mixture;
 l Prandtl mixing length
 C_v sediment concentration by volume;
 d_s sediment size.

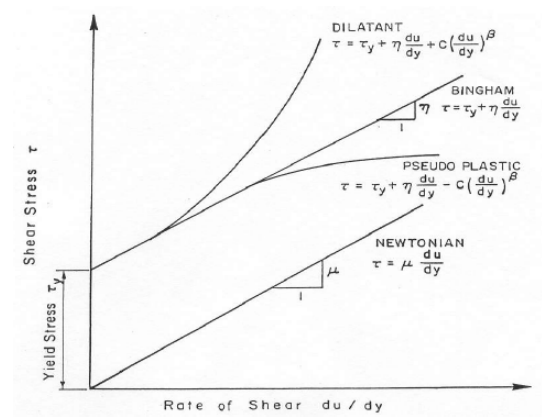


Fig. 7.23 – Shear stress as function of shear rate for fluid deformation models [FLO-2D, 2006].

--	--

• FRICTION SLOPE:

$$S_f = S_y + S_v + S_{td} =$$

$$= \frac{\tau_y}{\gamma_m h} + \frac{K\eta}{8\gamma_m} \frac{V}{h^2} + \frac{n_{td}^2 V^2}{h^{4/3}} \quad (\text{eq. 1})$$

[Julien & Lan, 1991]

$$\left\{ \begin{array}{l} S_y = \frac{\tau_y}{\gamma_m h} \quad \text{yield slope;} \\ S_v = \frac{K\eta}{8\gamma_m} \frac{V}{h^2} \quad \text{viscous slope;} \\ S_{td} = \frac{n_{td}^2 V^2}{h^{4/3}} \quad \text{turbulent-dispersive slope} \end{array} \right.$$

$$n_{td} = n_t b e^{mC_v}$$
 S_f total friction slope;
 τ_y Bingham yield stress;
 γ_m specific weight of the sediment mixture;

	<p>h depth; K resistance laminar flow parameter; η Bingham viscosity; V average velocity; n_{td} turbulent-dispersive Manning's n-value; n_t turbulent Manning's n-value; b coefficient = 0,0538; m exponent = 6,0896; C_v sediment concentration by volume; V_s sediment volume; V_w water volume.</p>
	<p>• VISCOSITY:</p> $\eta = \alpha_1 e^{\beta_1 C_v}$ <p>η viscosity; α_1, β_1 empirical coefficients; C_v sediment concentration by volume.</p>
	<p>• YIELD STRESS:</p> $\tau_y = \alpha_2 e^{\beta_2 C_v}$ <p>τ_y yield stress; α_2, β_2 empirical coefficients; C_v sediment concentration by volume.</p>

Main model feature:

Rheology [[De Toni et al., 2005]:

The physical parameters on which the model rheology is based are the internal friction angle ϕ and the bottom friction angle δ .

Volume conservation [FLO-2D™, 2006]:

FLO-2D™ is a simple volume conservation model that distributes a flood hydrograph over a system of square grid element. Volume conservation is an indication numerical stability and accuracy.

The motion representation:

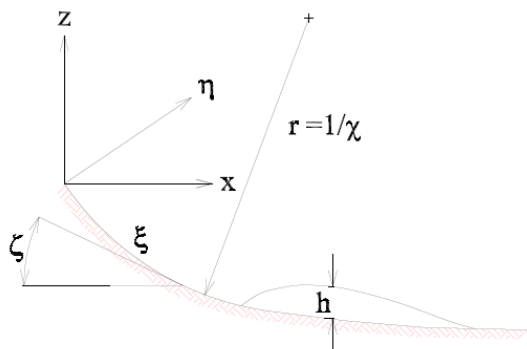


Fig. 7.24 – Absolute and curvilinear coordinates systems [De Toni et al., 2004].

Coordinate systems:

- { (x, z) absolute coordinates system;
- { (ξ, η) curvilinear coordinates system.

Channel Extension

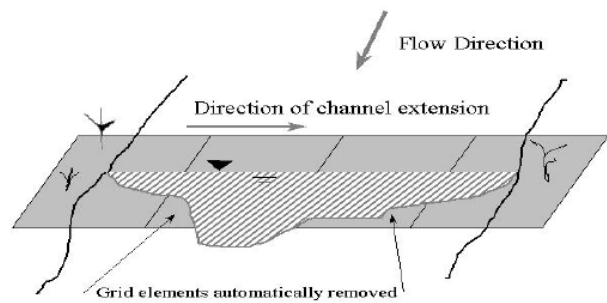


Fig. 7.25 – Channel extension over several grid elements [FLO-2D, 2006].

Model components:	
	<ul style="list-style-type: none"> • <u>GDS</u>, grid developer system, is a pre-processor that overlays the grid system in a DTM, interpolate and assign elevations to the grid elements; • <u>FLO-2D</u>; • <u>MAPPER</u> is a post-processor that generates maps of the FLO-2D model results.

INPUT			
Data	File	Data	File
Geometry – DTM	<ul style="list-style-type: none"> • CHANNEL.CSV • CHANNEL.SX • CHANNEL.DX 	Geometry – DTM	<ul style="list-style-type: none"> • FPLAIN.DAT • CADPTS.DAT
ϕ [°] internal friction angle;	<ul style="list-style-type: none"> • MATDEF.HH 	t [h] simulation time;	<ul style="list-style-type: none"> • CONT.DAT
h_n [m] snowpack depth;		B_v [-] bulking concentration;	
q_{max} [m a.s.l.] elevation max snow mass;		ARF [-] area reduction factor;	
q_{min} [m a.s.l.] elevation min snow mass;		F_r [-] Froude Number.	
d_ξ [m] initial step of the snow mass;		n [s/m ^{1/3}] Manning's roughness;	
u_ξ [m/s] velocity component.			
		A [m ²] surface detention;	<ul style="list-style-type: none"> • TOLER.DAT
		Q [m ³ /s] discharge;	<ul style="list-style-type: none"> • INFLOW.DAT
		t [h] time;	
		C_v [-] sediment concentration by volume;	
ρ [kg/m ³] flow density;	<ul style="list-style-type: none"> • TIMEDEF.HH 	η [poise] viscosity ;	<ul style="list-style-type: none"> • SED.DAT
δ [°] bottom friction angle;		τ_y [dynes/cm ²] yield stress;	
h_{fr1} [m] front depth 1;		α, β [-] empirical coefficients;	
h_{fr2} [m] front depth 2;		γ_m [kN/m ³] sediment specific gravity;	
p_1 [kPa] pressure 1;		K [-] resistance laminar flow parameter.	
p_2 [kPa] pressure 2;			
Slope data:	<ul style="list-style-type: none"> • CHANNEL.PEN 		
Snow mass:	<ul style="list-style-type: none"> • CHANNEL.MAT 		
Model parameters:	<ul style="list-style-type: none"> • CHANNEL.TIME 		

OUTPUT			
Data	File	Data	File
Avalanche profile in (ξ, η) :	<ul style="list-style-type: none"> • CHANNEL.CE 	Floodplain flow depth:	<ul style="list-style-type: none"> • DEFPF.OUT
Avalanche profile in (x, y) :	<ul style="list-style-type: none"> • CHANNEL.XY 		<ul style="list-style-type: none"> • DEPTH.OUT

Front depth 1 in (x, z) :	• CHANNEL.TH1		• DEPTH1TOL.OUT • FINALDEP.OUT
Front depth 2 in (x, z) :	• CHANNEL.TH2		
		Water surface elevation:	• FLOODWAY.OUT • INTERGWS.OUT
		Floodplain discharge:	• MAXQBYDIR.OUT • MAXQHYD.OUT • MAXQRESOLVED.OUT
Velocity profile in (ξ, v) :	• CHANNEL.CU	Floodplain velocity:	• FINALDIR.OUT • FINALVEL.OUT • VELDIREC.OUT • VELFP.OUT • VELOC.OUT
Pressure profile in (ξ, p) :	• CHANNEL.CP	Static pressure for each grid element is expressed as a force per unit length:	• STATICPRESS.OUT
Pressure profile 1 in (x, z) :	• CHANNEL.TP1		
Pressure profile 2 in (x, z) :	• CHANNEL.TP2		
		Manning's Roughness:	• ROUGHT.OUT • FPLAIN.RGH
		Volume conservation:	• SUMMARY.OUT
		Froude Number:	• SUPER.OUT
		Area reduction:	• SURFAREA.OUT
		Simulation time	• TIME.OUT • TIMEONEFT.OUT • TIMETOPEAK.OUT • TIMETWOFT.OUT
		Summary results:	• TOPO.ORI • BASE.OUT • FLO2DGIS.OUT

7.2.1 Models calibrations

Two events have been used to calibrate the physical parameters of the FLO-2D™ model.

Avalanche event n°1 – February 27th 1998. The deposit volume was about 1000 m³. The front stopped at the elevation of 1320 m a.s.l., little after the conjunction between channel 1 and channel 3. The average width of the deposit was about 8 m and the thickness about 3 m.

Measurements of mean velocity, performed between two sections (distant about 200 m) little upstream the conjunction between channel 1 and channel 3, gave the value of 3 m/s while the maximum depth was estimated between 1 m and 2 m [Scotton et al., 2006]. The avalanche starting elevation was estimated at 1700 m a.s.l.

For the FLO-2D™ model, the grid cell size of 10 m x 10 m has been chosen (mainly because of numerical problems). The rheological parameters have been chosen as in the Table 7.8 following the indication of Dent & Lang (1982). The boundary condition represented by the input hydrograph has been obtained from the previous work (Fig. 7.26).

Table 7.8 – Avalanche event n°1 – Channel 1 – February 27 th 1998.						
SnowScotton						
Simulation parameters				Deposit outputs		
Initial mass	upstream height	[m a.s.l.]	1700	front height	[m a.s.l.]	1321
	downstream height	[m a.s.l.]	1670	max. depth	[m]	3,0
	depth	[m]	1,7	length	[m]	176,0
	volume	[m ³]	1.000			
	ϕ internal friction angle	[°]	30			
δ bottom friction angle (channel/run-out)	[°]	22 – 29				
FLO-2D						
Simulation parameters				Deposit outputs		
Inflow	height	[m a.s.l.]	1670	max. depth	[m]	0,9
	volume	[m ³]	1.000			
	C_v	[-]	0,5			
	η	[Pa·s]	0 – 1			
	τ_y	[kPa]	0,5			
	γ_m	[kN/m ³]	3			
n (channel/run-out)	[s/m ^{1/3}]	0,05 – 0,1				
K	[-]	2000				

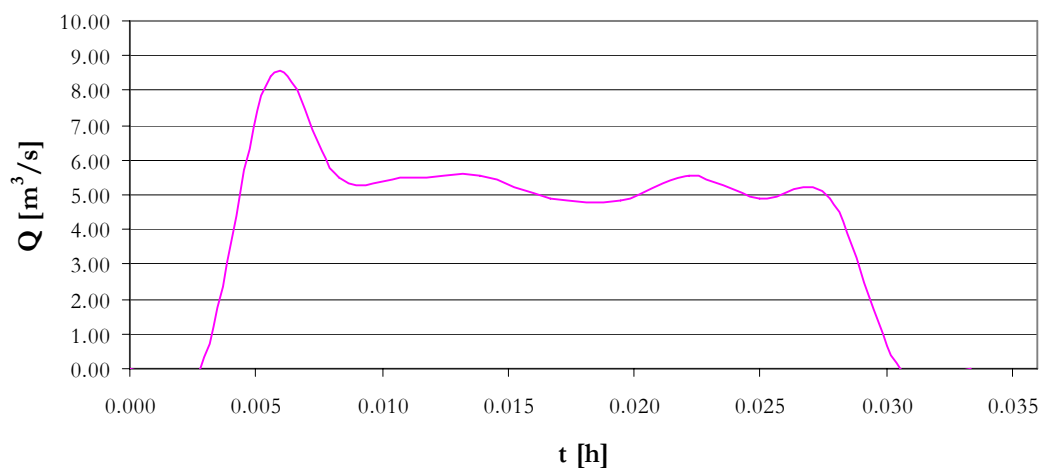
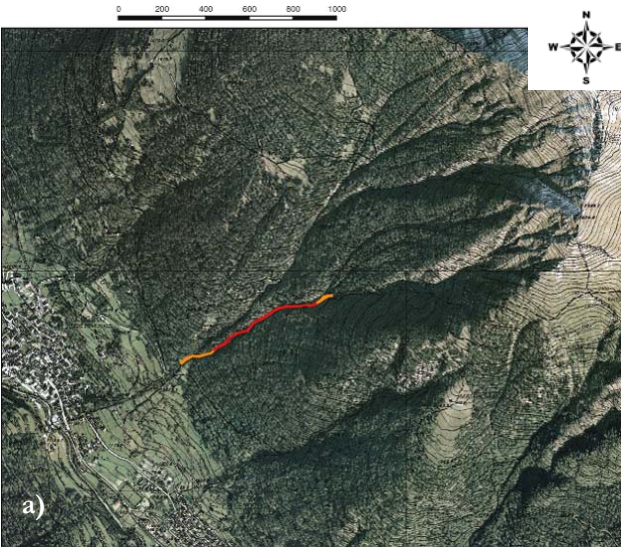


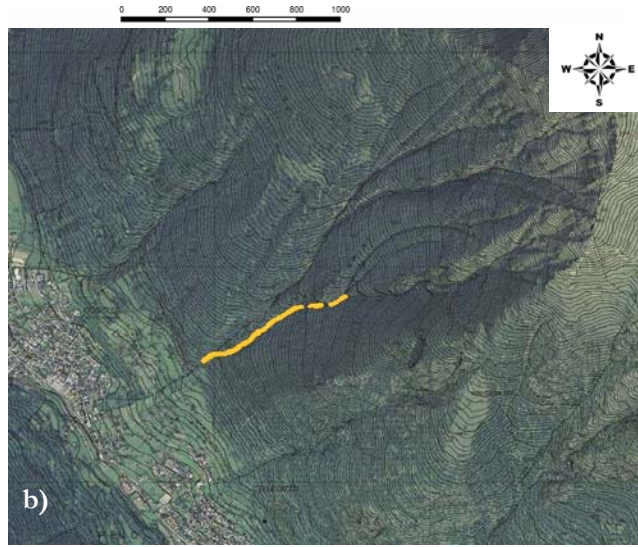
Fig. 7.26 – Avalanche event n° 1 – Channel 1 – February 27th 1998: input hydrograph for FLO-2D.

In Fig. 7.27 the mass distribution at the end of the propagation (velocity everywhere near to zero) of some simulations is showed. In the FLO-2D simulation n°2 a value of $\eta = 0$ is imposed to test the importance of this rheological parameter in the model.

SnowScotton

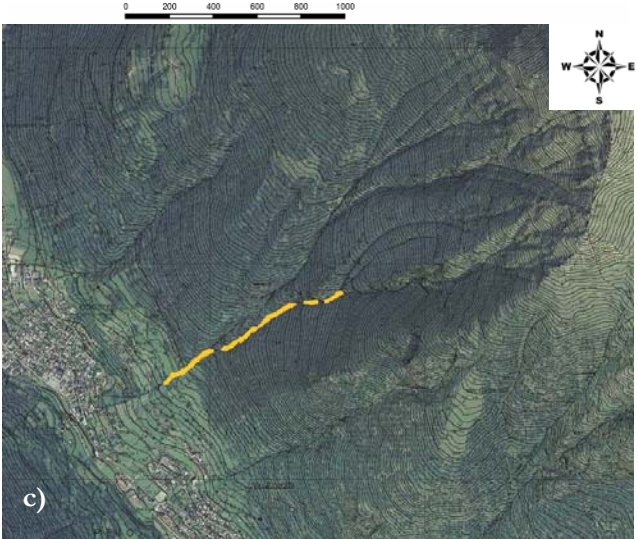


FLO-2D



Simulation n° 1 ($\eta = 1 \text{ Pa}\cdot\text{s}$, $\tau = 0,5 \text{ kPa}$)

FLO-2D



Simulation n° 2 ($\eta = 0 \text{ Pa}\cdot\text{s}$, $\tau = 0,5 \text{ kPa}$)

Fig. 7.27 – Avalanche event n°1 – Channel 1 – February 27th 1998:
 a) SnowScotton simulation [Scotton et al., 2006];
 b) FLO-2D simulation n°1; c) FLO-2D simulation n°2.

The most important parameters are the manning coefficient n and the yield stress τ_y . Nevertheless, a minor rule is assumed by the viscosity coefficient η as in showed in Fig. 7.27.

Avalanche event n° 2 – March 13th 1972. The event occurred on March 13th 1972 at 15.00 o'clock. The detachment area was located at the height of 2300 m a.s.l., with west exposure, at the head of channel 4 (Fig. 7.29). In consequence of thermal raise, from a surface 100 m wide and 200 m long, an avalanche of wet snow happened of about 40.000 m³. The flowing length was about 1900 m. The avalanche stopped at 1250 m a.s.l., producing a granular deposit of irregular form (with also snow blocks inside), 150 m long, 150 m wide and a volume of roughly 67.500 m³.

In the FLO-2DTM model, again a grid cell size of 10 m x 10 m has been used. As before, a fixed sediment concentration of 50% was assumed.

Table 7.9 – Avalanche event n°2 – Channel 4 – March 13 th 1972.						
SnowScotton						
Simulation parameters (initial mass)				Deposit outputs		
Initial mass	upstream height	[m a.s.l.]	2250	front height	[m a.s.l.]	1243
	downstream height	[m a.s.l.]	1950	max. depth	[m]	13,5
	depth	[m]	9,1	length	[m]	244,0
	volume	[m ³]	67.500			
	ϕ internal friction angle	[°]	30			
δ bottom friction angle (channel/run-out)	[°]	20 – 27				
FLO-2D						
Simulation parameters				Deposit outputs		
Inflow	height	[m a.s.l.]	1950	max. depth	[m]	5,0
	volume	[m ³]	67.500			
	C_v	[-]	0,5			
	η	[Pa·s]	1 – 10			
	τ_y	[kPa]	3 – 15			
	γ_m	[kN/m ³]	3			
n	[s/m ^{1/3}]	0,1				
K	[-]	2000				

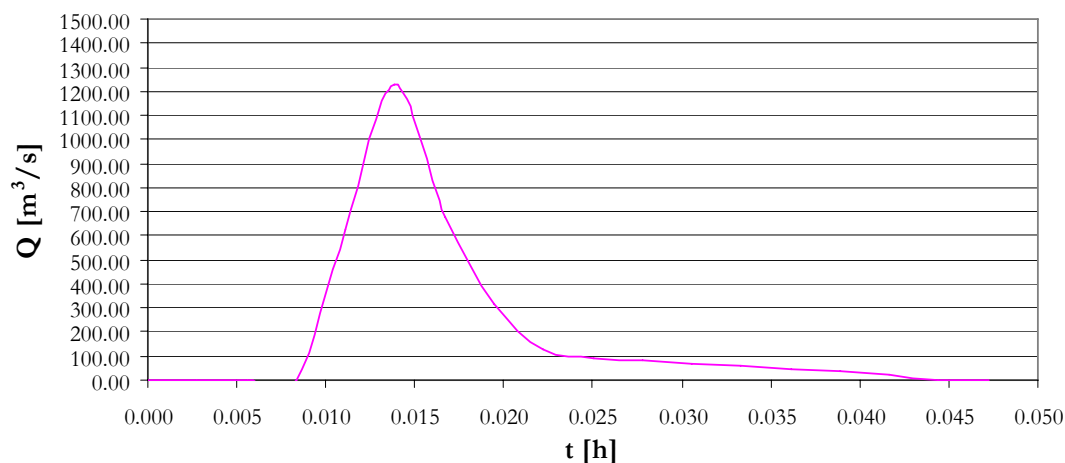
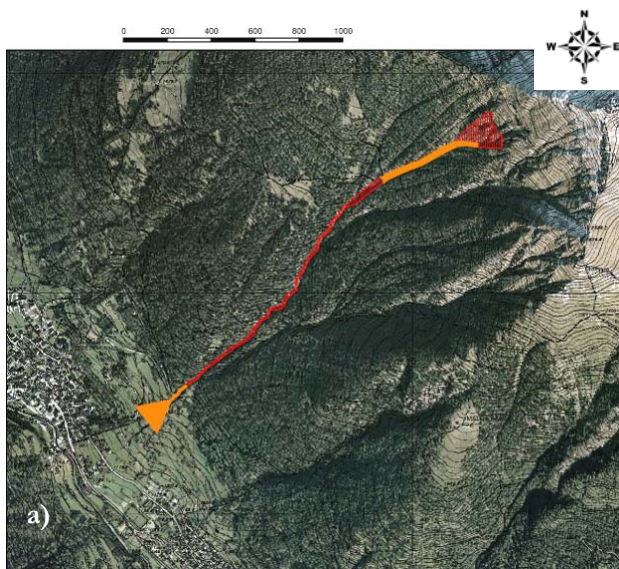
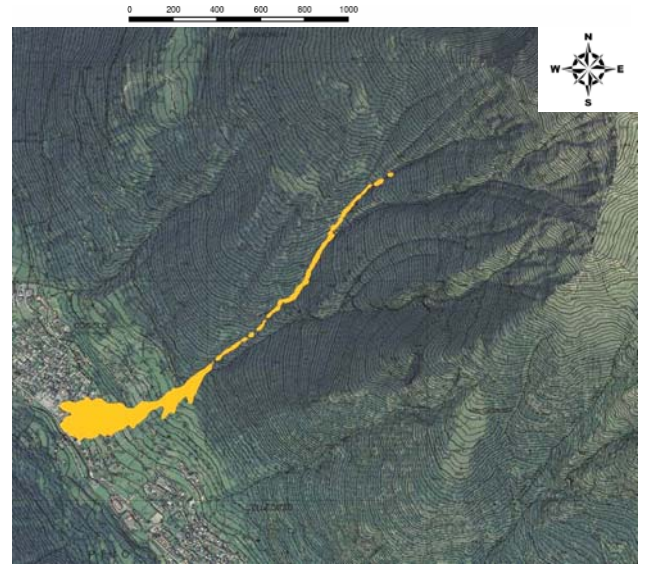


Fig. 7.28 – Avalanche event n°2 – Channel 4 – March 13th 1972: input hydrograph for FLO-2D.

SnowScotton

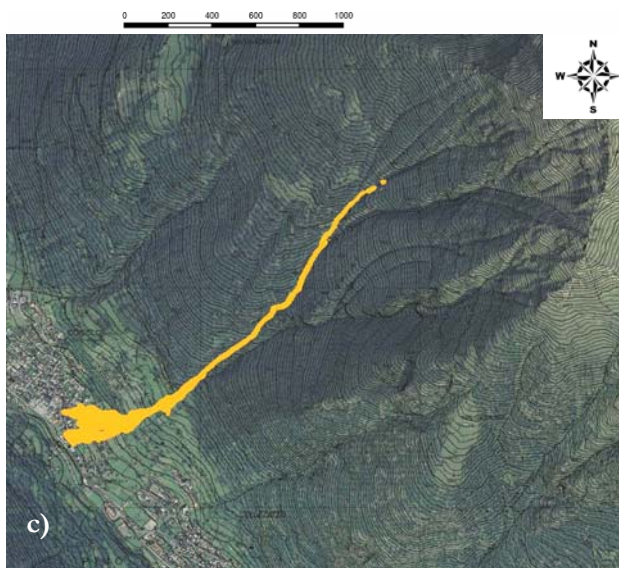


FLO-2D



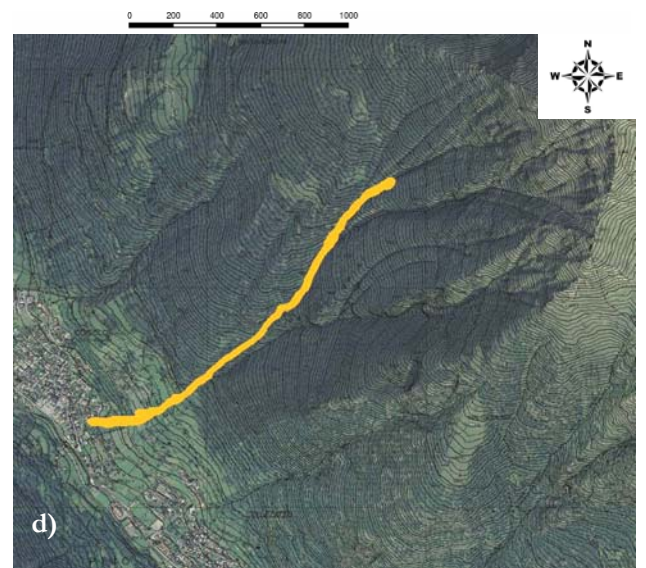
Simulation n° 1 ($\eta = 1 \text{ Pa}\cdot\text{s}$, $\tau = 3 \text{ kPa}$)

FLO-2D



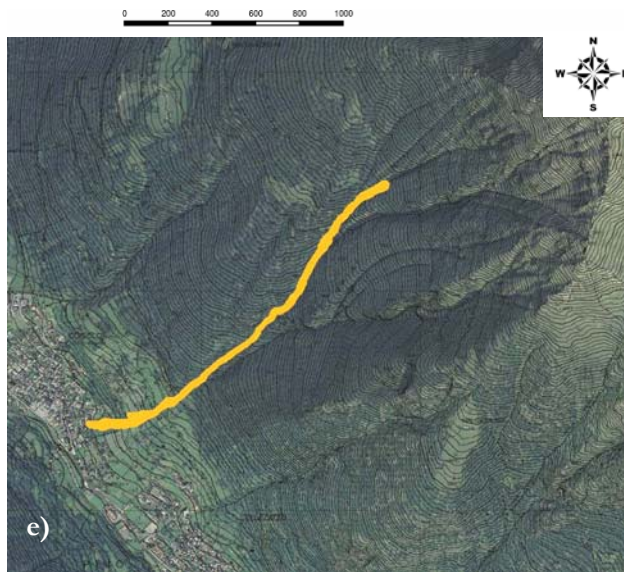
Simulation n° 2 ($\eta = 10 \text{ Pa}\cdot\text{s}$, $\tau = 3 \text{ kPa}$)

FLO-2D



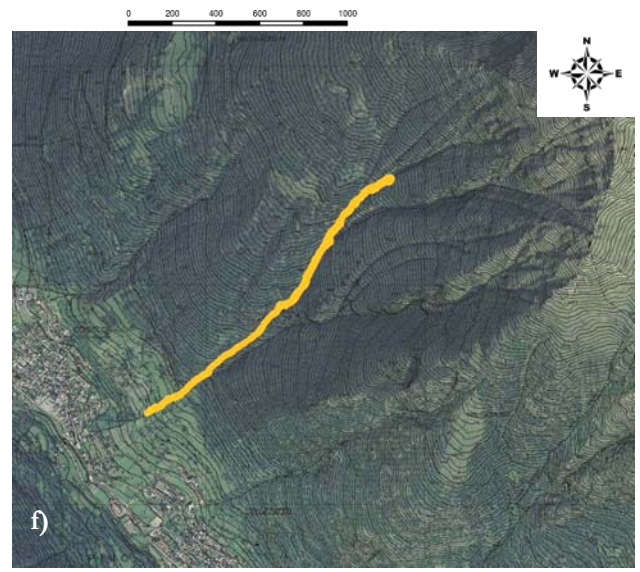
Simulation n° 3 ($\eta = 10 \text{ Pa}\cdot\text{s}$, $\tau = 10 \text{ kPa}$)

FLO-2D



Simulation n° 4 ($\eta = 0 \text{ Pa}\cdot\text{s}$, $\tau = 10 \text{ kPa}$)

FLO-2D



Simulation n° 5 ($\eta = 0 \text{ Pa}\cdot\text{s}$, $\tau = 15 \text{ kPa}$)

Fig. 7.29 – Avalanche event n°2 – Channel 4 – March 13th 1972:

- a) SnowScotton simulation [Scotton et al., 2006]; b) FLO-2D simulation n°1; c) FLO-2D simulation n°2; d) FLO-2D simulation n°3; e) FLO-2D simulation n°4; f) FLO-2D simulation n°5.

In Fig. 7.29 the mass distribution at the end of the propagation of some simulations is showed. Of minor importance appears the role of the viscosity η . On the contrary, to obtain a correct simulation of the stopping distance, much more important are the Manning coefficient n and the parameter τ_y . The physical meaning assumed by these parameters is quite uncertain.

7.3 Conclusions

In this chapter the behaviour of *Val dei Spini* snow avalanches site has been evaluated. The attention has been concentrated on dense snow avalanches in consideration of the historical data. The possibility to reproduce real events by means of FLO-2DTM has been tested.

Boundary conditions for FLO-2DTM model have been derived from a previous work that used a 1D-model based on the rheology of Savage & Hutter (1989) and was supported by a dedicated field study.

FLO-2DTM model showed severe stability problems under some combinations of initial and boundary conditions. It was possible to obtain a reasonable simulation for the calibration events but the physical meaning of the values assumed by the rheological parameters remains quite uncertain.

According to the above considerations particular attention should be paid in order to produce snow avalanches hazard maps.

Chapter 8

CONCLUSIONS

*I modelli sono quelle cose
a cui nessuno crede
tranne chi li ha creati.*

*I dati sono quelle cose
a cui tutti credono
tranne chi li ha raccolti.*

(Teodoro Georgiadis)

In alpine regions snow avalanches are one of the major natural threats for human settlements, activities and infrastructures.

Under the definition of snow avalanche many natural phenomena are considered. These actually vary and have to be treated very differently in order to mitigate the associated hazards.

Powder snow avalanches, for example, are very difficult to control because of the low value of their bulk density and the high value of the flow depth and velocity.

The technical approach to the mitigation of the associated risks is to avoid the initial movement of the snow cover or to produce frequent detachments of low volumes of snow by using explosives, thus generating no dangerous events. Very costly structure systems are normally realized, justified by the need to protect territories of important value.

Dense snow avalanches show dynamic properties that are quite different from those of powder avalanches. Generally, their velocity and depth are much lower, while their bulk density is much higher. Above all, they present the tendency to follow the topographical properties of the flowing surface. From an engineering point of view it is possible to interact with this kind of phenomena also in the flowing zone and -maybe in a more effective way- in the stopping area.

Engineering structures adopted to reduce the destructive power of dense snow avalanches -widely diffused in alpine regions- are the retarding mounds (cone-shaped and tooth-shaped structures) and the deflection dams, mainly located at the origin of the alluvial fan. The costs of this type of protection systems are certainly lower than in the previous case but, at the same time, the level of safety produced is lower, because it is hard to define -in a reliable way- the dynamic parameters of the design event.

The main aim of all the researches performed in this topic -from an engineering point of view- is to produce maps that allow proper land management (hazard maps, risks maps).

This research analyses some relevant aspects of the behaviour of granular fluxes which represent dense snow avalanches. The two performed experimental campaigns describe some aspects of the interaction between the size distribution of the granular mass and the dynamic motion characteristics and the interaction with retarding structures.

As far as hazard maps are concerned, the possibility of applying a 2-D commercial numerical model (FLO-2D™) to a field case for which the hazard maps were already defined (by means of a 1-D model based on the rheology of Savage & Hutter, 1989) has been evaluated.

The following paragraphs describe the main results of the research.

The experimental analyses show that the main dynamic characteristics of the granular flow are strongly influenced by the ratio between the mass of fine and large particles (the granular mass was obtained using two different diameters of glass beads).

In the canalised part of the flow a significant influence on front velocity and flow depth has been observed; in the accumulation area, maximum longitudinal distance and mass distribution depended greatly on the defined ratio.

In particular it was observed that the front velocity increased when some fine material was added up until a ratio equal to the 30 %. This remained constant afterwards (par. 4.8). The maximum flow depth decreased of roughly 10 % when the ratio was above 30 %.

The maximum stopping distance increased of about 30 % at the ratio value of 25%. An important diameter segregation was observed in the deposit.

The experimental results show the importance of taking into consideration -in experimental investigations aimed at calibrating physical parameters of numerical models- the influence of the size distribution of granular material. This could have a considerable effect on the definition of physical parameters used in the construction of hazard maps.

Much work has been done by scientists -also recently- in order to investigate the process of energy dissipation in the presence of retarding structures - also using reduced scale models [for instance Hákonardóttir et al. 2003; Sheikh et al. 2008]. The present work considers the impact force exerted on a system of three retarding structures and the longitudinal and cross-sectional spreading of the mixture (as a consequence of energy dissipation and deflection during the impact).

The experimental investigation gives some technical information that can be used in the designing process of retarding structures against dense snow avalanches. It provides some criteria to estimate the maximum total force acting on different types of structures, once the main physical parameters that characterize the flowing mass are defined (for instance, through numerical dynamic analysis). It proves that the dimensionless force is much bigger for systems that use tooth-shaped elements instead of cone-shaped structures, that the opening angle of the rear elements at which the cross-sectional and the longitudinal efficiency present their maximum value is around 26° and that maximum efficiency occurs when the dimensionless force is at its maximum.

The phenomena produced in the laboratory can be thought to represent real phenomena in the Froude similarity at a scale in the order of magnitude of roughly 1/100. Confirmation of the experimental results should be given at a higher scale.

The experimental results can be used in order to test the capability of numerical models to simulate the impact against retarding structures. This aspect assumes particular importance when the residual hazard map is to be evaluated as a consequence of the introduction of retarding structures in the motion field.

At the beginning the FLO-2D™ model has been tested with the aim to define a hazard map of the *Val dei Spini* avalanche site. The necessary physical parameters have been calibrated by means of two events and a comparison with the hazard maps already realized with a 1D model carried out.

In the present application the dominant rheological parameters of FLO-2D™ model are the Manning coefficient and the yield stress. Their values have been changed in a quite wide range also beyond the range indicated in the available literature.

A strong influence of the boundary conditions has been observed, in particular depending on the shape of the input hydrograph. As a consequence it has been impossible realize a reliable hazard map of the site on the basis of this particular code.

The most important limitations on application of the model are:

- the uncertain physical meaning of the rheological parameters. To obtain a good simulation of some parameters of the calibration events it was necessary to assign to them values quite far from those suggested in the available literature;
- the calculation time and numerical stability. Under many initial and boundary conditions (large avalanche volumes and small grid cell size) it was practically impossible to obtain a reliable solution.

References

- ANCEY, C., 1998. Guide Neige et Avalanches: Connaissances, Pratiques, Sécurité. Édisud, Aix-en-Provence, 320 pp.
- AMMANN, W.J., 2008. Integral risk management in avalanche protection and mitigation: the Swiss approach. In Hervás, J. (Ed.), Recommendations to deal with Snow Avalanches in Europe. European Commission, Joint Research Centre, EUR 20839 EN, pp. 27-38.
- AMMANN, W.J., FOHN, P.M.B., 1999. Snow Avalanches. Disaster Resilient Infrastructure IDNDR, Zurich, pp. 17–28.
- BAKKEHØI, S.E, NOREM, H., 1993. Comparing topographical and dynamical runout models by ideas of “Nearest Neighbour Method”. Proceedings of the 2nd Avalanche-Dynamics-Workshop in Innsbruck.
- BARBOLINI, M., 2005. Corso Neve e Valanghe A.A. 2004/05, Dipartimento di Ingegneria Idraulica e Ambientale dell’Università degli Studi di Pavia.
- BARBOLINI, M., CAPPABIANCA, F., 2002. Determinazione della relazione tra distanze di arresto e tempi di ritorno delle valanghe: un nuovo metodo basato sull’analisi statistica dei dati storici. *Neve e Valanghe*, No. 46, pp. 14-23.
- BARBOLINI, M., CORDOLA, M., NATALE, L., TECILLA, G., 2003. Hazard mapping and land use regulation in avalanche prone areas: recent development in Italy. In Hervás, J. (Ed.), Recommendations to deal with Snow Avalanches in Europe. European Commission, Joint Research Centre, EUR 20839 EN, pp. 39–50.
- BARBOLINI, M., GRUBER, U., KEYLOCK, C., NAAIM, M., SAVI, F., 2000. Application of statistical and hydraulic continuum dense snow avalanche models to five real European sites. *Cold Regions Science and Technology*, Elsevier, Vol. 31, pp. 133–149.
- BARBOLINI, M., ISSLER, D., 2005. Avalanche test sites and research equipments in Europe. An update overview. SATSIE – Avalanche Studies and Model Validation in Europe. European Commission, Deliverable D8.
- BARBOLINI, M., NATALE, L., TECILLA, G., CORDOLA, M., 2005. Linee guida metodologiche per la perimetrazione delle aree esposte al pericolo valanghe. Dipartimento di Ingegneria Idraulica e Ambientale dell’Università degli Studi di Pavia, AINEVA.
- BARTELT, P., GRUBER, U., 1997. Development and calibration of a Voellmy-fluid dense snow avalanche model based on a finite element method. Swiss Federal Institute of Snow and Avalanche Research, Internal report, No. 714, Davos.
- BERTHET-RAMBAUD, P., THIBERT, E., TAILLANDIER, J.-M., LIMAM, A., 2005. Snow avalanche action in structures using back-analysis of real damages or experimental obstacles behaviour. In Senneset, Flaate & Larsen, Landslides and Avalanches, ICFL 2005 Norway, Taylor & Francis Group, London, pp. 43–49.
- BEZZI, I., 2004. Interazione tra simulazioni di laboratorio di valanghe di neve dense e strutture passive di contenimento. Tesi di Laurea. Corso di Laurea in Ingegneria per l’Ambiente e il Territorio, Facoltà di Ingegneria, Università degli Studi di Trento.
- BOVIS, M.J., MEARS, A., 1976. Statistical prediction of snow avalanche runout from terrain variables in Colorado. *Arctic and Alpine Research*, No. 8, pp. 145–147.

- CAGNATI, A., 1999. La valutazione della stabilità del manto nevoso. Guida pratica per sci alpinisti. Edizioni Tamara Montagna, Padova.
- CASSASSA, G., MARITA, H., MAENO, N., 1991. Shear cell experiments of snow and ice friction. *Journal of Applied Physics*, Vol. 69, pp. 3745–3755.
- CRESTA, R., 1991. La difesa dal pericolo valanghe. *Rassegna Tecnica* 4/1991.
- CHU, T., HILL, G., MCCLUNG, D.M., NGUN, R., SHERKAT, R., 1995. Experiments on granular flows to predict avalanche run up. *Canadian Geotechnical Journal*, Vol. 32, pp. 285–295.
- D'ACCORDI, M., 1999. Studio di un sito valanghivo: dati di campo e modellazione numerica. Tesi di Dottorato, Facoltà di Ingegneria, Università degli Studi di Trento.
- DENT, J.D., BURREL, K.J., SCHMIDT, D.S., LOUGE, M.Y., ADAMS, E.E., JAZBUTIS, T.G., 1998. Density, velocity and friction measurements in a dry-snow avalanche. *Annals of Glaciology*, Vol. 26, pp. 247–252.
- DENT, J.D., LANG, T.E., 1982. Experiments on the mechanics of flowing snow. *Cold Regions Science and Technology*, Elsevier, Vol. 5, No. 3, pp. 253–258.
- DE TONI, S., SCOTTON, P., 2005. Two-dimensional mathematical and numerical model for the dynamics of granular avalanches. *Cold Regions Science and Technology*, Science Direct, Elsevier, Vol. 43, pp. 36–48.
- DE TONI, S., SCOTTON, P., BERTOLAZZI, E., 2004. Modello matematico e numerico bidimensionale per lo studio delle valanghe di neve densa. Dipartimento di Ingegneria Civile e Ambientale, Università degli Studi di Trento, Quaderni del Dipartimento IDR 2.
- DOMAAS, U., HARBITZ, C., 1998. Avalanche run-up heights on deflecting dams: Centre-of-mass computations compared to observations. In Hestnes, E. (Ed.), *25 Years of Snow Avalanche Research*, No. 203. Norwegian Geotechnical Institute, Voss, pp. 15–18.
- FARINA, B., 2000. Tecniche di progettazione e costruzione delle opere di difesa dalle valanghe nella Provincia di Bolzano. Tesi di Laurea, Corso di Laurea in Ingegneria per l'Ambiente e il Territorio, Facoltà di Ingegneria, Università degli Studi di Trento.
- FAUG, T., 2004. Simulation sur modèle réduit de l'influence d'un obstacle sur un écoulement à surface libre. Application aux ouvrages de protection contre les avalanches de neige. Thèse. Université Joseph Fourier, Unité de recherche ETNA – Cemagref – Groupement de Grenoble.
- FAUG, T., NAAIM, M., NAAIM-BOUVET, F., 2004. An equation for spreading length, centre of mass and maximum run-out shortenings of dense avalanche flows by vertical obstacles. *Cold Regions Science and Technology*, Science Direct, Elsevier, pp. 141–151.
- FLO-2D™, 2006. Users manual. Version 2006 (FLO Engineering Inc., Nutrioso, Arizona, USA).
- FRASER, C., 1970. L'enigma delle valanghe. Ed. Zanichelli, Bologna.
- FRUTIGER, H., MARTINELLI, Jr, M., 1983. A manual for planning structural control of avalanches. Italian edition: Regione del Veneto-Dipartimento Foreste, Centro Sperimentale per lo studio della neve, delle valanghe, della meteorologia alpina e della difesa idrogeologica. Manuale per la pianificazione delle opere di difesa dalle valanghe. Collana di studi e ricerche di carattere tecnico sui problemi di interesse regionale.
- GIVRY, M., PERFETTINI, P., 2004. Construire en montagne. La prise en compte du risque avalanche. Ministère de l'Écologie et du Développement Durable, Ministère de l'Équipement, des Transport, du Logement, du Tourisme et de la Mer.

- HÁKONARDÓTTIR, K.M., 2004. The interaction between snow avalanches and dams. Dissertation. School of Mathematics, University of Bristol.
- HÁKONARDÓTTIR, K.M., HOGG, A.J., JÓHANNESSON, T., KERN, M., TIEFENBACHER, F., 2003. Large-scale avalanche braking mound and catching dam experiments with snow: a study of the airborne jet. *Surveys in Geophysics*, Kluwer Academic Publishers, Netherlands, No. 24, pp. 543–554.
- HÁKONARDÓTTIR, K.M., HOGG A.J., JÓHANNESSON, T., TÓMASSON, G.G., 2003. A laboratory study of the retarding effects of braking mounds on snow avalanches. *Journal of Glaciology*, Vol. 49, No. 165, pp. 191–200.
- HÁKONARDÓTTIR, K.M., TÓMASSON, G.G., INDRÍÐASON, H.D., SIGURÐSSON, F., 2008. The design of avalanche protection dams based on new design criteria: three different case studies. Proceedings of the International Symposium on “Mitigative Measures against Snow Avalanches”, 11-14 March 2008, Egilsstaðir, Iceland, pp. 78–84.
- HAMMERSLAND, E., NOREM, H. AND HUSTAD, A. 2000. Evaluation of measures for snow avalanche protection. IVth International Conference on Snow Engineering, Trondheim.
- HÖLLER, P., 2007. Avalanche hazards and mitigation in Austria: a review. *Natural Hazards*, Springer, Vol. 43, pp. 81–101.
- HUTTER, K., SAVAGE, S.B., 1991. The dynamics of avalanches of granular materials from initiation to runout. Part I: Analysis, *Acta Mechanica* Vol.86, pp. 201–223.
- HUTTER, K., KOCH, T., PLUSS, C., SAVAGE, S.B., 1995. The dynamics of avalanches of granular materials from initiation to runout. Part II. Experiments, *Acta Mechanica*, Vol. 109, pp. 127–165.
- IRGENS, F., SCHIELDROP, B., HARBITZ, C.B., DOMAAS, U., OPSAHL, R. 1998. Simulations of dense-snow avalanches on deflecting dams. *Annals of Glaciology*, Vol. 26, pp. 265–271.
- ISSLER, D. 1998. Modelling of snow entrainment and deposition in powder-snow avalanches. *Annals of Glaciology*, Vol. 26, pp. 253–258.
- JAEDICKE, C., KERN, M.A., GAUER, P., BAILLIFARD, M.-A., PLATZER, K., 2008. Chute experiments on slushflow dynamics. *Cold Regions Sciences and Technology*, Vol. 51, pp. 156–167.
- JÓHANNESSON, T., HÁKONARDÓTTIR, K.M., 2003. Remarks on the design of avalanche braking mounds based on experiments in 3, 6, 9 and 34 m long chutes. VÍ-ÚR18, Reykjavik, Report 03024.
- JÓHANNESSON, T., HÁKONARDÓTTIR, K.M., HARBITZ, C.B., DOMAAS, U., 2008. Background for the determination of dam height in the SATSIE dam design guidelines. VÍ-VS-02, Reykjavik, Report 08003.
- JULIEN, P.Y., LAN, Y., 1991. Rheology of hyperconcentrations. *Journal Hydraul. Eng.*, Vol. 117, No. 3, pp. 346–353.
- KELLER, S., ITO, Y., NISHIMURA, K., 1998. Measurements of the velocity distribution in ping-pong-ball avalanches. *Annals of Glaciology*, Vol. 26, pp. 259–264.
- KERN, M.A., TIEFENBACHER, F., MCELWAIN, J.N. 2004. The rheology of snow in large chute flows. *Cold Regions Sciences and Technology*, Vol. 39, pp. 181–192.
- KEYLOCK, C., McCLUNG, D.M., MAGNÚSSON, M., 1999. Avalanche risk mapping by simulation. *Journal of Glaciology*, Vol. 45, No. 150, pp. 303–314.

- LANG, T.E., DAWSON, K.L., MARTINELLI, M. Jr., 1979. Numerical simulation of snow avalanche flow. Italian edition: CRESPI, M., CAGNATI, A., 1985. Simulazione numerica del moto delle valanghe. Regione del Veneto-Dipartimento Foreste, Centro Sperimentale per lo studio della neve, delle valanghe, della meteorologia alpina e della difesa idrogeologica, Collana di studi e ricerche di carattere tecnico sui problemi di interesse regionale.
- LANG, T.E., NAKAMURA, T., DENT, J.D., MARTINELLI, JR, M., 1985. Avalanche flow dynamics with material locking. *Annals of Glaciology*, Vol. 6, pp.5-8.
- LARSEN, J.O., NOREM, H., 1996. The effect of dam constructions as mitigative measures. 14 years of experience from a full-scale project. International Conference "Avalanches and Related Subjects", Proceedings. Kirovsk, Russia, 2–6 September 1996, Centre of Avalanche Safety of "Apatit" JSC, Glaciological Association, pp. 59–65.
- LIBBRECHT, K.G., 2007. The formation of snow crystals. Subtle molecular processes govern the growth of a remarkable variety of elaborate ice structures. *America Scientist*, Sigma Xi, The Scientific Research Society, Vol. 95, pp.52–59.
- LIED, K., BAKKEHØI, S., 1980. Empirical calculations of snow avalanche run-out distance based on topographic parameters. *Journal of Glaciology*, Vol. 26, No. 94, pp. 165–177.
- LIED, K., KRISTERSEN, K. 2003. Snøskred. Håndbok om Snøskred. Vett & Viten as., Oslo.
- LINARES-GUERRERO, E., GOUJON, C., ZENIT, R., 2007. Increased mobility of bi-disperse granular avalanches. *Journal of Fluid Mechanics*, Cambridge University Press, Vol. 593, pp. 475–504.
- MARGRETH, S., 2004. Avalanche control structures. SLF, Pôle Grenoblois d'Etudes et de Recherche pour la Prévention des Risques Naturels. UEE session 2004: Avalanches: Risque, zonage et protections.
- MARGRETH, S., AMMANN, W.J, 2003. Hazards scenarios for avalanches actions on bridges. International Symposium on "Snow and Avalanches", Davos Switzerland.
- MARTIN, S., COCCO, S., DAL PIAZ, G.,V., DAMINATO F., GASPARI, D., MONTRESO, L., PELLEGRINI G.,B., PROSSER, G., SURIAN, N., TOMMMASI, G., ZAMBOTTI, G., 2001. Carta geologica – scala 1:25.000, Tavola 42 IV "PEIO". Servizio Geologico – Provincia Autonoma di Trento.
- McCLUNG, D.M., LIED, K., 1987. Statistical and geometrical definition of snow avalanche runout. *Cold Regions Science and Technology*, Vol. 13, pp. 107–119.
- McCLUNG, D., SCHAEERER, P., 1996. Manuale delle valanghe. Formazione – Dinamica ed Effetti – Prevenzione e Sicurezza – Soccorso. Ed. Zanichelli, Bologna.
- MEARS, A.I., 1981. Design criteria for avalanche control structures in the run-out zone. Italian edition: CRESPI, M., CAGNATI, A. Criteri progettuali per la realizzazione di opere di difesa delle valanghe nella zona di arresto. Regione del Veneto – Dipartimento Foreste, Centro Sperimentale Valanghe e Difesa Idrogeologica, Collana di studi e ricerche di carattere tecnico sui problemi di interesse regionale.
- MENEGUS, F., SORANZO, M., 1986. Criteri per il dimensionamento di opere di difesa dai massi e dalle valanghe. Regione del Veneto – Dipartimento Foreste, Centro Sperimentale Valanghe e Difesa Idrogeologica, Quaderni di Ricerca No. 6.
- NAAIM, M., 1998. Dense avalanche numerical modelling, interaction between avalanche and structures. In Hestnes, E. (Ed.), 25 Years of Snow Avalanche Research, Voss 12-16 May 1998. Proceedings, Vol.203. NGI Publications, Oslo, pp. 187–191.

- NAAIM, M., ANCEY, C., 1992. Modelisation of dense avalanches. Proceedings of the European Summer University on Snow and Avalanches, 14-25 September 1992, Chamonix, France, Cemagref Publications, pp. 173–181.
- NATALE, L., NETTUNO, L., SAVI, F., 1994. Numerical simulation of snow dense avalanche: an hydraulic approach. Proceedings of the 24th Annual Pittsburgh Int. Conference on “Modelling and Simulations”, Pittsburgh (IASTED 1994), ACTA PRESS, pp. 233–236.
- NISHIMURA, K., MAENO, N., 1989. Contribution of viscous forces to avalanche dynamics. *Annals of Glaciology*, Vol. 13, pp. 202–206.
- NOREM, H., 1995. Snow engineering for roads. Handbook No. 174, Publ. Roads Adm., Oslo, Norway.
- NOREM, H., BRATENG, L.E., 2005. Effect of dams and mounds to retain snow avalanches. In Senneset, Flaate & Larsen, Landslide and avalanches, ICFL 2005, Norway, Taylor and Francis Group, London, pp. 279-285.
- PEDERZOLLI, P., 2006. Analisi sperimentale di opere passive per il controllo di valanghe di neve. Tesi di Laurea. Corso di Laurea in Ingegneria per l’Ambiente e il Territorio, Facoltà di Ingegneria, Università degli Studi di Trento.
- PERLA, R.I., CHENG, T.T., McCLUNG, D.M., 1980. A two parameter model of snow avalanche motion. *Journal of Glaciology*, Vol. 26, No. 94, pp. 197-207.
- PERLA, R.I., MARTINELLI, M.Jr., 1976, Avalanche Handbook. U.S. Department of Agriculture – Forest Service, Agriculture Handbook 489, pp. 238.
- PHILLIPS, J.C., HOGG, A.J., KERSWELL, R.R., THOMAS N.H., 2006. Enhanced mobility of granular mixtures of fine and coarse particles. *Earth and Planetary Science Letters*, Science Direct, Elsevier, pp. 466-480.
- PITTRACHER, M., 2008. Development, assessment and effect of a new avalanche braking system in the Mühlauer-Klamm, Innsbruck, Austria. Proceedings of the International Symposium on “Mitigative Measures against Snow Avalanches”, 11-14 March 2008, Egilsstaðir, Iceland, pp. 58–67.
- PLATZER, K.M., MARGRETH, S., BARTELT, P., 2004. Granular flow experiments to investigate dynamic avalanche forces for snow shed design. Snow Engineering V. Proceedings of the fifth international conference on snow engineering, 5-8 July 2004, Davos, Switzerland. Balkema, pp. 363-370.
- Provincia Autonoma di Trento, Servizio Prevenzione Calamità Pubbliche, 2003. Planimetria Stato di Progetto: Progetto Esecutivo per la costruzione delle opere di difesa attiva nei confronti delle valanghe a monte degli abitati di Cogolo e Celledizzo nel Comune di Peio – Scala 1:2000.
- Provincia Autonoma di Trento, Ufficio Previsioni e Organizzazione. Catasto Valanghe della Val dei Spini.
- Provincia Autonoma di Trento, Ufficio Previsioni e Organizzazione. CLPV, Carta di Localizzazione probabile delle Valanghe: Val dei Spini – Scala 1:10.000, PAT – Dipartimento Protezione Civile e Tutela del Territorio.
- Provincia Autonoma di Trento, Ufficio Previsioni e Organizzazione. CTP, Carta Tecnica Provinciale: n°04201 – 04205 – Scala 1:10.000, PAT – Sistema informativo Ambiente e Territorio.
- Provincia Autonoma di Trento, Ufficio Previsioni e Organizzazione. DTM, Digital Terrain Model: risoluzione 10x10 m e 1x1 m, PAT – Sistema informativo Ambiente e Territorio.

- Provincia Autonoma di Trento, Ufficio Previsioni e Organizzazione. Ortofoto digitale anno 2000, a colori risoluzione 1 m; anno 1994, b/n risoluzione 1 m.
- RAO, N.M., 1985. Avalanche protection and control in the Himalayas. *Def Sci J*, Vol. 35, No. 2, pp. 255–266.
- ROGNON, P., 2006. Rhéologie des matériaux granulaires cohésifs. Application aux avalanches de neige denses. Thèse. École Nationale des Ponts et Chaussées.
- ROSSI, D., Analisi sperimentale su opere passive per il controllo di valanghe di neve. Tesi di Laurea. Corso di Laurea in Ingegneria per l'Ambiente e il Territorio, Facoltà di Ingegneria, Università degli Studi di Trento.
- SALM, B., 2004. A short and personal history of snow avalanche dynamics. *Cold Regions Science and Technology*, Science Direct, Elsevier, pp. 83–92.
- SALM, B., BURKARD, A., GUBLER, H.U., 1990. Berechnung von fließlawinen. Eine anleitung für den praktiker mit beispielen. Mitteilung 47, Eidg. Institut für Schnee und Lawinenforschung, Davos.
- SANSONI, G., CAROCCI, M., RODELLA, R., 1999. Three-dimensional vision based on a combination of grey-code and phase-shift light projection: analysis and compensation of systematic errors. *Applied Optics*, Optical Society of America, Vol. 38, No. 31, pp. 6565–6573.
- SARTORIS, G., BARTELT, P., 2000. Upwinded finite difference schemes for dense snow avalanche modelling. *International Journal for Numerical Methods in Fluids*, Vol. 32, pp. 799-821.
- SATSIE Project – Avalanche Studies and Model Validation in Europe. European Commission. 2006 The design of avalanche protection dams. Recent practical and theoretical developments. 1-DRAFT.
- SAVAGE, S.B., HUTTER, K., 1989. The motion of a finite mass of granular material down a rough incline. *Journal of Fluid Mechanics*, Vol. 199, pp. 177–215.
- SCOTTON, P., ARMANINI, A., 1992. Experimental investigation of roughness effects of debris flow channels. 6th Workshop on Two – Phase Flow Prediction, Erlangen.
- SCOTTON, P., BARBERI, M., GADDO, M., 2002. Valanghe in Val dei Spini. *Neve e Valanghe*, AINEVA, No. 46.
- SCOTTON, P., DE TONI, S., SEBASTIANI M., 2006. Studio del sito valanghivo della Val dei Spini. Dipartimento di Ingegneria Civile e Ambientale, Università degli Studi di Trento.
- SCOTTON, P., MORO, F., (submitted). Experimental analysis of retarding structures in the defence against granular flow. *Natural Hazards*, Springer.
- SCOTTON, P., MORO, F., (submitted). Analisi sperimentale su opere passive di rallentamento di valanghe di neve densa. *Neve e Valanghe*, AINEVA.
- SHEIKH, A.H., VERMA, S. C., KUMAR, A., 2008. Interaction of retarding structures with simulated avalanches in snow chute. *Current Science*, Vol. 94, No. 7, pp. 916–921.
- SOMMERHALDER, E., 1964. Avalanche forces and the protection of objects, U.S. Department of Agriculture, Forest Service, Wasatch National Forest, Alta Avalanche Study Center.
- SOMMAVILLA, F., 2006. La difesa dalle valanghe. Seminario 25 maggio 2006, Courmayeur (AO), oral presentation.
- SURREL, Y., 1993. Phase stepping: a new self-calibrating algorithm. *Applied Optics*, Optical Society of America, Vol. 32, Issue 19, pp. 3598–3600.

- TAI, Y.C., GRAY, J.M.N.T., HUTTER, K., NOELLE, S., 2001. Flow of dense avalanches past obstructions. *Annals of Glaciology*, Vol.32, pp. 281–284.
- TAKEDA, M., MUTOH K., 1983, Fourier transform profilometry for the automatic measurement of 3-D object shapes. *Applied Optics*, Optical Society of America, Vol. 22, No. 24.
- TREMPER, B., 1994. Simple snow stability tests. *The Avalanche Review*, Vol. 13, No. 2, pp. 4–8.
- TÓMASSON, G.G., SIGURÐSSON, F., RAPIN, F., 1998. The avalanche situation in Neskaupstaður, Iceland. A preliminary defensive plan. In Hestnes, E. ed. 25 Years of snow Avalanche Research, Voss 12-16 May 1998. NGI Publ., Vol. 203, pp. 283–288.
- VINCENT, C., 2003. Recalage et fusion pour reconstruire de surfaces 3D obtenues par projection de franges. Application à un système de vision dédié à l'orthopédie. Thèse. Université Jean Monnet de Saint-Étienne.
- VOELLMY, A., 1955. Über die Zerstörungskraft von lawinen. *Schweizerische Bauzeitung*, Jahrgang.73.
- WOODS, A.W., HOGG, A. J., 1999. Experiments on granular flows passing over obstacles on an inclined chute. University of Bristol, Centre for Environmental and Geophysical Research, School of Mathematics.

<http://www.avalanche.org>. West Wide Avalanches Network.

<http://avalancheblast.com/english/indexe.htm>. Companies for the avalanche blast -Funflight und Helikopterdienste- Germany and -Professional, Technical, and Educational Services for the Alpine Enviroment- United States of America.

<http://cagem.bayindirlik.gov.tr>. Turkish Avalanche Team, General Directorate of Disaster Affair.

<http://cemadoc.cemagref.fr>. Database of publications and photos of Cemagref, France.

<http://map.search.ch>. Switzerland maps.

<http://www.meteotrentino.it>. Meteorological data of Trento Province.

<http://utahavalanchecenter.org>. Utah Avalanche Center.

<http://www.anena.org>. Anena, Association Nationale pour l'étude de la Neige et des Avalanches, France.

<http://www.arpa.veneto.it/csvdi>. Arabba Avalanche Centre, Veneto Region, Italy.

<http://www.incofil.com>. Company for the realization of avalanche protecting structures -Incofil srl- Italy.

<http://www.ign.fr>. IGN, Institut Géographique National, France.

<http://www.kfunigraz.ac.at>. Karl-Franzens-Universität Graz, Austria.

<http://www.orion.is/snow2008>. International Symposium on “Mitigative Measures against Snow Avalanches”, 11-14 March 2008, Egilsstaðir, Iceland.

<http://www.pcn.minambiente.it>. National cartographic database, Ministero dell'Ambiente e della Tutela del Territorio e del Mare, Italy.

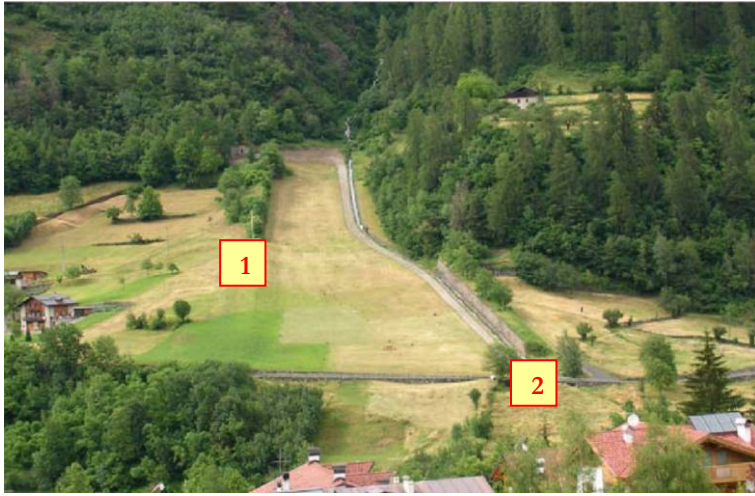
<http://www.slf.ch>. SLF, Swiss Federal Institute for Snow and Avalanche of Davos, Switzerland.

<http://www.snowcrystals.com>. Online guide to snowflakes, snow crystals, and other ice phenomena by Prof. Kenneth G. Libbrecht.

APPENDIX

DATA SHEETS OF AVALANCHE SITES WITH PASSIVE DEFENCE STRUCTURES

DEFLECTING DAMS OF MESTRIAGO, VAL DI SOLE, ITALY



GEOGRAPHICAL SETTING	
VILLAGE	Mestriago
MUNICIPALITY	Commezzadura
PROVINCE	Trento
REGION	Trentino Alto Adige
COUNTRY	Italy
WORKS FEATURES	
CONSTRUCTION YEAR	
ELEVATION	831 m s.l.m.
NUMBER AND TYPE	2 deflecting dams
H _{MAX}	
L _{MAX}	
W _{MAX} /Ø	
MATERIAL	Dry wall with square stones
AIM	Protection of Mestriago village

Deflecting dams 1 and 2
[photo by Bezzi, 2004].



Deflecting dam 1
[photo by Moro, 2007].



Deflecting dam 2
[photo by Moro, 2007].



[Ortho photo 2006, <http://www.pcn.minambiente.it>].

AVALANCHE FEATURES	
PAST EXTREME AVALANCHE EVENT	1986
DETACHMENT ELEVATION	
SLOPE INCLINATION	
CHANNEL WIDTH	

DEFLECTING DAMS OF TRAFOI, VALLE DI TRAFOI, ITALY



Deflecting dam 2
[photo by Moro, 2007].

GEOGRAPHICAL SETTING	
VILLAGE	Trafoi
MUNICIPALITY	Stelvio
PROVINCE	Bolzano
REGION	Trentino Alto Adige
COUNTRY	Italy
WORKS FEATURES	
CONSTRUCTION YEAR	
ELEVATION	1543 m s.l.m.
NUMBER AND TYPE	2 deflecting dams
H _{MAX}	~ 3,0 m
L _{MAX}	
W _{MAX} /Ø	
MATERIAL	Earth and base in heap of stones
AIM	Protection of the provincial way



Deflecting dam 2
[photo by Moro, 2007].



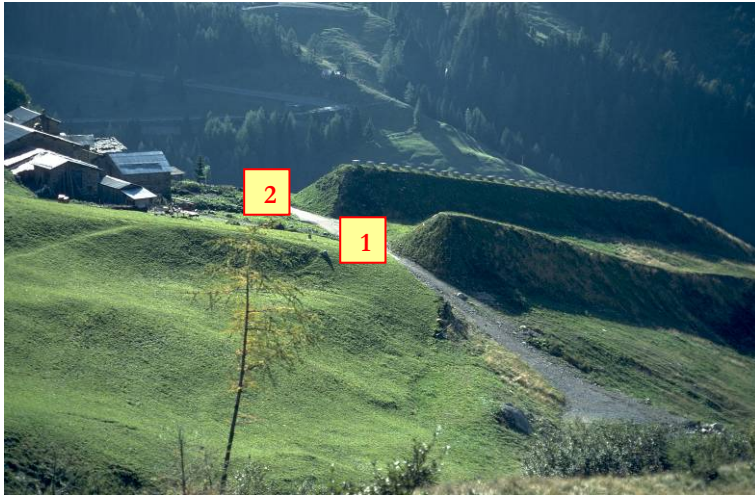
Deflecting dam 1
[photo by Moro, 2007].



[Ortho photo 2006, <http://www.pcn.minambiente.it>].

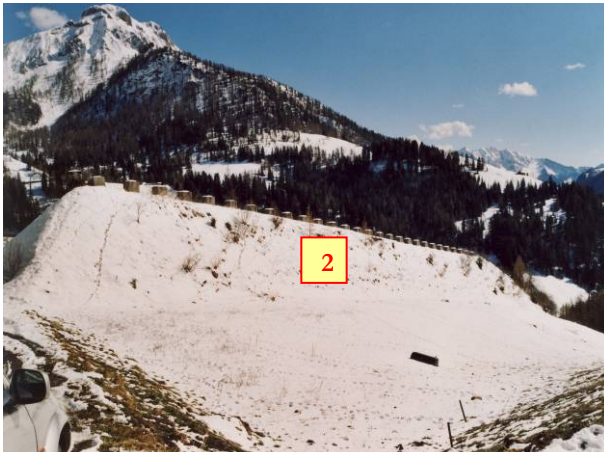
AVALANCHE FEATURES	
PAST EXTREME AVALANCHE EVENT	
DETACHMENT ELEVATION	2000-2200 m s.l.m.
SLOPE INCLINATION	
CHANNEL WIDTH	

DEFLECTING DAMS OF FOPPOLO, VALLE BREMBANA, ITALY

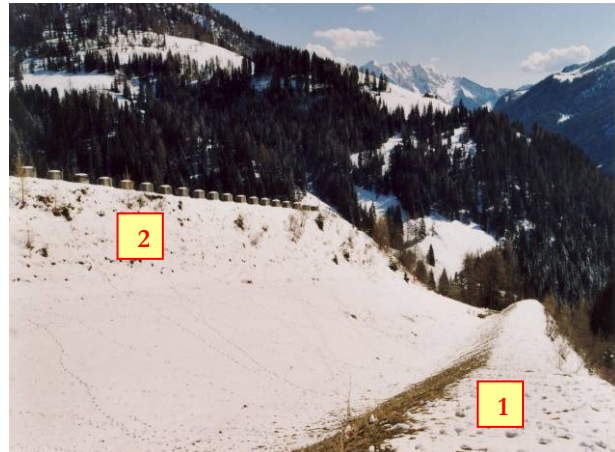


GEOGRAPHICAL SETTING	
VILLAGE	Foppolo
MUNICIPALITY	Foppolo
PROVINCE	Bergamo
REGION	Lombardia
COUNTRY	Italy
WORKS FEATURES	
CONSTRUCTION YEAR	
ELEVATION	1615 m s.l.m.
NUMBER AND TYPE	2 deflecting dams
H _{MAX}	
L _{MAX}	
W _{MAX} /Ø	
MATERIAL	Earth covered with concrete teeth
AIM	Protection of Foppolo village

Deflecting dams 1 and 2
[<http://cemadoc.cemagref.fr>].



Deflecting dam 2
[*photo by Moro, 2008*].



Deflecting dams 1 and 2
[*photo by Moro, 2008*].



[Ortho photo 2006, <http://www.pcn.minambiente.it>].

AVALANCHE FEATURES	
PAST EXTREME AVALANCHE EVENT	
DETACHMENT ELEVATION	
SLOPE INCLINATION	
CHANNEL WIDTH	

DEFLECTING DAM OF CAMINATA, VAL DI VIZZE, ITALY



Deflecting dam
[photo by Farina, 2000].

GEOGRAPHICAL SETTING	
VILLAGE	Caminata
MUNICIPALITY	Val di Vizze
PROVINCE	Bolzano
REGION	Trentino Alto Adige
COUNTRY	Italy
WORKS FEATURES	
CONSTRUCTION YEAR	
ELEVATION	948 m s.l.m.
NUMBER AND TYPE	1 deflecting dam
H _{MAX}	
L _{MAX}	
W _{MAX} /Ø	
MATERIAL	Earth and base in heap of stones
AIM	Protection of Caminata village



Deflecting dam
[photo by Farina, 2000].



Deflecting dam
[photo by Santi, 1985].



[Ortho photo 2006, <http://www.pcn.minambiente.it>].

AVALANCHE FEATURES	
PAST EXTREME AVALANCHE EVENT	
DETACHMENT ELEVATION	
SLOPE INCLINATION	
CHANNEL WIDTH	

RETARDING CONE-SHAPED STRUCTURES OF TASSÈ, VAL DI RABBI, ITALY



GEOGRAPHICAL SETTING	
VILLAGE	Tassè
MUNICIPALITY	Rabbi
PROVINCE	Trento
REGION	Trentino Alto Adige
COUNTRY	Italy
WORKS FEATURES	
CONSTRUCTION YEAR	
ELEVATION	1070 m s.l.m.
NUMBER AND TYPE	9 retarding cone-shaped structures
H _{MAX}	~ 10-12 m
W _{MAX} /Ø	~ 20 m
MATERIAL	Earth and covered by vegetation
DISPOSITION	In chessboard formation
AIM	Protection of the provincial way

Retarding cone-shaped structures
[photo by Trento Province, 1989].



Retarding cone-shaped structures
[photo by Trento Province].



Retarding cone-shaped structures
[photo by Moro, 2007].



AVALANCHE FEATURES	
PAST EXTREME AVALANCHE EVENT	
DETACHMENT ELEVATION	
SLOPE INCLINATION	
CHANNEL WIDTH	~ 40 m

[Ortho photo 2006, <http://www.pcn.minambiente.it>].

RETARDING CONE-SHAPED STRUCTURES OF ZANON, VAL NIGOLAIA, ITALY



GEOGRAPHICAL SETTING	
VILLAGE	Zanon
MUNICIPALITY	Rabbi
PROVINCE	Trento
REGION	Trentino Alto Adige
COUNTRY	Italy
WORKS FEATURES	
CONSTRUCTION YEAR	
ELEVATION	1095 m s.l.m.
NUMBER AND TYPE	7 retarding cone-shaped structures
H _{MAX}	~ 3-5 m
W _{MAX} /Ø	~ 10 m
MATERIAL	Earth, base of stones and upstream stone covered
DISPOSITION	Along the torrent
AIM	Protection of Zanon village

Retarding cone-shaped structures
[photo by Trento Province].



Retarding cone-shaped structures
[photo by Bezzi, 2004].



Retarding cone-shaped structures
[photo by Trento Province].



[Ortho photo 2006, <http://www.pcn.minambiente.it>].

AVALANCHE FEATURES	
PAST EXTREME AVALANCHE EVENT	
DETACHMENT ELEVATION	
SLOPE INCLINATION	
CHANNEL WIDTH	~ 30 m

RETARDING CONE-SHAPED STRUCTURES OF PASSO TONALE, VAL VERMIGLIO, ITALY



GEOGRAPHICAL SETTING	
VILLAGE	Passo Tonale
MUNICIPALITY	Vermiglio
PROVINCE	Trento
REGION	Trentino Alto Adige
COUNTRY	Italy
WORKS FEATURES	
CONSTRUCTION YEAR	
ELEVATION	1884 m s.l.m.
NUMBER AND TYPE	11 retarding cone-shaped structures
H _{MAX}	~ 9-10 m
W _{MAX} /Ø	~ 22 m
MATERIAL	Earth and upstream stone covered
DISPOSITION	In chessboard formation
AIM	Protection of "Passo Tonale - Passo Paradiso" cableway station

Retarding cone-shaped structures
[photo by Trento Province, 1989].



Retarding cone-shaped structures
[photo by Bezzi, 2004].

Retarding cone-shaped structures
[photo by Bezzi, 2004].



AVALANCHE FEATURES	
PAST EXTREME AVALANCHE EVENT	
DETACHMENT ELEVATION	
SLOPE INCLINATION	
CHANNEL WIDTH	~ 80 m

[Ortho photo 2006, <http://www.pcn.minambiente.it>].

RETARDING CONE-SHAPED STRUCTURES OF TRAFOI, VALLE DI TRAFOI, ITALY



Retarding cone-shaped structures
[photo by Moro, 2007].

GEOGRAPHICAL SETTING	
VILLAGE	Trafoi
MUNICIPALITY	Stelvio
PROVINCE	Bolzano
REGION	Trentino Alto Adige
COUNTRY	Italy
WORKS FEATURES	
CONSTRUCTION YEAR	
ELEVATION	1543 m s.l.m.
NUMBER AND TYPE	24 retarding cone-shaped structures
H _{MAX}	
W _{MAX} /Ø	
MATERIAL	Earth and upstream stone covered
DISPOSITION	In chessboard formation
AIM	Protection of Trafoi village



Retarding cone-shaped structures
[photo by Moro, 2007].



Retarding cone-shaped structures
[photo by Moro, 2007].



[Ortho photo 2006, <http://www.pcn.minambiente.it>].

AVALANCHE FEATURES	
PAST EXTREME AVALANCHE EVENT	
DETACHMENT ELEVATION	2000-2200 m s.l.m.
SLOPE INCLINATION	
CHANNEL WIDTH	

RETARDING CONE-SHAPED STRUCTURES OF LAGO CAVIA, VAL DI S. PELLEGRINO, ITALY



GEOGRAPHICAL SETTING	
VILLAGE	Lago Cavia
MUNICIPALITY	Falcade
PROVINCE	Belluno
REGION	Veneto
COUNTRY	Italy
WORKS FEATURES	
CONSTRUCTION YEAR	2006
ELEVATION	2124 m s.l.m.
NUMBER AND TYPE	5 retarding cone-shaped structures
H_{MAX} W_{MAX}/\varnothing MATERIAL	Earth and upstream stone covered
DISPOSITION	In chessboard formation
AIM	Protection of "Col Margherita - Lago Cavia" ski run

Retarding cone-shaped structures
[photo by Tomaselli, 2007].



Retarding cone-shaped structures
[photo by Moro, 2007].



Retarding cone-shaped structures
[photo by Moro, 2007].



AVALANCHE FEATURES	
PAST EXTREME AVALANCHE EVENT	
DETACHMENT ELEVATION	2200 m s.l.m.
SLOPE INCLINATION	
CHANNEL WIDTH	

[Ortho photo 2006, <http://www.pcn.minambiente.it>].

RETARDING CONE-SHAPED STRUCTURES OF PASSO BROCON, VALLE DEL TESINO, ITALY



GEOGRAPHICAL SETTING	
VILLAGE	Passo Brocon
MUNICIPALITY	Castello Tesino
PROVINCE	Trento
REGION	Trentino Alto Adige
COUNTRY	Italy
WORKS FEATURES	
CONSTRUCTION YEAR	
ELEVATION	1616 m s.l.m.
NUMBER AND TYPE	4 retarding cone-shaped structures
H_{MAX}	
W_{MAX}/\varnothing	~ 9 m
MATERIAL	Earth and covered by vegetation
DISPOSITION	In chessboard formation
AIM	Protection of the way to Passo Brocon



Retarding cone-shaped structures
[photo by Trento Province].



AVALANCHE FEATURES	
PAST EXTREME AVALANCHE EVENT	
DETACHMENT ELEVATION	
SLOPE INCLINATION	
CHANNEL WIDTH	~ 35 m

[Ortho photo 2006, <http://www.pcn.minambiente.it>].

RETARDING CONE-SHAPED STRUCTURES OF PLAN, VAL DI PLAN, ITALY



GEOGRAPHICAL SETTING	
VILLAGE	Plan
MUNICIPALITY	Moso in Passiria
PROVINCE	Bolzano
REGION	Trentino Alto Adige
COUNTRY	Italy
WORKS FEATURES	
CONSTRUCTION YEAR	
ELEVATION	1627 m s.l.m.
NUMBER AND TYPE	3 retarding cone-shaped structures
H_{MAX} W_{MAX}/\varnothing	
MATERIAL	Earth and upstream stone covered
DISPOSITION	
AIM	Protection of Plan village

Retarding cone-shaped structure
[photo by Farina, 2000].



Retarding cone-shaped structure
[photo by Farina, 2000].



Retarding cone-shaped structures
[photo by Farina, 2000].



[Ortho photo 2006, <http://www.pcn.minambiente.it>].

AVALANCHE FEATURES	
PAST EXTREME AVALANCHE EVENT	
DETACHMENT ELEVATION	
SLOPE INCLINATION	
CHANNEL WIDTH	

DIRECT PROTECTION STRUCTURES: PROTECTING WEDGE OF PEQUEREL, VAL CHISONE, ITALY



GEOGRAPHICAL SETTING	
VILLAGE	Pequerel
MUNICIPALITY	Fenestrelle
PROVINCE	Torino
REGION	Piemonte
COUNTRY	Italy
WORKS FEATURES	
CONSTRUCTION YEAR	1716
ELEVATION	1730 m s.l.m.
NUMBER AND TYPE	1 protecting wedge
H _{MAX}	~3,5 m
L _{MAX}	~90,0 m
W _{MAX} /Ø	~150,0 m
MATERIAL	Dry wall with square stones and concrete
AIM	Protection of the Pequerel village

Pequerel village
[photo by Municipality of Fenestrelle].



Protecting wedge
[photo by Moro, 2006].



Protecting wedge
[photo by Moro, 2006].



[Ortho photo 2006, <http://www.pcn.minambiente.it>].

AVALANCHE FEATURES	
PAST EXTREME AVALANCHE EVENT	1706
DETACHMENT ELEVATION	
SLOPE INCLINATION	
CHANNEL WIDTH	

**DIRECT PROTECTION STRUCTURES: PROTECTING WEDGE OF
S. LUCANO, VALLE DI S. LUCANO, ITALY**



Church of S. Lucano
[photo by Moro, 2006].

GEOGRAPHICAL SETTING	
VILLAGE	S. Lucano
MUNICIPALITY	Taibon Agordino
PROVINCE	Belluno
REGION	Piemonte
COUNTRY	Italy
WORKS FEATURES	
CONSTRUCTION YEAR	1635
ELEVATION	600 m s.l.m.
NUMBER AND TYPE	1 protecting wedge
H _{MAX}	~3,5 m
L _{MAX}	~7,0 m
W _{MAX} /Ø	~5,0 m
MATERIAL	Dry wall with square stones
AIM	Direct protection of S. Lucano Church



Church of S. Lucano
[photo by Moro, 2006].



Protecting wedge
[photo by Moro, 2006].



[Ortho photo 2006, <http://www.pcn.minambiente.it>].

AVALANCHE FEATURES	
PAST EXTREME AVALANCHE EVENT	
DETACHMENT ELEVATION	
SLOPE INCLINATION	
CHANNEL WIDTH	

**DIRECT PROTECTION STRUCTURES: PROTECTING WEDGE OF
DAVOS FRAUENKIRCH, LANDWASSER, SWITZERLAND**



Church of Davos Frauenkirch
[photo by Moro, 2006].

GEOGRAPHICAL SETTING	
VILLAGE	Davos Frauenkirch
MUNICIPALITY	Davos
DISTRICT	Prättigau/Davos
CANTON	Grisons
COUNTRY	Switzerland
WORKS FEATURES	
CONSTRUCTION YEAR	1700
ELEVATION	1500 m s.l.m.
NUMBER AND TYPE	Apse in shape of wedge
H _{MAX}	~10,5 m
L _{MAX}	~7,0 m
W _{MAX} /Ø	~10,0 m
MATERIAL	
AIM	Direct protection of the church of Davos Frauenkirch



Church of Davos Frauenkirch
[photo by Aebi, 2006].



Wedge-shaped apse
[Fraser, 1970].



[Ortho photo, <http://map.search.ch>].

AVALANCHE FEATURES	
PAST EXTREME AVALANCHE EVENT	1606
DETACHMENT ELEVATION	
SLOPE INCLINATION	
CHANNEL WIDTH	

**DIRECT PROTECTION STRUCTURES: RETARDING CONE-SHAPED STRUCTURE OF
PRESSON, VAL DI SOLE, ITALY**



**Retarding cone-shaped structure
[photo by Bezzi, 2004].**

GEOGRAPHICAL SETTING	
VILLAGE	Presson
MUNICIPALITY	Monclassico
PROVINCE	Trento
REGION	Trentino Alto Adige
COUNTRY	Italy
WORKS FEATURES	
CONSTRUCTION YEAR	
ELEVATION	745 m s.l.m.
NUMBER AND TYPE	1 retarding mound
H _{MAX}	~ 5 m
L _{MAX}	
W _{MAX} /Ø	~ 11 m
MATERIAL	Earth, upstream stone covered and now covered of vegetation
AIM	Direct protection of a house of Presson



**Retarding cone-shaped structure
[photo by Moro, 2007].**



**Retarding cone-shaped structure
[photo by Moro, 2007].**



[Ortho photo 2006, <http://www.pcn.minambiente.it>].

AVALANCHE FEATURES	
PAST EXTREME AVALANCHE EVENT	
DETACHMENT ELEVATION	
SLOPE INCLINATION	
CHANNEL WIDTH	

**DIRECT PROTECTION STRUCTURES: PROTECTING WEDGE OF
TASSÈ, VAL DI RABBI, ITALY**



Protecting wedge
[photo by Moro, 2007].

GEOGRAPHICAL SETTING	
VILLAGE	Tassè
MUNICIPALITY	Rabbi
PROVINCE	Trento
REGION	Trentino Alto Adige
COUNTRY	Italy
WORKS FEATURES	
CONSTRUCTION YEAR	
ELEVATION	1070 m s.l.m.
NUMBER AND TYPE	1 protecting wedge
H _{MAX}	
L _{MAX}	
W _{MAX} /Ø	
MATERIAL	Dry wall with square stones
AIM	Direct protection of a house of Tassè



Protecting wedge
[photo by Moro, 2007].



Protecting wedge
[photo by Moro, 2007].



[Ortho photo 2006, <http://www.pcn.minambiente.it>].

AVALANCHE FEATURES	
PAST EXTREME AVALANCHE EVENT	
DETACHMENT ELEVATION	
SLOPE INCLINATION	
CHANNEL WIDTH	

**DIRECT PROTECTION STRUCTURES: PROTECTING WEDGE OF
PORTA VESCOVO (1), VAL DI LIVINALLONGO, ITALY**



GEOGRAPHICAL SETTING	
VILLAGE	Porta Vescovo
MUNICIPALITY	Livinallongo del Col di Lana
PROVINCE	Belluno
REGION	Veneto
COUNTRY	Italy
WORKS FEATURES	
CONSTRUCTION YEAR	
ELEVATION	
NUMBER AND TYPE	1 protecting wedge
H _{MAX}	
L _{MAX}	
W _{MAX} /Ø	
MATERIAL	Reinforced concrete
AIM	Direct protection of "Arabba - Porta Vescovo" cableway pylon

Protecting wedge
[photo by Tomaselli, 2007].



Protecting wedge
[photo by Arabba Avalanche Centre].



Protecting wedge
[photo by Tomaselli, 2007].



[Ortho photo 2006, <http://www.pcn.minambiente.it>].

AVALANCHE FEATURES	
PAST EXTREME AVALANCHE EVENT	
DETACHMENT ELEVATION	2478 m s.l.m.
SLOPE INCLINATION	
CHANNEL WIDTH	

**DIRECT PROTECTION STRUCTURES: PROTECTING WEDGE OF
PORTA VESCOVO (2), VAL DI LIVINALLONGO, ITALY**



GEOGRAPHICAL SETTING	
VILLAGE	Porta Vescovo
MUNICIPALITY	Livinallongo del Col di Lana
PROVINCE	Belluno
REGION	Veneto
COUNTRY	Italy
WORKS FEATURES	
CONSTRUCTION YEAR	
ELEVATION	2200 m s.l.m.
NUMBER AND TYPE	1 protecting wedge
H _{MAX}	
L _{MAX}	
W _{MAX} /Ø	
MATERIAL	Reinforced concrete
AIM	Direct protection of "Arabba - Porta Vescovo" cableway pylon

Protecting wedge
[photo by Tomaselli, 2007].



Protecting wedge
[photo by Moro, 2007].



Protecting wedge
[photo by Moro, 2007].



[Ortho photo 2006, <http://www.pcn.minambiente.it>].

AVALANCHE FEATURES	
PAST EXTREME AVALANCHE EVENT	
DETACHMENT ELEVATION	2478 m s.l.m.
SLOPE INCLINATION	
CHANNEL WIDTH	

CATCHING DAM OF VILLE CLOZE, VAL CHISONE, ITALY



Catching dam
[photo by Moro, 2006].

GEOGRAPHICAL SETTING	
VILLAGE	Ville Cloze
MUNICIPALITY	Finestrelle
PROVINCE	Torino
REGION	Piemonte
COUNTRY	Italy
WORKS FEATURES	
CONSTRUCTION YEAR	1888/1901
ELEVATION	1100 m s.l.m.
NUMBER AND TYPE	1 catching dam
H _{MAX}	~2,0 m
L _{MAX}	~200 m
W _{MAX} /Ø	~2,0 m
MATERIAL	Dry wall with square stones
AIM	Protection of Ville Cloze village



Catching dam
[photo by Moro, 2006].



Catching dam
[photo by Municipality of Finestrelle].



[Ortho photo 2006, <http://www.pcn.minambiente.it>].

AVALANCHE FEATURES	
PAST EXTREME AVALANCHE EVENT	1885/1888
DETACHMENT ELEVATION	
SLOPE INCLINATION	
CHANNEL WIDTH	

CATCHING DAM OF CERTOSA, VAL SENALES, ITALY



Catching dam
[photo by Moro, 2007].

GEOGRAPHICAL SETTING	
VILLAGE	Certosa
MUNICIPALITY	Senales
PROVINCE	Bolzano
REGION	Trentino Alto Adige
COUNTRY	Italy
WORKS FEATURES	
CONSTRUCTION YEAR	2006
ELEVATION	1327 m s.l.m.
NUMBER AND TYPE	1 catching dam
H _{MAX}	~ 4,5 m
L _{MAX}	~ 250 m
W _{MAX} /Ø	~ 5,0 m
MATERIAL	Dry wall with square stones and concrete
AIM	Protection of the provincial way



Catching dam
[photo by Moro, 2007].



Catching dam
[photo by Moro, 2007].



[Ortho photo 2006, <http://www.pcn.minambiente.it>].

AVALANCHE FEATURES	
PAST EXTREME AVALANCHE EVENT	
DETACHMENT ELEVATION	2100-2400 m s.l.m.
SLOPE INCLINATION	36°
CHANNEL WIDTH	

**COMBINATIONS OF AVALANCHE PROTECTION STRUCTURES:
VERNAGO, VAL SENALES, ITALY**



GEOGRAPHICAL SETTING	
VILLAGE	Vernago
MUNICIPALITY	Senales
PROVINCE	Bolzano
REGION	Trentino Alto Adige
COUNTRY	Italy
WORKS FEATURES	
CONSTRUCTION YEAR	
ELEVATION	1640 m s.l.m.
NUMBER AND TYPE	<ul style="list-style-type: none"> • 1 deflecting dam; • 12 retarding cone-shaped structures; • 1 catching dam.
AIM	Protection of the provincial way

Deflecting dam 1, 2 and retarding cone-shaped structures
[photo by Bolzano Province].



Deflecting dam 1
[photo by Moro, 2007].



Deflecting dam 1
[photo by Moro, 2007].



Retarding cone-shaped structures
[photo by Moro, 2007].



Retarding cone-shaped structure
[photo by Bezzi, 2004].

COMBINATIONS OF AVALANCHE PROTECTION STRUCTURES:
VERNAGO, VAL SENALES, ITALY



Retarding cone-shaped structures
[photo by Bezzi, 2004].



Retarding cone-shaped structures
[photo by Bezzi, 2004].



Catching dam 2
[photo by Moro, 2007].



Catching dam 2
[photo by Moro, 2007].



[Ortho photo 2006, <http://www.pcn.minambiente.it>].

AVALANCHE FEATURES	
PAST EXTREME AVALANCHE EVENT	
DETACHMENT ELEVATION	1690 m s.l.m.
SLOPE INCLINATION	27°
CHANNEL WIDTH	35 m

**COMBINATIONS OF AVALANCHE PROTECTION STRUCTURES:
SON FORCA, VALLE D'AMPEZZO, ITALY**



Catching dam and protecting wedge
[photo by Tomaselli, 2007].

GEOGRAPHICAL SETTING	
VILLAGE	Grava di Stounies
MUNICIPALITY	Cortina d'Ampezzo
PROVINCE	Belluno
REGION	Veneto
COUNTRY	Italy
WORKS FEATURES	
CONSTRUCTION YEAR	2235 m s.l.m.
ELEVATION	<ul style="list-style-type: none"> • 1 catching dam; • 1 protecting wedge.
NUMBER AND TYPE	
AIM	Protection of "Son Forca" mountain dew and "Son Forca – Rio Gere" station



Catching dam and protecting wedge
[photo by Tomaselli, 2007].



Catching dam and protecting wedge
[photo by CAI of Lugo di Romagna].



[Ortho photo 2006, <http://www.pcn.minambiente.it>].

AVALANCHE FEATURES	
PAST EXTREME AVALANCHE EVENT	
DETACHMENT ELEVATION	
SLOPE INCLINATION	
CHANNEL WIDTH	

**COMBINATIONS OF AVALANCHE PROTECTION STRUCTURES:
FOPPOLO (1), VALLE BREMBANA, ITALY**



GEOGRAPHICAL SETTING	
VILLAGE	Foppolo
MUNICIPALITY	Foppolo
PROVINCE	Bergamo
REGION	Lombardia
COUNTRY	Italy
WORKS FEATURES	
CONSTRUCTION YEAR	1615 m s.l.m.
ELEVATION	
NUMBER AND TYPE	<ul style="list-style-type: none"> • 11 retarding tooth-shaped structures I; • 1 retarding tooth-shaped structure II; • 4 retarding tooth-shaped structures III; • 1 catching dam.
AIM	Protection of Foppolo village

Deflecting dam 1 and retarding tooth-shaped structures
[photo by Moro, 2008].



Retarding tooth-shaped structures I
[photo by Moro, 2008].



Retarding tooth-shaped structures I
[photo by Moro, 2008].



Retarding tooth-shaped structures I and II
[photo by Moro, 2008].



Retarding tooth-shaped structure II
[photo by Moro, 2008].

**COMBINATIONS OF AVALANCHE PROTECTION STRUCTURES:
FOPPOLO (1), VALLE BREMBANA, ITALY**



Retarding tooth-shaped structures III
[<http://cemadoc.cemagref.fr>].



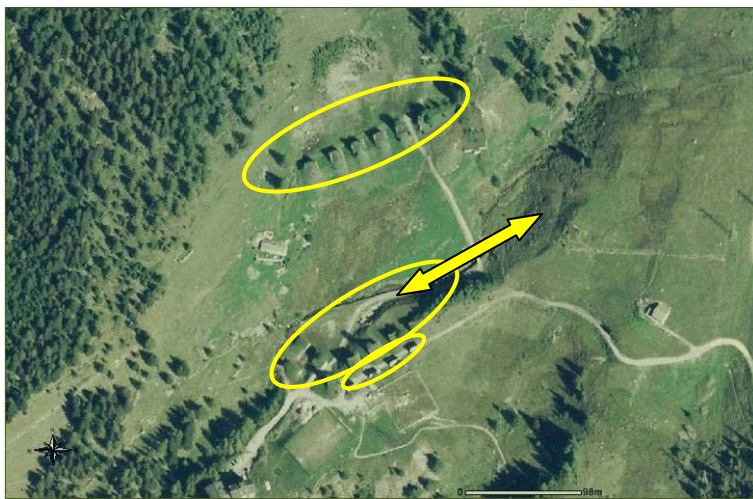
Retarding tooth-shaped structures III
[*photo by Moro, 2008*].



Catching dam 1
[*photo by Moro, 2008*].



Catching dam 1
[*photo by Moro, 2008*].



[Ortho photo 2006, <http://www.pcn.minambiente.it>].

AVALANCHE FEATURES	
PAST EXTREME AVALANCHE EVENT	
DETACHMENT ELEVATION	
SLOPE INCLINATION	
CHANNEL WIDTH	

**COMBINATIONS OF AVALANCHE PROTECTION STRUCTURES:
FOPPOLO (2), VALLE BREMBANA, ITALY**



GEOGRAPHICAL SETTING	
VILLAGE	Foppolo
MUNICIPALITY	Foppolo
PROVINCE	Bergamo
REGION	Lombardia
COUNTRY	Italy
WORKS FEATURES	
CONSTRUCTION YEAR	
ELEVATION	1615 m s.l.m.
NUMBER AND TYPE	<ul style="list-style-type: none"> • 3 deflecting dams; • 1 catching dam.
AIM	Protection of Foppolo village

**Deflecting dams 2, 3, 4 and catching dam 1
[photo by Bergamo Province].**



**Deflecting dams 2, 3 and 4
[photo by Moro, 2008].**



**Deflecting dam 3
[photo by Moro, 2008].**

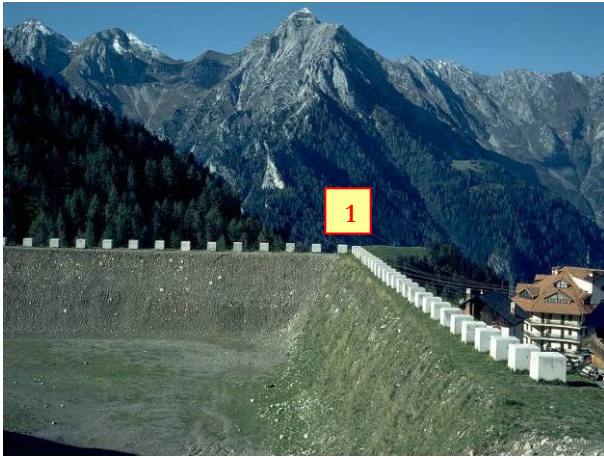


**Deflecting dam 4
[photo by Moro, 2008].**



**Deflecting dams 2, 4 and catching dam 1
[photo by Moro, 2008].**

COMBINATIONS OF AVALANCHE PROTECTION STRUCTURES:
FOPPOLO (2), VALLE BREMBANA, ITALY



Catching dam 1
[<http://cemadoc.cemagref.fr>].



Catching dam 1
[photo by Moro, 2008].



Catching dam 1
[photo by Moro, 2008].



Catching dam 1
[photo by Moro, 2008].



[Ortho photo 2006, <http://www.pcn.minambiente.it>].

AVALANCHE FEATURES	
PAST EXTREME AVALANCHE EVENT	
DETACHMENT ELEVATION	
SLOPE INCLINATION	
CHANNEL WIDTH	

**COMBINATIONS OF AVALANCHE PROTECTION STRUCTURES:
TRABUCHELLO, VALLE MENCUCCA, ITALY**



GEOGRAPHICAL SETTING	
VILLAGE	Trabuchello
MUNICIPALITY	Isola di Fronda
PROVINCE	Bergamo
REGION	Lombardia
COUNTRY	Italy
WORKS FEATURES	
CONSTRUCTION YEAR	
ELEVATION	
NUMBER AND TYPE	<ul style="list-style-type: none"> • 1 deflecting dam; • 6 retarding tooth-shaped structures.
AIM	Protection of the provincial way

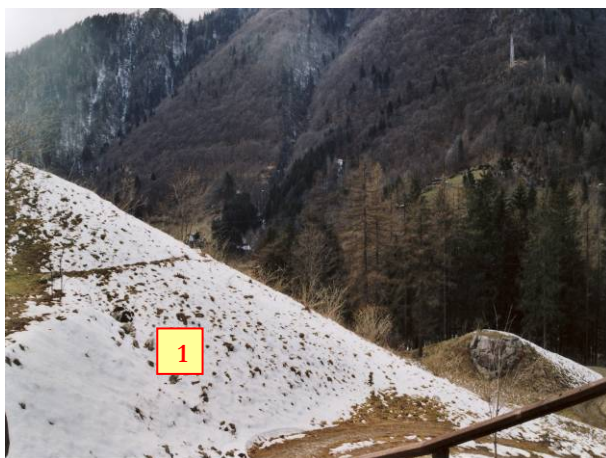
Deflecting dam 1
[photo by Moro, 2008].



Deflecting dam 1
[photo by Moro, 2008].



Deflecting dam 1
[photo by Moro, 2008].



Deflecting dam 1
[photo by Moro, 2008].



Retarding tooth-shaped structures
[photo by Moro, 2008].

COMBINATIONS OF AVALANCHE PROTECTION STRUCTURES:
TRABUCHELLO, VALLE MENCUCCA, ITALY



Retarding tooth-shaped structures
[photo by Moro, 2008].



Retarding tooth-shaped structures
[photo by Moro, 2008].



Retarding tooth-shaped structure
[photo by Moro, 2008].



Retarding tooth-shaped structures
[photo by Moro, 2008].



[Ortho photo 2006, <http://www.pcn.minambiente.it>].

AVALANCHE FEATURES	
PAST EXTREME AVALANCHE EVENT	
DETACHMENT ELEVATION	
SLOPE INCLINATION	
CHANNEL WIDTH	

**COMBINATIONS OF AVALANCHE PROTECTION STRUCTURES:
TACONNAZ, VALLEE DE CHAMONIX MONT BLANC, FRANCE**



**The Taconnaz avalanche site
[photo by Bellot, 2007].**

GEOGRAPHICAL SETTING	
VILLAGE	Taconnaz
MUNICIPALITY	Les Houches
DEPARTMENT	Haute-Savoie
REGION	Rhône-Alpes
COUNTRY	France
WORKS FEATURES	
CONSTRUCTION YEAR	1990
ELEVATION	1180-1250 m s.l.m.
NUMBER AND TYPE	<ul style="list-style-type: none"> • 1 deflecting dam; • 14 retarding tooth-shaped structures I; • 2 retarding tooth-shaped structures II; • 11 vertical walls; • 4 catching dams.
AIM	Protection of the Taconnaz, Vers-le-Nant, Côte-du-Mont villages



**The Taconnaz avalanche site
[http://cemadoc.cemagref.fr].**



**The Taconnaz avalanche site
[http://cemadoc.cemagref.fr].**



**Deflecting dam 5
[http://cemadoc.cemagref.fr].**



**Deflecting dam 5
[http://cemadoc.cemagref.fr].**

**COMBINATIONS OF AVALANCHE PROTECTION STRUCTURES:
TACONNAZ, VALLEE DE CHAMONIX MONT BLANC, FRANCE**



Retarding tooth-shaped structures I and vertical walls [http://cemadoc.cemagref.fr].



Retarding tooth-shaped structures I and vertical walls [http://cemadoc.cemagref.fr].



Retarding tooth-shaped structures I [http://cemadoc.cemagref.fr].



Retarding tooth-shaped structures I [http://cemadoc.cemagref.fr].



Vertical walls [http://cemadoc.cemagref.fr].



Vertical walls [http://cemadoc.cemagref.fr].

COMBINATIONS OF AVALANCHE PROTECTION STRUCTURES:
TACONNAZ, VALLEE DE CHAMONIX MONT BLANC, FRANCE



Retarding tooth-shaped structures II
[<http://cemadoc.cemagref.fr>].



Retarding tooth-shaped structures II
[<http://cemadoc.cemagref.fr>].



Catching dam 1
[<http://cemadoc.cemagref.fr>].



Catching dam 1
[photo by Moro, 2007].



[Ortho photo 2006, <http://www.ign.fr>].

AVALANCHE FEATURES	
PAST EXTREME AVALANCHE EVENT	1999
DETACHMENT ELEVATION	3000-4000 m s.l.m.
SLOPE INCLINATION	
CHANNEL WIDTH	

Creazione Divina

*Il vento soffiava lento, accarezzandolo dolcemente
le ondulate forme della montagna, formando sulla neve
dei disegni vivi, sensibilmente incantati.
L'apparente candido mantello, a tratti soffice,
velava in un'impalpabile atmosfera tutta
la sua irresistibile evanescenza.*

*Mentre salivo sorretto dalle mie sensazioni
avrei voluto immergermi in esse, fino a diventare
un piccolo, fragile, cristallo.*

*Il vento correva intorno senza farsi vedere,
spinto da chissà quale misteriosa passione.*

*Ero alla ricerca di creazione innate, ma quale
sia stato il punto segreto posto lì a sconvolgere il tempo
mi è difficile ancora adesso percepire;
comunque il tempo di capire arrivò ancora prima che aprissi gli occhi:*

*il vento cessò di esistere, la neve rifletteva i suoi colori nel cielo
fino a coprirlo intensamente di bianco.*

*Mi sentii come preso da tanti, insieme.
Rotolando lungo il pendio, ora nella neve,
ora nell'aria, combattevo contro questa inerzia futura
piena d'incertezze.
Non potendo vedere, coprivo le mie immagini
Con dei probabili colori. Mi sentivo avvolto in ogni parte del corpo,
come in una grandiosa carezza arrivata lì improvvisa.
Correva tutta la mia vita davanti, senza
che ne potessi fermare un attimo.
Sentendomi così immerso, il mio respiro rallentò lentamente
la sua sete. Aprendo gli occhi nel buoi vidi il bianco più
assoluto: cristalli argentati luccicavano intorno,
in un irreale attimo senza fine, in un'atmosfera così
stranamente persa. Mi resi conto solo allora di
essere in una creazione divina, impropriamente
chiamata valanga: non sapevo più se il cielo era
sotto o sopra. Il vento e le sue illusioni li
sentivo lontani.*

Le radici del tempo entrarono in me.

*Mi abbandonai così, senza reagire, lasciando
la mia immagine dentro di lei.
Mi senti di nuovo trasportare da questo suo stretto vestito bianco,
fino a sentirmi scuotere nelle sue mani.*

Poi il vuoto, il niente, l'incanto.

(Eraldo Meraldi)

(in *Neve e Valanghe*, AINEVA, No. 8, 1989).

